



**HAL**  
open science

# Novel chalcogenide based glasses, ceramics and polycrystalline materials for thermoelectric application

Bhuvanesh Srinivasan

► **To cite this version:**

Bhuvanesh Srinivasan. Novel chalcogenide based glasses, ceramics and polycrystalline materials for thermoelectric application. Material chemistry. Université de Rennes, 2018. English. NNT: 2018REN1S036 . tel-01974992

**HAL Id: tel-01974992**

**<https://theses.hal.science/tel-01974992>**

Submitted on 9 Jan 2019

**HAL** is a multi-disciplinary open access archive for the deposit and dissemination of scientific research documents, whether they are published or not. The documents may come from teaching and research institutions in France or abroad, or from public or private research centers.

L'archive ouverte pluridisciplinaire **HAL**, est destinée au dépôt et à la diffusion de documents scientifiques de niveau recherche, publiés ou non, émanant des établissements d'enseignement et de recherche français ou étrangers, des laboratoires publics ou privés.

# THESE DE DOCTORAT DE

L'UNIVERSITE DE RENNES 1  
COMUE UNIVERSITE BRETAGNE LOIRE

ECOLE DOCTORALE N° 596  
*Matière Molécules et Matériaux*  
Spécialité : Sciences des Matériaux

Par

**Bhuvanesh SRINIVASAN**

## **Novel Chalcogenide based Glasses, Ceramics and Polycrystalline Materials for Thermoelectric Application**

Thèse présentée et soutenue à Rennes, le 10 Décembre 2018  
Unité de recherche : Institut des Sciences Chimiques de Rennes, UMR CNRS 6226

### **Composition du Jury :**

Président	<b>Jean-François HALET</b>	Directeur de Recherche CNRS, Université de Rennes 1
Rapporteurs	<b>Sylvie HEBERT</b> <b>Annie PRADEL</b>	Directrice de Recherche CNRS, Université de Caen Normandie Directrice de Recherche CNRS, Université de Montpellier 2
Examineur	<b>Michael J. REECE</b>	Professeur, Queen Mary University of London
Directeur de thèse	<b>Bruno BUREAU</b>	Professeur, Université de Rennes 1
Co-directeur de thèse	<b>Catherine BOUSSARD-PLEDEL</b>	Ingénieur de Recherche CNRS, Université de Rennes 1
Invités	<b>Régis GAUTIER</b> <b>Sergio DI MATTEO</b>	Professeur, École Nationale Supérieure de Chimie de Rennes Professeur, Université de Rennes 1



# வணக்கம்!



Namaste



# **Acknowledgement**



## Acknowledgement

---

First and foremost, I would like to express my sincere gratitude to my academic advisors, Bruno Bureau and Catherine Boussard-Pledel, for their support and guidance. It has been a pleasure to work with them. They trusted in my abilities and gave me the freedom to design and execute my research plan and the liberty to work with different collaborators of my choice. I could not have imagined having a better, friendlier and kinder supervisors for my dissertation.

I offer my sincere gratitude to my industrial advisor, Mike Reece (Nanoforce Technology Ltd., Queen Mary University London), for his kindness and constant support. He provided access to his research facilities and hosted me for a 2 month secondment period, where I had the opportunity to learn about transport property measurements and flash-SPS processing techniques. The secondment was productive, both in terms of training and in terms of results obtained. I would also like to thank Francesco Gucci and Theo Saunders for their help and friendship.

I'm grateful to Sergio Di Matteo for sharing a positive opinion about the V&C lab, which helped me in arriving at a decision to take up this PhD position. I would like to sincerely thank him for recommending my application / candidature, without which I doubt to have got this competitive position. The project on synchrotron studies on Cu-As-Te glasses (Chapter 2 of the thesis) wouldn't have seen the light without his hard work and dedication. His immense contribution is not just limited to my PhD work, but also to my education at master's level (MaMaSELF).

One person whom I bothered a lot during my PhD is Régis Gautier. I'm indebted to him for his valuable contribution in my thesis work. Despite his busy schedule, he is always ready to help. It was only after his involvement, I gained confidence in my thesis. I just can't imagine how my thesis would have gone without his kind involvement. At times, I have put a lot pressure on him, which would have annoyed many others, but he always reacted with a kind smile. Also, I would like to extend my gratitude to his colleague, Bruno Fontaine, for his time and support.

I wouldn't have got the contact of Régis, without the help of Jean-François Halet (whom I shortly refer as JeF). It all started with a casual greeting, when he received an exchange student (Lakshmi) from India. Then it transformed into a productive collaboration, when we decided to work on the theoretical aspects. I'm thankful for the opportunity to work with JeF, who is always willing to help and share his knowledge. He has been a constant source of motivation and support, and has been my mentor and well-wisher, for which I'm truly grateful.

My sincere thanks also goes to Alain Gellé, who has dedicated a great amount of time and has put sustained efforts with the DFT calculations. It's such a pleasure to work with him, who is always ready to give and to learn the knowledge.



## Acknowledgement

---

I would also express my gratitude to François Cheviré for his constant support and kind help with the diffraction data; Vincent Dorcet and Valérie Demange for the TEM analysis; Sylvain Tricot for the Hall measurement; Carmelo Prestipino and Soraya Ababou-Girard for their work on the synchrotron studies on the Cu-As-Te glasses. My predecessor Shuo Cui is also thanked.

Richard Tuley is thanked for hosting me at European Thermodynamics Ltd., Leicester for a short secondment, which me an idea of the practical issues with thermoelectric module fabrications. Katarzyna Placha is thanked for her help during the stay at Leicester.

Many thanks to Sylvie Hébert and Annie Pradel for reviewing my PhD thesis, and other jury members for participating in the defense.

External collaborators, Kanishka Biswas (JNCASR, Bangalore) and Franck Gascoin (CRISMAT, Caen) are thanked for their valuable inputs (pertaining to Chapter 3 of this thesis). Lei Wei (Nanyang Technological University, Singapore) is acknowledged for his interest and further work on Cu-As-Te glass fibers. Pierre Lucas (University of Arizona, Tucson) is thanked for his participation in the mid-defense in June 2017, along with Régis and Sergio.

Special thanks to Thierry Pain, Thierry Jouan and Antoine Gautier for their assistance with the experimental set-ups and equipments. I sincerely thank all the members who were (and are) part of the V&C lab from Oct 2015 – Dec 2018 (both permanent and non-permanent staffs), for their kind help, support, acquaintances and friendship during my PhD tenure. Without all their precious support, it wouldn't have been possible to conduct this research. Friends from SelenOptics and Diafir are also acknowledged. Many thanks to Meenakshi Subudhi for providing Indian food for about 6 months.

I have been fortunate to be recruited in the CoACH-ETN program. Sincere thanks to the program management, consortium members, and dear fellow ESRs for making each and every moment of the time spent during the program (courses, workshops, trainings, consortium meetings, dinners, parties and leisure trips), a truly memorable one. The European Commission's Horizon 2020 research and innovation program under the Marie Skłodowska-Curie grant (GA. 642557) is acknowledged.

Last but not least, I thank my parents, all my friends, well-wishers and family members for their endless encouragement, love and care.





# **French Abstract**



## Préambule en Français

### Développement de verres, vitro-céramiques et céramiques à base de chalcogènes pour des applications en thermoélectricité

#### 1. Introduction

Un matériau thermoélectrique est un transducteur qui transforme une énergie d'origine thermique en énergie électrique et inversement. Ils sont à l'origine de dispositifs qui suscitent un grand intérêt pour des applications dans de nombreux domaines impliquant la conversion directe de la chaleur résiduelle en électricité, effet Seebeck, et, inversement, le refroidissement par effet Peltier. Un tel matériau peut en effet convertir directement la chaleur de différents systèmes (moteurs, soleil, corps vivants...) en électricité et ainsi servir de générateur électrique propre. Le marché des systèmes thermoélectrique est dominé par le tellure de bismuth  $\text{Bi}_2\text{Te}_3$  qui présente les performances les plus intéressantes. Cependant de nouveaux matériaux concurrents apparaissent aujourd'hui (Figure 1), soit grâce à leurs propriétés thermiques et électroniques fondamentales, soit à travers leur mise en forme ou texturation. L'amélioration des propriétés de ces systèmes est donc toujours un enjeu majeur en sciences des matériaux et différentes pistes de travail sont classiquement explorées.

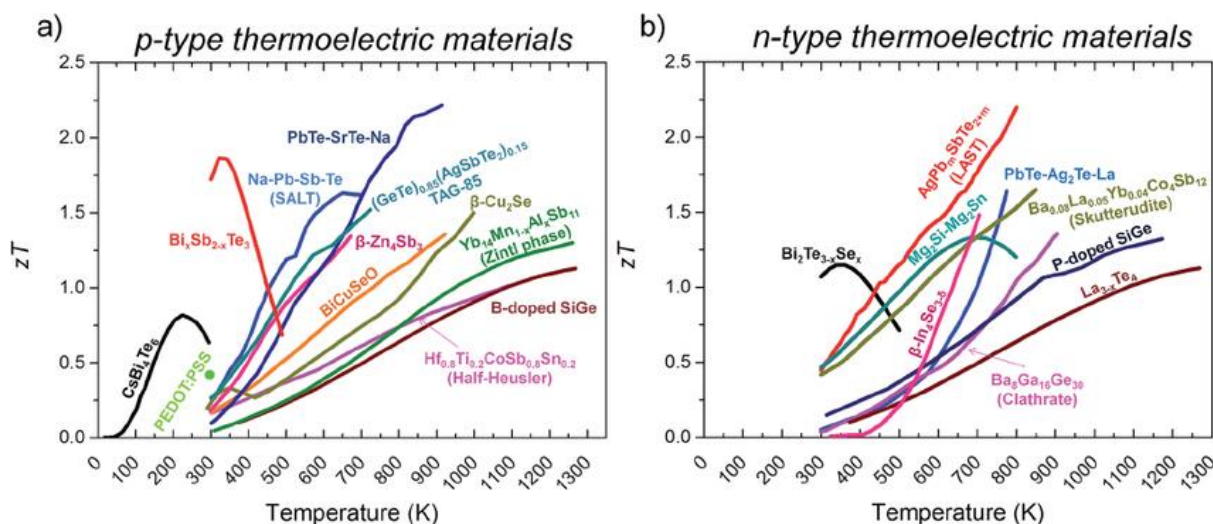
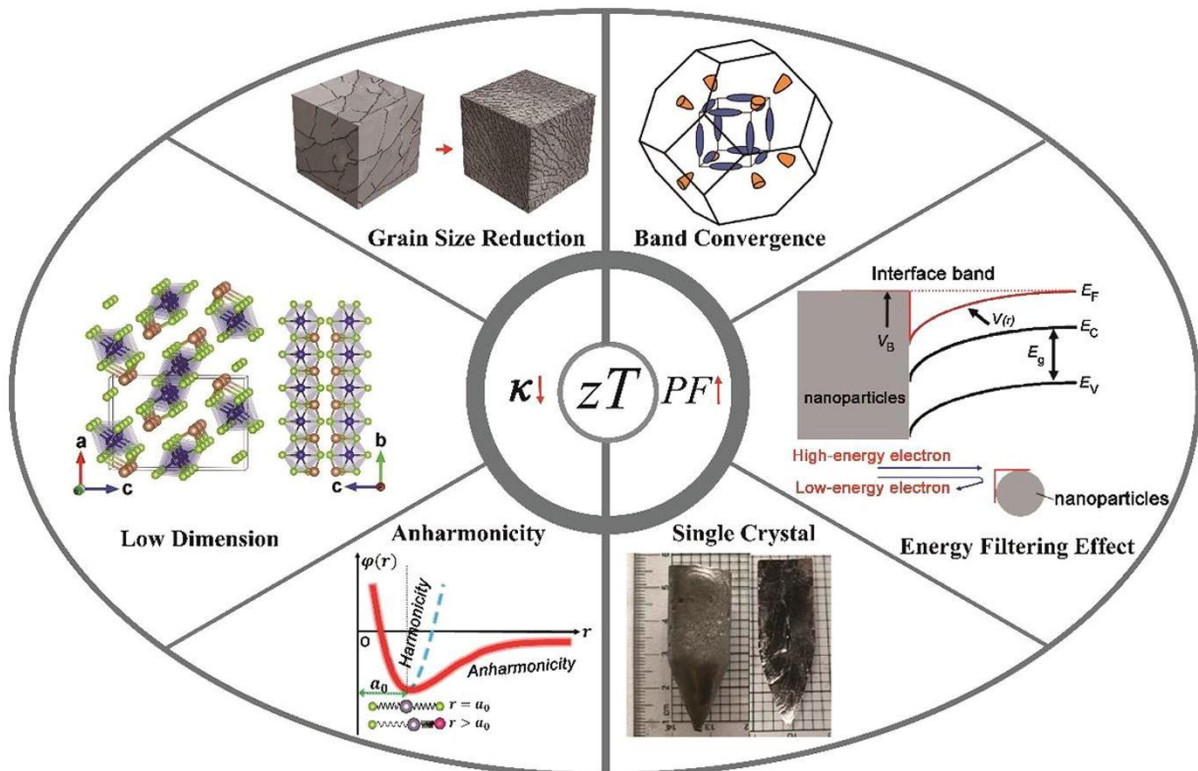


Figure 1. Matériaux thermoélectriques les plus connus, conducteur de type p (a) ou n (b).

Image courtesy: © RSC Advances, 2015.

Le premier enjeu en science de la matière réside dans l'amélioration de l'efficacité de la conversion thermoélectrique. La performance d'un matériau thermoélectrique est liée à la valeur du facteur de mérite  $zT$ , grandeur sans dimension, qui dépend directement de différents paramètres tels que le coefficient de Seebeck ( $S$ ), la conductivité électrique ( $\sigma$ ) et la conductivité thermique ( $\kappa$ ). Ainsi le  $zT$  est calculé à partir de l'équation  $zT = S^2\sigma/\kappa$ , où  $S^2\sigma$  est appelé le facteur de puissance (PF),  $\kappa$  comprend la conductivité thermique électronique  $\kappa_{\text{ele}}$  et la conductivité thermique de réseau  $\kappa_{\text{lat}}$  ( $\kappa = \kappa_{\text{ele}} + \kappa_{\text{lat}}$ ). Pour augmenter ce facteur de mérite il faut donc d'une part augmenter la conductivité électronique du matériau tout en limitant sa conductivité thermique. Cela peut se faire en travaillant sur la nature du matériau lui-même, où l'on voit que des compromis seront à trouver puisque l'augmentation de la conductivité électronique a pour conséquence une augmentation de la conductivité thermique d'origine électronique, et, souvent, diminue le coefficient Seebeck. Il est par ailleurs possible de diminuer la conductivité thermique de réseau en travaillant à la texturation des matériaux pour limiter la propagation des phonons (verres, matériaux polyphasés, composites, poly-cristallins, vitro-céramiques ...), cf. Figure 2.



**Figure 2.** Différentes stratégies mises en œuvre pour diminuer la conductivité thermique des échantillons, et/ou accroître le facteur de puissance en décorrélant la conductivité électronique du facteur de Seebeck. *Image courtesy:* © Materials Today, 2018.

Le second enjeu réside dans le coût que représente ces systèmes. Ce coût est lié au choix des éléments constitutif des matériaux développés. Ils peuvent être intrinsèquement cher (Argent, Or, Platine ...), rares ou difficile à extraire, ou bien encore nécessiter des processus de recyclage onéreux. Le coût du système dépendra également beaucoup des procédés de mise en forme nécessaire pour transformer un simple matériau en un système fonctionnel. In fine, il peut être industriellement intéressant de s'orienter vers un matériau aux propriétés fondamentales moins intéressantes (Seebeck,  $zT$ , ...) mais dont le coût de fabrication et /ou de mise en forme reste bas.

On voit donc que le développement d'un système thermoélectrique pertinent répond à des exigences complexes qui peuvent être contradictoires et que les enjeux en sciences de la matière sont riches.

Dans ce contexte, le laboratoire s'est engagé depuis quelques années dans un travail d'exploration du potentiel que représente les verres de chalcogénures pour ces applications. Les verres de chalcogénures sont, comme tous les verres, de mauvais conducteurs thermiques (environ  $0.5 \text{ W.m}^{-1}\text{K}^{-1}$ ) et sont caractérisés par un coefficient Seebeck important (plus de  $500 \mu\text{V/K}$ ). Parmi ceux-là, les systèmes potentiellement les plus intéressants sont les verres de tellure qui présentent un caractère semi-métallique, grâce à leur forte teneur en tellure, lui-même élément semi-conducteur. Par ailleurs, l'état vitreux est intrinsèquement un terrain peu favorable à la conduction de la chaleur à cause du désordre structural le caractérisant. Un verre, mauvais conducteur thermique et bon conducteur électrique, constitue donc un point de départ intéressant pour développer des composés pour la thermoélectricité. Enfin, l'intérêt final d'un matériau fonctionnel vitreux sera sa capacité à être facilement mise en forme par comparaison à son homologue cristallisé. En effet, les verres peuvent être considérés comme des liquides figés, sans ordre à longue distance et caractérisés par une transition vitreuse. Leurs propriétés viscoélastiques les rendent alors thermo-formables, propriétés à l'origine de la plupart de leurs applications technologiques. Il est en effet facile et peu coûteux de mettre en forme un matériau vitreux pour fabriquer toute sorte d'objets, des plus ordinaires (vitrage, bouteille ...) au plus sophistiqués (stockage nucléaire, fibres optiques).

Des travaux ont déjà été réalisés à Rennes et ailleurs (Montpellier, Nancy ...), qui tendent à confirmer le potentiel de ces matériaux sous forme strictement vitreuses, de vitrocéramiques, et de céramiques poly-cristallines. Des verres des systèmes Cu-Ge-Te, Cu-Si-Te, Cu-Ga-Te ou Cu-As-Te ont par exemple déjà fait l'objet de travaux antérieurs, sous forme vitreuses ou de vitrocéramiques. Des matériaux composites, mélange de phases cristallisées au sein de matrices



vitreuses ont également été préparés et caractérisés. Par rapport à cet état de l'art, des progrès restent à réaliser pour accroître encore la conductivité électronique de ces systèmes pour les rendre concurrentiels face à  $\text{Bi}_2\text{Te}_3$  ou  $\text{Sb}_2\text{Te}_3$ , matériaux cristallisés de référence pour ce type d'application.

Ces travaux de thèse sont l'occasion d'approfondir ces pistes de travail et de chercher à mieux comprendre les mécanismes permettant d'accroître la conductivité électronique dans des systèmes complexes. Ces travaux proposent également de s'éloigner de l'état vitreux, point d'entrée du laboratoire dans ces problématiques, pour étudier des formes différentes d'organisation et de texturation de la matière. De nombreux chapitres s'appuient également sur l'apport de calculs de densités électroniques et de structures de bandes en collaboration étroite avec l'équipe de chimie théorique de l'Institut des Sciences Chimiques de Rennes, ISCR UMR-CNRS n°6226.

Le **chapitre 2** fait le lien avec des travaux antérieurs, et sera consacré à l'étude des mécanismes de conduction dans les verres du système Cu-As-Te, en s'appuyant sur des modèles structuraux cristallisés. Les travaux réalisés sont le fruit d'une collaboration avec nos collègues de l'Institut de Physique de Rennes (IPR UMR CNRS-Rennes 1 n°6251).

Dans le **chapitre 3**, nous regarderons les conséquences de la recristallisation de verres de tellures du système Ge-Te-Se enrichis en élément, Cu et Bi, introduit dans l'idée d'augmenter la conductivité électronique.

Le **chapitre 4** concernent des travaux relatifs à des phases poly-cristallisées. Des échantillons de  $\text{CuPb}_{18}\text{SbTe}_{20}$  sont préparés suivant différentes méthodes de synthèse et leur comportement comparé à celui de leur équivalent à l'argent,  $\text{AgPb}_{18}\text{SbTe}_{20}$ .

Le **chapitre 5** est consacré à l'étude du même type de phases cristallisées au sein du système Pb-Sb-Te et vise à suivre les effets de l'introduction d'antimoine à partir du composé non stœchiométrique  $\text{Pb}_{0,98}\text{Te}$  c'est à dire  $\text{Pb}_{0,98-x}\text{Sb}_x\text{Te}$  (avec  $x = 0.01 - 0.12$ ).

Le **chapitre 6** concerne un travail plus théorique, visant à mieux comprendre le rôle joué par l'insertion de métaux conducteurs (Cu, Ag et Au) au sein du tellure de Germanium GeTe cristallisé.

Dans le **chapitre 7**, nous explorons les conséquences du dopage de GeTe par Al et Ba. Ces deux éléments sont potentiellement intéressants en tant qu'iso-électroniques de respectivement Ga ou In (pour la création de niveaux résonants) et du calcium Ca.

Dans **le chapitre 8**, nous revenons à un travail en sciences de la matière consacré à l'étude du co-dopage de GeTe et SnTe avec comme objectif d'améliorer les performances de ces matériaux pour des applications thermoélectriques.

Enfin, **le chapitre 9** est lui aussi consacré à du co-dopage de GeTe mais cette fois par Ga et Sb, échantillons préparés par Spark Plasma Sintering (SPS) et Flash-SPS ( $zT \sim 2$ ).

## **2. Etude du mécanisme de conduction au sein des verres Cu-As-Te**

L'introduction de cuivre au sein de matrice vitreuse du type As-Te et Ge-Te a été l'une des premières pistes envisagées pour améliorer les propriétés électroniques de ces verres. L'idée de base était que l'introduction de cuivre, porteur de charges électriques, dans la matrice doit contribuer à fortement augmenter la conductivité électronique du verre de base. En effet lorsque le point de départ du travail est une phase cristallisée présentant une conductivité électronique élevée, l'objectif consiste à diminuer la conductivité thermique du matériau en mettant en œuvre des stratégies tendant à mimer le comportement d'un verre au sein duquel les phonons se propagent intrinsèquement mal (« Phonon Glass Electron Crystal »). A l'inverse, lorsqu'on part d'un verre mauvais conducteur thermique, l'objectif consiste à augmenter la conductivité électronique tout en préservant cette faible conductivité thermique. Des résultats intéressants ont ainsi été obtenus dans les systèmes Cu-As-Te ou Cu-Ge-Te parfois en introduisant du sélénium pour stabiliser les verres et favoriser l'introduction du cuivre en proportion plus élevée. Par contre le rôle effectivement joué par le cuivre dans un tel matériau n'est pas clair.

Les résultats d'EXAFS et de XANES montrent que l'introduction du cuivre impacte l'environnement du tellure, et pas du tout celui de l'arsenic. Par ailleurs le XANES au seuil du tellure tend à montrer que la charge partielle portée par le tellure serait positive et que celle portée par le cuivre serait négative. Les spectres d'absorption électronique aux seuils du tellure et du cuivre montrent une proximité entre les résultats obtenus pour les verres Cu-As-Te et la phase  $\text{Cu}_2\text{Te}$  cristallisée. Les calculs DFT menés sur ce modèle structural pour déterminer les densités d'état électroniques montrent que la charge partielle portée par le tellure est effectivement positive et que celle du cuivre serait légèrement négative (Figure 3).

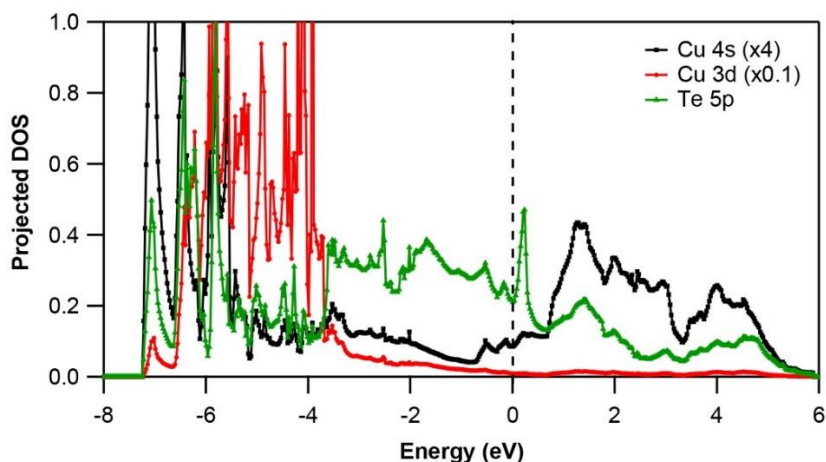


**Figure 3.** Densité d'état électronique calculé par DFT permettant de calculer une charge positive portée par le tellure et légèrement négative pour le cuivre.

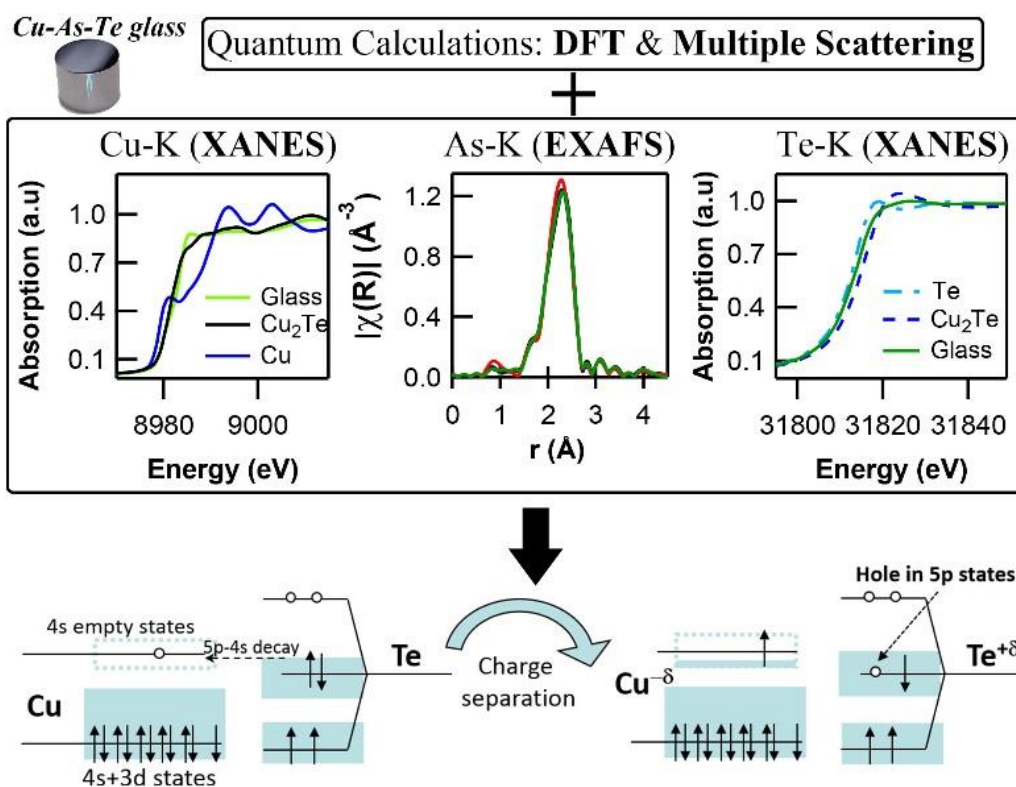


**Figure 4.** Proposition de mécanisme de conduction de trous dans les verres Cu-As-Te par transfert de charges des orbitales non liantes du tellure vers les orbitales 4s du cuivre.

Nous observons donc un transfert de charges des paires libres du tellures vers les orbitales 4S du cuivre. Enfin, nous montrons que les spectres de XANES au seuil du cuivre sont

très proches pour les verres et  $\text{Cu}_2\text{Te}$ . Le spectre de  $\text{Cu}_2\text{Te}$  ne peut être correctement reconstruit qu'en considérant une charge négative sur le cuivre. Par analogie nous pouvons alors expliquer l'augmentation de la conductivité dans les verres enrichis en cuivre par une conduction de trous générés dans les paires non liantes du tellure, et non pas par de la conduction des électrons apportés par le cuivre (Figure 4). Ce résultat contre intuitif montre que pour augmenter encore la conductivité de ces verres il faudra structurellement favoriser la création de liaisons Cu-Te et non pas des chemins de conduction à travers des liaisons Cu-Cu.

### 3. Matériaux issus de la recristallisation de verres GeTeSe enrichis en Bi ou Cu.

L'objet de ces travaux est d'explorer les propriétés thermoélectriques de matériaux issus de la recristallisation de verres issus du système Ge-Te-Se. Ces verres sont étudiés au sein de l'équipe pour leurs applications en optique. Le rôle du sélénium, présent avec un très faible taux, est de stabiliser ces compositions et de mieux maîtriser la synthèse et les phénomènes de recristallisation. L'idée est de former des vitrocéramiques avec des taux de cristallisation élevés pour atteindre des conductivités élevées, et de créer des joints de grains vitreux pour freiner la propagation des phonons. Afin d'accroître les conductivités encore les conductivités nous avons cherché à enrichir ces compositions en introduisant dans les compositions initiales du cuivre et du bismuth :  $(\text{Ge}_{20}\text{Te}_{77}\text{Se}_3)_{100-x}\text{M}_x$  ( $\text{M} = \text{Cu}$  or  $\text{Bi}$ ;  $x = 0, 5, 10, 15$ ). Les composés obtenus font apparaître différentes phases cristallisées telles  $\text{Bi}_2\text{Ge}_3\text{Te}_6$ ,  $\text{Bi}_2\text{GeTe}_4$ ,  $\text{GeTe}$  d'une part et  $\text{Cu}_2\text{GeTe}_3$ ,  $\text{CuGeTe}_2$  d'autre part. Une analyse fine par microscopie électronique à transmission a permis de mettre en évidence ces différentes phases.

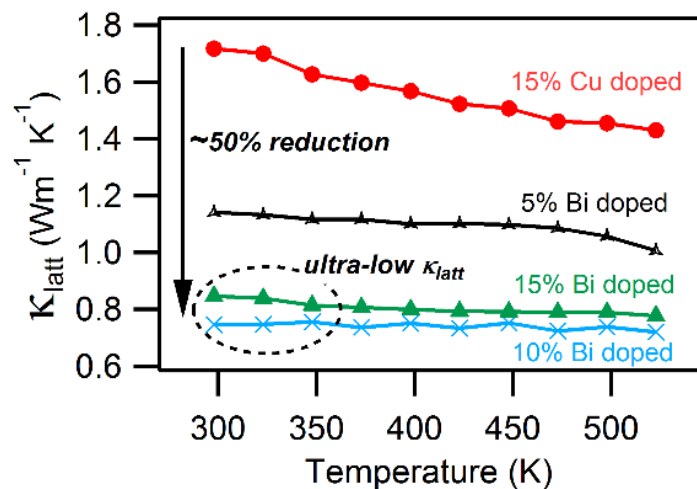
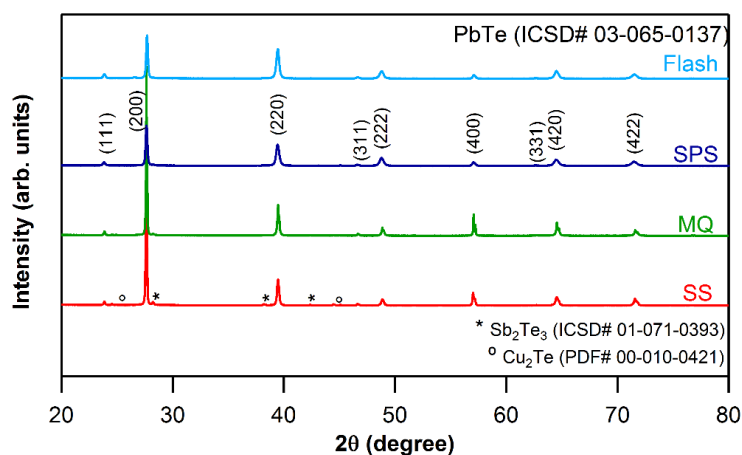


Figure 5. Evolution à la baisse des échantillons dopés Bismuth.

Ces composés, produit de la recristallisation des verres, montrent de fortes conductivités électriques de l'ordre de  $8.10^4 \text{ S.m}^{-1}$ . De même les conductivités thermiques obtenues pour les composés au bismuth sont intéressantes car particulièrement basses (Figure 5). Malheureusement les coefficients Seebeck mesurés sont bas également, et donc les facteurs de mérite restent autour de 0.1 limitant les perspectives pour des applications en thermoélectricité.

#### 4. Développement et caractérisation de phases $\text{MPb}_{18}\text{SbTe}_{20}$ ( $\text{M} = \text{Cu, Ag, Au}$ ) suivant différents modes de synthèse.

Les tellures de plomb sont parmi les matériaux qui ont été le plus étudiés en vue d'applications en thermoélectricité. En particulier  $\text{AgPb}_{18}\text{SbTe}_{20}$  s'est révélé particulièrement intéressant avec un  $zT$  d'environ 2.2 et a donné lieu à de nombreux travaux sur des compositions proches. Dans ce chapitre une étude de ce composé en substituant Ag par Cu est proposée. Ainsi des échantillons de formulation  $\text{CuPb}_{18}\text{SbTe}_{20}$  ont été préparés suivant différentes méthodes (refroidissement lent, rapide, par Spark Plasma Sintering, et Hybrid flash-SPS). Des échantillons semblables contenant de l'or,  $\text{AuPb}_{18}\text{SbTe}_{20}$  ont également été préparés pour réaliser une étude systématique  $\text{MPb}_{18}\text{SbTe}_{20}$  ( $\text{M} = \text{Cu, Ag, Au}$ ).



**Figure 6.** Diagramme DRX des échantillons au cuivre,  $\text{CuPb}_{18}\text{SbTe}_{20}$ , suivant les différents modes de synthèse mise en œuvre.

Les différents modes de synthèse génèrent des différences notables sur les propriétés des échantillons, en particulier sur la conductivité thermique qui est directement liée à la texturation du matériau. Ainsi, les échantillons préparés par Hybrid Flash-SPS présentent des

conductivités thermiques particulièrement basses dues à la présence de nano-dislocations et de nano-inclusions.

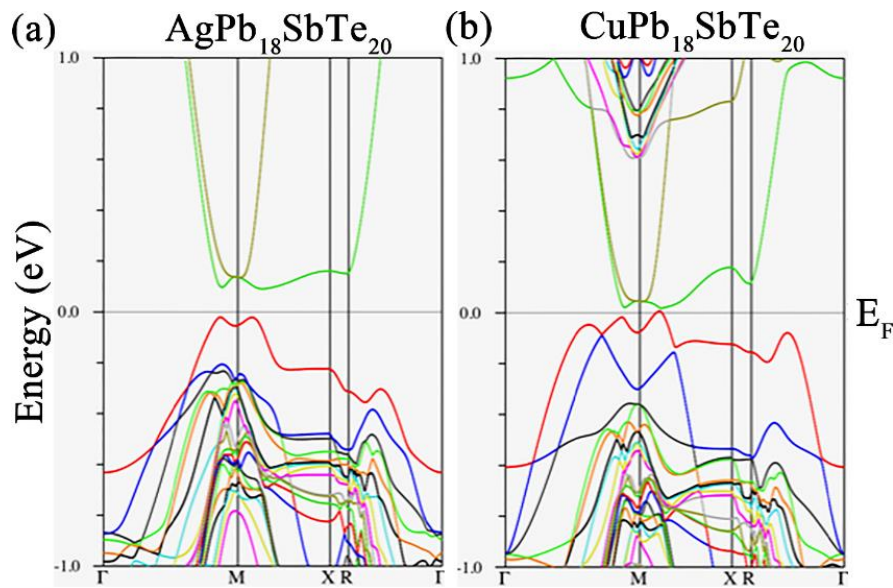


**Figure 7.** Structures de band calculées pour  $MPb_{18}SbTe_{20}$  ( $M = Cu, Ag$ ).

Afin de caractériser finement le comportement électronique de ces composés des calculs de structure de bande ont été réalisés (Figure 7). Les deux matériaux présentent un band gap direct avec un gap de 0,02 eV seulement pour  $CuPb_{18}SbTe_{20}$  contre 0,1 eV pour  $AgPb_{18}SbTe_{20}$ . Ce très faible band gap pour l'échantillon au Cuivre est une bonne nouvelle pour les propriétés de conduction électronique mais sont malheureusement aussi à l'origine du coefficient Seebeck environ deux fois plus bas pour ces nouveaux composés comparés à la référence à base d'Ag. Finalement, le facteur de mérite  $zT$  de l'échantillon préparé par Flash SPS atteint tout de même 0.9 à 700°K, mais cette valeur reste bien inférieure à celle de  $AgPb_{18}SbTe_{20}$  de 1.8 à la même température. Il est cependant intéressant de noter que ces expériences sont parmi les toutes premières qui mobilisent la technique dite Hybrid Flash-SPS et que ce sont les échantillons ainsi préparés qui présentent les meilleures performances thermoélectriques. Cette technique permet d'abaisser la conduction thermique  $\kappa$  de réseau tout en préservant la mobilité des charges grâce à l'apparition d'une nano-texturation des échantillons.

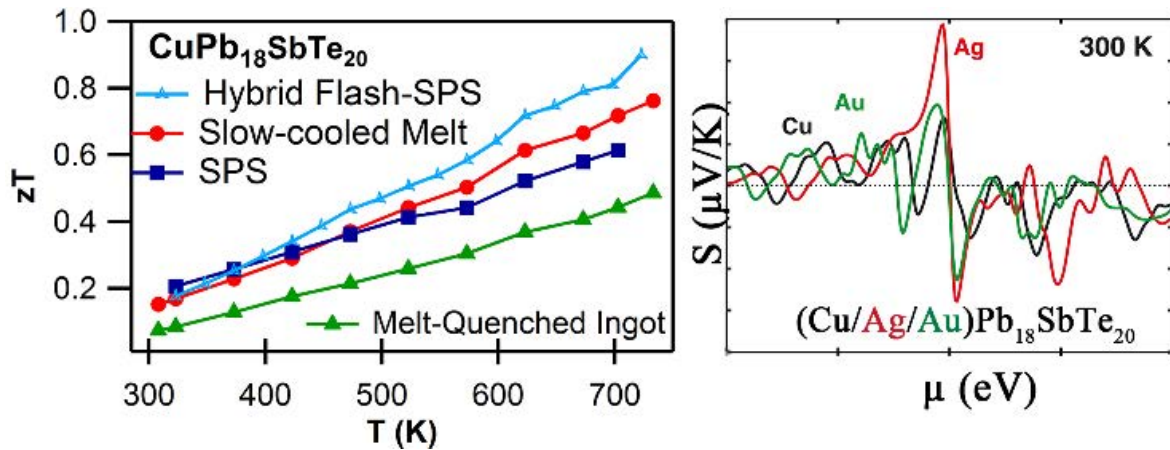


**Figure 8.** Les  $zT$  les plus élevés sont obtenus par Hybrid flash-SPS (à gauche); Calculs théoriques du coefficient de Seebeck à partir de l'équation de transport de Boltzmann confirmant que les valeurs attendues les plus élevées sont pour l'échantillon à l'Argent (à droite).

## 5. Optimisation des propriétés thermoélectriques de phases non-stœchiométriques du système Pb-Sb-Te

Une voie d'exploration classique pour la thermoélectricité réside dans le développement de solutions solides telle que PbTe au sein desquelles les phonons se propagent mal grâce au désordre statistique. Des travaux récents ont porté sur le système  $\text{Pb}_{0.96}\text{Sb}_{0.02}\text{Te}_{1-x}\text{Se}_x$  en jouant donc sur le taux de sélénium. D'autres ont porté sur le taux de substitution d'antimoine dans des composés stœchiométriques  $\text{Pb}_{1-x}\text{Sb}_x\text{Te}$ . L'objet de ce chapitre est de combiner ces deux stratégies et d'étudier les performances de matériaux du système  $\text{Pb}_{0.98-x}\text{Sb}_x\text{Te}$  ( $x = 0,01 - 0,12$ ). Il a cependant été difficile d'obtenir une seule phase cristallisée. En particulier au-delà de 4% de Sb, on observe l'apparition d'une seconde phase cristallisée correspondant à  $\text{Sb}_2\text{Te}_3$ .

Dans la phase majoritaire  $\text{Pb}_{0.98-x}\text{Sb}_x\text{Te}$ , l'antimoine se substitue au plomb lui-même déficitaire. Cette substitution de 4% a pour conséquence d'augmenter la concentration en porteur de charges et leur mobilité. Par ailleurs la vacance en plomb combinée à une texturation optimale obtenu pour 4% d'antimoine réduit la propagation des phonons thermiques et donc la conductivité thermique de cet échantillon. Finalement, pour le composé à 4% de Sb, le facteur de mérite  $zT$  passe à 0.8 pour ce composé non-stœchiométrique contre 0.3 pour le composé de départ stœchiométrique  $\text{Pb}_{1-x}\text{Sb}_x\text{Te}$  (Figure 9).

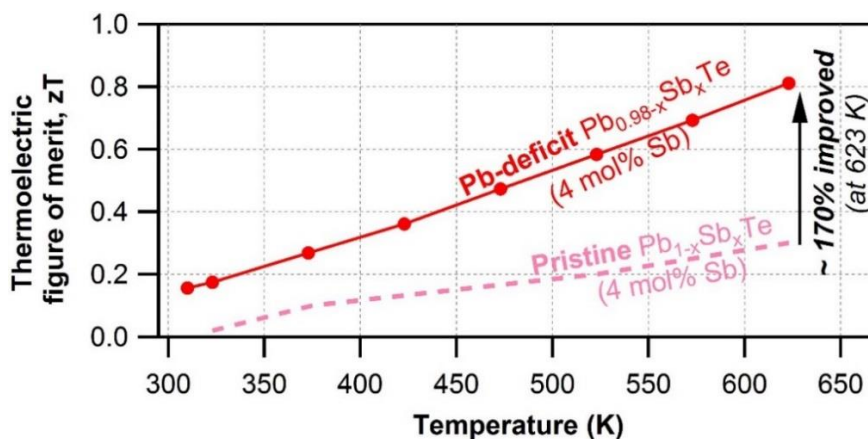


**Figure 9.** Augmentation du  $zT$  fonction de la température pour des échantillons déficitaires en Plomb.

## 6. Étude expérimentale et théorique des propriétés thermoélectriques de phases cristallisées GeTe dopées argent (Ag).

Récemment GeTe est apparu comme une base de travail intéressante comme alternative à PbTe. De multiples substitutions du germanium par différents métaux (Sb, Bi, Mn, Sn, Pb ...) ont permis d'obtenir des facteurs de mérite  $zT$  compris entre 1 et 2. Parmi celles-ci les échantillons présentant les propriétés les plus intéressantes sont ceux obtenus par co-dopage Ag/Sb (TAGS). Par contre le rôle de l'argent dans ce type de composé n'a jamais été regardé, nous proposons ici de regarder les propriétés de tels matériaux mais substitués par du cuivre, de l'argent ou de l'or,  $Ge_{1-x}M_xTe$  ( $M = Cu, Ag, Au$ ), en se focalisant d'abord sur l'échantillon à base d'argent. Il a ainsi été possible d'introduire jusqu'à 6% d'Ag en substitution du Germanium dans cette phase cristallisée. Dans tous les cas il a été difficile de totalement éviter l'apparition de phases secondaires de germanium cristallisé.

Pour mieux comprendre les conséquences de cette substitution sur les propriétés électroniques des matériaux, des calculs de structure de bande ont été entrepris. Ils montrent que l'énergie du niveau de Fermi diminue, que la densité d'état d'énergie au niveau de Fermi croît avec la substitution, augmentant la concentration en porteurs de charge (trous) en cohérence avec une diminution du coefficient de Seebeck (Figure 10). La conductivité thermique électronique augmente également ce qui est compensé par la diminution de la contribution du réseau à la conductivité thermique. Finalement, il apparaît que les modélisations proposées sont des outils riches et indispensables à une bonne appréhension des mécanismes et permettent de



comprendre pourquoi le facteur de mérite reste globalement stable pour ces composés quel que soit le taux de substitution. Les calculs du Seebeck montrent que les meilleurs résultats sont obtenus pour un dopage à l'argent plutôt que par du cuivre ou de l'or. Cependant, on peut surtout en conclure que les mono-substitution ne permettent pas d'avancée quantitative substantielle sur les propriétés des matériaux.

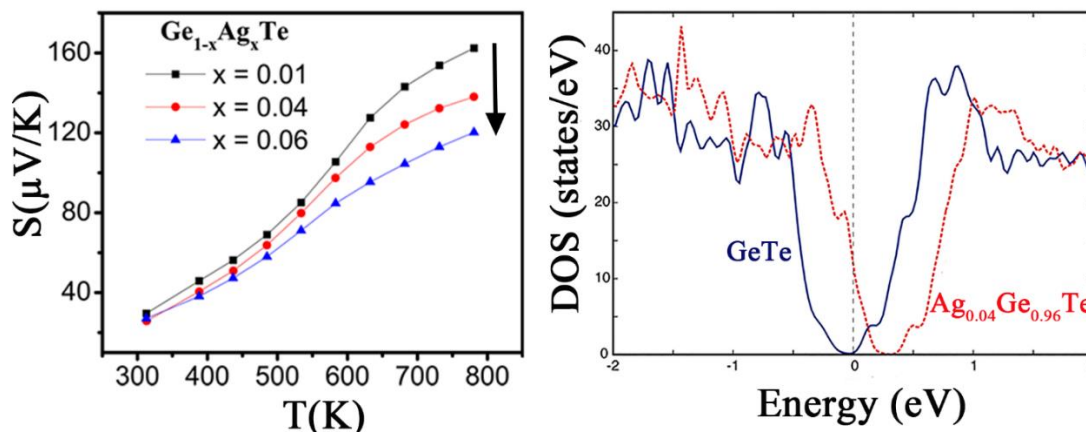


**Figure 10.** Evolution du coefficient de Seebeck fonction du dopage par Ag (gauche). Calcul de la DOS illustrant le décalage du niveau de Fermi pour la composition contenant de l'Ag (droite).

## 7. Étude du dopage de GeTe par Al ou Ba

Dans le prolongement du chapitre précédent, il est proposé ici de regarder les conséquences du dopage de GeTe par de l'aluminium Al ou du baryum Ba. Al, en tant qu'isoélectrique de Ga et In, pourrait être à l'origine de l'apparition de niveau résonant dans le haut de la bande de valence, Ba en tant que gros élément pourrait quant à lui favoriser la diffusion des phonons thermiques. Ainsi, des échantillons de formulation  $\text{Ge}_{1-x}\text{Al}_x\text{Te}$  ( $x = 0 - 0.08$ ) et  $\text{Ge}_{1-x}\text{Ba}_x\text{Te}$  ( $x = 0 - 0.06$ ) ont été préparés par SPS. Dans les deux cas les résultats sont décevants et se traduisent par une diminution des propriétés thermoélectriques comme l'illustre la Figure 11. Pour les composés dopés par de l'aluminium on observe bien l'apparition de niveaux résonants en haut de la bande de valence. Par contre la forme de la bande de valence, avec un accroissement du gap en énergie entre les 2 maxima, est préjudiciable à la mobilité de trous.

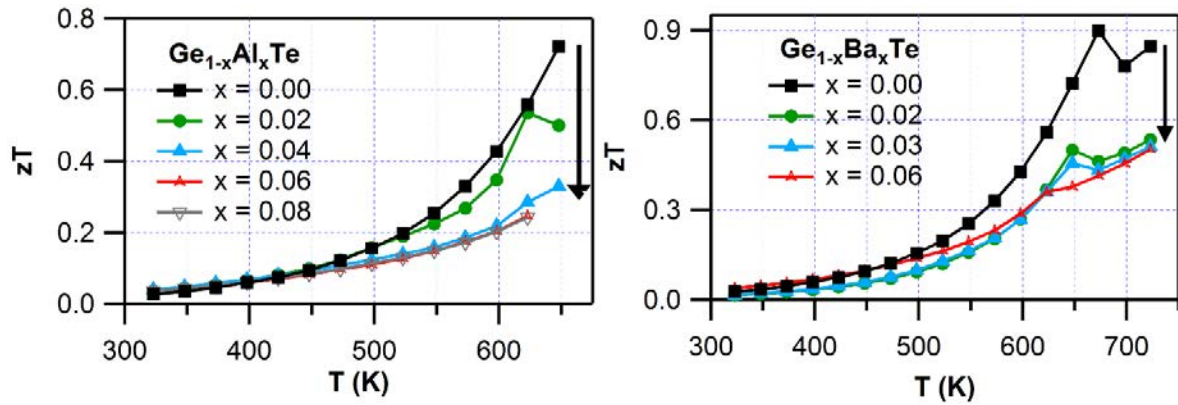


**Figure 11.** Evolution du  $zT$  en fonction du taux de substitution de Ge par Al (à gauche) et Ba (à droite).

### 8. Étude du co-dopage (Bi, In) de GeTe et (Ag, In, Sb) de SnTe.

Des travaux antérieurs ont montré l'intérêt du dopage de GeTe par Bi et In respectivement permettant d'accroître le facteur de mérite de GeTe par précipitation de nano-phases ou création d'états résonnants respectivement. L'idée est ici de co-doper GeTe pour chercher à cumuler les bénéfices des deux effets. La même stratégie est mise en œuvre pour suivre le co-dopage de SnTe par Sb (diffusion de phonons thermiques), In (création d'états résonnants) et Ag (structure électronique). Dans les deux cas les taux de substitution n'excèdent pas quelques pourcents.

Les conséquences de ces co-dopages résident dans une forte diminution de la conductivité électrique, qui s'accompagne d'une augmentation substantielle du coefficient de Seebeck. Globalement le facteur de puissance est à peu près stable. Plus intéressant, on constate une baisse importante de la conductivité thermique, en particulier de la composante électronique. Tout naturellement la figure de mérite résultante qui combine l'ensemble de ces paramètres est plus élevée en particulier dans une gamme de température « intermédiaire ».

Ainsi, à titre d'exemple, entre 500 et 600 K, le  $zT$  de  $\text{Ge}_{93}\text{Bi}_{0.05}\text{In}_{0.02}\text{Te}$  est multiplié par 2 par rapport à celui de GeTe pour atteindre 0.8 dès 600 K (Figure 12a). Des résultats comparables, quoiqu'un peu moins intéressants sont obtenus pour les substitutions sur SnTe (Figure 12b). Notons que pour GeTe dopé par In ou Bi seul, le  $zT$  peut atteindre 1.3 mais pour une valeur de température bien précise centrée sur environ 700 K. L'intérêt de ces échantillons co-dopés est d'obtenir des valeurs de  $zT$  qui restent relativement élevées, de l'ordre de 0.9, sur une gamme de

température s'étendant de 550 K à 800 K. Cette notion de  $zT$  moyen est extrêmement importante pour le développement de systèmes thermoélectriques.

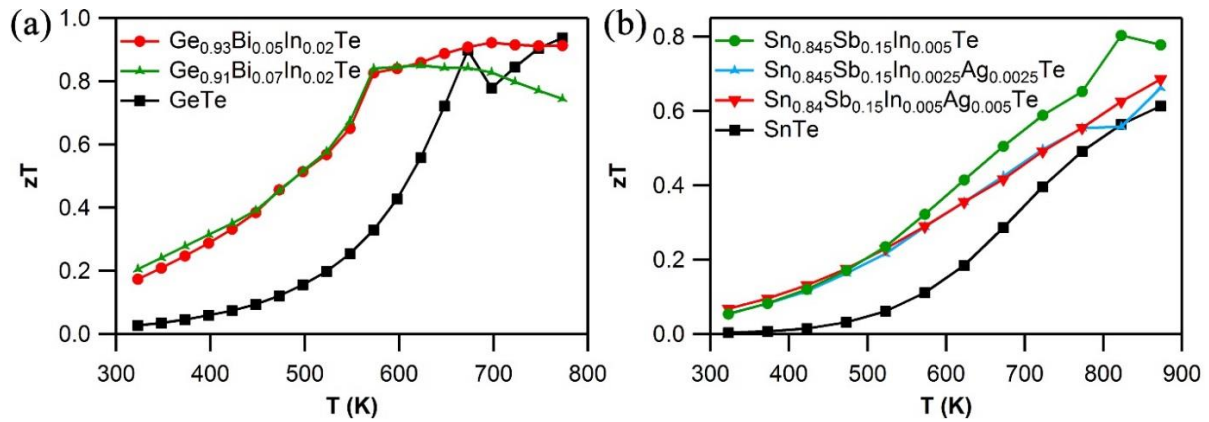


**Figure 12.**  $zT$  des composés synthétisés par substitution à partir de GeTe (a) et SnTe (b).

## 9. Étude expérimentale et théorique du co-dopage de GeTe par Ga et Sb.

Les résultats obtenus dans les chapitres précédents confirment la profonde interaction existante entre les conductivités électriques d'une part et le coefficient de Seebeck d'autre part, limitant les perspectives de croissance du facteur de puissance  $S^2\sigma$ . De nombreux travaux récents visent à décorrélérer ces deux propriétés pour les optimiser séparément. Ces stratégies dites d'ingénierie de structure de bandes sont complexes et nécessitent l'apport de la chimie théorique pour être pleinement appréhendées. Suivant l'exemple des travaux récents portant sur  $\text{Ge}_{1-x}\text{In}_x\text{Te}$ , la proposition est ici d'explorer les conséquences d'une co-substitution par Ga et Sb dans GeTe. Nous espérons ainsi combiner la création de niveaux résonants avec Ga (comme les produit In) et une dégénérescence de la structure de bandes avec Sb.

Le travail peut ainsi se décomposer en 3 étapes.

Tout d'abord la préparation d'échantillons substitués par Ga seul. Le taux optimal des d'états résonnants est obtenu pour 2% de gallium. Ces niveaux apparaissent au sommet de la bande de valence diminuant ainsi le band gap du matériau mais ne le comble pas totalement. Seule, cette substitution n'a qu'un effet marginal sur la valeur mesurée du Seebeck et du  $zT$  (+15%).

Ensuite la contribution de l'apport de la substitution par Sb a été regardée expérimentalement et théoriquement. Expérimentalement les conséquences sont remarquables puisqu'on observe un accroissement du  $zT$  de l'ordre de +80% pour les matériaux co-dopés. L'antimoine est un élément riche en électrons comparé au germanium, son introduction diminue donc la concentration en porteur de charges (semi-conducteur de type p), et donc augmente le Seebeck.

Par ailleurs, les simulations permettent d'isoler le rôle spécifique joué par Sb qui génère des niveaux donneurs spécifiques dans le bas de la bande de conduction. Surtout, pour l'échantillon co-dopé, les effets se combinent et l'antimoine permet de niveler les valeurs d'énergies du sommet des 2 bandes du niveau résonant créé par le Gallium en diminuant le gap de 64 meV (dopage) à 26 meV (co-dopage) comme illustré sur la Figure 13. Ceci facilite la mobilité de trous au sein de la bande de valence.

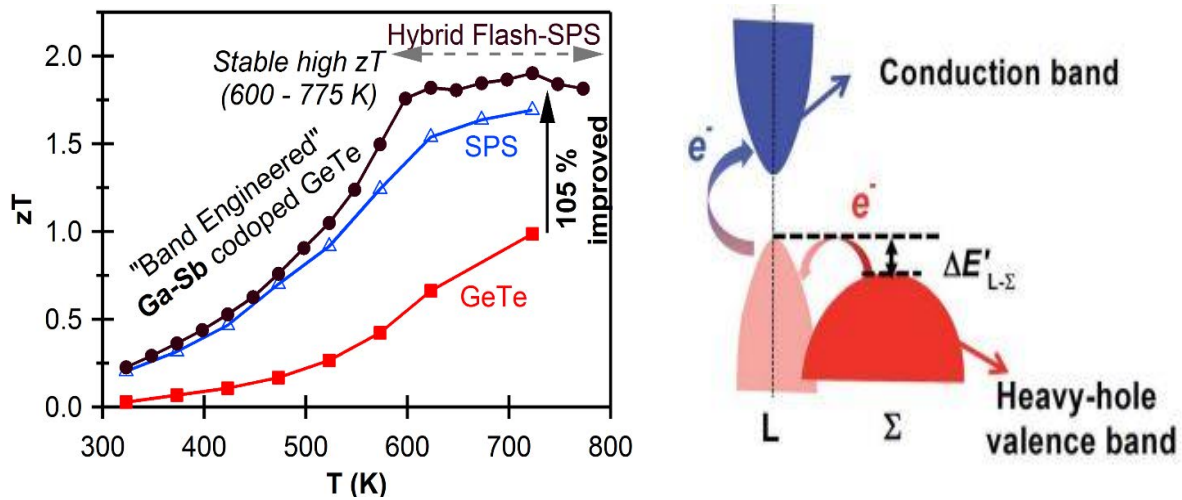


**Figure 13.** Gain mesuré sur le  $zT$  grâce à la mise en œuvre de la méthode de synthèse Hybrid Flash-SPS (à gauche); Représentation schématique de la structure de bande illustrant l'intérêt à niveler les écarts d'énergie au sein du haut de la bande de valence pour favoriser les phénomènes de conduction, ce qu'a permis le co-dopage de GeTe par Ga et Sb (à droite).

Enfin, la dernière étape du travail a consisté à jouer sur la méthode de synthèse du composé préparé par SPS et « hybrid » Flash-SPS tel que décrit au chapitre 4. Cette technologie « hybride » permet de maintenir l'échantillon pulvérulent et diminuer la taille des grains et donc d'abaisser la conductivité thermique. Elle a également pour effet de maintenir la mobilité des porteurs de charges à un niveau élevé. Finalement, comme le montre la Figure 13, on observe un gain supplémentaire sur le  $zT$  lié à la mise en œuvre de cette technique.

Tout compte fait, l'ensemble de ces réalisations, dopage, co-dopage puis Hybrid Flash-SPS a permis d'augmenter de 105% le facteur de mérite du matériau, passant de 0.95 pour GeTe à 1.95 pour l'échantillon final. Surtout, comme pour le co-dopage par In et Bi (chapitre 8), le  $zT$  garde une valeur élevée sur une large plage de température s'étendant de 600 à 800 K.

## 10. Conclusion

Pour résumer, les travaux de cette thèse a permis d'appréhender une large gamme de matériaux pour la thermoélectricité, allant des verres, des vitro-céramiques aux matériaux polycristallins, et différentes techniques de synthèses, allant de la fusion trempe, au frittage à chaud, jusqu'à différents types de SPS. Les stratégies mises en œuvre ont visé alternativement à accroître la conductivité électronique, augmenter le Seebeck et/ou augmenter la diffusion thermique. Beaucoup de tentatives ne se sont pas révélées fructueuses, mais elles ont permis malgré tout de confirmer l'importance du co-dopage pour déconnecter l'évolution de la conductivité électronique de celle du Seebeck. Elles ont aussi été l'occasion de montrer l'importance des calculs de structure de bandes et de densité d'états pour mieux comprendre les conséquences des évolutions structurales et de formulation, parfois contre intuitive.

Des résultats prometteurs ont aussi été obtenus par co-dopage de GeTe par Bi et In d'une part, Ga et Sb d'autre part. Ces co-dopages ont permis d'accroître le  $zT$  de façon substantielle (jusqu'à  $zT \sim 2$ ) et de les maintenir à des niveaux élevés sur de larges plages de températures. Alternativement, un travail sur des composés non-stœchiométriques déficitaires en Pb s'est également révélé prometteur.





# **Table of Contents**





## Chapter 1

### General Introduction – A Bird’s Eye View on Thermoelectrics

1.1	Introduction .....	1
1.2	Basic Thermoelectric Principles .....	2
1.2.1	Thermoelectric Effect .....	2
1.2.1.1	Seebeck Effect .....	2
1.2.1.2	Peltier Effect .....	3
1.2.1.3	Thomson Effect .....	5
1.3	Applications of Thermoelectrics .....	6
1.4	Timeline of Thermoelectrics – History and Milestones .....	8
1.5	Key Thermoelectric Parameters .....	10
1.5.1	Figure of Merit .....	10
1.5.2	Thermoelectric Device Efficiency .....	11
1.6	Conflicting Thermoelectric Material Properties .....	12
1.6.1	Carrier Concentration – Seebeck Coefficient – Electrical Conductivity .....	12
1.6.2	Effective Mass – Mobility .....	13
1.6.3	Electronic Thermal Conductivity – Electrical Conductivity .....	14
1.7	Approaches to Enhance Thermoelectric Performance .....	14
1.7.1	Phonon-Glass Electron-Crystal (PGEC) Approach .....	14
1.7.1.1	Skutterudites .....	15
1.7.1.2	Clathrates .....	16
1.7.1.3	Zintl Compounds .....	17
1.7.1.4	Half-Heusler Compounds .....	18
1.7.1.5	Conducting Chalcogenide Glasses .....	19
1.7.2	Band Engineering Approach .....	20
1.7.2.1	Convergence of Electronic Band Valleys .....	20
1.7.2.2	Electronic Resonance States .....	22
1.7.2.3	Synergistic Band Effects .....	23
1.7.2.4	Bipolar Effects .....	24
1.7.3	Nanostructure Engineering .....	24
1.7.3.1	Dimensionality Reduction .....	24
1.7.3.2	Phonon Scattering .....	25
1.7.3.2.1	Atomic-scale Scattering .....	25

## Table of Contents

---

	1.7.3.2.2 Nano-scale Scattering .....	25
	1.7.3.2.3 Meso-scale Scattering .....	27
	1.7.3.2.4 Multiscale Hierarchical Architectures .....	28
1.8	Graphical Summary of State-of-the-art TE Materials & Strategic Approaches ...	30
	References .....	31

## Chapter 2

### Possible Mechanism for Hole Conductivity in Cu-As-Te Thermoelectric Glasses

2.1	Introduction .....	40
2.2	Materials and Methods .....	41
2.2.1	Glass Synthesis .....	41
2.2.2	Synchrotron Measurements .....	41
2.2.3	FDMNES (Multiple Scattering based Quantum Calculations) .....	42
2.3	Results and Discussion .....	42
2.3.1	As K-edge (XANES and EXAFS) and Te K-edge (XANES and FDMNES).....	42
2.3.2	Density of States (DOS) .....	44
2.3.3	Cu-K edge (XANES and FDMNES) .....	46
2.3.4	A Model for Glass Conductivity .....	47
2.4	Conclusion .....	49
	References .....	50

## Chapter 3

### Thermoelectrics of Highly-Crystallized Ge-Te-Se Glasses Doped with Cu/Bi

3.1	Introduction .....	55
3.2	Materials and Methods .....	55
3.2.1	Reagents .....	55
3.2.2	Synthesis .....	56
3.2.3	Powder X-ray Diffraction .....	56
3.2.4	Hall Measurements .....	56
3.2.5	Measurement of Electrical Transport Properties .....	57
3.2.5.1	Description of LSR-3 Equipment .....	57
3.2.6	Measurement of Thermal Transport Properties .....	58

## Table of Contents

---

3.2.6.1	Description of LFA-457 Equipment .....	59
3.2.7	Microscopic Analysis .....	60
3.3	Results and Discussion .....	61
3.3.1	Sample Notations and Dopant Induced Crystallization .....	61
3.3.2	Structural and Microscopic Investigation .....	61
3.3.4	Thermoelectric Properties .....	66
3.4	Conclusion .....	71
	References .....	72

## Chapter 4

### Effect of Processing Route on the Thermoelectric Performance of $\text{CuPb}_{18}\text{SbTe}_{20}$

4.1	Introduction .....	77
4.2	Materials and Methods .....	78
4.2.1	Reagents .....	78
4.2.2	Synthesis .....	78
4.2.3	Computational Procedures .....	80
4.3	Results and Discussion .....	81
4.3.1	Structural Analysis .....	81
4.3.2	Thermal Transport Properties .....	83
4.3.3	Nano and Microstructural Investigation .....	84
4.3.4	Electrical Transport Properties .....	87
4.3.5	Investigation of Electronic Band Structures .....	90
4.3.6	Thermoelectric Figure of Merit, $zT$ .....	92
4.4	Conclusion .....	93
	References .....	94

## Chapter 5

### Enhancement in Thermoelectric Performance of *n*-type Pb-deficit Pb-Sb-Te Alloys

5.1	Introduction .....	100
5.2	Materials and Methods .....	101
5.2.1	Reagents .....	101
5.2.2	Synthesis .....	101

## Table of Contents

---

5.3	Results and Discussion .....	101
5.3.1	Structural Analysis .....	101
5.3.2	Microstructural Analysis .....	102
5.3.3	Thermoelectric Properties .....	104
5.4	Conclusion .....	108
	References .....	108

## Chapter 6

### Coinage Metal Insertion on the Thermoelectric Properties of GeTe Solid-State Solutions

6.1	Introduction .....	113
6.2	Materials and Methods .....	114
6.2.1	Reagents .....	114
6.2.2	Synthesis .....	114
6.2.3	Computational Procedures .....	114
6.3	Results and Discussion .....	115
6.3.1	Structural Analysis .....	115
6.3.2	Electrical Transport Properties .....	117
6.3.3	Investigation of Electronic Band Structures and Density of States .....	119
6.3.4	Thermal Transport Properties and Figure of Merit .....	121
6.4	Conclusion .....	123
	References .....	124

## Chapter 7

### Detrimental Effects of Doping Al and Ba on the Thermoelectric Performance of GeTe

7.1	Introduction .....	130
7.2	Materials and Methods .....	130
7.2.1	Reagents .....	130
7.2.2	Synthesis .....	130
7.2.3	Computational Procedures .....	131
7.3	Results and Discussion .....	131

## Table of Contents

---

7.3.1	Structural Analysis .....	131
7.3.2	Thermoelectric Properties of $\text{Ge}_{1-x}\text{Al}_x\text{Te}$ and $\text{Ge}_{1-x}\text{Ba}_x\text{Te}$ Systems.....	133
7.3.3	Investigation of Electronic Band Structures and Density of States .....	136
7.4	Conclusion .....	138
	References .....	138

## Chapter 8

### Thermoelectric Performance of Codoped (Bi, In)-GeTe and (Ag, In, Sb)-SnTe Materials

8.1	Introduction .....	142
8.2	Materials and Methods .....	143
8.2.1	Reagents .....	143
8.2.2	Synthesis .....	143
8.3	Results and Discussion .....	143
8.3.1	Structural Analysis .....	143
8.3.2	Thermoelectric Properties .....	145
8.3.2.1	Transport Properties for (Bi, In)-GeTe Codoped System .....	145
8.3.2.2	Transport Properties for (Ag, In, Sb)-SnTe Codoped System .....	147
8.3.2.3	Figure of Merit for GeTe and SnTe Codoped Systems .....	148
8.4	Conclusion .....	149
	References .....	150

## Chapter 9

### Realizing a Stable High $zT \sim 2$ over a Broad Temperature Range in $\text{Ge}_{1-x-y}\text{Ga}_x\text{Sb}_y\text{Te}$ via Band Engineering and Hybrid Flash-SPS Processing

9.1	Introduction .....	152
9.2	Materials and Methods .....	153
9.2.1	Reagents .....	153
9.2.2	Synthesis .....	153
9.2.3	Computational Procedures .....	154
9.3	Results and Discussion .....	155
9.3.1	Structural Analysis .....	155

## Table of Contents

---

9.3.2	Thermoelectric Properties of $\text{Ge}_{1-x}\text{Ga}_x\text{Te}$ and $\text{Ge}_{1-x-y}\text{Ga}_x\text{Sb}_y\text{Te}$ Systems.....	155
9.3.3	Investigation of Electronic Band Structures and Density of States .....	160
9.3.4	Comparison of SPS vs Hybrid Flash-SPS for Processing of $\text{Ge}_{1-x-y}\text{Ga}_x\text{Sb}_y\text{Te}$	165
9.4	Conclusion .....	168
	References .....	169
<b>Conclusion &amp; Outlook .....</b>		<b>176</b>
<b>Annexures .....</b>		<b>181</b>
<b>Short CV – Bhuvanesh Srinivasan .....</b>		<b>206</b>







# **Chapter 1**

**General Introduction - A Bird's Eye View on Thermoelectrics**



## 1.1 Introduction

Within the realms of exploring alternative means to power the planet, the requirement of generating and storing energy sustainably represents one of the critical challenges across the boundaries of the science and technology in the 21<sup>st</sup> century. In this regard, thermoelectric (TE) materials and devices have drawn increasing interest and attention due to their potential to reversibly convert waste heat into fruitful electricity. Among the several approaches for solid-state compound conversion between heat and electricity including fuel cells,<sup>1</sup> photovoltaics,<sup>2</sup> batteries<sup>3</sup> and supercapacitors,<sup>3</sup> TE devices have significant potential in tackling the challenges of energy sustainability and offers excellent features: extensive lifetime, highly reliable and scalable, environmentally friendly, quiet, lower maintenance costs, etc.<sup>4-6</sup>

According to Zion Market’s research report, global thermoelectric generator market was valued at around 279.3 million USD in 2015 and it is expected to generate a revenue of 610.0 million USD by end of 2021, growing at a compound annual growth rate (CAGR) of slightly above 13.8% between 2016 and 2021 (Annexure 1, Figure A1.1). However, lack of awareness and low efficiency of thermoelectric devices may curb the demand of thermoelectric generators in the near future. Hence, aiming to improve their efficiency and to find a sustainable solution to the energy problems, the research on TE devices and materials have gained increasing limelight and momentum in the last decade. This PhD thesis is one such sincere attempt contributing to the development of thermoelectric research.

The PhD thesis is developed within the frame work of CoACH-ETN, a project funded by European Commission’s Horizon 2020 research and innovation program under the Marie Skłodowska-Curie grant (GA. 642557). CoACH (Composites, Advanced glasses and Ceramics for High growth industries) provides career development and training opportunities for young researchers who are in their first 4 years of research career in both the public and private sectors. Politecnico di Torino, Italy coordinates the CoACH project. It is a highly multi-disciplinary and inter-sectorial program with 5 academic and 10 industrial partners from seven different European countries. The program aims to promote international excellence in the field of glasses, ceramics and composite science and technology, modelling, design, characterization and commercialization of advanced glass, ceramic and composite based products. CoACH-ETN provides training-through-research in glasses, ceramics and composites in four key sectors: (i) Health, (ii) Energy, (iii) Information and Communication Technology, and (iv) Environment. This PhD thesis is designed to operate within the work package 2 (WP2), *i.e.*, for energy applications.

This introductory chapter shall give an overview of thermoelectrics, including its brief history, underlying basic principles, potential applications, conflicts / challenges involved in improving the efficiency, different strategic approaches in tackling the challenges and the state-of-the-art TE materials.

## **1.2 Basic Thermoelectric Principles**

Thermal energy is usually a byproduct of other forms of energy such as chemical energy, mechanical energy, and electrical energy. Joule heating, the process in which electrical energy is transformed into thermal energy, is related, though it is not generally termed a thermoelectric effect. Joule heating is what causes wires to heat up when current runs through them, and is the basis for electric stoves, toasters, etc. The thermoelectric effects (Seebeck–Peltier and Thomson effects) are thermodynamically reversible, whereas Joule heating is not.

### **1.2.1 Thermoelectric Effect**

The thermoelectric effect is a phenomenon by which a temperature difference is directly converted into electric voltage and vice versa. A thermoelectric device creates voltage when there is a difference in temperature on each side. Conversely, when a voltage is applied to it, the heat is transferred from one side to the other, creating a temperature difference. This effect can be used to generate electricity, measure temperature or change the temperature of objects. Because the direction of heating and cooling is determined by the polarity of the applied voltage, thermoelectric devices can also be used as temperature controllers. The term "thermoelectric effect" encompasses three separately identified effects: Seebeck effect, Peltier effect, and Thomson effect.

#### **1.2.1.1 Seebeck Effect**

The Seebeck effect is the conversion of temperature difference directly into electricity and is named after a German physicist Thomas Johann Seebeck, who discovered this phenomenon in 1821.

When two ends of dissimilar conductors are held at different temperatures (Seebeck used copper and bismuth), electrons at the hot junction at higher thermal velocities diffuse to the cold junction. Seebeck discovered that making one end of a metal bar hotter or colder than the other produced an electromotive force (emf) between the two ends. Different metals (or semiconductors)

have different free electron densities. When two different materials come into contact with each other, the electron diffusion will occur at the interface to eliminate the electron density difference. Meanwhile, the electron diffusion rate is proportional to the temperature at interface. Therefore, as long as the temperature difference between the two materials is maintained, electron diffusion will continue by generating a stable voltage. This phenomenon is schematized in Figure 1.1.

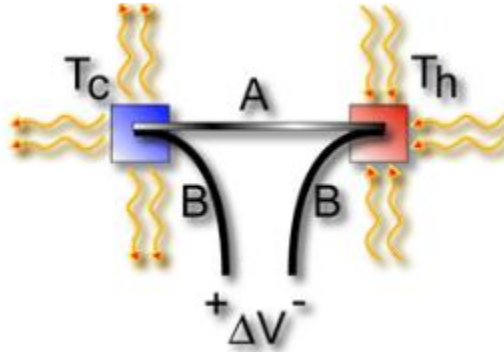


**Figure 1.1** A model of Seebeck effect circuit. The voltage difference,  $\Delta V$ , produced across the terminals of an open circuit made from a pair of dissimilar metals, A and B, whose two junctions are held at different temperatures, is directly proportional to the difference between the hot and cold junction temperatures ( $T_h - T_c$ ).

The Seebeck coefficient ( $S$ ), also referred as ‘thermopower’, can be expressed in terms of voltage build up ( $\Delta V$ ) and temperature gradient applied to the materials ( $\Delta T$ ) as,

$$S = -\frac{\Delta V}{\Delta T} = -\frac{V_h - V_c}{T_h - T_c} \quad (1.1)$$

### 1.2.1.2 Peltier Effect

The converse of Seebeck effect is the Peltier effect, where a temperature difference is created by passing an electric current between two junctions (two dissimilar metals). The effect is named after a French physicist Jean-Charles Athanase Peltier, who discovered this phenomenon in 1834.

This effect may sound similar to Joule heating described above, but in fact it is not. In Joule heating, the current is only increasing the temperature in the material in which it flows. In Peltier effect based devices, a temperature difference is created: one junction becomes cooler and other junction becomes hotter.

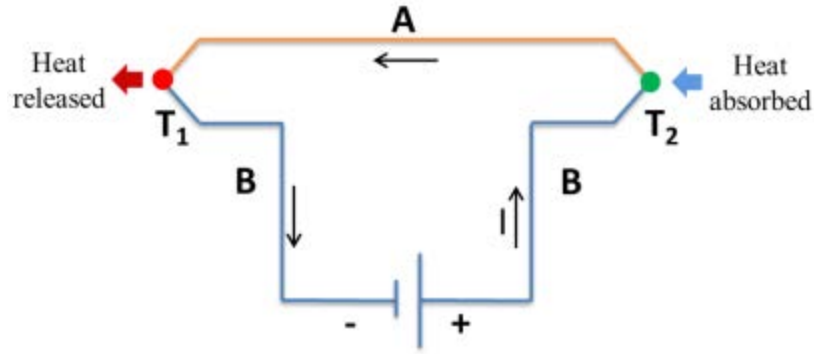


**Figure 1.2** Peltier effect circuit

Peltier effect is even stronger in circuits containing dissimilar semiconductors. If the current is reversed, heat generated by current flowing in one direction is absorbed. This effect can be explained from carrier energies. Electron conductors are analyzed as an example. For a metallic junction, the energy levels of electrons in different metals are different. In Figure 1.2, if the electron energy level in metal A is lower than in metal B, due to the existence of electric potential in a circuit, the electrons are pulled out from metal A to metal B at the green point. At this upper junction, the kinetic energy of electron will be converted to potential energy and electrons will move more slowly. Since the temperature is just a representation of the average speed of the random movements of the particles, the temperature at the upper junction will decrease. On the contrary, potential energy will be converted to kinetic energy at the lower junction (red point) by releasing heat. Similar to metallic conjunction, the directional movement of charge carriers can generate thermal effects (endothermic or exothermic phenomenon) at the interface. The Peltier heat generated per unit time ( $Q$ ) at the junction of conductor A and B (red point) is equal to,

$$Q = (\Pi_A - \Pi_B) I \quad (1.2)$$

where  $\Pi_A$ ,  $\Pi_B$  are Peltier coefficient of conductors A, B and  $I$  is the electric current from A to B.

Due to Peltier effect, the TE conjunctions can be used in applications ranging from travel coolers/warmers to laboratory instruments and communications systems. By cascading or pyramiding Peltier devices, quite large temperature differences can be generated.

### 1.2.1.3 Thomson Effect

The Thomson effect was predicted and subsequently observed by William Thomson (Lord Kelvin), a Scots-Irish mathematical physicist and engineer, in 1854. It describes the heating or cooling of a current-carrying conductor with a temperature gradient. Any current-carrying conductor (except for a superconductor) with a temperature difference between two points either absorbs or emits heat, depending on the material. If a current density ( $J$ ) passes through a homogeneous conductor, the heat production ( $Q$ ) per unit volume is:

$$Q = \rho J^2 - \tau J \frac{dT(x)}{dx} \quad (1.3)$$

where  $\rho$  is material resistivity,  $\tau$  is Thomson coefficient,  $dT/dx$  is the temperature gradient along the wire. Compared with the other two thermoelectric effects, Thomson effect is directly measurable for any given material. On the contrary, no direct method exists for determining absolute Seebeck or Peltier coefficients for one material.

### 1.2.1.4 Kelvin Relations

Indeed, the three thermoelectric coefficients mentioned above are not independent of each other. In 1854, Lord Kelvin found relationships among them, implying that Thomson, Peltier, and Seebeck effects are different manifestations of one effect (uniquely characterized by the Seebeck coefficient).

The first Kelvin relation is,

$$\tau = T \frac{dS}{dT} \quad (1.4)$$

The second Kelvin relation is,

$$\Pi = ST \quad (1.5)$$

where  $T$  is the absolute temperature. This relation expresses a subtle and fundamental connection between  $S$ ,  $\Pi$ , and  $\tau$ .



### 1.3 Applications of Thermoelectrics

Applications of thermoelectric modules cover a wide spectrum of product areas. These include equipment used by military, medical, industrial, consumer, scientific/laboratory, and telecommunication organizations. The technology has aroused worldwide interest in many fields, including waste heat recovery and solar heat utilization (power generation mode, as shown in Figure 1.3.a), and temperature-controlled seats, portable picnic coolers and thermal management in microprocessors (active refrigeration mode, as shown in Figure 1.3.b). Besides power generation and refrigeration, they also find applications in sensitive measurements of temperatures (thermocouple), detection of heat radiation (thermopiles, where an array of thermocouples are connected in series).

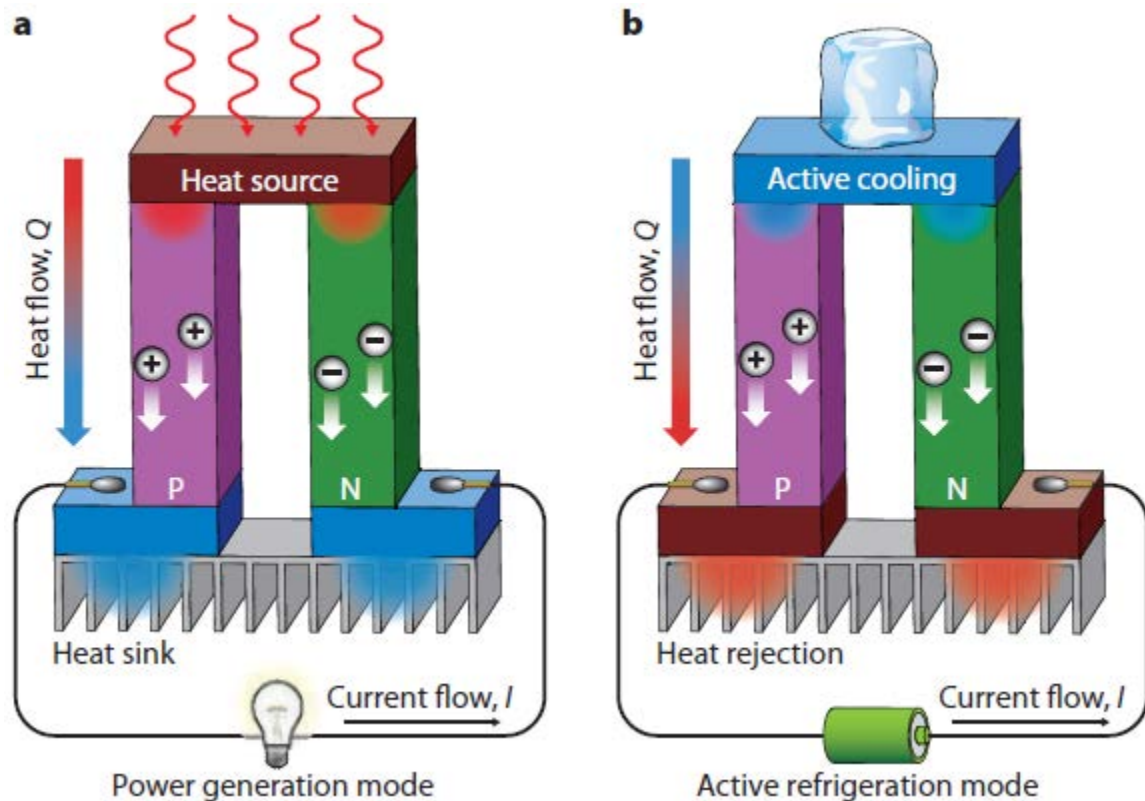


**Figure 1.3** Schematic illustrations of a thermoelectric module for (a) power generation (Seebeck effect), (b) active refrigeration (Peltier effect). (a) An applied temperature difference causes charge carriers in the material (electrons or holes) to diffuse from the hot side to the cold side, resulting in a flow of current through the circuit. (b) Heat evolves at the upper junction and is absorbed at the lower junction when a current is made to flow through the circuit. *Image courtesy:* © NPG Asia Materials, 2010.<sup>5</sup>

Thermoelectric devices contain many TE legs (Figure 1.4, bottom) consisting of  $n$ -type (containing free electrons) and  $p$ -type (containing free holes) thermoelectric elements wired electrically in series and thermally in parallel (Figure 1.4, top). A TE generator uses heat flow across a temperature gradient to power an electric load through the external circuit. The temperature difference provides the voltage from the Seebeck effect, while the heat flow drives the electrical current, which therefore determines the power output. In a Peltier cooler, the external circuit is a dc power supply, which drives the electric current and heat flow, thereby cooling the top surface due to the Peltier effect. In both devices the heat rejected must be removed through a heat sink.

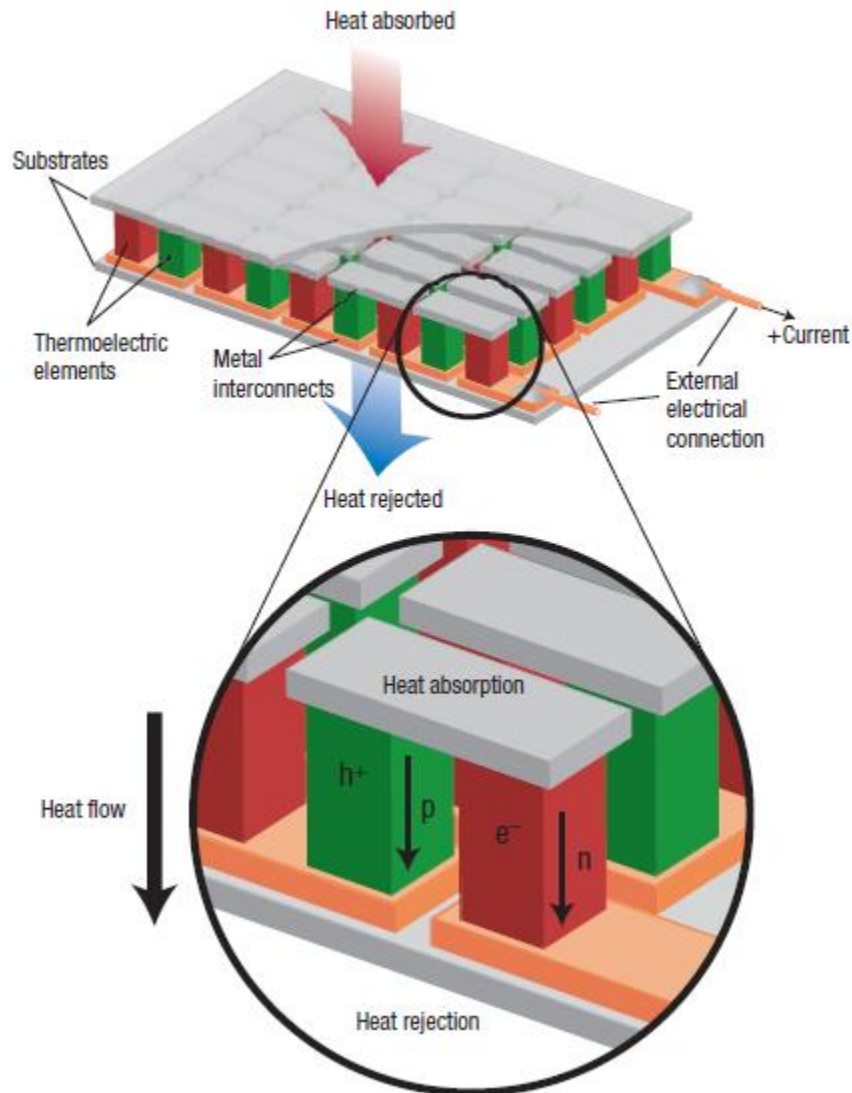


**Figure 1.4** Thermoelectric module showing the direction of charge flow on both cooling and power generation. *Image courtesy:* © Nature Materials, 2008.<sup>7</sup>

For the past 40 years, thermoelectric generators have reliably provided power in remote terrestrial and extraterrestrial locations, most notably on deep space probes such as *Voyager*. Solid-state Peltier coolers provide precise thermal management for optoelectronics and passenger seat cooling in automobiles. In the future, thermoelectric systems could harness waste heat and/or provide efficient electricity through co-generation. One key advantage of thermoelectrics is their scalability — waste heat and co-generation sources can be as small as a home water heater or as large as industrial or geothermal sources.

#### 1.4 Timeline of Thermoelectrics – History and Milestones

Year	Discovery / Milestones in Thermoelectric Applications
1821	Seebeck effect
1834	Peltier effect
1834	Thomson effect and Kelvin relations
1909	Altenkirch correctly derived the maximum efficiency of a thermoelectric generator (1909) and performance of a cooler (1911), which later developed into the 'thermoelectric figure of merit' ( $zT$ ).
1928	Ioffe began to develop the modern theory of semiconductor physics in order to describe thermoelectric energy conversion. This opened up the understanding of how to engineer thermoelectric materials, as well as providing the basis for understanding the physics of transistors and microelectronics.
1930	The first radio powered by thermoelectrics was publicized.
1947	Maria Telkes constructed the first thermoelectric power generator (TEG) with an efficiency of 5%.
1954	H. Julian Goldsmid successfully cooled a surface to 0° C using a thermoelectric Peltier cooler based on Bismuth telluride ( $\text{Bi}_2\text{Te}_3$ ).

- 1959 Westinghouse unveiled a full-size home refrigerator based on Bismuth Telluride ( $\text{Bi}_2\text{Te}_3$ ) Peltier thermoelectrics (but commercially unsuccessful).
- US President Dwight D. Eisenhower unveiled the first Radioactive Thermoelectric Generator "*SNAP III*".
- 1968 *SNAP-19* became the first radioisotope TEG to be flown on a NASA spacecraft. Another thermoelectric SNAP generator made it to the moon the next year.
- 1970 The first cardiac pacemaker powered by a miniature radioisotope TEG, made by Medtronic, was implanted into a human in France.
- 1975 A group of entrepreneurs acquired Lead Telluride ( $\text{PbTe}$ ) thermoelectric technology from 3M to produce remote terrestrial power generation products, forming Global Thermoelectrics.
- 1977 NASA launched *Voyagers 1* and *2* powered by MHW-RTG3, a Silicon Germanium ( $\text{SiGe}$ ) TEG.
- 1993 Hicks and Dresselhaus published a theory paper indicating that nanotechnology may offer significant advances in the efficiency of TE materials, ushering in the modern era of thermoelectrics.
- 1995 John Fairbanks at the US Department of Energy began a program to develop thermoelectric generators for automotive engines after Porsche did a prototype study using Iron Silicide TE materials.
- 1998 Seiko introduced the Thermic watch, the first watch powered from body heat, which has in it a  $\text{Bi}_2\text{Te}_3$  thermoelectric generator.
- 1999 Amerigon (now called Gentherm) was founded by Dr. Lon Bell, Advisor to Alphabet Energy, and introduced the first thermoelectric seat coolers in the Lincoln Navigator and Toyota's Lexus using  $\text{Bi}_2\text{Te}_3$ .
- 2001 RTI revealed the first significant breakthrough in TE material efficiency in forty years by using nanoscale materials, thus starting a new era of rapid advances

in TE materials. Nanostructures were then studied in many new TE materials systems, some of which include the Tellurides, Skutterudites, Half Heuslers, Silicides, etc.

- 2004 The US Department of Energy (DOE), in conjunction with General Motors, BMW, Caterpillar, and others, funded a program for automotive TE generators that became the driving force for much of the research in the field of TE generators for the next several years.
- 2013 *Voyager 1* became the first manmade object to exit the solar system and enter interstellar space after being continuously powered by a TEG for 36 years.
- 2014 Alphabet Energy introduced the E1, the first-ever TEG for industrial waste-heat recovery, and the most powerful thermoelectric generator ever built.

*Source of information about the timeline: Official website of Alphabet Energy, Inc (California, US).*

## 1.5 Key Thermoelectric Parameters

### 1.5.1 Figure of Merit

The thermoelectric material’s potential to convert waste heat into electricity is quantified by the dimensionless figure of merit ( $zT$ ) as given by the following equation,

$$zT = \frac{S^2 \sigma T}{\kappa_{latt} + \kappa_e} = \frac{S^2 \sigma T}{\kappa_{total}} \quad (1.6)$$

where  $S$ ,  $\sigma$ ,  $T$ ,  $\kappa_{total}$  are Seebeck coefficient, electrical conductivity, absolute temperature and total thermal conductivity respectively.  $\kappa_{total}$ , also represented as  $\kappa$  or  $\kappa_{tot}$ , is the sum of thermal conductivity contributions from lattice phonons ( $\kappa_{latt}$ ) and electrons ( $\kappa_e$ ). The term  $S^2\sigma$  is defined as ‘power factor’ (PF), which evaluates the ability of a TE material to produce useful electricity.

A potential material usable for applications in the field of thermoelectrics must have a higher  $zT$  value. From the above equation 1.6, it is clear that a material with interesting thermoelectric properties (*i.e.*, higher  $zT$ ) must concurrently possess high Seebeck coefficient, high electrical conductivity, and low thermal conductivity.

### 1.5.2 Thermoelectric Device Efficiency

In general, efficiency of a device is defined as a ratio of net power output to heat input. The maximum efficiency ( $\eta_{\max}$ )<sup>8</sup> of a thermoelectric generator (build using both *p*-type and *n*-type TE materials) is given by the following equation,

$$\eta_{\max} = \frac{T_H - T_C}{T_H} \frac{\sqrt{1 + zT} - 1}{\sqrt{1 + zT} + \frac{T_C}{T_H}} = \frac{\Delta T}{T_H} \frac{\sqrt{1 + zT} - 1}{\sqrt{1 + zT} + \frac{T_C}{T_H}} \quad (1.7)$$

where  $T_H$  and  $T_C$  are the hot and cold side temperature, and the first part of the equation  $\Delta T/T_H$  refers to the Carnot efficiency.

From Equation 1.7 and Figure 1.5, we can see that the high value of efficiency for a TEG can be obtained, if the value of  $zT$  is enhanced. When  $zT$  approaches infinity,  $\eta_{\max}$  approaches the Carnot limit. However, none of the present state-of-the-art TE materials exhibit  $zT$  larger than 3.<sup>9</sup>

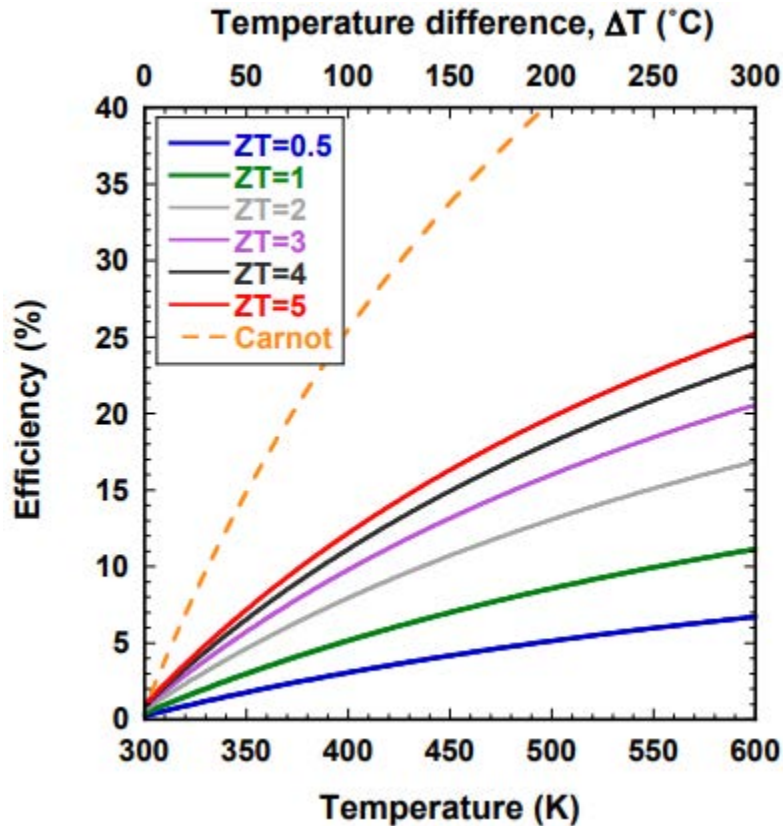


**Figure 1.5** Thermoelectric power generating efficiency. *Image courtesy:* © D.J. Paul, School of Engineering, University of Glasgow.

## 1.6 Conflicting Thermoelectric Material Properties

As mentioned in the previous section, to maximize the thermoelectric figure of merit ( $zT$ ) of a material, a large thermopower (absolute value of the Seebeck coefficient), high electrical conductivity, and low thermal conductivity are required. As these transport characteristics depend on interrelated material properties, a number of parameters need to be optimized to maximize  $zT$ . Hence the fundamental aspect to the field of TE materials is the need to optimize a variety of conflicting properties. Some of the key conflicts are listed below.

### 1.6.1 Conflict: Carrier Concentration – Seebeck Coefficient – Electrical Conductivity

To ensure a high Seebeck coefficient, a single type of charge carrier ( $n$ -type or  $p$ -type) should remain or dominate the transport in the material system, as mixed  $n$ -type and  $p$ -type charge carriers will lead to the opposite Seebeck effect and hence low thermopower. In order to achieve single type of carrier, it is necessary to select materials with suitable energy bandgaps and appropriate doping.

To gain maximum power factor, both Seebeck coefficient and electrical conductivity has to be larger. But both these parameters ( $S, \sigma$ ) are interlinked by carrier concentration ( $n$ ), but it a contrary way. Low carrier concentration insulators and even semiconductors have large Seebeck coefficients, as can be understood from Equation 1.8 ( $S$  inversely proportional to  $n$ ). However, low carrier concentration also results in low electrical conductivity, as per Equation 1.9 ( $\sigma$  directly proportional to  $n$ ).

For metals or degenerate semiconductors, the Seebeck coefficient is given by,

$$S = \frac{8\pi^2 k_B^2 m^* T}{3eh^2} \left(\frac{\pi}{3n}\right)^{2/3} \quad (1.8)$$

where  $m^*$ ,  $k_B$ ,  $e$  and  $h$  are effective mass, Boltzmann constant, electron charge and Planck constant, respectively.

The electrical conductivity and electrical resistivity ( $\rho$ ) are related to  $n$  through the carrier mobility ( $\mu$ ),

$$1/\rho = \sigma = ne\mu \quad (1.9)$$

Figure 1.6 shows the compromise between large thermopower and high electrical conductivity in thermoelectric materials that must be struck to maximize the figure of merit,  $zT$  ( $S^2\sigma T/\kappa$ ). This peak (for power factor) typically occurs at carrier concentrations between  $10^{19}$  and

$10^{21} \text{ cm}^{-3}$  (depending on the material system), which falls in between common metals and semiconductors — that is, concentrations found in heavily doped semiconductors.

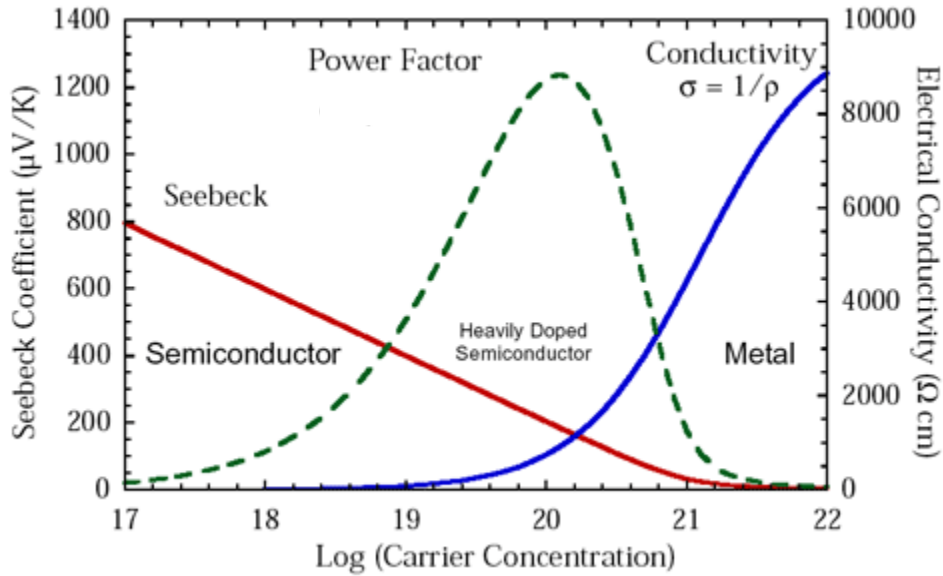


**Figure 1.6** Optimizing thermoelectric power factor ( $PF = S^2\sigma$ ) through tuning of charge carrier concentration. Maximizing the  $zT$  of TE material involves a compromise of  $S$  and  $\sigma$ . The thermoelectric power factor peaks at carrier concentration window between  $10^{19}$  and  $10^{21} \text{ cm}^{-3}$ , the values of which are typically exhibited by heavily doped semiconductors. *Image courtesy:* © Division of Engineering & Applied Sciences, California Institute of Technology.

### 1.6.2 Conflict: Effective Mass – Mobility

The effective mass of the charge carrier provides another conflict, as large effective masses produce high thermopower but low electrical conductivity. The  $m^*$  in Equation 1.8 refers to the density-of states (DOS) effective mass, which increases with flat, narrow bands with high density of states at the Fermi surface ( $E_F$ ). However, as the inertial effective mass is also related to  $m^*$ , heavy carriers will move with slower velocities, and therefore small mobilities, which in turn leads to low electrical conductivity (Equation 1.9). The exact relationship between effective mass and mobility is complex, and depends on electronic structure, scattering mechanisms and anisotropy.

High  $\mu$  and low  $m^*$  is typically found in materials made from elements with small electronegativity differences, whereas high  $m^*$  and low  $\mu$  are found in materials with narrow bands



such as ionic compounds.<sup>7</sup> A balance must be found for the effective mass (or bandwidth) for the dominant charge carrier, *i.e.*, a compromise between high  $m^*$  and high  $\mu$ .

### 1.6.3 Conflict: Electronic Thermal Conductivity – Electrical Conductivity

In TE materials, the thermal conductivity ( $\kappa_{\text{total}}$ ) stems from two sources: (1) electrons and holes transporting heat ( $\kappa_e$ ), and (2) phonons travelling through the lattice ( $\kappa_{\text{latt}}$ ).

$$\kappa_{\text{total}} = \kappa_{\text{latt}} + \kappa_e \quad (1.10)$$

To maximize  $zT$ , it is paramount to have lower thermal conductivity and higher electrical conductivity. But the electronic thermal conductivity (which needs to be minimum) is directly related (*i.e.*, direct proportionality) to the electrical conductivity (which infact needs to be maximum) through the Wiedemann-Franz law,

$$\kappa_e = L\sigma T = ne\mu LT \quad (1.11)$$

where  $L$  is the Lorenz factor.

In short, taking into account all these inherent material conflicts, the tactic lies in the strategy to strike the right balance and compromise between these transport properties (or parameters) in achieving a high thermoelectric efficiency.

## 1.7 Approaches to Enhance Thermoelectric Performance

The approaches to reach high values of  $zT$  rely on strategies aimed at either increasing the power factor or decreasing the thermal conductivity. Several approaches have evolved during the recent years. The theory behind some of those best adopted approaches are briefly discussed in this section.

### 1.7.1 Phonon-Glass Electron-Crystal (PGEC) Approach

Slack<sup>10</sup> suggested that the best thermoelectric material would behave as “phonon-glass electron-crystal”, which means that the material must concurrently possess low lattice thermal conductivity, as in the case of a glass where phonons are effectively scattered or disrupted at the

atomic scale from transporting heat, as well as have high electrical conductivity, like a crystal where there is a high level of electron mobility to transport charge and heat. Materials with complex crystal structures and large unit cells are being pursued in hopes of discovering effective PGECs. Typical examples of PGEC thermoelectric materials are the partially filled clathrates,<sup>11</sup> skutterudites<sup>12</sup> and Zintl compounds.<sup>13,14</sup>

### 1.7.1.1 Skutterudites

The skutterudite is a type of arsenide mineral that was first discovered in Norway in 1845. They crystallize in the  $\text{CoAs}_3$ -type structure with the cubic space group  $Im\bar{3}$ .<sup>15,16</sup> The structure is composed of eight corner-shared  $\text{XY}_6$  ( $X = \text{Co, Rh, Ir}$ ;  $Y = \text{P, As, Sb}$ ) octahedra. In fact, the  $\text{CoAs}_3$ -structure type is a severely distorted version of the perovskite  $\text{AB}_3$  type structure.<sup>17</sup> Figure 1.7 show that the linked octahedral produce a void at the center of the  $(\text{XY}_6)_8$  cluster, where the void space occupies a body-centered position of the cubic lattice. This void is large enough to accommodate large metal atoms (as ‘rattlers’) to form filled skutterudites.

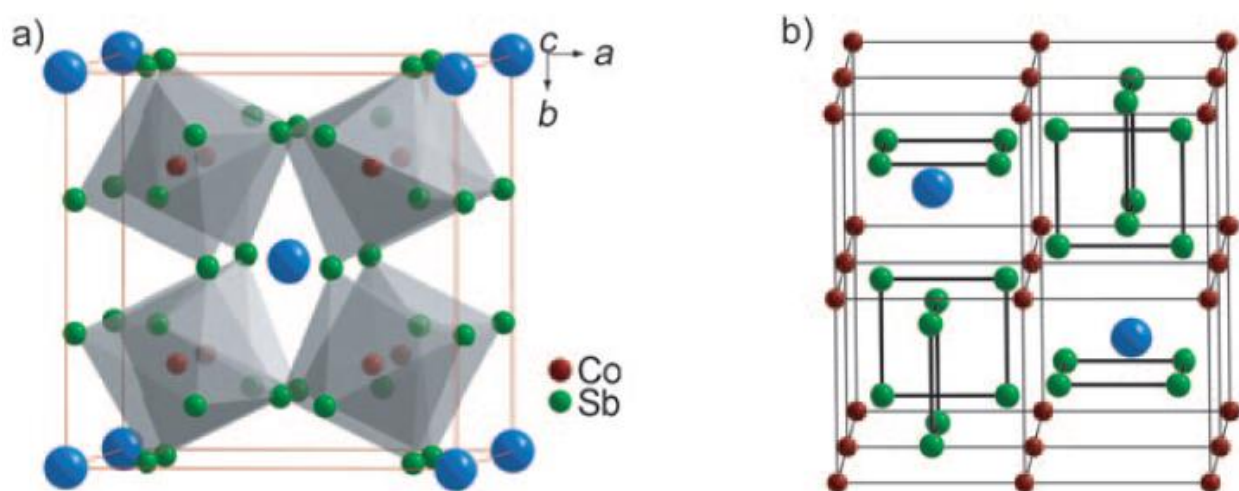


**Figure 1.7** Model structures of the skutterudite,  $\text{CoSb}_3$ ; the void cages are filled with blue spheres for clarity. a) The unit cell of skutterudite structure. The transition metals (Co) are at the center of octahedra formed by pnictogen atoms (Sb). b) The model shifted by the fractional coordinates  $1/4, 1/4, 1/4$  from the unit cell. The Co atoms are connected for clarity. The only chemical bonds in this model are those of the Sb squares. *Image courtesy:* © *Angew. Chem. Int. Ed.*, 2009.<sup>17</sup>

The original thermoelectric skutterudite  $\text{CoSb}_3$  has a very high power factor, but its lattice thermal conductivity ( $\sim 10 \text{ W/mK}$  at 300 K)<sup>17</sup> is too high to result in a good thermoelectric material. One successful chemical approach for optimizing these materials turned out to be void-filling in the structure with many different elements (as ‘rattlers’) including lanthanide, actinide, alkaline-earth, alkali, thallium, and group-IV elements.<sup>17,18</sup> Since the void-filling atoms can act as electron donors or acceptors, partially filling the void space of skutterudites could lead to an optimum electron concentration. At the same time, these atoms can also act as strong phonon-scattering centers to greatly reduce the lattice thermal conductivity. The smaller and heavier the ion in the voids, the larger the disorder that is produced and, therefore, the larger the reduction in the lattice thermal conductivity. The “rattling” effect of these void-filling atoms has resulted in improvements in the thermoelectric properties of several skutterudite materials (with  $zT > 1.3$  at 800 K).<sup>19,20</sup>

### 1.7.1.2 Clathrates

Clathrates or clathrate compounds consist of regular lattices of cages in which guest atoms or molecules are encapsulated. Cages with restricted geometry form the basic framework of a lattice with translational invariance. Clathrates are also called host-guest complexes. Typical examples of host-guest complexes are inclusion compounds and intercalation compounds.<sup>21</sup> There are several main types of clathrates, based on their cage structures (Figure 1.8).<sup>11</sup>

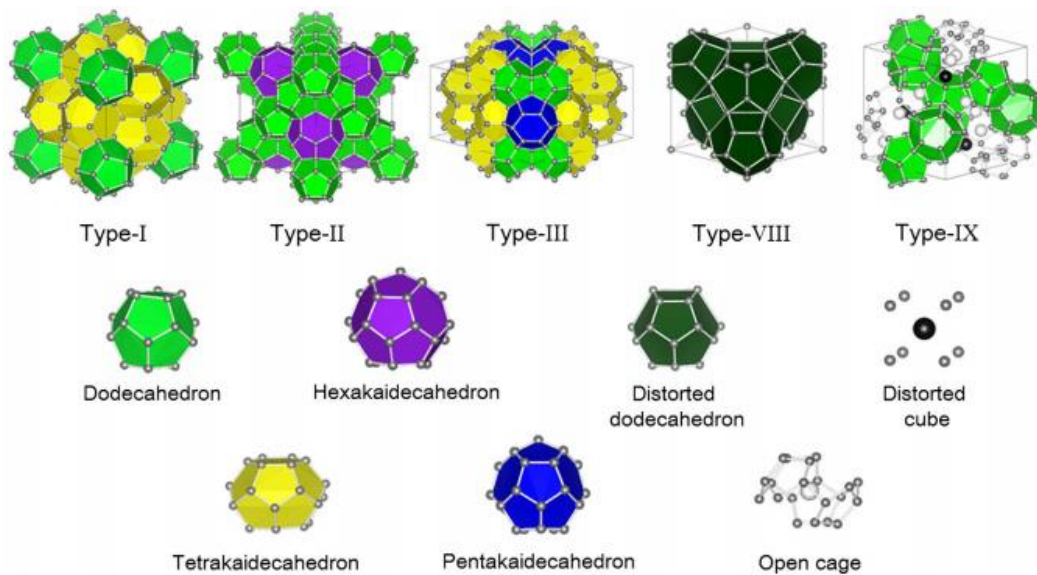


**Figure 1.8** Crystal structures of type-I, type-II, type-III, type-VIII, and type-IX intermetallic clathrates. *Image courtesy:* © Rev. Mod. Phys., 2014.<sup>11</sup>

Type I is the most common form, which constitute networked cages consisting of nanoscale tetrakaidecahedrons with 14 flat faces (14-hedrons) and dodecahedrons with 12 flat faces (12-hedrons),<sup>11</sup> in which the group-1 or -2 element in the periodic table can fill in the cages (as rattling guest atoms).

In the cages of clathrates, the guest atoms are thought to effectively “rattle” and scatter lattice phonons, suppressing the lattice thermal conductivity. It has been observed that not only are the “rattling” atoms important, but that the open nature of the framework also results in low thermal conductivity.<sup>22</sup> Strategically designed clathrates, especially of the  $R_8Ga_{16}Ge_{30}$  family (with the guest atom  $R = Ba, Sr, \text{ and } Eu$ ), have reportedly exhibited improved thermoelectric performances.<sup>11,17</sup>

### 1.7.1.3 Zintl Compounds

A Zintl compound contains a valence-balanced combination of both ionically and covalently bonded atoms.<sup>23</sup> The mostly ionic cations donate electrons to the covalently bound anionic species. The covalent bonding allows higher mobility of the charge carrier species than that found in purely ionic materials. The combination of the bonding types lead to complex structures with the possibility of multiple structural units in the same structure.<sup>7,24,25</sup>

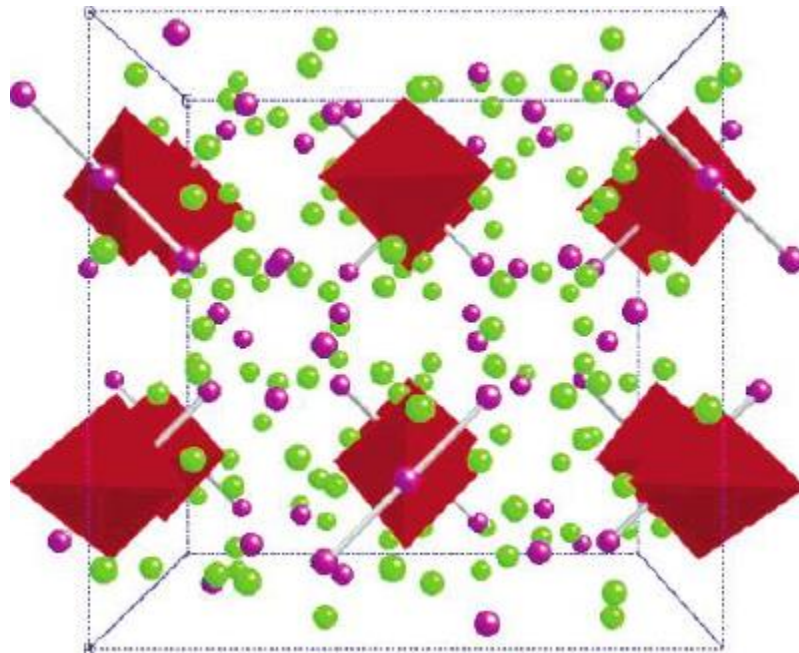


**Figure 1.9** Body-centered,  $I41/acd$  crystal structure of  $Yb_{14}MnSb_{11}$ . The green and purple spheres represent Yb and Sb, respectively. The  $MnSb_4$  tetrahedron is shown as a filled red polyhedron. *Image courtesy: © Chem. Mater., 2006.*<sup>12</sup>

As these compounds combine distinct regions of covalent bonding and ionically bonded cations that can be easily substituted for precise tuning of electronic properties, it leads to the desired ‘electron-crystal’ behavior. The complex structures and disorder creates ‘phonon-glass’ properties resulting in low lattice thermal conductivity, thus making many Zintl compounds as natural PGEC materials.

One best example for these Zintl compounds is the  $\text{Yb}_{14}\text{MnSb}_{11}$ , which contains  $[\text{MnSb}_4]^{9-}$  tetrahedra, polyatomic  $[\text{Sb}_3]^{7-}$  anions, as well as isolated  $\text{Sb}^{3-}$  anions and  $\text{Yb}^{2+}$  cations (Figure 1.9).<sup>12,13</sup> This structural complexity, despite the crystalline order, enables extremely low lattice thermal conductivity, resulting in  $zT \sim 1.0$  at 900 °C.<sup>13</sup>

Such high  $zT$  values have been obtained for several complex structured Zintl phase compounds, such as  $\text{Zn}_4\text{Sb}_3$ ,  $\text{Yb}_9\text{Mn}_{4.2}\text{Sb}_9$ ,  $\text{YbZn}_2\text{Sb}_2$ ,  $\text{YbCd}_2\text{Sb}_2$ ,  $\text{BaZn}_2\text{Sb}_2$ ,  $\text{BaGa}_2\text{Sb}_2$ ,  $\text{Eu}_5\text{In}_2\text{Sb}_6$ ,  $\text{Yb}_5\text{In}_2\text{Sb}_6$ ,  $\text{EuZn}_2\text{Sb}_2$ , etc.<sup>23</sup>

#### 1.7.1.4 Half-Heusler Compounds

Though not as pertinent PGEC class of materials as Zintl, clathrates and skutterudites, Half-Heuslers (HH) are another class of compounds of considerable interest for high-temperature TE applications (due to their high melting points of 1100–1300 °C as well as their chemical stability with essentially zero sublimation at temperatures near 1000 °C).

HH compounds are ternary intermetallics with a general formula  $\text{ABX}$ , where A is usually the most electropositive transition metal, B is a less electropositive transition metal and X is a main group element. A typical HH compound has a cubic  $\text{MgAgAs}$ -type structure with the  $F\bar{4}3m$  space group. It consists of three filled interpenetrating face centered cubic (fcc) sublattices and one vacant fcc sublattice.<sup>17</sup> Additionally, if the vacant sublattice is filled by the transition metal B, the corresponding Heusler structure with formula  $\text{AB}_2\text{X}$  is obtained (Figure 1.10). The properties of HH compounds depend strongly on the valence electron count (VEC) of the constituent elements, which determine the band structure and consequently the physical properties of these compounds.<sup>26</sup>

$\text{MNiSn}$  ( $\text{M} = \text{Ti, Hf, Zr}$ ) is a well-studied family of HH compounds. In the unit cell of these compounds, M and Sn occupy a NaCl lattice, while Ni occupies fcc sublattice.<sup>17</sup> The Heusler intermetallic compounds with fully filled sublattices are metals (full-Heusler alloys), whereas the vacant Ni atom sites in half-Heusler compounds give rise to narrow bands resulting in  $d$ -orbital hybridization and substantial semiconducting character of the compounds. The narrow bands give rise to a large effective mass in these compounds and a large thermopower.

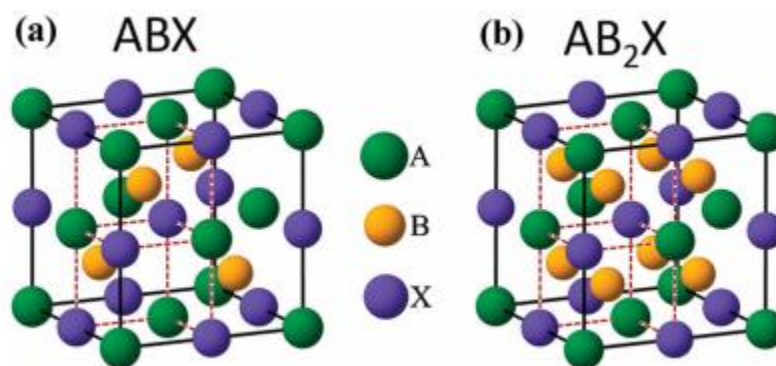


**Figure 1.10** Crystal structure of half-Heusler  $ABX$  (a) and Heusler  $AB_2X$  (b) compounds. *Image courtesy:* © *Adv. Energy Mater.*, 2015. <sup>26</sup>

Chemical manipulations help to optimize the TE properties of HH compounds. For example, doping on the Sn site provides the charge carriers, while doping the Ti and Ni sites causes mass fluctuation disorder and increased atomic disorder at the transition-metal sites that can lead to the reduction of thermal conductivity.<sup>17</sup> When metallic elements are doped to the half-Heusler families of ZrNiSn, TiCoSb and FeNbSb, they are known to exhibit  $zT > 1$  at higher temperatures.<sup>26–28</sup>

### 1.7.1.5 Conducting Chalcogenide Glasses

Till early 2010, the explored or the designed materials based on PGEC model were only crystalline materials like skutterudites, Zintl compounds, clathrates, as described in the previous passages. Post 2010, a revival in a different approach to the PGEC principle appeared. It deals with the possibility of designing electrically conductive glassy phases, based on chalcogenide-telluride glasses, which are known to inherently possess high Seebeck coefficient and low thermal conductivity. The main limiting factor in these chalcogenide glasses is their mediocre electrical conductivity. During our earlier European ITN project (GlaCERCo), the researchers from our laboratory in Rennes jointly with the team from Prof. Pierre Lucas’ group (from University of Arizona, U.S) found that doping glasses with metals like Cu could lead to a huge enhancement in the electrical conductivity without involving any crystallization, and retaining the characteristic high Seebeck coefficient and low thermal conductivity.<sup>29,30</sup> Similar kind of semiconducting / conducting chalcogenide glasses have also been extensively explored for potential TE applications by a group of scientists jointly from Lisbon, Montpellier, Limoges and Nancy.<sup>31–35</sup> More details regarding chalcogenide glasses for thermoelectrics are discussed in detail in Chapters 2 and 3.

## 1.7.2 Band Engineering Approach

As mentioned earlier,  $S$  and  $\sigma$  are highly inter-twined and present a greater challenge in enhancing the power factor, which is paramount for better energy conversion efficiency. Advances in recent times have shown that the concept of ‘band structure engineering’, which includes convergence of electronic band valleys,<sup>36,37</sup> quantum confinement of electron charge carriers,<sup>38</sup> electron filtering,<sup>39</sup> inducing resonant levels by impurities near the Fermi level,<sup>40</sup> nestification,<sup>41</sup> dimensionality reduction,<sup>42</sup> deformation potential coefficient,<sup>43</sup> and effective mass,<sup>44</sup> are effective in decoupling  $S$  and  $\sigma$  to achieve high TE efficiency.

### 1.7.2.1 Convergence of Electronic Band Valleys

If there are more than one type of charge carriers, carrier contributions from different bands must be considered. In order to simplify the calculation, a two-band model is usually deemed sufficient.<sup>45</sup> A classic example when the two band model is used concerns the case of intrinsically generated electrons in the conduction band and the corresponding number of holes in the valence band. Another often encountered situation is charge carriers of the same sign arising from different bands, *e.g.* light (L) and heavy bands ( $\Sigma$ ). In a system that contains two valence (or conduction) bands, the total electrical conductivity and Seebeck coefficient be expressed as,

$$\sigma = \sigma_1 + \sigma_2 \quad (1.12)$$

$$S = \frac{S_1\sigma_1 + S_2\sigma_2}{\sigma_1 + \sigma_2} \quad (1.13)$$

where the subscripts 1 and 2 represent transport properties of carriers in the individual band.

The basic physics underlying the thermoelectric phenomena emphasizes that good TE materials require high band degeneracy and multiple valleys near the Fermi level to maximize their thermoelectric power factor, PF.<sup>46</sup> This can be understood based on Equations (1.12) and (1.13). Having two bands containing carriers of the same sign but different  $m^*$  and  $\mu$  (meaning different  $S$  and  $\sigma$  values), say for *e.g.* light (L) and heavy hole ( $\Sigma$ ) valence bands, the PF is maximized when  $S_1\sigma_1$  and  $S_2\sigma_2$  have comparable values. If the bands deviate greatly from each other near the Fermi level, the PF diminishes due to a rapid reduction of  $S$  (more carriers in the band) or  $\sigma$  (less carriers in the

band). However, when the band edges of the two bands overlap, both bands can yield high values of the product of  $S$  and  $\sigma$ .

Overlapping band edges are well documented in many classical TE materials. It was shown that  $\sigma$  and therefore the PF, was enhanced from the convergence of many ‘degenerate valleys’ within the electronic band structure of PbTe.<sup>45</sup> Increasing the number of degenerate valleys increases the entropy per charge that can pass through the materials, thus resulting in a higher  $S$  and  $\sigma$ . Taking advantage of multiple bands is one of the general strategies applied in the search for and improvement of bulk thermoelectric materials. Pei and Snyder<sup>37</sup> have shown that the positions of L and  $\Sigma$  valence bands in PbTe shift as a function of temperature and they completely overlap (at around 500 K), *i.e.*, band convergence (Figure 1.11), which leads to an improved TE performance. In this case, the convergence of the  $\Sigma$  band with 12 valleys and the L band with 4 valleys in  $p$ -type  $\text{PbTe}_{1-x}\text{Se}_x$  alloys, leads to an extraordinary  $zT$  value of  $\sim 1.8$  at about 850 K.<sup>37</sup> In addition to the favorable convergence of multi-valleys, the high degeneracy of the  $\Sigma$  band also played a crucial role in its high performance.

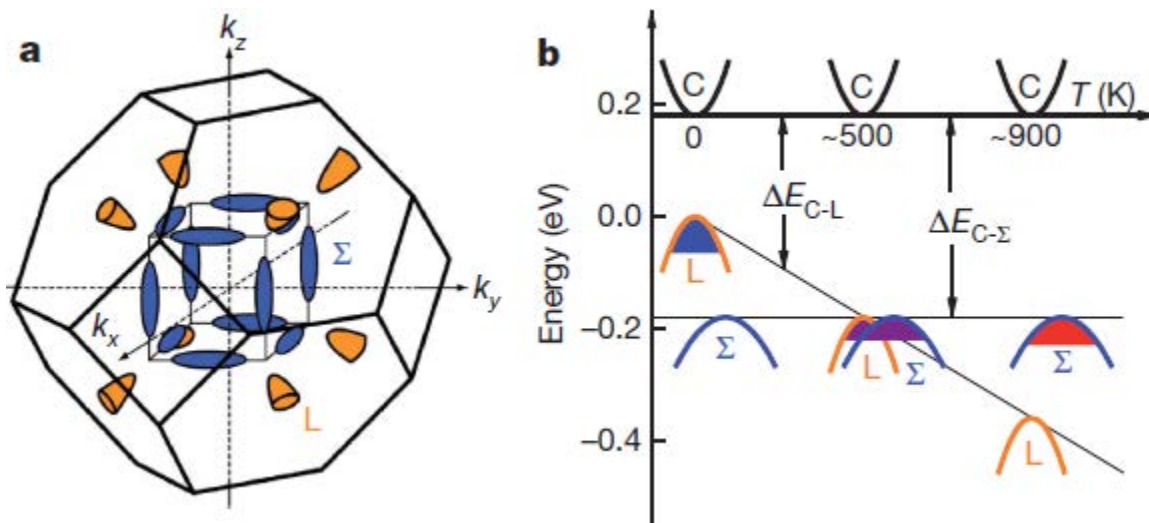


**Figure 1.11** Valence band structure of  $\text{PbTe}_{1-x}\text{Se}_x$ . (a) Brillouin zone showing the low degeneracy hole pockets (orange) centered at the L point, and the high degeneracy hole pockets (blue) along the  $\Sigma$  line. (b) Relative energy of the valence bands in  $\text{PbTe}_{0.85}\text{Se}_{0.15}$ . At 500K, the two valence bands converge, resulting in transport contributions from both the L and  $\Sigma$  bands. *Image courtesy:* © Nature, 2011.<sup>37</sup>

A more common approach is to adjust the composition of solid solutions to realize the band convergence. This is particularly applicable in the case of solid solutions that have a wide solubility range, as the compositional adjustments or doping may cause considerable changes in the band



structure. In the past few years (more intensely in the past 3 years), an extensive work has gone through to enhance the  $zT$  via electronic band convergence in chalcogenide based solid solutions, especially in the doped PbTe, SnTe and GeTe family of materials. Such notable dopant induced band convergence in those classes of solid solution includes, Mg doped PbTe,<sup>47</sup> K or Na doped PbTe,<sup>48,49</sup> Sn and Na codoped PbTe,<sup>50</sup> Mg doped SnTe,<sup>36</sup> Cd doped SnTe,<sup>51</sup> Ca doped SnTe,<sup>52</sup> Hg doped SnTe,<sup>53</sup> Bi and Pb codoped SnTe,<sup>54</sup> Mn doped GeTe,<sup>55</sup> Bi and Pb codoped GeTe,<sup>56</sup> Sb doped GeTe,<sup>57</sup> Sb and Bi codoped GeTe,<sup>58</sup> all of which exhibited a phenomenal thermoelectric properties. This approach has also been successfully applied to  $Mg_2Si_{1-x}Sn_x$  solid solutions and half-Heusler alloys.<sup>46,59,60</sup>

### 1.7.2.2 Electronic Resonance States

According to the Wilson and Mott theory, the energy dependence of the carrier concentration,  $n$  or mobility,  $\mu$  near the Fermi level determines the Seebeck coefficient.

$$S = \frac{\pi^2 T k_B^2}{3q} \left( \frac{dn(E)}{ndE} + \frac{d\mu(E)}{\mu dE} \right)_{E=E_F} \quad (1.14)$$

Hence based on the above Mott’s relationship, the Seebeck coefficient can be enhanced in couple of ways:<sup>61</sup> (i) by increasing the energy dependence of  $\mu(E)$ , which is usually achieved by critical carrier scattering near phase transitions and by charge carrier relaxations, or (ii) by increasing the energy dependence of  $n(E)$ , which could originate from an unconventional distortion / local increase in the density of states  $g(E)$ , if proper dopants are introduced. If those dopants have energy levels in a band of the host material, they may create resonant levels which can distort the DOS near the  $E_F$ , which leads to an increase in effective mass of the carriers without changing the carrier concentration and contribute to an enhanced thermopower.

It must be noted that unlike the band convergence, the electron resonant state strongly scatters carriers and thus can have a deleterious effect on the power factor by degrading the electrical conductivity. To benefit from the presence of resonant states, any enhancement in the Seebeck effect must significantly exceed the damage done to the electrical conductivity.

This approach has been applied effectively to several classes of chalcogenide based materials to enhance their thermoelectric performance. Some notable examples of resonant dopant induced TE enhancement ( $zT > 1$ ) includes, Ga/In/Tl doped PbTe,<sup>62–65</sup> Al doped PbTe,<sup>66</sup> Al doped PbSe,<sup>67</sup> Tl doped PbSe,<sup>68</sup> In doped PbTe,<sup>69,70</sup> In doped  $PbTe_{1-y}S_y$ ,<sup>71</sup> In doped SnTe,<sup>40</sup> and In doped GeTe.<sup>71</sup>

Figure 1.12 demonstrates the creation of In-induced resonance state in cubic-GeTe, which usually features like a hump.

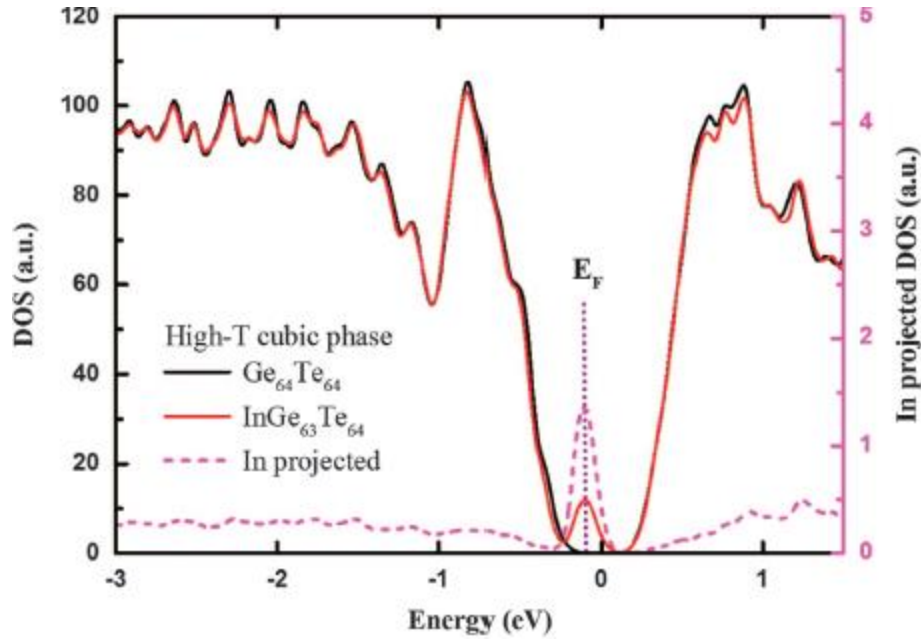


**Figure 1.12** The calculated density of states (DOS) for high temperature cubic  $\text{InGe}_{63}\text{Te}_{64}$  showing an abrupt change (hump) of DOS at  $E_F$ , i.e., formation of resonance state. *Image courtesy:* © NPJ Asia Mater., 2017.<sup>71</sup>

### 1.7.2.3 Synergistic Band Effects

The recent developments have shown that it is possible to achieve both band convergence and resonance state in a material, if optimally doped with suitable elements that have distinct but complementary roles, and the resultant synergistic effect of band convergence and resonant level can effectively enhance the  $zT$ . Formation of the resonance level is known to enhance the room temperature  $S$  value, whereas the high temperature  $S$  value can be significantly enhanced through the convergence of the valence bands.<sup>36,40</sup> Since the formation of the resonance level and the convergence of band valleys complement one another, the synergistic effect of these two concepts can significantly enhance the overall power factor.

Such synergistic effects have proven to be successful in chalcogenides, especially in enhancing the thermoelectric performance of SnTe based materials. Some notable examples of these synergistic / co-adjuvant effect of resonant level and band convergence are successfully realized in In-Ag codoped SnTe,<sup>72</sup> In-Mg codoped  $\text{Sn}_{1-x}\text{Pb}_x\text{Te}$ ,<sup>73</sup> In-Cd codoped SnTe,<sup>74</sup> In-Mn codoped SnTe,<sup>75</sup> In-Hg codoped SnTe.<sup>76</sup> In all these cases, In doping fostered the resonant state near the  $E_F$  (Infact, In is irreplaceable in introducing such element-selective resonant level near  $E_F$ ),<sup>76</sup> and other dopants (Ag, Mg, Cd, Mn, Hg) helped in band convergence.

### 1.7.2.4 Bipolar Effects

As already mentioned, to achieve high thermopower, there has to be only one type of charge carrier contributing to the transport processes. But, most of the TE materials are narrow band gap semiconductors, where there is a high chance for the existence of mixed carriers (holes and electrons). In narrow band gap semiconductors, the carriers in the valence band can partially hop to the conduction band, and vice versa, thus resulting in the creation of electron-hole pairs. Such bipolar effects are detrimental to the TE properties, because minority carriers that are thermally excited across the band gap can decrease the thermopower. Bipolar effects can be suppressed either by increasing the carrier density, so that the majority carriers shift the  $E_F$  and decrease the onset of minority carrier effects by increasing the energy required to do so, or by opening up the band gap, which can delay the onset of thermally activated minority carriers at elevated temperatures.

### 1.7.3 Nanostructure Engineering

#### 1.7.3.1 Dimensionality Reduction

Nanostructure engineering, such as forming quantum dots and wells,<sup>77</sup> nanowires and nanotubes,<sup>78,79</sup> and thin films,<sup>80</sup> have been recognized as an effective way to modulate physical and chemical properties. If the dimensionality of the material is decreased and approaches nanometer length scales, the new variable of length scale becomes available for the control of material properties.<sup>38,81</sup> Dresselhaus,<sup>42</sup> proposed the possibility to cause dramatic differences in the electronic density of states, when the system size decreases from 3D crystalline solids to 2D (quantum wells) to 1D (quantum wires) and finally to 0D (quantum dots) allowing new opportunities to decouple electronic and thermal transport properties (quantum-confinement effects).

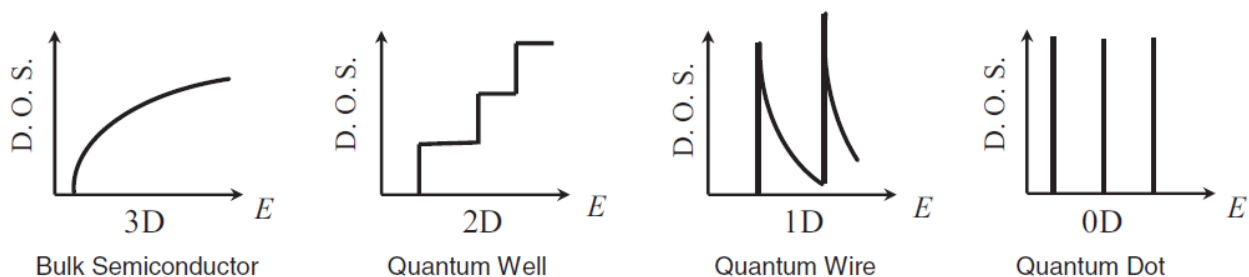


**Figure 1.13** Electronic density of states for (a) bulk 3D crystalline semiconductor, (b) 2D quantum well, (c) 1D nanowire or nanotube, and d) 0D quantum dot. *Image courtesy:* © Adv. Mater., 2007.<sup>42</sup>

Similar concepts such as, carrier-pocket engineering<sup>82</sup> energy filtering,<sup>39,83</sup> and the semimetal-semiconductor transition<sup>84</sup> have further advanced the potential for using low-dimensional materials to enhance the thermoelectric performance.

### **1.7.3.2 Phonon Scattering**

The minimization of lattice thermal conductivity can come through solid solution alloying (point defects), dislocation, elastic and/or plastic strain, displacement layers, nanoscale precipitates, and meso-scale grains. Each microstructural constituent in the bulk material can potentially scatter different frequency heat-carrying phonons.

#### **1.7.3.2.1 Atomic-scale Scattering (short wavelength phonons)**

Point defects, including intrinsic and charge-balance vacancies, interstitials, anti-site defects and impurities, are defects that occur only at or around a single atomic site and are not significantly extended in space in any dimension. Whether the alloying elements introduce charge or structural disorder, there are inevitable structural effects at the atomic scale. Even when their nominal sizes are similar to that of the host atoms, there are often atomic shifts away from the ideal lattice sites. These off-site atoms create force differences (strain field fluctuations) and mass contrast (mass fluctuations) between the host atoms and the impurity atoms. The dopant atoms also create unit cell volume differences. Therefore, point defects with these differences scatter long frequency (short wavelength) phonons. Given that most thermoelectric materials are doped and contain an intrinsic (equilibrium) population of point defects, especially at elevated temperatures, this atomic-scale phonon scattering mechanism is ubiquitous in most thermoelectrics.

#### **1.7.3.2.2 Nano-scale Scattering (mid to long wavelength phonons)**

Materials with embedded nanoparticles seem to demonstrate significantly reduced thermal conductivity.<sup>85</sup> This, of course, depends on the nature of the ‘contrast’ and impedance between the second phase and the matrix as well as the nature of interfaces between the two phases. Such nanoparticles, strains, and dislocations can scatter low to mid frequency (mid to long wavelength) phonons.<sup>86</sup> Figure 1.14 shows a schematic representation of three types of precipitate–matrix interfaces: (i) coherent (with possible elastic strain), (ii) incoherent (with minimal interactions

between the phases), and (iii) semi-coherent (misfit dislocations separated by elastic strain). These three scenarios embody different atomic configurations and associated local interfacial relaxation mechanisms. The phonon scattering effect also depends on the mass difference and bond stiffness, which is similar to that of point defects, but with a different length-scale.

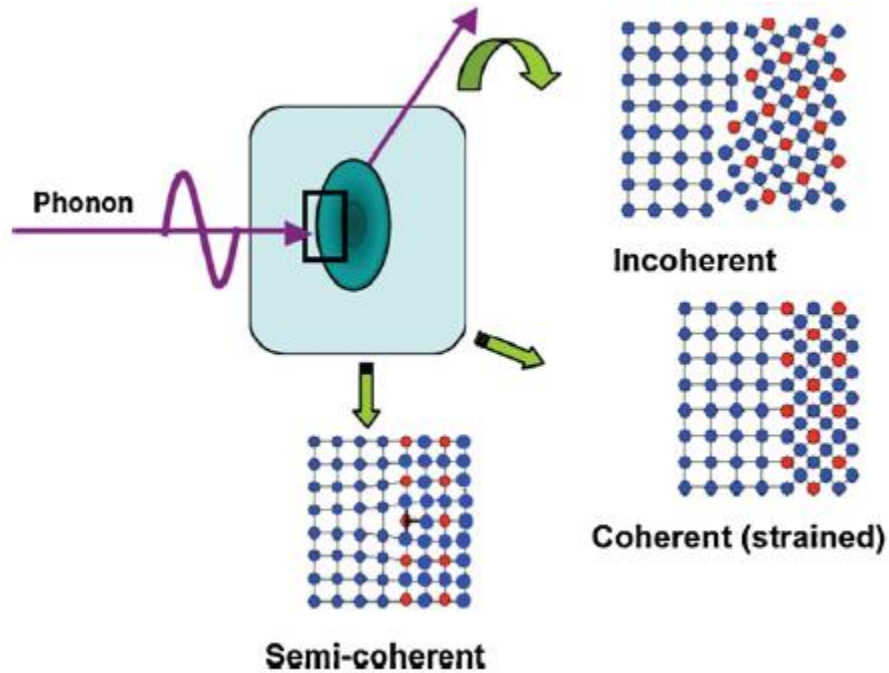


**Figure 1.14** Schematic representation of phonon scattering by different precipitate-matrix interfaces. *Image Courtesy:* © Materials Today, 2013.<sup>87</sup>

In general, attempts to control the formation of nanoparticles in bulk materials involve a microstructure engineering approach, whereby phase separation processes are manipulated to generate nanoparticles (second phase) that are embedded within the parent thermoelectric material. This has been clearly demonstrated in several alloy systems, especially in PbTe based systems using a variety of approaches, including precipitation,<sup>88</sup> nucleation and growth<sup>89</sup> and spinodal decomposition,<sup>90</sup> eutectic,<sup>91</sup> and matrix encapsulation methods.<sup>92</sup> The major matrix phase and secondary minor phase must be judiciously chosen considering phase stability and compatibility, utilizing natural phase separation and precise thermal treatment to selectively induce the minor phase to precipitate as nanoparticles.<sup>87</sup>

Coherent precipitates often represent elastic strain across the interfaces, while semi-coherent precipitates contain plastic strain in the form of dislocations, separated by an elastically strained material. Both types of strain can largely affect the phonon scattering. Dislocation scattering involves another atomic- and sub-nanometer scale scattering mechanism. A dislocation mediated by

the higher order terms in the potential energy of a real crystal is a crystallographic defect within a crystal structure, and includes edge-, screw- and often mixed character. Dislocations also form at phase boundaries or inside bulk single crystals. Though they have an atomic-scale origin, dislocation effects (in terms of lattice strain) often extend several nanometers in length away from its core. Thus, no matter the type of dislocation, phonons can scatter by dislocations via distinct mechanisms, as observed in Cl doped  $\text{AgPb}_{18}\text{SbSe}_{20}$  alloys.<sup>93</sup>

### 1.7.3.2.3 Meso-scale Scattering (long wavelength phonons)

Structures with interfaces that scatter the phonons more strongly than they scatter electrons are beneficial to thermoelectric materials because they can produce a net increase in  $zT$ . Interfaces, including grain- and phase-boundaries, represent discontinuities across two grains or phases in bulk materials. Boundaries, usually referring to grain boundaries, tend to decrease both the electrical and thermal conductivity. Grain boundaries can be considered as those defects which change the stiffness (or acoustic impedance) across them, thereby providing additional mechanism for phonon scattering. Considering the size effect of grain boundaries at the meso-scale, they mostly scatter the low frequency (long wavelength) phonons. Though the interfaces are effective in scattering long mean-free-path electrons and phonons, it is important to note that they have little effect when the mean-free-paths are smaller than the spacing between the interfaces. The varied contributions to phonon scattering by structures at all length-scales (*i.e.*, atomic-, nano- and meso-scale) to various mean free paths have been calculated and reported in the literature for PbTe based<sup>94</sup> and Si/Ge based systems.<sup>95,96</sup> For these specific systems, it indicates that around 25% of the  $\kappa_{\text{latt}}$  value of PbTe is contributed by phonon modes with mean free paths of less than 5 nm, which can be primarily attributed to scattering by a combination of atomic-scale solid-solution alloying and/or dislocations, and about 55% of  $\kappa_{\text{latt}}$  is governed by phonon modes with mean free paths between 5 and 100 nm, which can be scattered by nanoscale particles embedded in PbTe and associated interphase interfaces and spatially distributed strains,<sup>94</sup> as shown in Figure 1.15. The remaining 20%  $\kappa_{\text{latt}}$  in PbTe, however, is contributed by phonon modes with mean free paths of 0.1–1 mm. The mesoscale grain structures are comparable in size to those long mean free paths and thus can scatter a notable fraction of those additional (long wavelength) phonons.

One way to achieve such meso-scale scattering is to preferentially align the grains along favorable transport directions by controlling the crystallographic texture of such materials, either by mechanical alignment of the starting powders in sintered materials or to process colloidal

suspensions of materials under a high magnetic field to induce alignments due to anisotropy in the magnetic susceptibility.<sup>97</sup> Grain size reduction, has also been the most explored method of harnessing interfacial scattering processes to improve thermoelectric performance. Other approaches includes, improvement in grain boundary properties by forming thin layers of a second phase at the boundaries, nano inclusions within the grain interiors, producing lamellar nanostructures, etc.<sup>97</sup>

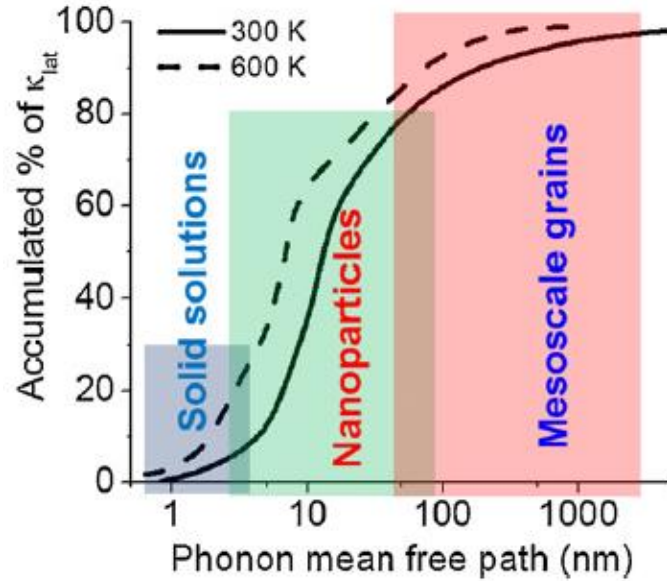


**Figure 1.15** Contributions of phonons with varied mean free paths to the accumulated  $\kappa_{latt}$  value for PbTe at different temperatures. Phonons with short, medium and long mean free paths can be effectively scattered by atomic-scale point defects, nanoscale precipitates and mesoscale grain boundaries, respectively. *Image courtesy:* © Materials Today, 2013.<sup>87</sup>

#### 1.7.3.2.4 Multiscale Hierarchical Architectures (all wavelength phonon scattering)

As explained in previous section, the acoustic phonons in a material carry most of the heat and they have a spectrum of wavelengths and mean free paths (MFP), each of which contributes to the total thermal conductivity. Solid solution alloying / point defects scatter short MFP phonons due to either mass contrast or local bond strain induced by the defects. The scattering of medium MFP phonons is best achieved through nanostructuring. The meso-scale grain boundaries mostly scatter the long MFP phonons. Therefore, to scatter all MFP ranges from nano- to micro-length scales, “all-scale / multi-scale hierarchical architectures” are needed. This means that all the features, *i.e.*, solid solution point defects, nanostructures and grain boundary interfaces must be integrated in a single sample, as shown in Figure 1.16 (a) and (b).

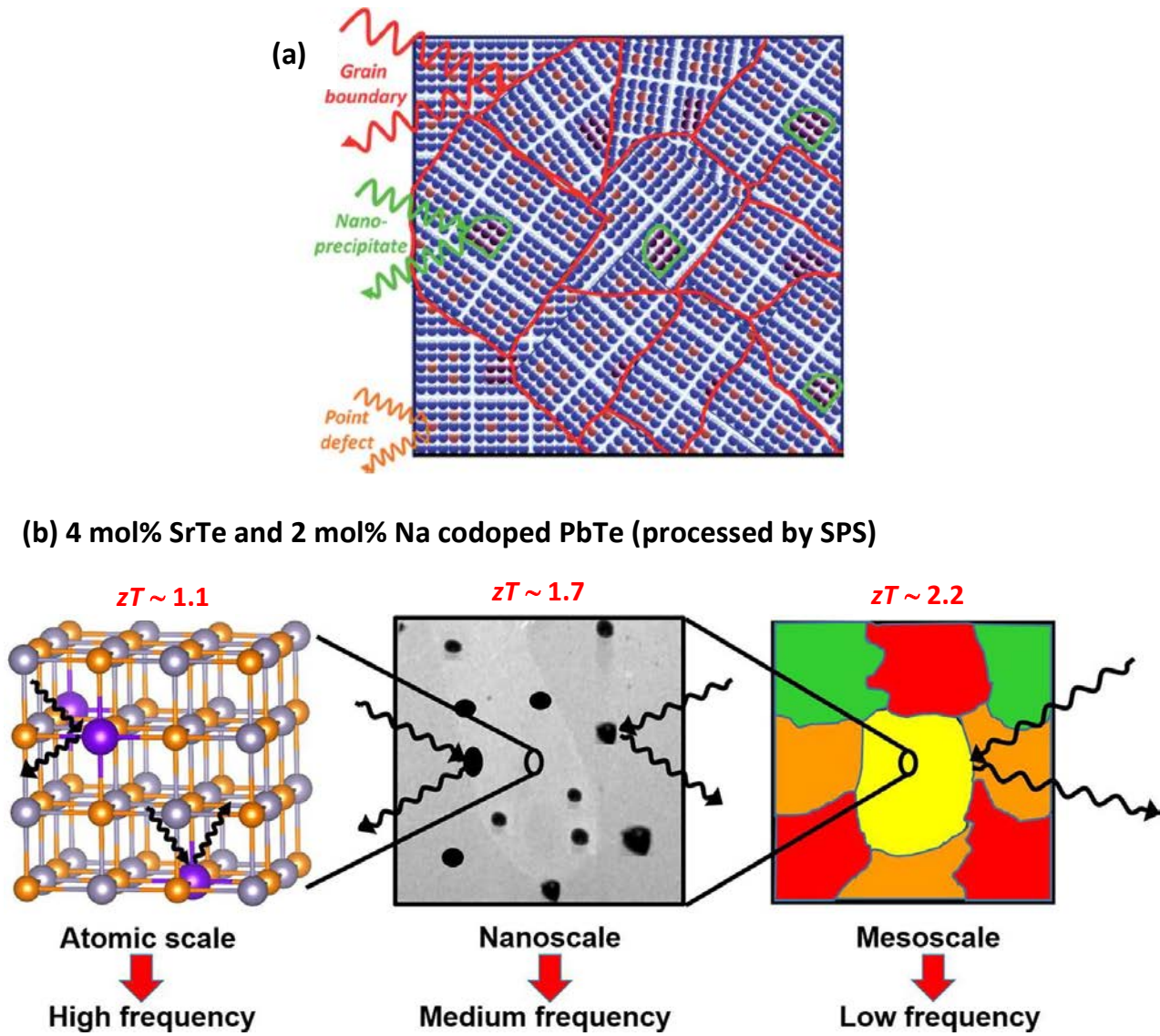


**Figure 1.16** Hierarchical architectures with all length-scale structures (solid-solution point defects, nano-scale precipitates and grain boundaries) to scatter short, medium and long wavelength phonons, respectively. *Image courtesy:* Figure (a) © Energy & Environ., 2014;<sup>98</sup> Figure (b) © Materials Today, 2018<sup>99</sup> (Adapted from © Nature, 2012).<sup>86</sup>

The multi-scale hierarchical architectures have the potential to significantly reduce the thermal conductivity down to the minimum theoretical limit,<sup>86</sup> which has been the main design principle for the thermoelectric materials in the past couple of years. The all-scale hierarchical architectures were successfully applied to Sr and Na codoped PbTe (processed by spark plasma sintering), as elucidated in Figure 1.16 (b),<sup>86</sup> and then later to several other PbTe based<sup>98</sup> and Bi<sub>2</sub>Te<sub>3</sub> based materials.<sup>100</sup>



1.8 Graphical Summary of the State-of-the-art TE Materials and Strategic Approaches

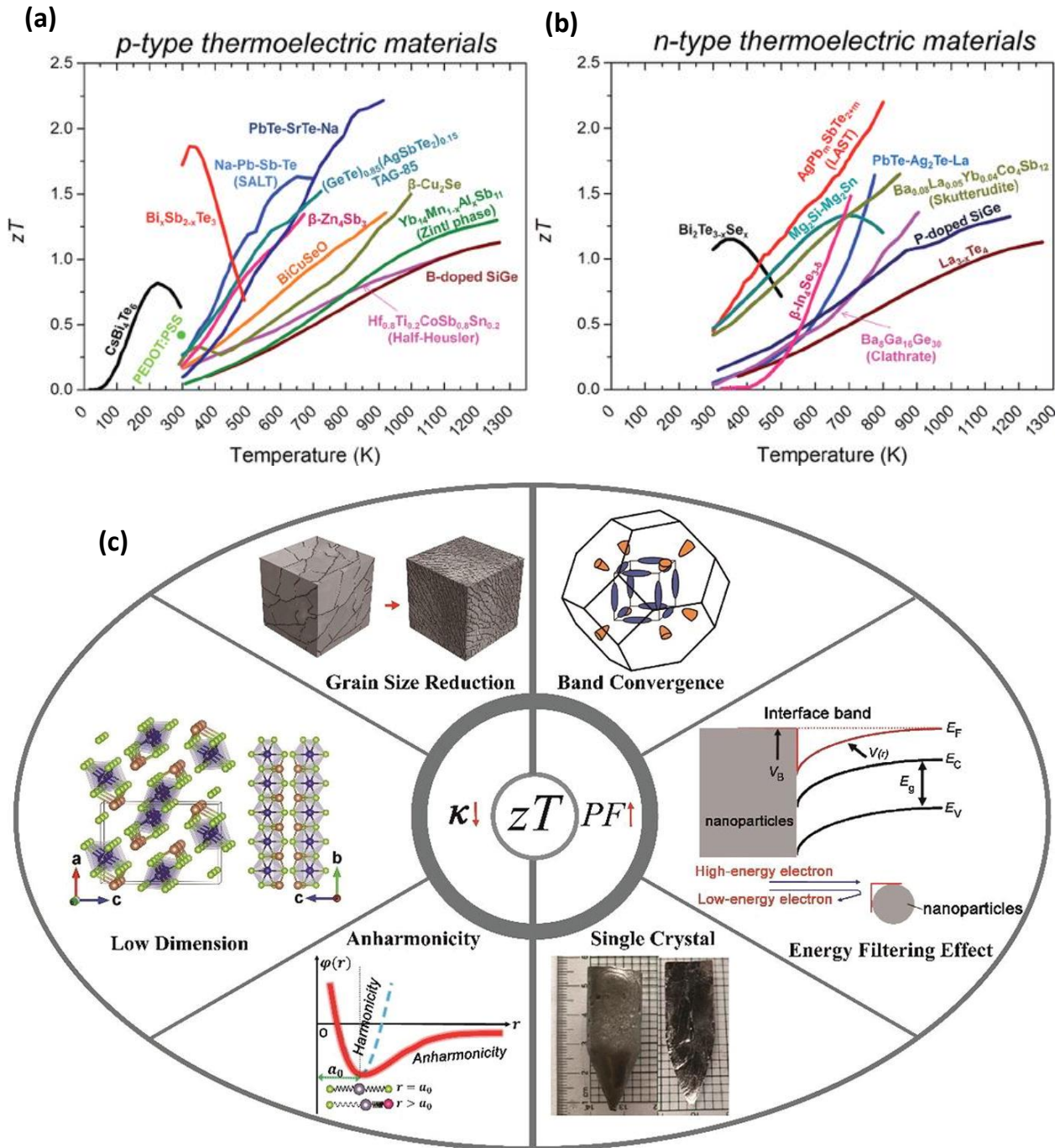


**Figure 1.17** State-of-the-art in thermoelectrics: some best known p-type (a) and n-type (b) TE materials, and (c) the different approaches adopted so far to suppress the thermal conductivity or to enhance the thermoelectric power factor (by decoupling  $\sigma$  and  $S$ ). *Image courtesy: Figures (a), (b) © RSC Advances, 2015;<sup>19</sup> Figure (c) © Materials Today, 2018.<sup>99</sup>*

## References

- (1) Jacobson, A. J. Materials for Solid Oxide Fuel Cells. *Chem. Mater.* **2010**, *22* (3), 660–674.
- (2) Grätzel, M. Recent Advances in Sensitized Mesoscopic Solar Cells. *Acc. Chem. Res.* **2009**, *42*, 1788–1798.
- (3) Liu, C.; Li, F.; Ma, L.-P.; Cheng, H.-M. Advanced Materials for Energy Storage. *Adv. Mater.* **2010**, *22* (8), E28–E62.
- (4) LaLonde, A. D.; Pei, Y.; Wang, H.; Jeffrey Snyder, G. Lead Telluride Alloy Thermoelectrics. *Mater. Today* **2011**, *14* (11), 526–532.
- (5) Li, J.-F.; Liu, W.-S.; Zhao, L.-D.; Zhou, M. High-Performance Nanostructured Thermoelectric Materials. *NPG Asia Mater.* **2010**, *2* (4), 152–158.
- (6) Ma, Y.; Hao, Q.; Poudel, B.; Lan, Y.; Yu, B.; Wang, D.; Chen, G.; Ren, Z. Enhanced Thermoelectric Figure-of-Merit in p-Type Nanostructured Bismuth Antimony Tellurium Alloys Made from Elemental Chunks. *Nano Lett.* **2008**, *8* (8), 2580–2584.
- (7) Snyder, G. J.; Toberer, E. S. Complex Thermoelectric Materials. *Nat. Mater.* **2008**, *7* (2), 105–114.
- (8) Snyder, G. J.; Ursell, T. S. Thermoelectric Efficiency and Compatibility. *Phys. Rev. Lett.* **2003**, *91* (14), 148301.
- (9) Li, J.; Zhang, X.; Chen, Z.; Lin, S.; Li, W.; Shen, J.; Witting, I. T.; Faghaninia, A.; Chen, Y.; Jain, A.; et al. Low-Symmetry Rhombohedral GeTe Thermoelectrics. *Joule* **2018**, *2* (5), 976–987.
- (10) Slack, G. A. CRC Handbook of Thermoelectrics (ed. Rowe, M.) 407–440 (CRC, Boca Raton, 1995).
- (11) Takabatake, T.; Suekuni, K.; Nakayama, T.; Kaneshita, E. Phonon-Glass Electron-Crystal Thermoelectric Clathrates: Experiments and Theory. *Rev. Mod. Phys.* **2014**, *86* (2), 669–716.
- (12) Brown, S. R.; Kauzlarich, S. M.; Gascoin, F.; Snyder, G. J. Yb<sub>14</sub>MnSb<sub>11</sub>: New High Efficiency Thermoelectric Material for Power Generation. *Chem. Mater.* **2006**, *18* (7), 1873–1877.
- (13) Kauzlarich, S. M.; Brown, S. R.; Snyder, G. J. Zintl Phases for Thermoelectric Devices. *Dalton Trans.* **2007**, No. 21, 2099–2107.
- (14) Toberer, E. S.; May, A. F.; Snyder, G. J. Zintl Chemistry for Designing High Efficiency Thermoelectric Materials. *Chem. Mater.* **2010**, *22* (3), 624–634.
- (15) Sales, B. C.; Mandrus, D.; Williams, R. K. Filled Skutterudite Antimonides: A New Class of Thermoelectric Materials. *Science* **1996**, *272* (5266), 1325–1328.

- (16) Nolas, G. S.; Morelli, D. T.; Tritt, T. M. Skutterudites: A Phonon-Glass-Electron Crystal Approach to Advanced Thermoelectric Energy Conversion Applications. *Annu. Rev. Mater. Sci.* **1999**, *29* (1), 89–116.
- (17) Sootsman, J. R.; Chung, D. Y.; Kanatzidis, M. G. New and Old Concepts in Thermoelectric Materials. *Angew. Chem. Int. Ed.* **2009**, *48* (46), 8616–8639.
- (18) Chen, Z.-G.; Han, G.; Yang, L.; Cheng, L.; Zou, J. Nanostructured Thermoelectric Materials: Current Research and Future Challenge. *Prog. Nat. Sci. Mater. Int.* **2012**, *22* (6), 535–549.
- (19) Rull-Bravo, M.; Moure, A.; Fernández, J. F.; Martín-González, M. Skutterudites as Thermoelectric Materials: Revisited. *RSC Adv.* **2015**, *5* (52), 41653–41667.
- (20) Zhao, W.; Wei, P.; Zhang, Q.; Dong, C.; Liu, L.; Tang, X. Enhanced Thermoelectric Performance in Barium and Indium Double-Filled Skutterudite Bulk Materials via Orbital Hybridization Induced by Indium Filler. *J. Am. Chem. Soc.* **2009**, *131* (10), 3713–3720.
- (21) Patschke, R.; Zhang, X.; Singh, D.; Schindler, J.; Kannewurf, C. R.; Lowhorn, N.; Tritt, T.; Nolas, G. S.; Kanatzidis, M. G. Thermoelectric Properties and Electronic Structure of the Cage Compounds  $A_2BaCu_8Te_{10}$  ( $A = K, Rb, Cs$ ): Systems with Low Thermal Conductivity. *Chem. Mater.* **2001**, *13* (2), 613–621.
- (22) Nolas, G. S.; Beekman, M.; Gryko, J.; Lambertson, G. A.; Tritt, T. M.; McMillan, P. F. Thermal Conductivity of Elemental Crystalline Silicon Clathrate  $Si_{136}$ . *Appl. Phys. Lett.* **2003**, *82* (6), 910–912.
- (23) Bhardwaj, A.; Misra, D. K. Enhancing Thermoelectric Properties of a p-Type  $Mg_3Sb_2$ -Based Zintl Phase Compound by Pb Substitution in the Anionic Framework. *RSC Adv.* **2014**, *4* (65), 34552–34560.
- (24) Toberer, E. S.; Zevalkink, A.; Crisosto, N.; Snyder, G. J. The Zintl Compound  $Ca_5Al_2Sb_6$  for Low-Cost Thermoelectric Power Generation. *Adv. Funct. Mater.* **2010**, *20* (24), 4375–4380.
- (25) Wang, H. F.; Cai, K. F.; Chen, S. Preparation and Thermoelectric Properties of  $BaMn_{2-x}Zn_xSb_2$  Zintl Compounds. *J. Mater. Sci. Mater. Electron.* **2012**, *23* (12), 2289–2292.
- (26) Zhu, T.; Fu, C.; Xie, H.; Liu, Y.; Zhao, X. High Efficiency Half-Heusler Thermoelectric Materials for Energy Harvesting. *Adv. Energy Mater.* **2015**, *5* (19), 1500588.
- (27) Fu, C.; Bai, S.; Liu, Y.; Tang, Y.; Chen, L.; Zhao, X.; Zhu, T. Realizing High Figure of Merit in Heavy-Band p-Type Half-Heusler Thermoelectric Materials. *Nat. Commun.* **2015**, *6*, 8144.
- (28) Kirievsky, K.; Shlimovich, M.; Fuks, D.; Gelbstein, Y. An Ab Initio Study of the Thermoelectric Enhancement Potential in Nano-Grained  $TiNiSn$ . *Phys. Chem. Chem. Phys.* **2014**, *16* (37), 20023–20029.

- (29) Lucas, P.; Conseil, C.; Yang, Z.; Hao, Q.; Cui, S.; Boussard-Pledel, C.; Bureau, B.; Gascoin, F.; Caillaud, C.; Gulbiten, O.; et al. Thermoelectric Bulk Glasses Based on the Cu–As–Te–Se System. *J. Mater. Chem. A* **2013**, *1* (31), 8917–8925.
- (30) Cui, S.; Boussard-plédel, C.; Calvez, L.; Rojas, F.; Chen, K.; Ning, H.; Reece, M. J.; Guizouarn, T.; Bureau, B. Comprehensive Study of Tellurium Based Glass Ceramics for Thermoelectric Application. *Adv. Appl. Ceram.* **2015**, *114*, S42–S47.
- (31) Vaney, J. B.; Delaizir, G.; Alleno, E.; Rouleau, O.; Piarristeguy, A.; Monnier, J.; Godart, C.; Ribes, M.; Escalier, R.; Pradel, A.; et al. A Comprehensive Study of the Crystallization of Cu–As–Te Glasses: Microstructure and Thermoelectric Properties. *J. Mater. Chem. A* **2013**, *1* (28), 8190–8200.
- (32) Vaney, J. B.; Piarristeguy, A.; Pradel, A.; Alleno, E.; Lenoir, B.; Candolfi, C.; Dauscher, A.; Gonçalves, A. P.; Lopes, E. B.; Delaizir, G.; et al. Thermal Stability and Thermoelectric Properties of  $\text{Cu}_x\text{As}_{40-x}\text{Te}_{60-y}\text{Se}_y$  Semiconducting Glasses. *J. Solid State Chem.* **2013**, *203*, 212–217.
- (33) Gonçalves, A. P.; Lopes, E. B.; Rouleau, O.; Godart, C. Conducting Glasses as New Potential Thermoelectric Materials: The Cu–Ge–Te Case. *J. Mater. Chem.* **2010**, *20* (8), 1516–1521.
- (34) Gonçalves, A. P.; Delaizir, G.; Lopes, E. B.; Ferreira, L. M.; Rouleau, O.; Godart, C. Chalcogenide Glasses as Prospective Thermoelectric Materials. *J. Electron. Mater.* **2011**, *40* (5), 1015–1017.
- (35) Gonçalves, A. P.; Lopes, E. B.; Delaizir, G.; Vaney, J. B.; Lenoir, B.; Piarristeguy, A.; Pradel, A.; Monnier, J.; Ochin, P.; Godart, C. Semiconducting Glasses: A New Class of Thermoelectric Materials? *J. Solid State Chem.* **2012**, *193*, 26–30.
- (36) Banik, A.; Shenoy, U. S.; Anand, S.; Waghmare, U. V.; Biswas, K. Mg Alloying in SnTe Facilitates Valence Band Convergence and Optimizes Thermoelectric Properties. *Chem. Mater.* **2015**, *27* (2), 581–587.
- (37) Pei, Y.; Shi, X.; LaLonde, A.; Wang, H.; Chen, L.; Snyder, G. J. Convergence of Electronic Bands for High Performance Bulk Thermoelectrics. *Nature* **2011**, *473* (7345), 66–69.
- (38) Hicks, L. D.; Dresselhaus, M. S. Effect of Quantum-Well Structures on the Thermoelectric Figure of Merit. *Phys. Rev. B* **1993**, *47* (19), 12727–12731.
- (39) Zide, J. M. O.; Vashaee, D.; Bian, Z. X.; Zeng, G.; Bowers, J. E.; Shakouri, A.; Gossard, A. C. Demonstration of Electron Filtering to Increase the Seebeck Coefficient in InGaAs/InGaAlAs Superlattices. *Phys. Rev. B* **2006**, *74* (20), 205335.

- (40) Zhang, Q.; Liao, B.; Lan, Y.; Lukas, K.; Liu, W.; Esfarjani, K.; Opeil, C.; Broido, D.; Chen, G.; Ren, Z. High Thermoelectric Performance by Resonant Dopant Indium in Nanostructured SnTe. *Proc. Natl. Acad. Sci.* **2013**, *110* (33), 13261–13266.
- (41) Lin, S.; Li, W.; Chen, Z.; Shen, J.; Ge, B.; Pei, Y. Tellurium as a High-Performance Elemental Thermoelectric. *Nat. Commun.* **2016**, *7*, 10287.
- (42) Dresselhaus, M. S.; Chen, G.; Tang, M. Y.; Yang, R. G.; Lee, H.; Wang, D. Z.; Ren, Z. F.; Fleurial, J.-P.; Gogna, P. New Directions for Low-Dimensional Thermoelectric Materials. *Adv. Mater.* **2007**, *19* (8), 1043–1053.
- (43) Wang, H.; Pei, Y.; LaLonde, A. D.; Snyder, G. J. Weak Electron–Phonon Coupling Contributing to High Thermoelectric Performance in n-Type PbSe. *Proc. Natl. Acad. Sci.* **2012**, *109* (25), 9705–9709.
- (44) Pei, Y.; LaLonde, A. D.; Wang, H.; Snyder, G. J. Low Effective Mass Leading to High Thermoelectric Performance. *Energy Environ. Sci.* **2012**, *5* (7), 7963–7969.
- (45) Pei, Y.; Wang, H.; Snyder, G. J. Band Engineering of Thermoelectric Materials. *Adv. Mater.* **2012**, *24* (46), 6125–6135.
- (46) Shi, X.; Chen, L.; Uher, C. Recent Advances in High-Performance Bulk Thermoelectric Materials. *Int. Mater. Rev.* **2016**, *61* (6), 379–415.
- (47) Zhao, L. D.; Wu, H. J.; Hao, S. Q.; Wu, C. I.; Zhou, X. Y.; Biswas, K.; He, J. Q.; Hogan, T. P.; Uher, C.; Wolverton, C.; et al. All-Scale Hierarchical Thermoelectrics: MgTe in PbTe Facilitates Valence Band Convergence and Suppresses Bipolar Thermal Transport for High Performance. *Energy Environ. Sci.* **2013**, *6* (11), 3346–3355.
- (48) Zhang, Q.; Cao, F.; Liu, W.; Lukas, K.; Yu, B.; Chen, S.; Opeil, C.; Broido, D.; Chen, G.; Ren, Z. Heavy Doping and Band Engineering by Potassium to Improve the Thermoelectric Figure of Merit in p-Type PbTe, PbSe, and PbTe<sub>1-y</sub>Se<sub>y</sub>. *J. Am. Chem. Soc.* **2012**, *134* (24), 10031–10038.
- (49) Androulakis, J.; Todorov, I.; Chung, D.-Y.; Ballikaya, S.; Wang, G.; Uher, C.; Kanatzidis, M. Thermoelectric Enhancement in PbTe with K or Na Codoping from Tuning the Interaction of the Light- and Heavy-Hole Valence Bands. *Phys. Rev. B* **2010**, *82* (11), 115209.
- (50) Roychowdhury, S.; Shenoy, U. S.; Waghmare, U. V.; Biswas, K. Tailoring of Electronic Structure and Thermoelectric Properties of a Topological Crystalline Insulator by Chemical Doping. *Angew. Chem. Int. Ed.* **2015**, *54* (50), 15241–15245.
- (51) Tan, G.; Zhao, L.-D.; Shi, F.; Doak, J. W.; Lo, S.-H.; Sun, H.; Wolverton, C.; Dravid, V. P.; Uher, C.; Kanatzidis, M. G. High Thermoelectric Performance of P-Type SnTe via a Synergistic Band Engineering and Nanostructuring Approach. *J. Am. Chem. Soc.* **2014**, *136* (19), 7006–7017.

- (52) Al Rahal Al Orabi, R.; Mecholsky, N. A.; Hwang, J.; Kim, W.; Rhyee, J.-S.; Wee, D.; Fornari, M. Band Degeneracy, Low Thermal Conductivity, and High Thermoelectric Figure of Merit in SnTe–CaTe Alloys. *Chem. Mater.* **2016**, *28* (1), 376–384.
- (53) Tan, G.; Shi, F.; Doak, J. W.; Sun, H.; Zhao, L.-D.; Wang, P.; Uher, C.; Wolverton, C.; Dravid, V. P.; Kanatzidis, M. G. Extraordinary Role of Hg in Enhancing the Thermoelectric Performance of p-Type SnTe. *Energy Environ. Sci.* **2014**, *8* (1), 267–277.
- (54) Zhang, X.; Wang, D.; Wu, H.; Yin, M.; Pei, Y.; Gong, S.; Huang, L.; Pennycook, S. J.; He, J.; Zhao, L.-D. Simultaneously Enhancing the Power Factor and Reducing the Thermal Conductivity of SnTe via Introducing Its Analogues. *Energy Environ. Sci.* **2017**, *10* (11), 2420–2431.
- (55) Zheng, Z.; Su, X.; Deng, R.; Stoumpos, C.; Xie, H.; Liu, W.; Yan, Y.; Hao, S.; Uher, C.; Wolverton, C.; et al. Rhombohedral to Cubic Conversion of GeTe via MnTe Alloying Leads to Ultralow Thermal Conductivity, Electronic Band Convergence, and High Thermoelectric Performance. *J. Am. Chem. Soc.* **2018**, *140* (7), 2673–2686.
- (56) Wu, D.; Zhao, L.-D.; Hao, S.; Jiang, Q.; Zheng, F.; Doak, J. W.; Wu, H.; Chi, H.; Gelbstein, Y.; Uher, C.; et al. Origin of the High Performance in GeTe-Based Thermoelectric Materials upon Bi<sub>2</sub>Te<sub>3</sub> Doping. *J. Am. Chem. Soc.* **2014**, *136* (32), 11412–11419.
- (57) Perumal, S.; Roychowdhury, S.; Negi, D. S.; Datta, R.; Biswas, K. High Thermoelectric Performance and Enhanced Mechanical Stability of p-Type Ge<sub>1-x</sub>Sb<sub>x</sub>Te. *Chem. Mater.* **2015**, *27* (20), 7171–7178.
- (58) Perumal, S.; Bellare, P.; Shenoy, U. S.; Waghmare, U. V.; Biswas, K. Low Thermal Conductivity and High Thermoelectric Performance in Sb and Bi Codoped GeTe: Complementary Effect of Band Convergence and Nanostructuring. *Chem. Mater.* **2017**, *29* (24), 10426–10435.
- (59) Liu, X.; Zhu, T.; Wang, H.; Hu, L.; Xie, H.; Jiang, G.; Snyder, G. J.; Zhao, X. Low Electron Scattering Potentials in High Performance Mg<sub>2</sub>Si<sub>0.45</sub>Sn<sub>0.55</sub> Based Thermoelectric Solid Solutions with Band Convergence. *Adv. Energy Mater.* **2013**, *3* (9), 1238–1244.
- (60) Liu, W.; Tan, X.; Yin, K.; Liu, H.; Tang, X.; Shi, J.; Zhang, Q.; Uher, C. Convergence of Conduction Bands as a Means of Enhancing Thermoelectric Performance of Mg<sub>2</sub>Si<sub>1-x</sub>Sn<sub>x</sub> Solid Solutions. *Phys. Rev. Lett.* **2012**, *108* (16), 166601.
- (61) Wu, L.; Li, X.; Wang, S.; Zhang, T.; Yang, J.; Zhang, W.; Chen, L.; Yang, J. Resonant Level-Induced High Thermoelectric Response in Indium-Doped GeTe. *NPG Asia Mater.* **2017**, *9* (1), e343.
- (62) Hoang, K.; Mahanti, S. D. Electronic Structure of Ga-, In-, and Tl-Doped PbTe: A Supercell Study of the Impurity Bands. *Phys. Rev. B* **2008**, *78* (8), 085111.

- (63) Heremans, J. P.; Jovovic, V.; Toberer, E. S.; Saramat, A.; Kurosaki, K.; Charoenphakdee, A.; Yamanaka, S.; Snyder, G. J. Enhancement of Thermoelectric Efficiency in PbTe by Distortion of the Electronic Density of States. *Science* **2008**, *321* (5888), 554–557.
- (64) Yu, B.; Zhang, Q.; Wang, H.; Wang, X.; Wang, H.; Wang, D.; Wang, H.; Snyder, G. J.; Chen, G.; Ren, Z. F. Thermoelectric Property Studies on Thallium-Doped Lead Telluride Prepared by Ball Milling and Hot Pressing. *J. Appl. Phys.* **2010**, *108* (1), 016104.
- (65) Zhang, Q.; Wang, H.; Zhang, Q.; Liu, W.; Yu, B.; Wang, H.; Wang, D.; Ni, G.; Chen, G.; Ren, Z. Effect of Silicon and Sodium on Thermoelectric Properties of Thallium-Doped Lead Telluride-Based Materials. *Nano Lett.* **2012**, *12* (5), 2324–2330.
- (66) Zhang, Q.; Yang, S.; Zhang, Q.; Chen, S.; Liu, W.; Wang, H.; Tian, Z.; Broido, D.; Gang Chen; Ren, Z. Effect of Aluminum on the Thermoelectric Properties of Nanostructured PbTe. *Nanotechnology* **2013**, *24* (34), 345705.
- (67) Zhang, Q.; Wang, H.; Liu, W.; Wang, H.; Yu, B.; Zhang, Q.; Tian, Z.; Ni, G.; Lee, S.; Esfarjani, K.; et al. Enhancement of Thermoelectric Figure-of-Merit by Resonant States of Aluminium Doping in Lead Selenide. *Energy Environ. Sci.* **2012**, *5* (1), 5246–5251.
- (68) Zhang, Q.; Cao, F.; Lukas, K.; Liu, W.; Esfarjani, K.; Opeil, C.; Broido, D.; Parker, D.; Singh, D. J.; Chen, G.; et al. Study of the Thermoelectric Properties of Lead Selenide Doped with Boron, Gallium, Indium, or Thallium. *J. Am. Chem. Soc.* **2012**, *134* (42), 17731–17738.
- (69) Bali, A.; Wang, H.; Snyder, G. J.; Mallik, R. C. Thermoelectric Properties of Indium Doped PbTe<sub>1-y</sub>Se<sub>y</sub> Alloys. *J. Appl. Phys.* **2014**, *116* (3), 033707.
- (70) Bali, A.; Chetty, R.; Sharma, A.; Rogl, G.; Heinrich, P.; Suwas, S.; Misra, D. K.; Rogl, P.; Bauer, E.; Mallik, R. C. Thermoelectric Properties of In and I Doped PbTe. *J. Appl. Phys.* **2016**, *120* (17), 175101.
- (71) Zhang, Q.; Chere, E. K.; Wang, Y.; Kim, H. S.; He, R.; Cao, F.; Dahal, K.; Broido, D.; Chen, G.; Ren, Z. High Thermoelectric Performance of n-Type PbTe<sub>1-y</sub>S<sub>y</sub> Due to Deep Lying States Induced by Indium Doping and Spinodal Decomposition. *Nano Energy* **2016**, *22*, 572–582.
- (72) Banik, A.; Shenoy, U. S.; Saha, S.; Waghmare, U. V.; Biswas, K. High Power Factor and Enhanced Thermoelectric Performance of SnTe-AgInTe<sub>2</sub>: Synergistic Effect of Resonance Level and Valence Band Convergence. *J. Am. Chem. Soc.* **2016**, *138* (39), 13068–13075.
- (73) Roychowdhury, S.; Shenoy, U. S.; Waghmare, U. V.; Biswas, K. An Enhanced Seebeck Coefficient and High Thermoelectric Performance in p-Type In and Mg Co-Doped Sn<sub>1-x</sub>Pb<sub>x</sub>Te via the Co-Adjuvant Effect of the Resonance Level and Heavy Hole Valence Band. *J. Mater. Chem. C* **2017**, *5* (23), 5737–5748.

- (74) Tan, G.; Shi, F.; Hao, S.; Chi, H.; Zhao, L.-D.; Uher, C.; Wolverton, C.; Dravid, V. P.; Kanatzidis, M. G. Codoping in SnTe: Enhancement of Thermoelectric Performance through Synergy of Resonance Levels and Band Convergence. *J. Am. Chem. Soc.* **2015**, *137* (15), 5100–5112.
- (75) Wang, L.; Tan, X.; Liu, G.; Xu, J.; Shao, H.; Yu, B.; Jiang, H.; Yue, S.; Jiang, J. Manipulating Band Convergence and Resonant State in Thermoelectric Material SnTe by Mn–In Codoping. *ACS Energy Lett.* **2017**, *2* (5), 1203–1207.
- (76) Tan, X. J.; Liu, G. Q.; Xu, J. T.; Shao, H. Z.; Jiang, J.; Jiang, H. C. Element-Selective Resonant State in M-Doped SnTe (M = Ga, In, and Tl). *Phys. Chem. Chem. Phys.* **2016**, *18* (30), 20635–20639.
- (77) Harman, T. C.; Taylor, P. J.; Spears, D. L.; Walsh, M. P. Thermoelectric Quantum-Dot Superlattices with High ZT. *J. Electron. Mater.* **2000**, *29* (1), L1–L2.
- (78) Hochbaum, A. I.; Chen, R.; Delgado, R. D.; Liang, W.; Garnett, E. C.; Najarian, M.; Majumdar, A.; Yang, P. Enhanced Thermoelectric Performance of Rough Silicon Nanowires. *Nature* **2008**, *451* (7175), 163–167.
- (79) Samal, A. K.; Pradeep, T. Room-Temperature Chemical Synthesis of Silver Telluride Nanowires. *J. Phys. Chem. C* **2009**, *113* (31), 13539–13544.
- (80) Venkatasubramanian, R.; Siivola, E.; Colpitts, T.; O’Quinn, B. Thin-Film Thermoelectric Devices with High Room-Temperature Figures of Merit. *Nature* **2001**, *413* (6856), 597–602.
- (81) Hicks, L. D.; Dresselhaus, M. S. Thermoelectric Figure of Merit of a One-Dimensional Conductor. *Phys. Rev. B* **1993**, *47* (24), 16631–16634.
- (82) Koga, T.; Cronin, S. B.; Dresselhaus, M. S.; Liu, J. L.; Wang, K. L. Experimental Proof-of-Principle Investigation of Enhanced Z3DT in (001) Oriented Si/Ge Superlattices. *Appl. Phys. Lett.* **2000**, *77* (10), 1490–1492.
- (83) Ravich, Y. I.; Efimova, B. A.; Tamarchenko, V. I. Scattering of Current Carriers and Transport Phenomena in Lead Chalcogenides. *Phys. Status Solidi B* **1971**, *43* (1), 11–33.
- (84) Hicks, L. D.; Harman, T. C.; Dresselhaus, M. S. Use of Quantum-well Superlattices to Obtain a High Figure of Merit from Nonconventional Thermoelectric Materials. *Appl. Phys. Lett.* **1993**, *63* (23), 3230–3232.
- (85) Cook, B. A.; Kramer, M. J.; Haringa, J. L.; Han, M.-K.; Chung, D.-Y.; Kanatzidis, M. G. Analysis of Nanostructuring in High Figure-of-Merit  $\text{Ag}_{1-x}\text{Pb}_m\text{SbTe}_{2+m}$  Thermoelectric Materials. *Adv. Funct. Mater.* **2009**, *19* (8), 1254–1259.
- (86) Biswas, K.; He, J.; Blum, I. D.; Wu, C.-I.; Hogan, T. P.; Seidman, D. N.; Dravid, V. P.; Kanatzidis, M. G. High-Performance Bulk Thermoelectrics with All-Scale Hierarchical Architectures. *Nature* **2012**, *489* (7416), 414–418.



- (87) He, J.; Kanatzidis, M. G.; Dravid, V. P. High Performance Bulk Thermoelectrics via a Panoscopic Approach. *Mater. Today* **2013**, *16* (5), 166–176.
- (88) Hsu, K. F.; Loo, S.; Guo, F.; Chen, W.; Dyck, J. S.; Uher, C.; Hogan, T.; Polychroniadis, E. K.; Kanatzidis, M. G. Cubic  $\text{AgPb}_m\text{SbTe}_{2+m}$ : Bulk Thermoelectric Materials with High Figure of Merit. *Science* **2004**, *303* (5659), 818–821.
- (89) Girard, S. N.; He, J.; Li, C.; Moses, S.; Wang, G.; Uher, C.; Dravid, V. P.; Kanatzidis, M. G. In Situ Nanostructure Generation and Evolution within a Bulk Thermoelectric Material to Reduce Lattice Thermal Conductivity. *Nano Lett.* **2010**, *10* (8), 2825–2831.
- (90) Androulakis, J.; Lin, C.-H.; Kong, H.-J.; Uher, C.; Wu, C.-I.; Hogan, T.; Cook, B. A.; Caillat, T.; Paraskevopoulos, K. M.; Kanatzidis, M. G. Spinodal Decomposition and Nucleation and Growth as a Means to Bulk Nanostructured Thermoelectrics: Enhanced Performance in  $\text{Pb}_{1-x}\text{Sn}_x\text{Te}$ – $\text{PbS}$ . *J. Am. Chem. Soc.* **2007**, *129* (31), 9780–9788.
- (91) Sootsman, J. R.; He, J.; Dravid, V. P.; Ballikaya, S.; Vermeulen, D.; Uher, C.; Kanatzidis, M. G. Microstructure and Thermoelectric Properties of Mechanically Robust  $\text{PbTe}$ – $\text{Si}$  Eutectic Composites. *Chem. Mater.* **2010**, *22* (3), 869–875.
- (92) Sootsman, J. R.; Pcionek, R. J.; Kong, H.; Uher, C.; Kanatzidis, M. G. Strong Reduction of Thermal Conductivity in Nanostructured  $\text{PbTe}$  Prepared by Matrix Encapsulation. *Chem. Mater.* **2006**, *18* (21), 4993–4995.
- (93) Qian Zhang, Y. L. Increased Thermoelectric Performance by Cl Doping in Nanostructured  $\text{AgPb}_{18}\text{SbSe}_{20-x}\text{Cl}_x$ . *Nano Energy* **2013**, *2* (6), 1121–1127.
- (94) Qiu, B.; Bao, H.; Zhang, G.; Wu, Y.; Ruan, X. Molecular Dynamics Simulations of Lattice Thermal Conductivity and Spectral Phonon Mean Free Path of  $\text{PbTe}$ : Bulk and Nanostructures. *Comput. Mater. Sci.* **2012**, *53* (1), 278–285.
- (95) Tian, Z.; Esfarjani, K.; Chen, G. Enhancing Phonon Transmission across a  $\text{Si}/\text{Ge}$  Interface by Atomic Roughness: First-Principles Study with the Green’s Function Method. *Phys. Rev. B* **2012**, *86* (23), 235304.
- (96) Esfarjani, K.; Chen, G.; Stokes, H. T. Heat Transport in Silicon from First-Principles Calculations. *Phys. Rev. B* **2011**, *84* (8), 085204.
- (97) Medlin, D. L.; Snyder, G. J. Interfaces in Bulk Thermoelectric Materials: A Review for Current Opinion in Colloid and Interface Science. *Curr. Opin. Colloid Interface Sci.* **2009**, *14* (4), 226–235.
- (98) Zhao, L.-D.; Dravid, V. P.; Kanatzidis, M. G. The Panoscopic Approach to High Performance Thermoelectrics. *Energy Environ. Sci.* **2013**, *7* (1), 251–268.

- (99) Zhou, X.; Yan, Y.; Lu, X.; Zhu, H.; Han, X.; Chen, G.; Ren, Z. Routes for High-Performance Thermoelectric Materials. *Mater. Today* **2018**.
- (100) Li, S.; Xin, C.; Liu, X.; Feng, Y.; Liu, Y.; Zheng, J.; Liu, F.; Huang, Q.; Qiu, Y.; He, J.; et al. 2D Hetero-Nanosheets to Enable Ultralow Thermal Conductivity by All Scale Phonon Scattering for Highly Thermoelectric Performance. *Nano Energy* **2016**, *30*, 780–789.



# **Chapter 2**

**Possible Mechanism for Hole Conductivity in Cu-As-Te**

**Thermoelectric Glasses**



## 2.1 Introduction

As elaborated in Chapter 1, the main paradigm in the present researches on thermoelectric materials is strongly focused on the “phonon glass electron crystal” (PGEC) model,<sup>1-3</sup> which proposes an offbeat combination of glass-like low-thermal conductivity and crystal-like high-electrical conductivity. To remind, the final goal for the optimization of a thermoelectric device is to maximize the figure of merit,  $zT = S^2\sigma T/\kappa$ , where  $S$  is the Seebeck coefficient,  $\sigma$  the electrical conductivity,  $T$  the absolute temperature and  $\kappa$  is the total thermal conductivity. In short, the search is for low  $\kappa$  and high  $\sigma$  and  $S$  materials.

In the pursuit of the PGEC model, several frameworks have been analyzed, mostly based on engineering complex crystal structures such as skutterudites or Zintl compounds, as discussed in Chapter 1. In the former case, thermal conductivity is reduced by rattling dopant atoms in cage structure,<sup>4,5</sup> whereas in the latter a high degree of valence imbalance and disorder is the key to increase the  $zT$  value.<sup>6,7</sup> So far the thermoelectric potential was established in several material classes, including tellurides,<sup>8-12</sup> selenides,<sup>13,14</sup> half-heuslers<sup>15,16</sup> and silicides.<sup>17,18</sup>

More recently, a revival in a different approach to the PGEC principle appeared.<sup>19-21</sup> It deals with the possibility of designing electrically conductive glassy phases, based on chalcogenide-telluride glasses, which are known to inherently possess high Seebeck coefficient and low thermal conductivity. The main limiting factor in these chalcogenide glasses is their mediocre electrical conductivity. Yet, during our earlier European ITN project (GlaCERCo), the researchers from our laboratory in Rennes jointly with the team from Prof. Pierre Lucas’ group (from University of Arizona, U.S) found that doping glasses with Cu could lead to a huge enhancement in the electrical conductivity, consistent with the parallel work from a laboratory in Nancy (Institut Jean Lamour - Université de Lorraine), France.<sup>22-25</sup> For example, the 20% Cu-doping in arsenic telluride showed an increase in  $\sigma$  by almost 5 orders of magnitude ( $\sim 6$  S/m)<sup>22</sup> compared to the pristine arsenic telluride glass ( $\sim 10^{-4}$  S/m), without dismantling the amorphous structure of the glass (*i.e.*, without introducing crystallization) and simultaneously retaining its characteristic high Seebeck coefficient and low thermal conductivity. In spite of the deep experimental investigation by Lucas *et al.*,<sup>22</sup> no explanation about the physical mechanism leading to this huge increase in electric conductivity was found.

In order to shed light on the mechanism for the huge increase of conductivity that was found with Cu doping, these Cu-As-Te glasses have been analyzed by X-ray Absorption Spectroscopy, both in near-edge (XANES) and in the extended region (EXAFS) at the European Synchrotron Radiation Facility (ESRF) in Grenoble. Experimental data have been modeled by means of a multiple-scattering

based theoretical technique (FDMNES). This Chapter presents our experimental and theoretical results, as well as the proposed mechanism for the increase of the conductivity in the Cu-As-Te glasses with Cu doping.

This Chapter, which involves an extensive contribution from collaborators, is a continuity of the work that was initiated during the tenure of previous PhD student (Shuo Cui), who defended her thesis in Rennes on 10<sup>th</sup> December, 2014 (within the framework of GlaCERCo-ITN project).

## 2.2 Materials and Methods

### 2.2.1 Glass Synthesis

The Cu-As-Te glass samples were synthesized using the conventional vacuum sealed-tube melt quenching technique. Appropriate stoichiometric amounts of high purity (5N) starting elements were introduced in a silica tube that had previously been etched with hydrofluoric (HF) acid, rinsed with distilled water and dried under vacuum. The ampules were sealed under a vacuum of  $10^{-6}$  Torr, then placed in a rocking furnace and slowly heated up to 850 °C over a period of 8 hours, then held at that temperature for 10 hours. The furnace temperature was then ramped down to 600 °C and held for 45 min before quenching the ampules in water. The tubes were then annealed for 3 hours at several degrees ( $\sim 5$  °C) lower than their glass transition temperature ( $T_g$ ) to relieve internal stresses. Schematics of glass synthesis is shown in Annexure 2 (Figure A2.1). For information, these glasses were thermally quite stable with  $T_g$  around 170 °C and  $T_c$  (crystallization temperature) around 270 °C (more details in Annexure 2, Figure A2.2).

### 2.2.2 Synchrotron Measurements

X-ray Absorption Spectroscopic measurements, both XANES (X-ray Absorption Near Edge Structure) and EXAFS (Extended X-ray Absorption Fine Structure), were performed at ESRF's BM23 beamline,<sup>26</sup> at the K-edges of As, Te and Cu. XANES spectra was collected at Cu K-edge (8979 eV) in fluorescence detection due to the relatively small amount of copper in the samples. Te K-edge was instead studied in transmission, due to the large Te concentrations. We remark that the beamline BM23, equipped with a 311 crystal monochromator, is suited for high-energy measurements (Te K-edge is at 31814 eV). Its high photon flux characterized by a remarkable stability leads to a high signal-to-noise ratio even in fluorescence.

### 2.2.3 FDMNES (Multiple Scattering Quantum Calculations)

The results of XANES measurements were theoretically interpreted using the *ab-initio* FDMNES (Finite Difference Method Near Edge Spectroscopy) simulations package,<sup>27</sup> based on a multiple scattering approach that makes it akin to local density approximation in usual DFT (Density Functional Theory) calculations. The advantage of the multiple-scattering approach compared to the usually-implemented DFT schemes is that it is much faster at the relatively high energies reached by XANES experiments (up to 40 eV above the Fermi level). The input data are the electronic charge distributions of the ions in the cluster. Solving Poisson's equation, the Coulomb potential is obtained, and the exchange-correlation term is calculated in the Hedin-Lundqvist approximation.<sup>28</sup> For all our calculations, we have checked for the convergence with the radius size (usually a radius of  $\sim 7 \text{ \AA}$ ).

## 2.3 Results and Discussion

### 2.3.1 As K-edge (XANES and EXAFS) and Te K-edge (XANES and FDMNES)

Measured X-ray absorption spectra at the As K-edge and at the Te K-edge are shown in Figure 2.1. The main result at the As K-edge (Figure 2.1.a) is that Cu doping does not affect significantly the valence of As, as no noticeable chemical shift is present in the As K-edge spectrum with increasing Cu content. The only clear change in the As XANES spectrum is present in the region above 11870 eV, and might therefore be related to the structural changes. However, EXAFS data (Fourier transform of the  $k^2\chi(k)$  signal, *i.e.*,  $|\chi(r)| (\text{\AA}^{-3})$ ), reported in the inset of Figure 2.1.a, show that Cu-doping does not affect appreciably the local structure around As atoms. In particular, the curves of 2% and 5% Cu-doped compounds are practically identical to that of the undoped compound, and the changes above 11870 eV should rather be related to further nearest-neighbor shells (*e.g.* Cu-Te bonds). If we look instead at the Te K-edge, in Figure 2.1.b, an appreciable shift of the edge towards higher energy appears with increasing Cu content. We remark that the relative energy shift of Cu<sub>2</sub>Te and Te metal with glasses was measured with special care, the former being collected from the transmitted part of the beam measuring the glasses spectra. This implies that Cu atoms mainly affect the environment of Te-atoms and not that of As atoms. EXAFS data at the Te-K edge, not shown, point to the same result, with a clear change with Cu-doping. A quantitative analysis, however, was not possible for the moment, in the absence of a reliable model for the glass structure. We remind that a shift of the main edge towards higher energy is usually interpreted in terms of a positive valence of the absorbing ion.



In our case, a positive Te valence, given the absence of changes at the As K-edge, would lead to a negative Cu valence, which is against a simple application of electronegativity rules.

Because of the counterintuitive result, and as other interpretations might be possible (see Kim *et al.*<sup>29</sup> and discussion below), we have decided to analyze it with two different theoretical approaches: i) XANES measurements are theoretically interpreted using the FDMNES (Finite Difference Method Near-Edge Spectroscopy) simulations package,<sup>27</sup> based on a multiple scattering technique, partitioning the space into muffin-tin spheres close to the atoms and interstitial regions, with projection of the wave function into a spherical-harmonics local basis-set;<sup>30</sup> ii) in parallel, to analyze the Cu-Te charge transfer, we performed ab-initio calculation based on density functional theory. We used projector-augmented-wave (PAW) approach implemented in the Vienna Ab initio Simulation Package (VASP).<sup>31,32</sup>

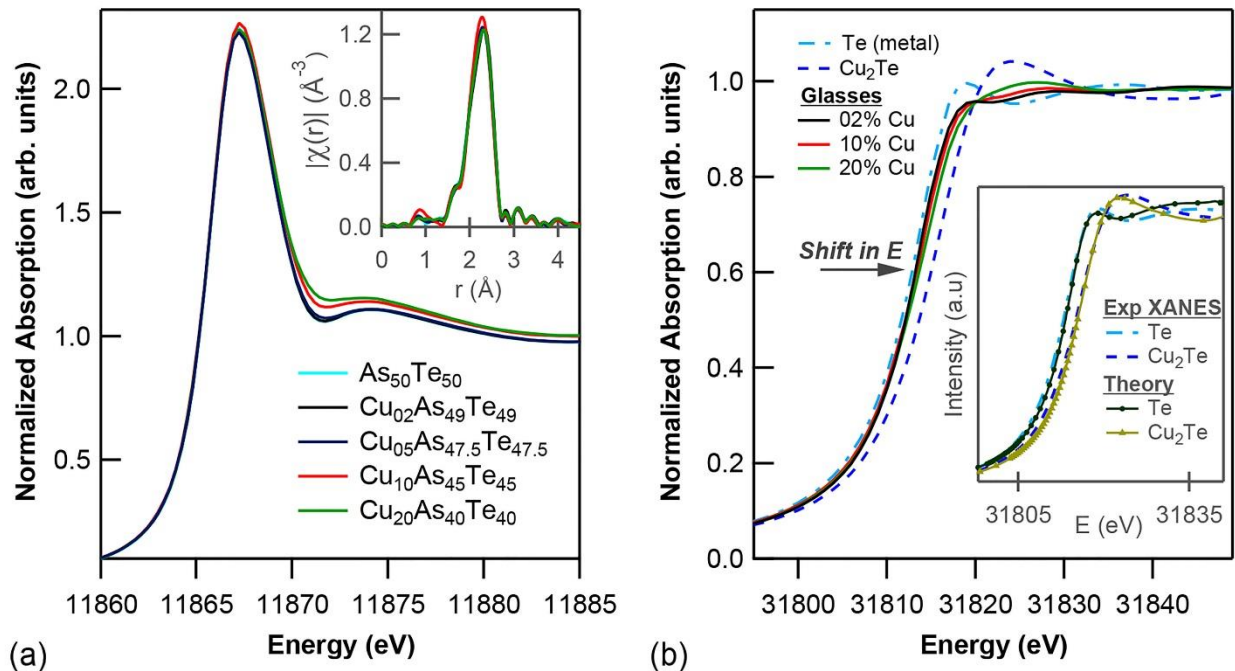


**Figure 2.1** (a) As K-edge XANES spectra of five glasses with increasing Cu content. No noticeable change in the chemical shift appears. Insert shows the Fourier transform of the  $k^2\chi(k)$  EXAFS signal which also points to negligible structural changes around As. (b) XANES spectra of three glasses at the Te K-edge, in comparison with Te and  $\text{Cu}_2\text{Te}$ . The chemical shift points to a positive valence of Te ions both in the glasses and in  $\text{Cu}_2\text{Te}$ . The inset shows the very good agreement between FDMNES calculations and experimental spectra.

Though we could not arrive at a definitive conclusion about the local structure of our glasses around Te, but the close similarity in the XANES spectra of our Cu-As-Te glasses and  $\text{Cu}_2\text{Te}$ , both at the Te K-edge (Figure 2.1.b) and at the Cu K-edge (Figure 2.3 below), suggests that their local structure might be close. The glasses and  $\text{Cu}_2\text{Te}$  spectra look very similar also at the Cu-L<sub>3</sub> edge (not shown). In particular, from Figure 2.1.b, increasing the Cu/Te ratio leads to an increasing positive-energy shift with Cu content, from the glasses up to  $\text{Cu}_2\text{Te}$ . So we decided to study at first the chemical shift of  $\text{Cu}_2\text{Te}$ , described in terms of the Nowotny structure<sup>33</sup> (space group  $P6/mmm$ , N. 191) with Cu-Te distance fixed to 2.56 Å, as obtained from our EXAFS results at the Te K-edge. The inset of Figure 2.1.b shows how well FDMNES ab-initio calculations allow reproducing the relative chemical shift and shapes of Te metal and  $\text{Cu}_2\text{Te}$  spectra.

### 2.3.2 Density of States (DOS)

From the orbitally-projected DOS analysis of the calculation for  $\text{Cu}_2\text{Te}$ , we get a very slight negative charge on Cu ions (-0.01) and a positive charge on Te ions (+0.02). We remark that in the literature, a much bigger negative charge on Cu ions (-0.2) was found in Kashida *et al.*<sup>34</sup> using a self-consistent LMTO (Linear Muffin-Tin Orbital) approach.

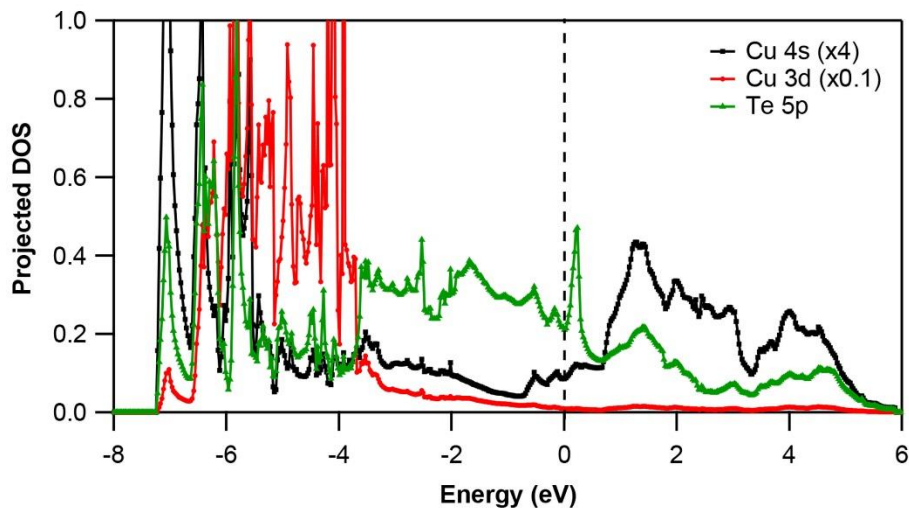


**Figure 2.2** DFT calculations: orbitally-projected DOS for  $\text{Cu}_2\text{Te}$ . Cu 3d and 4s energy distribution is compared to Te 5p distribution.

In order to double-check these results within the VASP package, we evaluated the charge on each atom following the partitioning of space introduced by Bader.<sup>35,36</sup> FFT grids were increased upto

24 x 24 x 40. Because of the presence of Cu atoms, the electronic density is expected to be sensitive to the value of the Coulomb repulsion,<sup>37</sup> that was included (LDA+U, where LDA stands for Local Density Approximation) with the approach of Dudarev *et al.*<sup>38</sup> The calculation was performed with Coulomb repulsion on both 3d states ( $U_d = 7.5$  eV) and 5p states ( $U_p = 1$  eV). Brillouin-zone integration was performed using a 9 x 9 x 5 Monkhorst-Pack k-mesh, and DOS calculation using a 21 x 21 x 13 mesh. Our results provided a tiny positive value for Cu (+0.008). We should notice that, given the low value of the charge transfer, both our FDMNES and VASP results, differently of the one of Kashida *et al.*,<sup>34</sup> are compatible with the absence of any charge-transfer in Cu<sub>2</sub>Te, thereby leading to a purely covalent picture of the Cu-Te bonding with no ionicity. We also remark that, even in VASP calculations, Cu ions can be made slightly negative by increasing the Coulomb repulsion  $U_p$  to 2 eV. We remind that the specific value of the Coulomb repulsion can be sample-dependent, because of different screening effects. Usual values for  $U_p$  range from 1 to 2 eV and for  $U_d$  from 5 to 9 eV.

The reason why increasing the Coulomb repulsion of 5p states leads to positive Te ions can be very simply understood from the analysis of the orbitally-projected DOS shown in Figure 2.2. The Cu 3d states lay -3.5 to -6.5 eV below the Fermi level and are coupled with 5p bonding levels of Te roughly at the same energy. Non-bonding Te 5p states (the dangling bond), are located from -3.5 eV to zero, in good agreement with XPS/XES measurements,<sup>39</sup> that show Cu 3d levels around -3.5 eV and 5p Te states between -3.5 and zero. In such a situation, the Coulomb repulsion acts in such a way as to rise the energy of Te 5p non-bonding (and empty antibonding) states, compared to Cu states. Given the presence of empty Cu 4s states just above the Fermi energy, this mechanism can lead to some charge transfer from Te 5p to Cu 4s states, thereby making Te slightly positive, in keeping with the finding of Kashida *et al.*<sup>34</sup> This might be also what happens in the glasses, as detailed in the following section. We finally remark that this behavior is peculiar to Cu-Te compounds. In fact, though the shift towards higher energy at the Te K-edge compared to Te metal takes place also in CdTe,<sup>29</sup> the above interpretation cannot be extended to that case because Cd 5s states are totally filled for the isolated atom and the electron charge transfer from Te to Cd cannot take place even if Te 5p levels are raised in energy by the same Coulomb mechanism<sup>37</sup>. The interpretation given by Kim *et al.*<sup>29</sup> for CdTe was rather based on a purely ionic approach with Te<sup>2-</sup> ions, leading to the complete filling of 5p states and to the transition to 6p states, higher in energy. However, this picture is untenable to explain the shift to higher energy of our glasses: even in the hypothesis of a charge transfer from Cu to Te, making Te negative, 2% to 20% Cu-doping would allow only a limited filling of the 5p band, not a complete filling, against the interpretation of Kim *et al.*<sup>29</sup>

### 2.3.3 Cu-K edge (XANES and FDMNES)

Before moving back to the glasses, we decided to analyze the chemical shift of  $\text{Cu}_2\text{Te}$  also at the Cu K-edge.

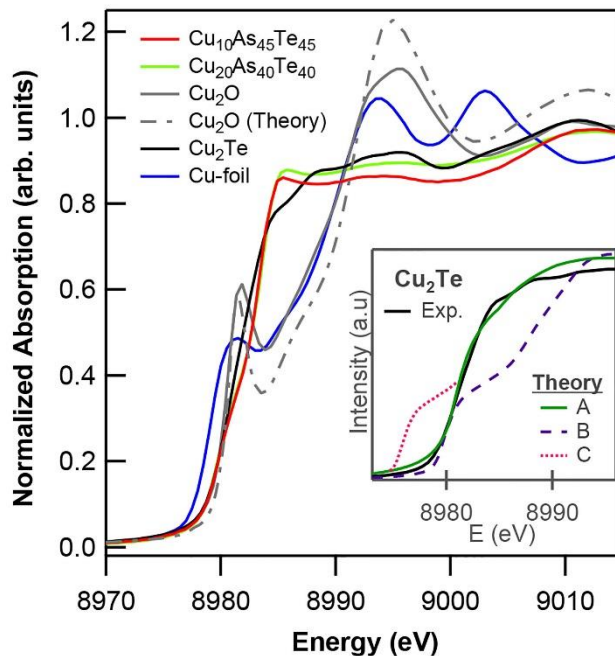


**Figure 2.3** XANES spectra at the Cu K-edge for Cu-doped glasses. The spectra of Cu-metal,  $\text{Cu}_2\text{Te}$  and  $\text{Cu}_2\text{O}$  are shown for comparison of the chemical shift. The FDMNES calculation for  $\text{Cu}_2\text{O}$  is also shown. Insert shows  $\text{Cu}_2\text{Te}$  raising edge of experimental spectra in comparison with theoretical spectra. Curves A, B and C are explained in the main text.

Looking at Figure 2.3, around 8980 eV,  $\text{Cu}_2\text{Te}$  and the glasses appear to have the same chemical shift as  $\text{Cu}_2\text{O}$  (which is known to be  $\text{Cu}^{+1}$ ), as all edges move to higher energy compared to Cu-metal,  $\text{Cu}^0$ . Because of this analogy with  $\text{Cu}_2\text{O}$ , in previous photoemission studies on  $\text{Cu}_2\text{Te}$ ,<sup>39</sup> Cu had been attributed the positive valence +1, in apparent contradiction with what stated above. However, the two cases are profoundly different for two main reasons. The first is that O 2p states are much lower in energy than Cu 3d, the latter lying between 0 and -3 eV, the former between -4 eV and -7 eV,<sup>40</sup> so that the pd-Coulomb repulsion does not raise in energy the O 2p, but the Cu 3d. The second is that Cu 3d states are partly empty, with the formation of hybridized 4s-3d<sub>z<sup>2</sup></sub> orbitals leading to incomplete 3d<sub>z<sup>2</sup></sub> shell and occupied Cu 4s states (the so-called Orgel model<sup>41</sup> of  $\text{Cu}_2\text{O}$ ). Therefore

its density of states is different than that of  $\text{Cu}_2\text{Te}$  shown in Figure 2.2 This difference is confirmed by our FDMNES calculation. For  $\text{Cu}_2\text{Te}$  we used the same input used to describe the Te K-edge (in the inset of Figure 2.1.b), with slightly negative Cu valence and totally filled 3d states. It is shown as curve A in the inset of Figure 2.3 and it reproduces correctly the chemical shift of the experimental profile. For  $\text{Cu}_2\text{O}$ , the experimental data are quite well reproduced by a FDMNES input with incompletely filled 3d shell (see main panel of Figure 2.3). The chemical shift, in particular, is very well described in both cases. In order to understand why the two different chemical valences for  $\text{Cu}_2\text{O}$  and  $\text{Cu}_2\text{Te}$  can lead to the same chemical shift at the Cu K-edge, we performed an analogous FDMNES calculation with the same electronic configuration for Cu as in  $\text{Cu}_2\text{O}$  (*i.e.*, unfilled 3d shell). It leads to a very poor agreement with the experiment (curve B in the inset of Figure 2.3), though the chemical shift is the same. The reason for the failure of the chemical-shift rule at the Cu K-edge for  $\text{Cu}_2\text{Te}$  can be understood reminding that Cu K-edge XANES probes empty 4p states of Cu. In the case of  $\text{Cu}_2\text{Te}$ , all Cu orbitals (3d, 4s and also 4p) are slightly lower-lying than the corresponding orbitals in  $\text{Cu}_2\text{O}$  and 5p Te states are much higher in energy than 2p O states. This leads to a band-crossing of the lowest-lying Cu 4p states with the highest-lying Te 5p states and we found with FDMNES that a small amount of Cu 4p states is filled. Extended 4p states are more difficult to handle with VASP calculations and, as they scarcely contribute to the DOS, they have been neglected in Figure 2.3. If these states had been empty, they would have appeared as a prolongation of curve A, corresponding to curve C in the inset of Figure 2.3. Had they been empty, they would have restored the expected negative energy-shift of the  $\text{Cu}_2\text{Te}$  edge compared to  $\text{Cu}_2\text{O}$  and Cu. In this sense, the failure of the chemical-shift rule in this case can be explained as a consequence of accidental band-crossing.

### 2.3.4 A Model for Glass Conductivity

XANES data show that glasses have a chemical shift of the same sign as the  $\text{Cu}_2\text{Te}$  sample. Generally, a typical framework valid for crystal calculations might not be simply transferred to glasses, where the dopant is not forced on a lattice site. But given the fact that Cu-doping has no influence on the local structure around As atoms in Cu-As-Te glasses, as evident from As-K edge XANES and EXAFS results, we can therefore extend the interpretation of electron charge transfer from Te to Cu for the glasses as well. Based on these experimental (XANES and EXAFS) and theoretical (FDMNES and DFT) findings, a global picture explaining the enhancement of electrical conductivity with Cu doping in these glasses can be proposed: electrical conductivity is determined by the holes created in non-bonding Te 5p orbitals (lone pair) by Cu acceptors. The mechanism is depicted in

Figure 2.4 and works in the presence of Cu-Te bonds, which should therefore be maximized in order to optimize the value of  $\sigma$ . The 4s electronic states of copper, just below the energy level of the highest Te 5p non-bonding states (the lone pair), efficiently collect Te 5p electrons and create a hole charge-reservoir in Te 5p energy levels. These mobile holes created in the lone pair state of Te is responsible for the huge raise in electrical conductivity in these Cu doped arsenic telluride glasses. The hole conductivity is confirmed by the positive measured Seebeck coefficient in these doped glasses.<sup>22-24</sup>

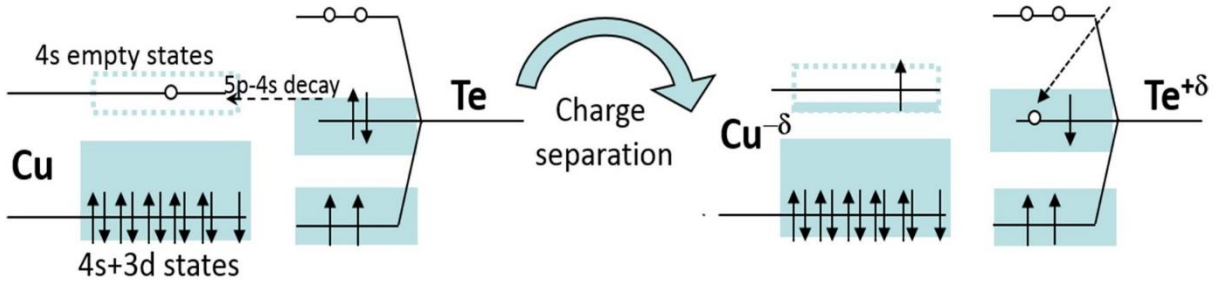


**Figure 2.4** Proposed mechanism for hole conductivity in Cu-doped telluride glass. Empty Cu-4s levels, with a low-energy tail below the higher-energy level of 5p Te lone pairs, more efficiently increase the hole concentration in the 5p Te orbitals.

As shown in Figure 2.4, the hole formation in the valence band of Te is enormously enhanced by the presence of Cu atoms with empty 4s states just below the higher-lying 5p Te states of the lone pair. In this case, the hole-creating process is much faster, as the lone pair is unstable with respect to the filling of the Cu empty level. We remark that the number of holes created in the valence band of Te by this mechanism does not correspond to the number of Cu atoms, but rather, because of the 8-N rule,<sup>42</sup> to the number of Cu-Te bonds. This simple picture is coherent with the behavior of  $\sigma$ , that increases with increasing Te and decreasing As for fixed amount of Cu.<sup>22</sup> This picture calls for the need to find a protocol to optimize the sample preparation so as to minimize the number of Cu-Cu bonds and optimize the number of Cu-Te bonds, for a given amount of Cu-doping.

At fixed hole concentration, the other critical parameter to increase the electric conductivity is the hole mobility, that in our model strongly depends on both Cu-Te and Te-Te bond connectivity. Indeed, once the holes have been formed (with a concentration proportional to the number of Cu-Te bonds), they must be able to hop and, for that, Te-Te bonds are needed. Therefore, the correlation of Cu-Te and Te-Te bond distributions plays a fundamental role in the mobility. This picture can explain why thermal treatments, that modify the global Cu-Te and Te-Te connectivity, affect the value of  $\sigma$ , as found by Lucas *et al.*,<sup>22</sup> where samples with the same amount of Cu and Te content differ in the

value of  $\sigma$  because of different annealing procedures. Interestingly, in this model, the creation of copper islands in the glass would decrease  $\sigma$  because it would not allow the creation of hole-centers. For all these reasons, the Cu-As-Te ternary glasses behave like extrinsic semiconductors with quite high hole concentrations and relatively low hole mobility. If this picture is correct, the logarithmic decrease of resistivity with increasing temperature<sup>43</sup> should be attributed to an increase of the hole mobility with temperature, rather than a change in the hole concentration.

## 2.4 Conclusion

Our XANES measurements at the Te K-edges for Cu-As-Te glasses point to a positive valence for Te, which increases with increasing Cu content. This is confirmed by multiple-scattering calculation. Though DFT calculations do not allow for a definite conclusion on this point, from the analysis of the orbitally-projected DOS of the calculation for Cu<sub>2</sub>Te, we get a very slight negative charge on Cu ions (-0.01) and a positive one on Te ions (+0.02). Combining all the experimental findings at As, Te and Cu K-edges with their theoretical interpretation through multiple-scattering and DFT calculations, we find that a small electron charge transfer from Te 5p non-bonding states to Cu 4s empty states is a possible interpretation. These findings suggest an interesting interpretation to explain the huge increase in  $\sigma$  with Cu in these Cu-As-Te *p*-type glasses. The electrical conductivity is not determined by Cu orbitals, but by the holes created in non-bonding Te 5p orbitals. The role of Cu atoms is to act as acceptors, tuning the hole concentration in Te 5p orbitals. The proposed mechanism for hole conductivity in Cu-As-Te glasses reckons heavily on the Cu-Te and Te-Te bond connectivity rather than Cu-Cu bonding. In other words, the critical parameter to increase electrical conductivity is the number of Cu-Te bonds that are formed and not simply the number of Cu atoms. These results can lead to more precise investigations of the local environment of these glasses so as to optimize the doping strategies, in order to enhance the thermoelectric performance. Future theoretical and experimental investigations might confirm our prediction: in particular, it would be interesting to look for positive correlations between the increase in electrical conductivity and the increase in Cu-Te bonds by the study of Cu-Te pair distribution function.

➤ **Adaptation**

The results presented in this chapter have been published in the Journal of Physical Chemistry C (ACS). Hence, this chapter is an adaptation from that publication – **B. Srinivasan et al., J. Phys. Chem. C, 2017, 121, 14045–14050.**

➤ **Author Contributions**

The experimental activities were designed and performed during the tenure of earlier PhD student (Shuo Cui). Since the beginning of 2016, Bhuvanesh Srinivasan (B.S) coordinated the continuity of that work (until its completion in June 2017). The credit for this work must be given to Prof. Sergio Di Matteo from IPR, Rennes, who performed an extensive ab-initio calculations (FDMNES) and dedicated a great amount of time in processing and interpreting the results. B.S assisted him in the FDMNES calculations for the As-K edge, in narrowing down the possible structures, and in the preparation of the manuscript. The DFT computations were performed by Dr. Alain Gellé (IPR Rennes), and XAS data treatment was by Dr. Carmelo Prestipino (ISCR Rennes).

➤ **Further Work & Outreach**

Very recently, we again synthesized these glasses and tried some fiber drawing experiments for Prof. Lei Wei from School of Electrical and Electronic Engineering, Nanyang Technological University, Singapore. Prof. Wei's team studied these glass fibers and concluded that they are of potential interest for thermal sensing and positioning applications. This work has been published in **ACS Applied Materials & Interfaces**. [DOI: 10.1021/acsami.8b20307](https://doi.org/10.1021/acsami.8b20307)

## References

- (1) Tritt, T. M.; Subramanian, M. A. Thermoelectric Materials, Phenomena, and Applications: A Bird's Eye View. *MRS Bull.* **2006**, 31, 188.
- (2) Snyder, G. J.; Toberer, E. S. Complex Thermoelectric Materials. *Nat. Mater.* **2008**, 7 (2), 105–114.
- (3) Takabatake, T.; Suekuni, K.; Nakayama, T.; Kaneshita, E. Phonon-Glass Electron-Crystal Thermoelectric Clathrates: Experiments and Theory. *Rev. Mod. Phys.* **2014**, 86 (2), 669–716.



- (4) Zhao, W.; Wei, P.; Zhang, Q.; Dong, C.; Liu, L.; Tang, X. Enhanced Thermoelectric Performance in Barium and Indium Double-Filled Skutterudite Bulk Materials via Orbital Hybridization Induced by Indium Filler. *J. Am. Chem. Soc.* **2009**, *131* (10), 3713–3720.
- (5) Wu, L.; Meng, Q.; Jooss, C.; Zheng, J.-C.; Inada, H.; Su, D.; Li, Q.; Zhu, Y. Origin of Phonon Glass–Electron Crystal Behavior in Thermoelectric Layered Cobaltate. *Adv. Funct. Mater.* **2013**, *23* (46), 5728–5736.
- (6) Snyder, G. J.; Christensen, M.; Nishibori, E.; Caillat, T.; Iversen, B. B. Disordered Zinc in  $\text{Zn}_4\text{Sb}_3$  with Phonon-Glass and Electron-Crystal Thermoelectric Properties. *Nat. Mater.* **2004**, *3* (7), 458–463.
- (7) Toberer, E. S.; May, A. F.; Snyder, G. J. Zintl Chemistry for Designing High Efficiency Thermoelectric Materials. *Chem. Mater.* **2010**, *22* (3), 624–634.
- (8) Gelbstein, Y.; Davidow, J. Highly Efficient Functional  $\text{GexPb}_{1-x}\text{Te}$  Based Thermoelectric Alloys. *Phys. Chem. Chem. Phys.* **2014**, *16* (37), 20120–20126.
- (9) Rosenberg, Y.; Gelbstein, Y.; Dariel, M. P. Phase Separation and Thermoelectric Properties of the  $\text{Pb}_{0.25}\text{Sn}_{0.25}\text{Ge}_{0.5}\text{Te}$  Compound. *J. Alloys Compd.* **2012**, *526*, 31–38.
- (10) Banik, A.; Vishal, B.; Perumal, S.; Datta, R.; Biswas, K. The Origin of Low Thermal Conductivity in  $\text{Sn}_{1-x}\text{Sb}_x\text{Te}$ : Phonon Scattering via Layered Intergrowth Nanostructures. *Energy Environ. Sci.* **2016**, *9* (6), 2011–2019.
- (11) Gelbstein, Y. Phase Morphology Effects on the Thermoelectric Properties of  $\text{Pb}_{0.25}\text{Sn}_{0.25}\text{Ge}_{0.5}\text{Te}$ . *Acta Mater.* **2013**, *61* (5), 1499–1507.
- (12) Hsu, K. F.; Loo, S.; Guo, F.; Chen, W.; Dyck, J. S.; Uher, C.; Hogan, T.; Polychroniadis, E. K.; Kanatzidis, M. G. Cubic  $\text{AgPb}_m\text{SbTe}_{2+m}$ : Bulk Thermoelectric Materials with High Figure of Merit. *Science* **2004**, *303* (5659), 818–821.
- (13) Zhao, L.-D.; Lo, S.-H.; Zhang, Y.; Sun, H.; Tan, G.; Uher, C.; Wolverton, C.; Dravid, V. P.; Kanatzidis, M. G. Ultralow Thermal Conductivity and High Thermoelectric Figure of Merit in SnSe Crystals. *Nature* **2014**, *508* (7496), 373–377.
- (14) Chen, Z.; Ge, B.; Li, W.; Lin, S.; Shen, J.; Chang, Y.; Hanus, R.; Snyder, G. J.; Pei, Y. Vacancy-Induced Dislocations within Grains for High-Performance PbSe Thermoelectrics. *Nat. Commun.* **2017**, *8*, 13828.
- (15) Kirievsky, K.; Shlimovich, M.; Fuks, D.; Gelbstein, Y. An Ab Initio Study of the Thermoelectric Enhancement Potential in Nano-Grained TiNiSn. *Phys. Chem. Chem. Phys.* **2014**, *16* (37), 20023–20029.

- (16) Zhu, T.; Fu, C.; Xie, H.; Liu, Y.; Zhao, X. High Efficiency Half-Heusler Thermoelectric Materials for Energy Harvesting. *Adv. Energy Mater.* **2015**, *5* (19), 1500588.
- (17) Gelbstein, Y.; Tunbridge, J.; Dixon, R.; Reece, M. J.; Ning, H.; Gilchrist, R.; Summers, R.; Agote, I.; Lagos, M. A.; Simpson, K.; et al. Physical, Mechanical, and Structural Properties of Highly Efficient Nanostructured n- and p-Silicides for Practical Thermoelectric Applications. *J. Elec Mater.* **2014**, *43* (6), 1703–1711.
- (18) Du, B.; Gucci, F.; Porwal, H.; Grasso, S.; Mahajan, A.; Reece, M. J. Flash Spark Plasma Sintering of Magnesium Silicide Stannide with Improved Thermoelectric Properties. *J. Mater. Chem. C* **2017**, *5* (6), 1514–1521.
- (19) Gonçalves, A. P.; Lopes, E. B.; Rouleau, O.; Godart, C. Conducting Glasses as New Potential Thermoelectric Materials: The Cu–Ge–Te Case. *J. Mater. Chem.* **2010**, *20* (8), 1516–1521.
- (20) Gonçalves, A. P.; Delaizir, G.; Lopes, E. B.; Ferreira, L. M.; Rouleau, O.; Godart, C. Chalcogenide Glasses as Prospective Thermoelectric Materials. *J. Elec Mater.* **2011**, *40* (5), 1015–1017.
- (21) Srinivasan, B.; Boussard-Pledel, C.; Dorcet, V.; Samanta, M.; Biswas, K.; Lefèvre, R.; Gascoin, F.; Chevirié, F.; Tricot, S.; Reece, M.; et al. Thermoelectric Properties of Highly-Crystallized Ge-Te-Se Glasses Doped with Cu/Bi. *Materials* **2017**, *10* (4), 328.
- (22) Lucas, P.; Conseil, C.; Yang, Z.; Hao, Q.; Cui, S.; Boussard-Pledel, C.; Bureau, B.; Gascoin, F.; Caillaud, C.; Gulbiten, O.; et al. Thermoelectric Bulk Glasses Based on the Cu–As–Te–Se System. *J. Mater. Chem. A* **2013**, *1* (31), 8917–8925.
- (23) Vaney, J. B.; Delaizir, G.; Alleno, E.; Rouleau, O.; Piarristeguy, A.; Monnier, J.; Godart, C.; Ribes, M.; Escalier, R.; Pradel, A.; et al. A Comprehensive Study of the Crystallization of Cu–As–Te Glasses: Microstructure and Thermoelectric Properties. *J. Mater. Chem. A* **2013**, *1* (28), 8190–8200.
- (24) Cui, S.; Boussard-Plédel, C.; Calvez, L.; Rojas, F.; Chen, K.; Ning, H.; Reece, M. J.; Guizouarn, T.; Bureau, B. Comprehensive Study of Tellurium Based Glass Ceramics for Thermoelectric Application. *Adv. Appl. Ceram.* **2015**, *114*, S42–S47.
- (25) Vaney, J. B.; Piarristeguy, A.; Pradel, A.; Alleno, E.; Lenoir, B.; Candolfi, C.; Dauscher, A.; Gonçalves, A. P.; Lopes, E. B.; Delaizir, G.; et al. Thermal Stability and Thermoelectric Properties of  $\text{Cu}_x\text{As}_{40-x}\text{Te}_{60-y}\text{Se}_y$  Semiconducting Glasses. *J. Solid State Chem.* **2013**, *203*, 212–217.
- (26) Mathon, O.; Beteva, A.; Borrel, J.; Bugnazet, D.; Gatla, S.; Hino, R.; Kantor, I.; Mairs, T.; Munoz, M.; Pasternak, S.; et al. The Time-Resolved and Extreme Conditions XAS (TEXAS) Facility at

- the European Synchrotron Radiation Facility: The General-Purpose EXAFS Bending-Magnet Beamline BM23. *J. Synchrotron Rad.* **2015**, *22* (6), 1548–1554.
- (27) Joly, Y. X-Ray Absorption near-Edge Structure Calculations beyond the Muffin-Tin Approximation. *Phys. Rev. B* **2001**, *63* (12), 125120.
- (28) Hedin, L.; Lundqvist, B. I. Explicit Local Exchange-Correlation Potentials. *J. Phys. C: Solid State Phys.* **1971**, *4* (14), 2064.
- (29) Kim, M. G.; Kim, D.-H.; Kim, T.; Park, S.; Kwon, G.; Kim, M. S.; Shin, T. J.; Ahn, H.; Hur, H.-G. Unusual Li-Ion Storage through Anionic Redox Processes of Bacteria-Driven Tellurium Nanorods. *J. Mater. Chem. A* **2015**, *3* (33), 16978–16987.
- (30) Savrasov, S. Y.; Savrasov, D. Y. Full-Potential Linear-Muffin-Tin-Orbital Method for Calculating Total Energies and Forces. *Phys. Rev. B* **1992**, *46* (19), 12181–12195.
- (31) Kresse, G.; Furthmüller, J. Efficient Iterative Schemes for Ab Initio Total-Energy Calculations Using a Plane-Wave Basis Set. *Phys. Rev. B* **1996**, *54* (16), 11169–11186.
- (32) Kresse, G.; Joubert, D. From Ultrasoft Pseudopotentials to the Projector Augmented-Wave Method. *Phys. Rev. B* **1999**, *59* (3), 1758–1775.
- (33) Nowotny, H. Z. Die Krystalstruktur von Cu<sub>2</sub>Te. *Metallkunde* **1946**, *37*, 40.
- (34) Kashida, S.; Shimosaka, W.; Mori, M.; Yoshimura, D. Valence Band Photoemission Study of the Copper Chalcogenide Compounds, Cu<sub>2</sub>S, Cu<sub>2</sub>Se and Cu<sub>2</sub>Te. *J. Phys. Chem. Solids* **2003**, *64* (12), 2357–2363.
- (35) Bader, R. F. W. Atoms in Molecules. In *Encyclopedia of Computational Chemistry*; John Wiley & Sons, Ltd, 2002.
- (36) Tang, W.; Sanville, E.; Henkelman, G. A Grid-Based Bader Analysis Algorithm without Lattice Bias. *J. Phys.: Condens. Matter* **2009**, *21* (8), 084204.
- (37) Wei, S.-H.; Zunger, A. Role of Metal d States in II-VI Semiconductors. *Phys. Rev. B* **1988**, *37* (15), 8958–8981.
- (38) Dudarev, S. L.; Botton, G. A.; Savrasov, S. Y.; Humphreys, C. J.; Sutton, A. P. Electron-Energy-Loss Spectra and the Structural Stability of Nickel Oxide: An LSDA+U Study. *Phys. Rev. B* **1998**, *57* (3), 1505–1509.
- (39) Domashevskaya, E. P.; Gorbachev, V. V.; Terekhov, V. A.; Kashkarov, V. M.; Panfilova, E. V.; Shchukarev, A. V. XPS and XES Emission Investigations of d-p Resonance in Some Copper Chalcogenides. *J. Electron. Spectro. Rel. Phenomena* **2001**, *114–116*, 901–908.

- (40) Wang, Y.; Lany, S.; Ghanbaja, J.; Fagot-Revurat, Y.; Chen, Y. P.; Soldera, F.; Horwat, D.; Mücklich, F.; Pierson, J. F. Electronic Structures of  $\text{Cu}_2\text{O}$ ,  $\text{Cu}_4\text{O}_3$ , and  $\text{CuO}$ : A Joint Experimental and Theoretical Study. *Phys. Rev. B* **2016**, *94* (24), 245418.
- (41) Orgel, L. E. Stereochemistry of Metals of the B Sub-Groups. Part I. Ions with Filled d-Electron Shells. *J. Chem. Soc.* **1958**, No. 0, 4186–4190.
- (42) Liu, J. Z.; Taylor, P. C. A General Structural Model for Semiconducting Glasses. *Solid State Commun.* **1989**, *70* (1), 81–85.
- (43) Gonçalves, A. P.; Lopes, E. B.; Delaizir, G.; Vaney, J. B.; Lenoir, B.; Piarristeguy, A.; Pradel, A.; Monnier, J.; Ochin, P.; Godart, C. Semiconducting Glasses: A New Class of Thermoelectric Materials? *J. Solid State Chem.* **2012**, *193*, 26–30.



# **Chapter 3**

**Thermoelectrics of Highly-Crystallized Ge-Te-Se Glasses Doped with  
Cu/Bi**



### 3.1 Introduction

In the past few years, the idea of thermoelectric glasses has gained some limelight. Telluride glasses,<sup>1</sup> particularly known for their low thermal conductivity of  $0.12 \text{ WK}^{-1}\text{m}^{-1}$  and simple glass-making process, makes them ideal candidates. An array of compositions of chalcogenide based semiconducting glasses and glass-ceramics with low thermal conductivity and relatively high electrical conductivity for a glassy phase have been previously reported.<sup>2-4</sup> Though these kind of semiconducting glasses, especially Cu-doped telluride glasses, exhibit high Seebeck coefficient of around  $600 \mu\text{V/K}$  at room temperature,<sup>2,3,5-9</sup> their high degree of structural disorder causes large electron scatterings that results in low mobility and electrical conductivity. This ultimately pulls down the power factor and overall  $zT$  to values that are too low for any relevant large-scale industrial applications.

The budding prospect from the semiconducting IV–VI group is the GeTe based system. Previous reports from our lab on Te-rich, high-purity  $\text{Ge}_{20}\text{Te}_{77}\text{Se}_3$  ternary glasses focused mainly on optical fibers and far infra-red sensing applications due to their good transparency to long wavelengths and inherently low level of optical losses.<sup>10,11</sup> These GeTe-based stable glass systems, though extensively studied for optical purposes, are not well explored for thermoelectric applications, especially the crystallized composition of these glasses.

Understanding the fact that pure glass phase alone will not produce materials with high  $zT$  values (due to their low electrical conductivity), in this study, we employed a different approach of intentional crystallization of Ge–Te–Se glass compositions by heavily doping with metal or semi-metal (Cu or Bi). The underlying idea is that the heavy doping in glasses could partially or completely collapse the glassy network (*i.e.*, formation of some crystallized phases) and could potentially improve the electrical transport properties and at the same time may retain at least some of the characteristic features of glasses like low thermal conductivity, *i.e.*, an approach toward phonon-glass electron-crystal model.

### 3.2 Materials and Methods

#### 3.2.1 Reagents

Ge (Umicore, 5N), Te (JGI, 5N), Se (Umicore, 5N), Cu (Alfa Aesar, 5N), Bi (Strem Chemicals, 5N) were used for synthesis without involving any further purification processes.



### 3.2.2 Synthesis

The samples of  $(\text{Ge}_{20}\text{Te}_{77}\text{Se}_3)_{100-x}\text{M}_x$  ( $\text{M} = \text{Cu}$  or  $\text{Bi}$ ;  $x = 0, 5, 10, 15$ ) were synthesized using the conventional melt quenching method. Appropriate stoichiometric amounts of the starting elements of Ge, Te, Se, Cu, or Bi were introduced in a silica tube (diameter  $\sim 10$  mm) that had previously been cleaned with hydrofluoric (HF) acid, rinsed with distilled water and dried under vacuum. The ampoules were sealed under a vacuum of  $10^{-6}$  Torr, then placed in a rocking furnace and slowly heated up to  $850^\circ\text{C}$  over a period of 8 h, then held at that temperature for 12 h before being quenched in water. The tubes were then annealed at  $100^\circ\text{C}$  for 3 h. The obtained ingots were cut and polished to required shapes and dimensions for various thermoelectric measurements.

This section of this chapter also elaborates the techniques used (characterization methods / tools) for understanding the structural, micro and nano-structural, electrical and thermal transport properties of TE materials that are presented in this thesis. These characterization details described in this chapter applies also for the remaining chapters, and hence they are not repeated.

### 3.2.3 Powder X-ray Diffraction

X-ray diffraction (XRD) patterns were recorded at room temperature in the  $2\theta$  range  $15$ - $120^\circ$  with a step size of  $0.026^\circ$  and a scan time per step of 400 s using a PANalytical X'Pert Pro diffractometer (Cu K- $L_{2,3}$  radiation,  $\lambda = 1.5418 \text{ \AA}$ , PIXcel 1D detector). Data Collector and HighScore Plus software packages were used, respectively, for recording and analyzing the patterns. The lattice parameters that are presented in some chapters of this thesis were estimated from Le Bail-type profile fits carried out with the Fullprof program and the pseudo-Voigt profile function.<sup>12</sup>

### 3.2.4 Hall Measurements

The Hall measurements were carried out at room temperature using a home-made four-point probe setup (van der Pauw method), where a fixed magnetic field of  $0.112$  T and dc current of  $15$  mA was applied. The measurements were made on square-shaped samples of dimensions  $\sim 5 \times 5 \times 2$  mm<sup>3</sup>. The carrier concentration ( $n$ ) and mobility ( $\mu$ ) were computed from carrier sheet density ( $n_s$ ), sheet resistance ( $R_s$ ) and Hall Voltage ( $V_H$ ) using the following equations,

$$n_s = n \times t = \frac{IB}{e|V_H|} \quad (3.1)$$

$$\mu = 1/(en_s R_s) \quad (3.2)$$

where  $e$ ,  $B$ ,  $I$  and  $t$  are the charge of the electron, magnetic field, current and thickness of the sample, respectively. For most cases, the values of carrier density obtained were quite consistent with a standard deviation of less than 2%.

### 3.2.5 Measurement of Electrical Transport Properties

The electrical resistivity and Seebeck coefficient were measured simultaneously from room temperature to higher temperature using a commercial instrument (LSR-3, Linseis Inc.), in a He atmosphere. The measurements were made on parallelepiped-shaped samples of dimensions  $\sim 10 \times 2 \times 2 \text{ mm}^3$ . The electrical transport properties for the samples that are presented in Chapter 4 – 9 were obtained using LSR-3 equipment, whereas they were obtained using ZEM-3 instrument (ULVAC) for the samples that are presented in this current chapter (Chapter 3).

#### 3.2.5.1 Description of LSR-3 Equipment



**Figure 3.1** An external view of LSR-3 platform/equipment. *Image courtesy:* © Linseis.

A prism or cylindrical sample was set in a vertical position between the upper and lower blocks in the heating furnace (shown in Figure 3.2). While the sample was heated to, and held, at a specified temperature, it was heated by the heater in the lower block to provide a temperature gradient. Seebeck coefficient was measured by measuring the upper and lower temperatures ( $T_1$  and  $T_2$ ) with the thermocouples pressed against the side of the sample, followed by measurement of

thermal electromotive force ( $dE$ ) between the same wires on one side of the thermocouple. Electrical resistance was measured by the dc four terminal method, in which a constant current  $I$  was applied to both ends of the sample to measure and determine voltage drop ( $dV$ ) between the same wires of the thermocouple by subtracting the thermo-electromotive force between the leads.

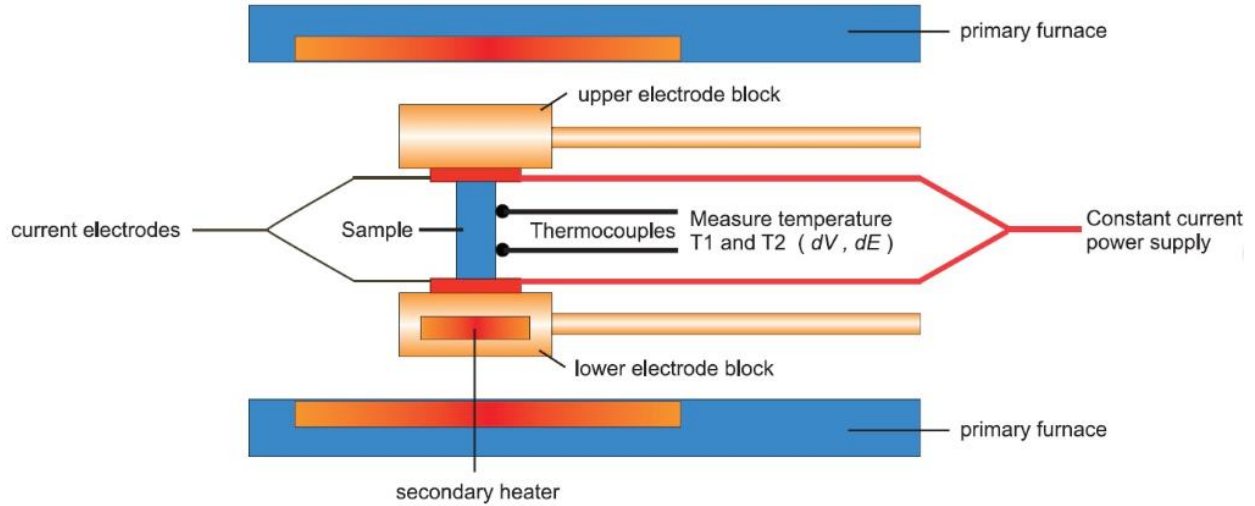


**Figure 3.2** The schematics of an internal view of LSR-3 platform/equipment. *Image courtesy:* © Linseis.

### 3.2.6 Measurement of Thermal Transport Properties

The thermal diffusivity,  $D$ , was measured from room temperature to higher temperature using the laser flash diffusivity method in a Netzsch LFA-457 instrument. Thermal diffusivity (in  $\text{mm}^2/\text{s}$ ) is a material-specific property for characterizing unsteady heat conduction. This value describes how quickly a material reacts to a change in temperature. Disc shaped samples of 10 mm diameter and  $\sim 2$  mm thickness were used for the measurements. For the samples that are presented in Chapters 4 - 9, the heat capacity ( $C_p$ ) was derived using the Dulong–Petit relation as in equation (3.3),

$$C_p = 3R/M \quad (3.3)$$

where  $R$  is the gas constant and  $M$  is the molar mass. Dulong–Petit relation holds well for most kind of thermoelectric materials.<sup>13–17</sup> For the samples that are presented in this chapter, temperature-dependent  $C_p$  was derived using a standard sample (pyroceram) in LFA-457.

The total thermal conductivity,  $\kappa_{\text{total}}$  (or  $\kappa$ ) was calculated using equation (3.4),

$$\kappa_{total} = DC_p\rho \quad (3.4)$$

where  $\rho$  is the density of the sample, which was measured using Archimedes' principle.

To better understand the thermal transport properties, the contributions from electronic and lattice parts were calculated. The lattice thermal conductivity ( $\kappa_{latt}$ ) was estimated from  $\kappa_{total}$  by subtracting the electronic contribution ( $\kappa_e$ ) via Wiedemann-Franz law, as in equation (3.5),

$$\kappa_e = L\sigma T \quad (3.5)$$

where  $\kappa_e$  is the electronic thermal conductivity, and  $L$  is the Lorenz number computed by the condensed version of Single Parabolic Band model with acoustic phonon scattering (SPB-APS),<sup>18,19</sup> as in equation (3.6),

$$L = 1.5 + \exp\left[-\frac{|S|}{116}\right] \quad (3.6)$$

where Seebeck coefficient ( $S$ ) is in  $\mu\text{VK}^{-1}$  and Lorenz number ( $L$ ) is in  $10^{-8} \text{W}\Omega\text{K}^{-2}$ .

### 3.2.6.1 Description of LFA-457 Equipment

In carrying out a thermal diffusivity measurement, the lower surface of a plane parallel sample was first heated by a short energy pulse (shown in Figure 3.3). The resulting temperature change on the upper surface of the sample was then measured (as a function of time) with an infrared detector. The mathematical analysis of this temperature/time function allowed the determination of the thermal diffusivity.

For adiabatic conditions,

$$D = 0.1388 \frac{b^2}{t_{0.5}}$$

where,  $t_{0.5}$  is time value at half signal height (called 'half time'), *i.e.*, time at 50% of the temperature increase (measured at the rear of the test piece), and  $b$  is the sample thickness.

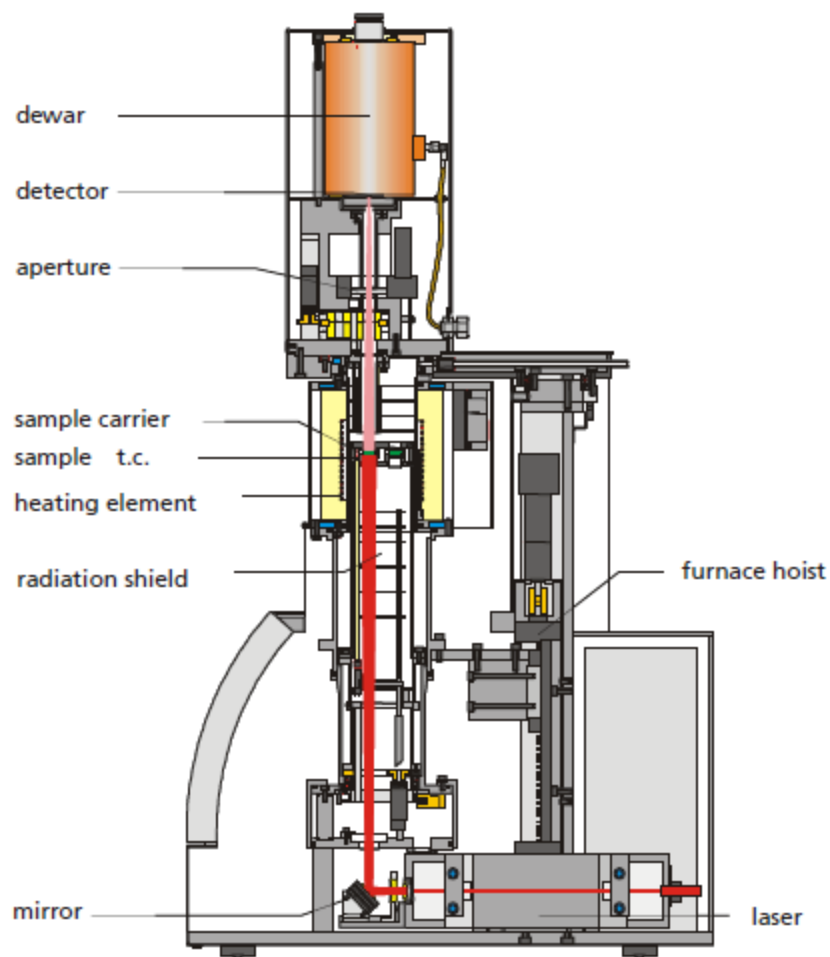


**Figure 3.3** The schematics of laser flash apparatus (LFA-457 platform). *Image courtesy:* © Netzsch.

The uncertainties in the results for the values of electrical and thermal transport properties were ~ 5% and ~ 7%, respectively, and for the overall  $zT$ , the uncertainty was ~ 12%. In this thesis, error bars in the figures are not shown to increase the readability of the curves.

### 3.2.7 Microscopic Analysis

Scanning electron microscopy (SEM) and Energy Dispersive X-Ray Spectroscopy (EDX) analysis were performed using a JEOL JSM 7100F microscope on the polished bulk or fractured surface of the samples. Transmission electron microscopy (TEM) investigations were carried out using a JEOL 2100F microscope on electron-transparent samples prepared by polishing, dimpling and ion beam milling.

### 3.3 Results and Discussion

#### 3.3.1 Sample Notations and Dopant Induced Crystallization

The samples  $(\text{Ge}_{20}\text{Te}_{77}\text{Se}_3)_{100-x}\text{M}_x$  ( $\text{M} = \text{Cu}$  or  $\text{Bi}$ ;  $x = 0, 5, 10, 15$ ) that were prepared by vacuum sealed-tube melt quenching technique and their acronyms are presented in Table 3.1.

**Table 3.1** Sample compositions and their notations.

<b>M</b>	<b>X</b>	<b>Sample</b>	<b>Acronyms</b>
	0	$\text{Ge}_{20}\text{Te}_{77}\text{Se}_3$	GTS
Cu	5	$(\text{Ge}_{20}\text{Te}_{77}\text{Se}_3)_{95}\text{Cu}_5$	GTS-Cu05
	10	$(\text{Ge}_{20}\text{Te}_{77}\text{Se}_3)_{90}\text{Cu}_{10}$	GTS-Cu10
	15	$(\text{Ge}_{20}\text{Te}_{77}\text{Se}_3)_{85}\text{Cu}_{15}$	GTS-Cu15
Bi	5	$(\text{Ge}_{20}\text{Te}_{77}\text{Se}_3)_{95}\text{Bi}_5$	GTS-Bi05
	10	$(\text{Ge}_{20}\text{Te}_{77}\text{Se}_3)_{90}\text{Bi}_{10}$	GTS-Bi10
	15	$(\text{Ge}_{20}\text{Te}_{77}\text{Se}_3)_{85}\text{Bi}_{15}$	GTS-Bi15

The samples GTS and GTS-Cu05 were found to be stable glasses, and their stability criteria ( $\Delta T$ ) was around 100 °C ( $\Delta T = T_c - T_g$ , where  $T_c$  is the crystallization temperature and  $T_g$  is the glass-transition temperature). GTS-Cu10 was found to be a partially crystallized glass. The electrical conductivities of these samples were extremely low, so they are not presented in this thesis chapter. Please refer to the Supporting Info section of B. Srinivasan *et al.*<sup>20</sup> or Annexure 3 (Figures A3.1 and A3.2) for details regarding these glassy samples.

It is worth noting that the glassy network in GTS was completely destroyed with addition of more than 10% Cu and 5% of Bi. The thesis chapter focusses only on the thermoelectric-related properties of the completely-crystallized compositions of GTS-Cu15, GTS-Bi05, GTS-Bi10, and GTS-Bi15.

#### 3.3.2 Structural and Microscopic Investigation

Powder X-ray diffraction (PXRD) results for GTS-Cu15 (Figure 3.4) show that the samples were well crystallized and three major phases exists, namely  $\text{Cu}_2\text{GeTe}_3$ , Te and GeTe. The peaks for  $\text{Cu}_2\text{GeTe}_3$  phase were indexed based on a cubic blende-type structure with  $F\bar{4}3m$  space group ( $n^\circ 216$ ),<sup>21</sup> considering Cu and Ge atoms sharing the same lattice position without any cation ordering,

while the Te and GeTe peaks were indexed based on the trigonal structure with the  $P3_121$  space group (n°152) and rhombohedral structure with  $R3m$  (n°160) space group, respectively. The weight ratios of these phases indicated in the inset pie-chart of Figure 3.4 shows  $\text{Cu}_2\text{GeTe}_3$  as the main phase in GTS-Cu15 sample.

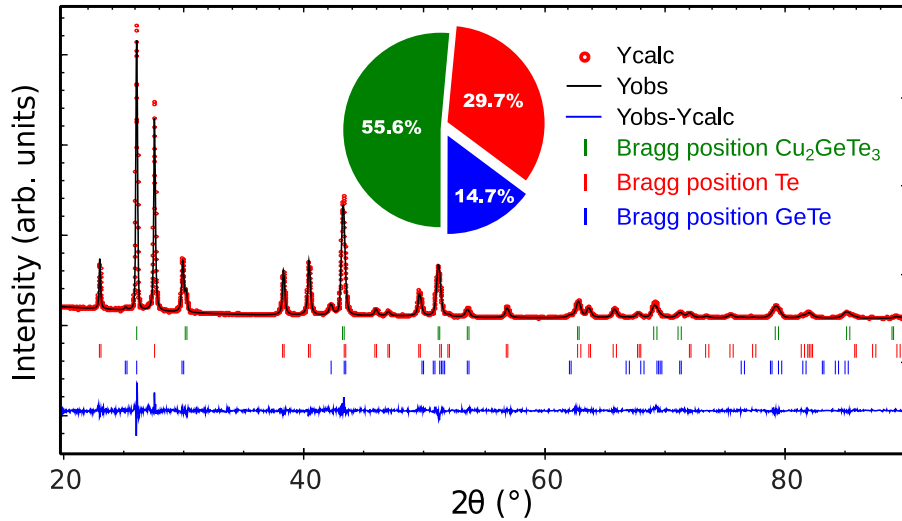


**Figure 3.4** Rietveld refinement pattern for the GTS-Cu15 sample-observed (black line), calculated (red), and difference (blue line) XRD diffraction profiles. The vertical markers correspond to the position of the Bragg reflections for the different phases. The inset pie-chart illustrates the weight contribution of the different phases in the sample.

PXRD analyses performed on Bi-doped GTS samples (Figure 3.5) show that all samples contained a bulk proportion of crystalline Te phase (PDF#078-2312, space group  $P3_121$ , n°152) and various Bi-containing phases depending on the initial experimental composition. For instance, GTS-Bi05 contained  $\text{Bi}_2\text{Ge}_3\text{Te}_6$  phase (PDF#050-0735, space group  $R3m$ , n°160), GTS-Bi10 contained small amounts of  $\text{Bi}_2\text{Ge}_3\text{Te}_6$  and  $\text{Bi}_{2.5}\text{Ge}_{1.5}\text{Te}_5$  (PDF#089-0991, space group  $P\bar{3}m1$ , n°164) phases, while increasing the Bi content favored the crystallization of Bi-rich Bi-Ge-Te phases, as GTS-Bi15 exhibited a much larger content of  $\text{Bi}_{2.5}\text{Ge}_{1.5}\text{Te}_5$  and  $\text{Bi}_2\text{GeTe}_4$  (PDF#087-2092, space group  $R3m$ , n°166).

At this point, it is essential to mention that in Bi-doped samples an anonymous phase that could not be indexed based on the current available crystallographic databases was present in considerable proportion. This could be a new phase of Bi-Ge-Te and the exact composition of this phase was difficult to estimate in SEM-EDX.

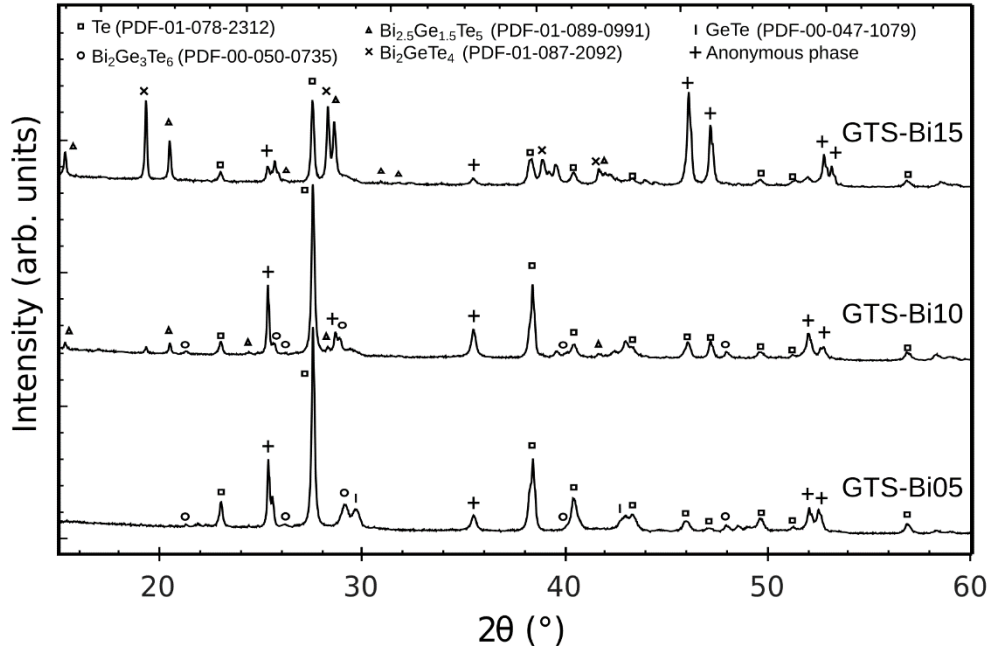


**Figure 3.5** PXRD patterns for Bi-doped GTS samples (showing multiple crystalline phases).

The SEM images of GTS-Cu15 with different levels of magnification (Figure 3.6) show several dark patchy domains (dendritic formation) in the backdrop of brighter regions. EDX analysis found that the dark domains correspond to the main phase of  $\text{Cu}_2\text{GeTe}_3$ , while the bright matrix appeared to be predominantly Te and GeTe phases, establishing solid agreement with XRD and refinement results (Figure 3.4). Figure 3.6.a clearly shows that  $\text{Cu}_2\text{GeTe}_3$  grew as dendrites. In short, Te-rich phases comprising GeTe in minor proportions were embedded in the  $\text{Cu}_2\text{GeTe}_3$  main phase.

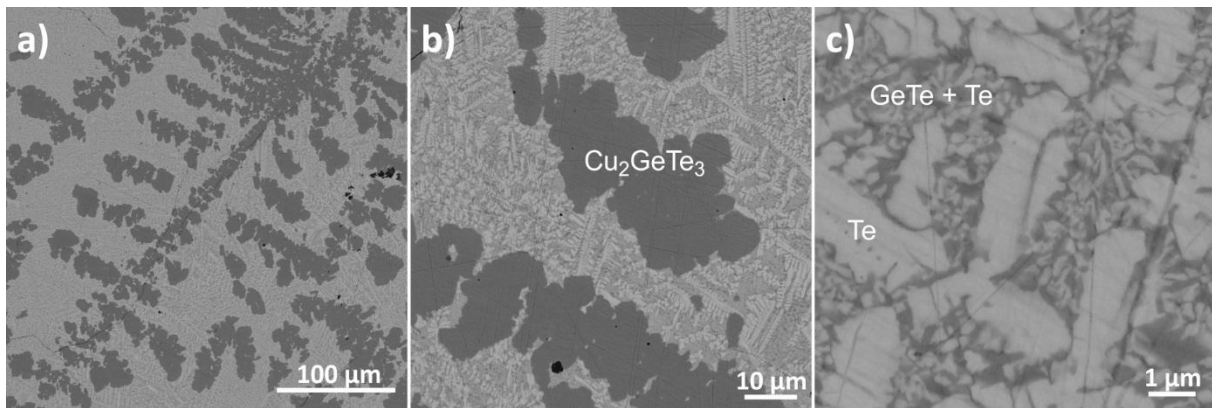


**Figure 3.6** SEM images of GTS-Cu15 sample, (a,b) shows two distinct regions, the dark grey region is identified as the  $\text{Cu}_2\text{GeTe}_3$  major phase (dendritic growth) and a brighter region; and (c) the higher magnification image of bright region was found to be a mixture of Te and GeTe phases.



Furthermore, TEM micrographs on these GTS-Cu15 samples, as in Figure 3.7, show large and well-dispersed crystallized regions of the  $\text{Cu}_2\text{GeTe}_3$  phase. The Figure 3.7.a presents a dark field (DF) image obtained from the reflection pointed by an arrow in the inset. The inset presents the selected area electron diffraction (SAED) pattern of the crystal where the strong reflection are indexed in the cubic cell of  $\text{Cu}_2\text{GeTe}_3$  and the weak ones could not be indexed. The left part of this crystal phase shows a contrast between white and grey areas, whereas the right part shows a homogeneous grey contrast.

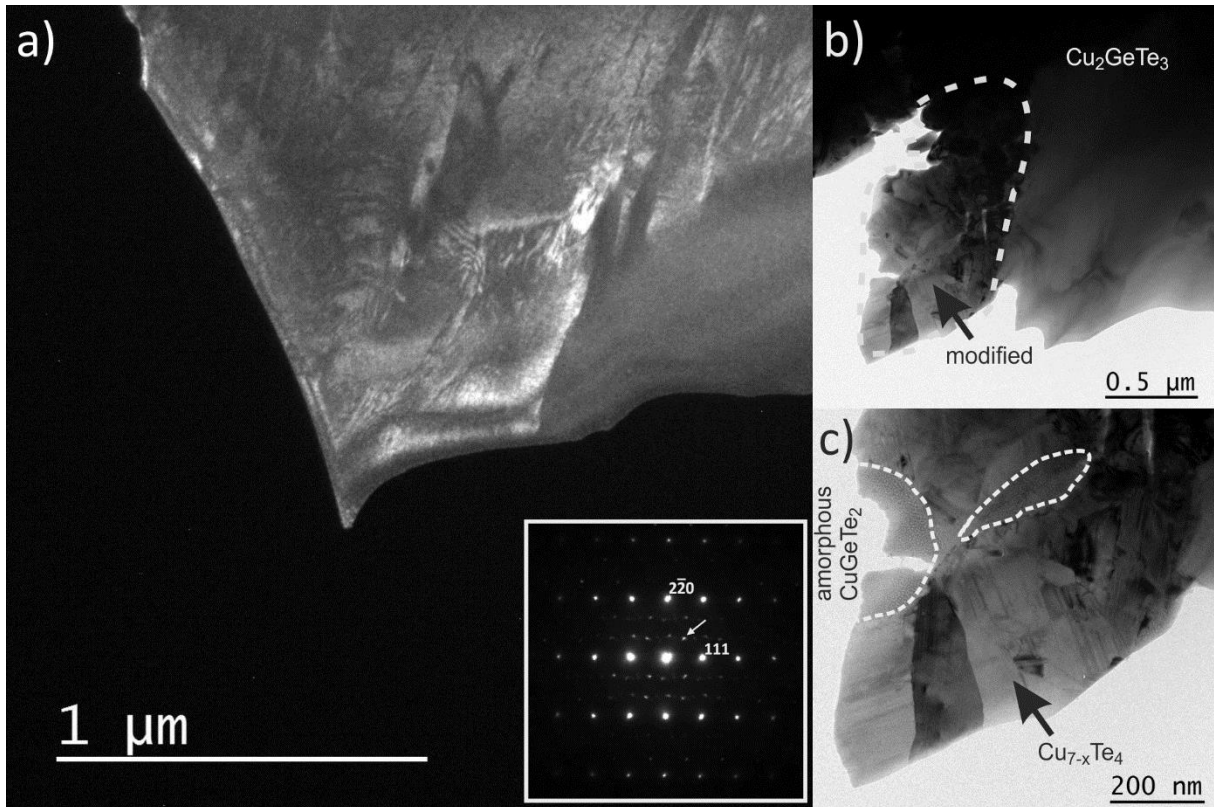


**Figure 3.7** TEM micrographs of GTS-Cu15 (a) Low magnification dark field (DF) image of a  $\text{Cu}_2\text{GeTe}_3$  crystallite domain. Inset shows the SAED pattern of the left part of the crystal showing strong reflections that can be indexed in the cubic cell of  $\text{Cu}_2\text{GeTe}_3$ . The DF image is made with one of these reflections (see arrow); (b) Bright field (BF) image of a  $\text{Cu}_2\text{GeTe}_3$  crystallite phase. The dotted region on the BF image is the one that was apparently modified by ion beam milling; (c) Enlargement of the modified area showing the segregation between crystalline  $\text{Cu}_{7-x}\text{Te}_4$  and an amorphous phase of composition  $\text{CuGeTe}_2$ .

Figure 3.7.b shows a more magnified image of a  $\text{Cu}_2\text{GeTe}_3$  crystallite zone in bright field (BF), where a large and homogeneous crystal of  $\text{Cu}_2\text{GeTe}_3$  main phase and a small polycrystalline area (dotted region) are observed. EDX analysis on this dotted region found it to have, on average, the

same composition as that of the main phase. Enlargement of this modified surface, Figure 3.7.c, shows a mixture of crystallized and amorphous regions which were found to be  $\text{Cu}_{7-x}\text{Te}_4$  and  $\text{CuGeTe}_2$  phases, respectively, by EDX. As these phases were unidentified in PXRD and SEM, they could have evolved during the sample preparation process of ion beam milling; some regions of the main  $\text{Cu}_2\text{GeTe}_3$  phase that were close to the ion milled area were dissociated into crystalline  $\text{Cu}_{7-x}\text{Te}_4$  and amorphous  $\text{CuGeTe}_2$  phases. The presence of stacking faults in the  $\text{Cu}_{7-x}\text{Te}_4$  phase of the modified region are explained pictorially using HRTEM images in the Figure 3.8. Interesting features that could kindle the thermoelectric properties like nanostructured defect layers or mesostructured grain boundaries were non-existent for this heavily Cu-doped GTS-Cu15 sample.

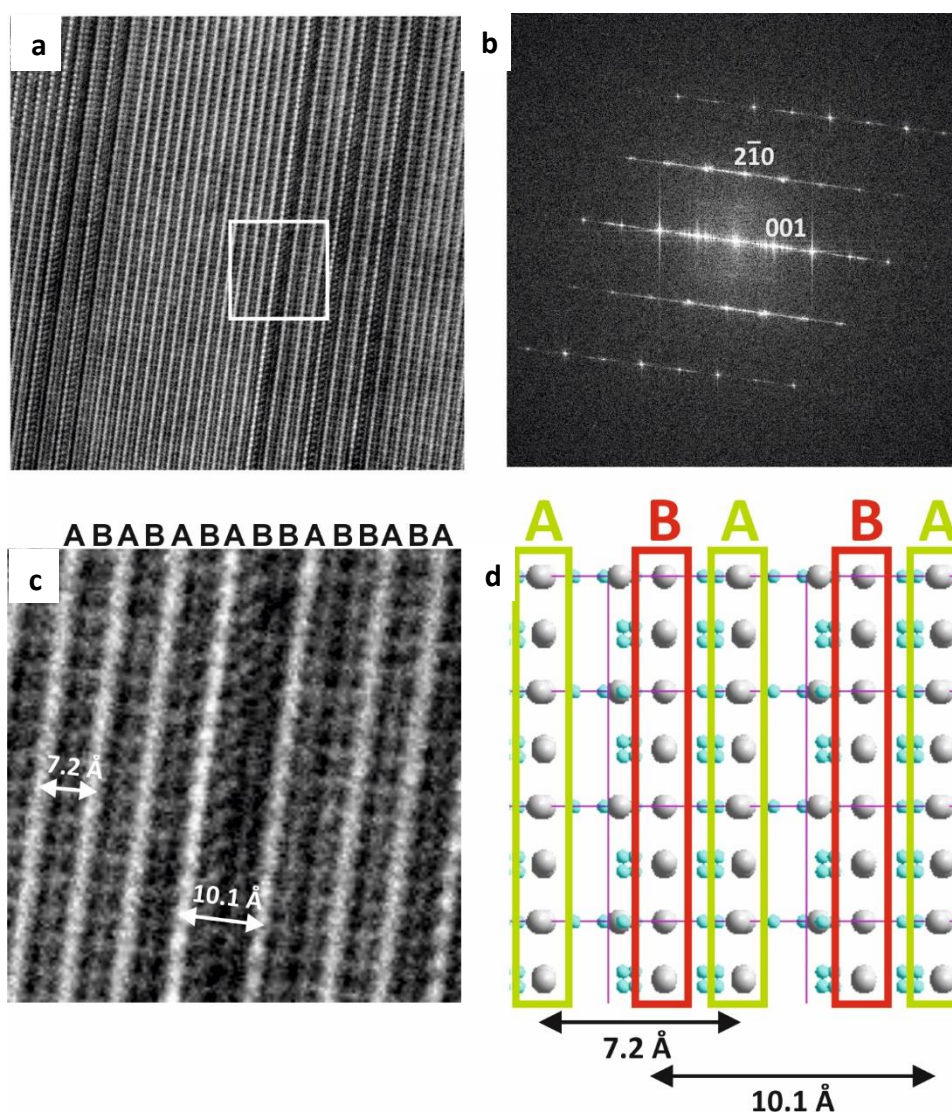


**Figure 3.8** (a) HRTEM image of ion-beam modified region in GTS-Cu15 showing stacking faults in  $\text{Cu}_{7-x}\text{Te}_4$  phase (EDS Cu/Te = 1.16) oriented along the  $[120]$  zone axis, as shown in the Fast Fourier

Transform of the image in Figure (b). (c) On enlarging the image, stacking faults along  $c$ -axis with two different spacing between “white” planes ( $7.2 \text{ \AA}$  and  $10.1 \text{ \AA}$ ), are seen. The investigation of the structure of  $\text{Cu}_7\text{Te}_4$  [Baranova, R.V. *Kristallografiya* (1967) 12, (2) p266-p273] along the zone axis  $[120]$  points to two kinds of “Te” planes (A and B on the figure) with different spacing between them, as in figure (d). The  $7.2 \text{ \AA}$  spacing corresponds to the  $c$  unit cell parameter of  $\text{Cu}_7\text{Te}_4$  whereas the  $10.1 \text{ \AA}$  spacing corresponds to the  $c$ -parameter plus the shortest distance between A and B.

Figure 3.9 displays SEM images of GTS-Bi15 where two major phases are visible, a pale bright region and another darker region. EDX analyses found the bright region to be Te phase and the grey region to be Bi-Ge-Te phase (BGT) with variable compositions, especially the Bi/Ge ratio. This tentatively matches with the PXRD results as well.

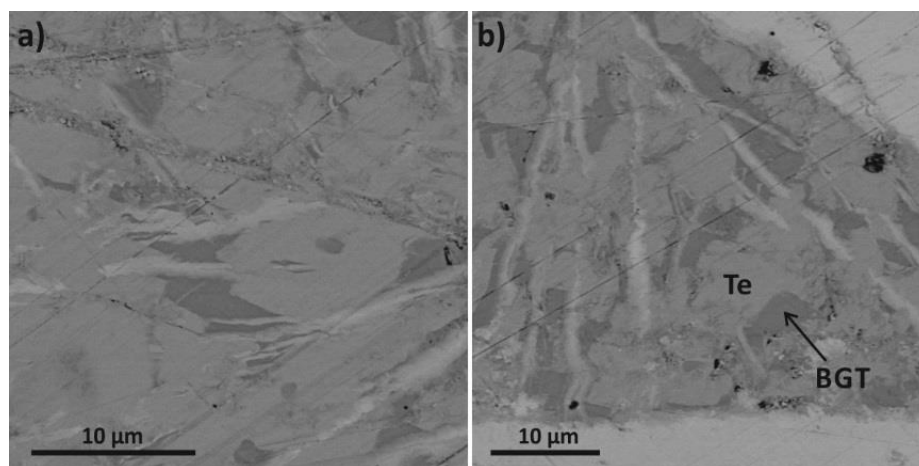


**Figure 3.9** (a,b) SEM images of GTS-Bi15 sample showing regions of Te phase (pale bright) and Bi-Ge-Te (BGT) phase (darker regions).

### 3.3.4 Thermoelectric Properties

The electrical conductivity as a function of temperature of the GTS samples is presented in Figure 3.10.a. With increasing temperature, the electrical conductivity of all of the samples decreased, which is the archetypal behavior of a degenerate semiconductor.<sup>22,23</sup> Since the Hall voltage was positive in all these samples, holes are the major charge carriers ( $p$ -type). Results from Hall measurements tabulating the carrier concentration ( $n$ ) and mobility ( $\mu$ ), are presented in Table 3.2. With an increase in Cu/Bi content, the electrical conductivity increased due to coherent raising of the carrier

concentration values and the transformation from a glassy state to a completely crystallized form (*i.e.*, transition from a glassy state of GTS to crystalline GTS-Cu10 or GTS-Bi05 and further).

**Table 3.2** Hall measurement results for carrier concentration and mobility at room temperature.

Sample	Carrier Concentration, $n$ ( $\text{cm}^{-3}$ )	Mobility, $\mu$ ( $\text{cm}^2 \text{V}^{-1} \text{s}^{-1}$ )
GTS-Cu15	$2.81 \times 10^{20}$	24.25
GTS-Bi05	$1.09 \times 10^{20}$	36.5
GTS-Bi10	$2.38 \times 10^{20}$	16.8
GTS-Bi15	$2.39 \times 10^{20}$	25.57

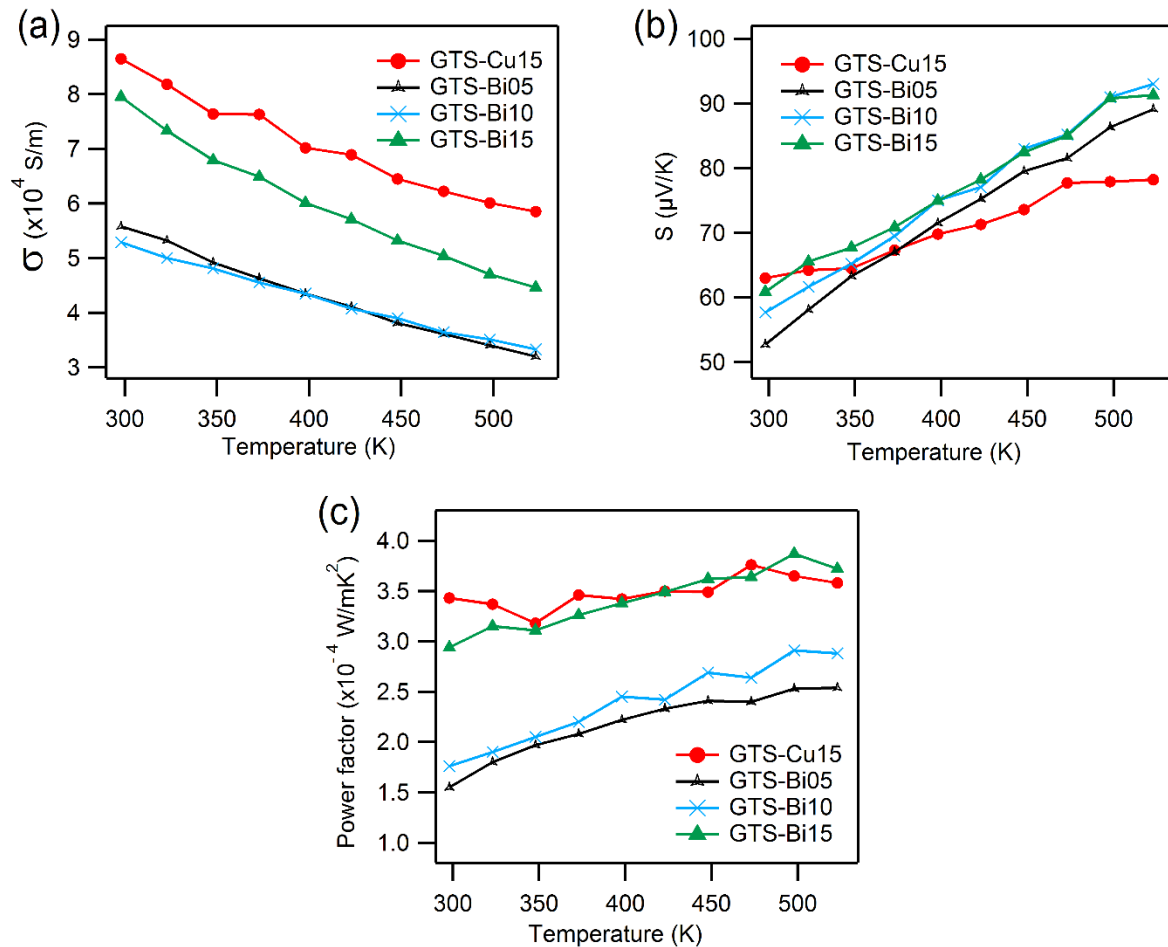


**Figure 3.10** Electrical transport properties: (a) Electrical conductivity,  $\sigma$ ; (b) Seebeck coefficient,  $S$ ; and (c) thermoelectric power factor,  $S^2\sigma$ , as a function of temperature.

It is interesting to note the variation of mobility in Bi-doped samples. Despite GTS-Bi10 having twice the carrier concentration values of GTS-Bi05, its carrier charge mobility was reduced by half and this cumulative effect is observed in Figure 3.10.a, where the electrical conductivities of both of these samples are almost the same. It seems like there is a threshold for the increase in conductivity versus Bi content. GTS-Bi15 exhibited much higher conductivity due to high charge carrier density and mobility. It is also seen that Cu doped GTS samples are more electrically conductive compared to the Bi-doped ones, due to high carrier concentration and hole mobility. It is known that, in such a case of heavy doping, an additional carrier scattering mechanism (*i.e.*, alloy scattering) comes into play due to the random distribution of different atoms in the same lattice site.<sup>24,25</sup> This explains the reason for modest mobility in these samples.

Figure 3.10.b shows the temperature dependent Seebeck coefficient ( $S$ ) results. The Seebeck coefficient being positive for all of the compositions over the entire temperature range indicates  $p$ -type charge carriers, which is in good agreement with the Hall measurement results. Interestingly, room temperature  $S$ -values marginally increased with dopant level and did not follow the expected trend according to the variation of carrier densities. However, such an anomalous change is difficult to explain. For samples doped with Bi, the  $S$ -value increased from  $\sim 60 \mu\text{V/K}$  at RT to  $\sim 90 \mu\text{V/K}$  at 523 K, yet these  $S$ -values are nowhere close to the state-of-the-art  $p$ -type thermoelectric materials.<sup>26-31</sup> Though these experiments to improve the thermoelectric properties by highly crystallizing the glass compositions vastly improved the  $\sigma$  values, the  $S$ -values were drastically reduced because of systematic loss of characteristic telluride glass features, as telluride glasses are known for their exceptionally high Seebeck coefficient values.<sup>2,3,5</sup>

For comparison, it is useful to mention the properties of undoped Ge-Te glass. At room temperature, it possess a high Seebeck coefficient of  $\sim 960 \mu\text{V/K}$ , but the electrical conductivity is too low ( $\sim 10^{-3} \text{ S/m}$ ).<sup>4-6</sup> The room-temperature electrical transport properties of some of the phases are presented in Table 3.3. This gives a general idea on the role of contribution of constituent phases to the TE properties. For example, XRD results in Figure 3.5 show more intense Te peaks for GTS-Bi05 and GTS-Bi10, while the Te peaks are less intense for GTS-Bi15. Moreover, GTS-Bi15 has proportionately more Bi-Ge-Te phases, which are far superior in conductivity ( $\sigma > 10^4 \text{ S/m}$ ) when compared to the Te phase ( $\sigma \approx 70 \text{ S/m}$ ). This reflects in the decreased values of  $\sigma$  for GTS-Bi05 and GTS-Bi10 and relatively higher  $\sigma$  for GTS-Bi15 (Figure 3.10.a). As the physical properties for some of the phases are not yet known, a more cogent explanation could not be presented at this juncture.

The temperature dependence of the thermoelectric power factor, calculated using the electrical conductivity and Seebeck coefficient as  $S^2\sigma$ , is displayed in Figure 3.11.c. GTS-Cu15 and GTS-Bi15

have almost the same power factor values, and comparatively higher than the other samples. The power factor for these heavily-doped samples did not improve much with temperature. Once again, although these systems demonstrated decent levels of electrical conductivity, the mediocre Seebeck coefficient values in all cases reduced the power factor, which is almost one order of magnitude lower than the existing well-known *p*-type thermoelectric materials.<sup>13,26,32,33</sup>

**Table 3.3** Electrical transport properties of constituent phases (at ~300 K).

Phases	$\sigma$ (S/m)	$S$ ( $\mu\text{V/K}$ )	References
$\text{Bi}_2\text{GeTe}_4$	$5 \times 10^4$	92	34
$\text{Bi}_2\text{Ge}_3\text{Te}_6$	$6 \times 10^4$	32	34,35
GeTe	$8 \times 10^5$	25	36,37
Te	70	250	This work

Figure 3.11(a, b) displays the specific heat,  $C_p$ , and thermal diffusivity,  $D$ , as a function of temperature. The measured  $C_p$  values, within the experimental limits, are close to the values expected from Dulong-Petit law. The temperature dependent total thermal conductivity,  $\kappa_{\text{total}}$  derived from  $D$  and  $C_p$  is presented in Figure 3.11.c. The lattice thermal conductivity ( $\kappa_{\text{latt}}$ ), estimated from  $\kappa_{\text{total}}$  by subtracting the electronic contribution ( $\kappa_e$ ) via the Wiedmann-Franz law is presented in Figure 3.11.d. For the values of  $L$  and  $\kappa_e$ , please refer Annexure 3 (Figures A3.4 and A3.5). As seen from the Figure 3.11(c, d), the majority of the contribution for thermal conductivity comes from the lattice part.  $\kappa_{\text{total}}$  for Bi-doped samples were relatively lower compared to the Cu-doped ones, due to the more metallic properties of Cu. Even though GTS-Cu15 and GTS-Bi15 possessed almost the same (comparable) power factor values and  $\kappa_e$  values, GTS-Cu15 exhibited a  $\kappa_{\text{total}}$  value of  $\sim 2.25 \text{ Wm}^{-1} \text{ K}^{-1}$  at room temperature, whereas GTS-Bi10 and GTS-Bi15 exhibited a  $\kappa_{\text{total}}$  value of  $\sim 1.07 \text{ Wm}^{-1} \text{ K}^{-1}$  and  $\sim 1.3 \text{ Wm}^{-1} \text{ K}^{-1}$  at room temperatures, which is about a 50% reduction in comparison to that of the Cu-doped sample. This reduction is primarily because of significantly lower lattice contribution, presumably arising due to nanoprecipitate formation, which would produce effective phonon scattering in the lattices of heavily Bi-doped GTS samples. It has already been reported that Bi substitution in GeTe solid-state solutions can result in segregation of Bi-rich nanoprecipitates.<sup>23</sup> In addition, such types of inclusions can cause collective phonon scattering from nanoprecipitates, meso-structured grain boundaries, and other crystallographic defects that could pave the way for reduction in lattice thermal conductivity.<sup>32,38,39</sup> In this work, for heavily-doped GTS-Bi samples, an

ultra-low lattice thermal conductivity of  $\sim 0.7 \text{ Wm}^{-1}\text{K}^{-1}$  was achieved at 523 K.  $\kappa_{\text{total}}$  obtained for these doped crystalline materials, especially for the Bi-doped ones, are essentially in the range or comparable with the  $\kappa_{\text{total}}$  values of some of the well-known effective thermoelectric materials.<sup>27,28,32,40-44</sup>

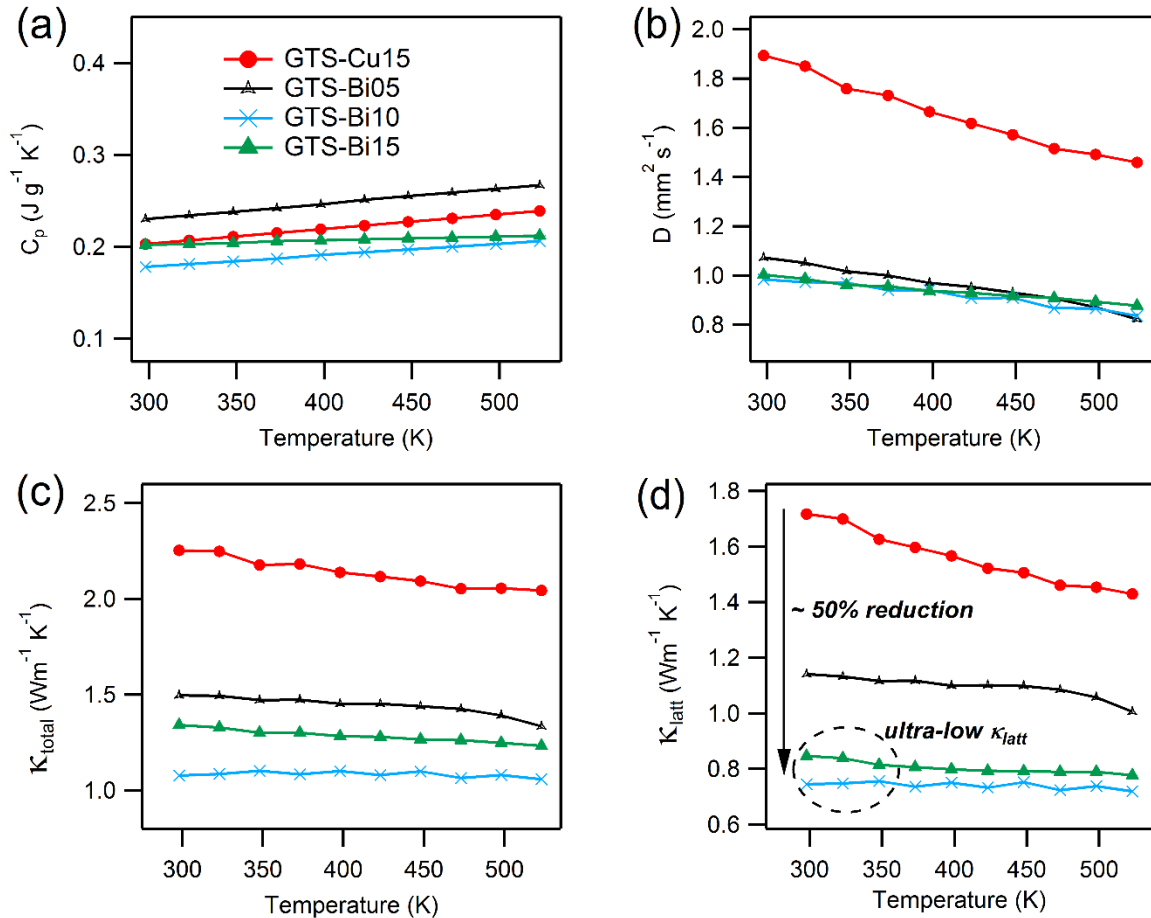


**Figure 3.11** Temperature-dependent (a) specific heat capacity,  $C_p$ ; (b) thermal diffusivity,  $D$ ; (c) total thermal conductivity,  $\kappa_{\text{total}}$ ; and (d) lattice thermal conductivity,  $\kappa_{\text{latt}}$  for Cu- and Bi-doped GTS samples. Color code legend applies to all of the plots.

The existence of several (random) phases in these heavily doped materials makes it difficult to explain all the trend or changes that are happening in their thermal and electrical transport properties.

In any case, though these heavily-doped GTS samples possessed extremely low thermal conductivity, their  $zT$  values were still quite low (Figure 3.12). It is their adversely low power factor

that affected the overall  $zT$  of these materials, proving time and again that optimizing one parameter alone does not necessarily lead to improved efficiency, and an optimized blend of all properties is the indispensable criteria for an impactful thermoelectric device.

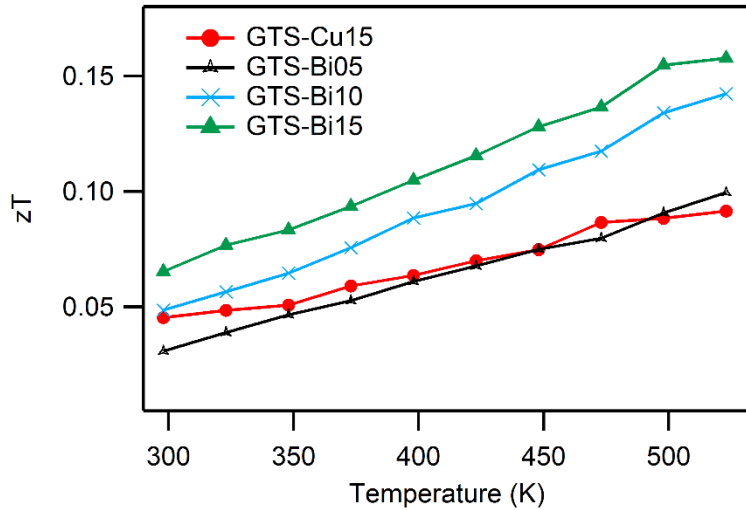


**Figure 3.12** Dimensionless Figure of merit,  $zT$  for Cu- and Bi-doped GTS samples, showing a maximum  $zT$  of  $\sim 0.16$  for GTS-Bi15 and  $\sim 0.092$  for GTS-Cu15 at 523 K.

### 3.4 Conclusion

High-quality ingots of  $(\text{Ge}_{20}\text{Te}_{77}\text{Se}_3)_{100-x}\text{M}_x$  ( $\text{M} = \text{Cu}$  or  $\text{Bi}$ ;  $x = 5, 10, 15$ ) were obtained using a vacuum sealed-tube melt quenching technique. With excess doping of Cu and Bi, the glassy network in pristine  $\text{Ge}_{20}\text{Te}_{77}\text{Se}_3$  was destroyed and highly-crystallized samples with multiple phases were produced. These  $p$ -type materials had high electrical conductivity ( $\sim 8 \times 10^4 \text{ S/m}$ ) due to increased charge carrier density. Significantly lower total thermal conductivity was exhibited by these crystallized materials. Bi-doped samples demonstrated better thermoelectric features compared to Cu-doped samples. Moreover, TEM micrographs corroborated that heavily Cu-doped samples lack nano/meso-scale architectures. Ultra-low lattice thermal conductivity of  $\sim 0.7 \text{ Wm}^{-1} \text{ K}^{-1}$  was achieved for crystalline samples that were doped with 10 at % and 15 at % Bi, presumably due to Bi-rich nanoprecipitation. The high electrical conductivity coupled with low thermal transport provides the scope for further improvements in overall thermoelectric properties, especially the Seebeck coefficient, by proper optimization of parameters in crystallized glass compositions.



➤ **Adaptation**

The results presented in this chapter have been published in Materials (MDPI). Hence, this chapter is an adaptation from that publication – **B. Srinivasan *et al.*, Materials, 2017, 10, 328.**

➤ **Author Contributions**

B.S conceived the project, designed and performed experiments, analyzed the results and wrote the journal manuscript. Dr. François Cheviré helped with the Rietveld refinement for the GTS-Cu15 sample.

## References

- (1) Zhang, S.-N.; He, J.; Zhu, T.-J.; Zhao, X.-B.; Tritt, T. M. Thermal Conductivity and Specific Heat of Bulk Amorphous Chalcogenides  $\text{Ge}_{20}\text{Te}_{80-x}\text{Se}_x$  ( $x = 0,1,2,8$ ). *J. Non-Cryst. Solids* **2009**, *355* (2), 79–83.
- (2) Lucas, P.; Conseil, C.; Yang, Z.; Hao, Q.; Cui, S.; Boussard-Pledel, C.; Bureau, B.; Gascoin, F.; Caillaud, C.; Gulbiten, O.; et al. Thermoelectric Bulk Glasses Based on the Cu–As–Te–Se System. *J. Mater. Chem. A* **2013**, *1* (31), 8917–8925.
- (3) Cui, S.; Boussard-plédel, C.; Calvez, L.; Rojas, F.; Chen, K.; Ning, H.; Reece, M. J.; Guizouarn, T.; Bureau, B. Comprehensive Study of Tellurium Based Glass Ceramics for Thermoelectric Application. *Adv. Appl. Ceram.* **2015**, *114*, S42–S47.
- (4) Zhu, T. J.; Yan, F.; Zhao, X. B.; Zhang, S. N.; Chen, Y.; Yang, S. H. Preparation and Thermoelectric Properties of Bulk in Situ Nanocomposites with Amorphous/Nanocrystal Hybrid Structure. *J. Phys. D: Appl. Phys.* **2007**, *40* (19), 6094.
- (5) Gonçalves, A. P.; Lopes, E. B.; Delaizir, G.; Vaney, J. B.; Lenoir, B.; Piarristeguy, A.; Pradel, A.; Monnier, J.; Ochin, P.; Godart, C. Semiconducting Glasses: A New Class of Thermoelectric Materials? *J. Solid State Chem.* **2012**, *193*, 26–30.
- (6) Gonçalves, A. P.; Lopes, E. B.; Rouleau, O.; Godart, C. Conducting Glasses as New Potential Thermoelectric Materials: The Cu–Ge–Te Case. *J. Mater. Chem.* **2010**, *20* (8), 1516–1521.
- (7) Vaney, J. B.; Delaizir, G.; Alleno, E.; Rouleau, O.; Piarristeguy, A.; Monnier, J.; Godart, C.; Ribes, M.; Escalier, R.; Pradel, A.; et al. A Comprehensive Study of the Crystallization of Cu–As–Te

- Glasses: Microstructure and Thermoelectric Properties. *J. Mater. Chem. A* **2013**, *1* (28), 8190–8200.
- (8) Vaney, J. B.; Piarristeguy, A.; Pradel, A.; Alleno, E.; Lenoir, B.; Candolfi, C.; Dauscher, A.; Gonçalves, A. P.; Lopes, E. B.; Delaizir, G.; et al. Thermal Stability and Thermoelectric Properties of  $\text{Cu}_x\text{As}_{40-x}\text{Te}_{60-y}\text{Se}_y$  Semiconducting Glasses. *J. Solid State Chem.* **2013**, *203*, 212–217.
- (9) Gonçalves, A. P.; Delaizir, G.; Lopes, E. B.; Ferreira, L. M.; Rouleau, O.; Godart, C. Chalcogenide Glasses as Prospective Thermoelectric Materials. *J. Electron. Mater.* **2011**, *40* (5), 1015–1017.
- (10) Conseil, C.; Shiryaev, V. S.; Cui, S.; Boussard-Pledel, C.; Troles, J.; Velmuzhov, A. P.; Potapov, A. M.; Suchkov, A. I.; Churbanov, M. F.; Bureau, B. Preparation of High Purity Te-Rich Ge-Te-Se Fibers for 5-15 Micrometre Infrared Range. *J. Lightwave Tech.* **2013**, *31* (11), 1703–1707.
- (11) Wilhelm, A. A.; Boussard-Plédel, C.; Coulombier, Q.; Lucas, J.; Bureau, B.; Lucas, P. Development of Far-Infrared-Transmitting Te Based Glasses Suitable for Carbon Dioxide Detection and Space Optics. *Adv. Mater.* **2007**, *19* (22), 3796–3800.
- (12) Rodríguez-Carvajal, J. Recent Advances in Magnetic Structure Determination by Neutron Powder Diffraction. *Physica B: Condensed Matter* **1993**, *192* (1), 55–69.
- (13) Fahrnbauer, F.; Souchay, D.; Wagner, G.; Oeckler, O. High Thermoelectric Figure of Merit Values of Germanium Antimony Tellurides with Kinetically Stable Cobalt Germanide Precipitates. *J. Am. Chem. Soc.* **2015**, *137* (39), 12633–12638.
- (14) Li, J.; Zhang, X.; Lin, S.; Chen, Z.; Pei, Y. Realizing the High Thermoelectric Performance of GeTe by Sb-Doping and Se-Alloying. *Chem. Mater.* **2017**, *29* (2), 605–611.
- (15) Wu, L.; Li, X.; Wang, S.; Zhang, T.; Yang, J.; Zhang, W.; Chen, L.; Yang, J. Resonant Level-Induced High Thermoelectric Response in Indium-Doped GeTe. *NPG Asia Mater* **2017**, *9* (1), e343.
- (16) Schröder, T.; Rosenthal, T.; Giesbrecht, N.; Maier, S.; Scheidt, E.-W.; Scherer, W.; Snyder, G. J.; Schnick, W.; Oeckler, O. TAGS-Related Indium Compounds and Their Thermoelectric Properties – the Solid Solution Series  $(\text{GeTe})_x\text{AgIn}_y\text{Sb}_{1-y}\text{Te}_2$  ( $x = 1-12$ ;  $y = 0.5$  and  $1$ ). *J. Mater. Chem. A* **2014**, *2* (18), 6384–6395.
- (17) Schröder, T.; Rosenthal, T.; Giesbrecht, N.; Nentwig, M.; Maier, S.; Wang, H.; Snyder, G. J.; Oeckler, O. Nanostructures in Te/Sb/Ge/Ag (TAGS) Thermoelectric Materials Induced by Phase Transitions Associated with Vacancy Ordering. *Inorg. Chem.* **2014**, *53* (14), 7722–7729.

- (18) Srinivasan, B.; Gautier, R.; Gucci, F.; Fontaine, B.; Halet, J.-F.; Cheviré, F.; Boussard-Pledel, C.; Reece, M. J.; Bureau, B. Impact of Coinage Metal Insertion on the Thermoelectric Properties of GeTe Solid-State Solutions. *J. Phys. Chem. C* **2018**, *122* (1), 227–235.
- (19) Kim, H.-S.; Gibbs, Z. M.; Tang, Y.; Wang, H.; Snyder, G. J. Characterization of Lorenz Number with Seebeck Coefficient Measurement. *APL Materials* **2015**, *3* (4), 041506.
- (20) Srinivasan, B.; Boussard-Pledel, C.; Dorcet, V.; Samanta, M.; Biswas, K.; Lefèvre, R.; Gascoin, F.; Cheviré, F.; Tricot, S.; Reece, M.; et al. Thermoelectric Properties of Highly-Crystallized Ge-Te-Se Glasses Doped with Cu/Bi. *Materials* **2017**, *10* (4), 328.
- (21) Palatnik, L.; Komnik, Y.; Koshkin, V.; Belava, E. A Group of Ternary Semiconducting Compounds. *Doklady Akademii Nauk* **1961**, *SSSR 137*, 68–71.
- (22) Banik, A.; Vishal, B.; Perumal, S.; Datta, R.; Biswas, K. The Origin of Low Thermal Conductivity in  $\text{Sn}_{1-x}\text{Sb}_x\text{Te}$ : Phonon Scattering via Layered Intergrowth Nanostructures. *Energy Environ. Sci.* **2016**, *9* (6), 2011–2019.
- (23) Perumal, S.; Roychowdhury, S.; Biswas, K. Reduction of Thermal Conductivity through Nanostructuring Enhances the Thermoelectric Figure of Merit in  $\text{Ge}_{1-x}\text{Bi}_x\text{Te}$ . *Inorg. Chem. Front.* **2016**, *3* (1), 125–132.
- (24) Wang, H.; LaLonde, A. D.; Pei, Y.; Snyder, G. J. The Criteria for Beneficial Disorder in Thermoelectric Solid Solutions. *Adv. Funct. Mater.* **2013**, *23* (12), 1586–1596.
- (25) Gelbstein, Y.; Davidow, J. Highly Efficient Functional  $\text{Ge}_x\text{Pb}_{1-x}\text{Te}$  Based Thermoelectric Alloys. *Phys. Chem. Chem. Phys.* **2014**, *16* (37), 20120–20126.
- (26) Poudeu, P. F. P.; D'Angelo, J.; Downey, A. D.; Short, J. L.; Hogan, T. P.; Kanatzidis, M. G. High Thermoelectric Figure of Merit and Nanostructuring in Bulk P-Type  $\text{Na}_{1-x}\text{Pb}_m\text{Sb}_y\text{Te}_{m+2}$ . *Angew. Chem. Int. Ed.* **2006**, *45* (23), 3835–3839.
- (27) Pei, Y.; Shi, X.; LaLonde, A.; Wang, H.; Chen, L.; Snyder, G. J. Convergence of Electronic Bands for High Performance Bulk Thermoelectrics. *Nature* **2011**, *473* (7345), 66–69.
- (28) Zhang, Q.; Cao, F.; Liu, W.; Lukas, K.; Yu, B.; Chen, S.; Opeil, C.; Broido, D.; Chen, G.; Ren, Z. Heavy Doping and Band Engineering by Potassium to Improve the Thermoelectric Figure of Merit in P-Type PbTe, PbSe, and  $\text{PbTe}_{1-y}\text{Se}_y$ . *J. Am. Chem. Soc.* **2012**, *134* (24), 10031–10038.
- (29) Jiehe Sui, J. S. Effect of Cu Concentration on Thermoelectric Properties of Nanostructured P-Type  $\text{MgAg}_{0.97-x}\text{Cu}_x\text{Sb}_{0.99}$ . *Acta Mater.* **2015**, *87*.
- (30) Yu, B.; Zhang, Q.; Wang, H.; Wang, X.; Wang, H.; Wang, D.; Wang, H.; Snyder, G. J.; Chen, G.; Ren, Z. F. Thermoelectric Property Studies on Thallium-Doped Lead Telluride Prepared by Ball Milling and Hot Pressing. *J. Appl. Phys.* **2010**, *108* (1), 016104.

- (31) Ma, Y.; Hao, Q.; Poudel, B.; Lan, Y.; Yu, B.; Wang, D.; Chen, G.; Ren, Z. Enhanced Thermoelectric Figure-of-Merit in p-Type Nanostructured Bismuth Antimony Tellurium Alloys Made from Elemental Chunks. *Nano Lett.* **2008**, *8* (8), 2580–2584.
- (32) Perumal, S.; Roychowdhury, S.; Negi, D. S.; Datta, R.; Biswas, K. High Thermoelectric Performance and Enhanced Mechanical Stability of P-Type  $\text{Ge}_{1-x}\text{Sb}_x\text{Te}$ . *Chem. Mater.* **2015**, *27* (20), 7171–7178.
- (33) Zhang, Q.; Liao, B.; Lan, Y.; Lukas, K.; Liu, W.; Esfarjani, K.; Opeil, C.; Broido, D.; Chen, G.; Ren, Z. High Thermoelectric Performance by Resonant Dopant Indium in Nanostructured SnTe. *Proc. Natl. Acad. Sci.* **2013**, *110* (33), 13261–13266.
- (34) Kuznetsova, L. A.; Kuznetsov, V. L.; Rowe, D. M. Thermoelectric Properties and Crystal Structure of Ternary Compounds in the  $\text{Ge}(\text{Sn,Pb})\text{Te}-\text{Bi}_2\text{Te}_3$  Systems. *J. Phys. Chem. Solids* **2000**, *61* (8), 1269–1274.
- (35) Shelimova, L. E.; Karpinsky, O. G.; Kretova, M. A.; Avilov, E. S.; Fleurial, J. P. Crystal Structure and Thermoelectric Properties of the Mixed Layered Compounds of the  $(\text{GeTe})_m(\text{Bi}_2\text{Te}_3)_m$  Homologous Series. In *XVI International Conference on Thermoelectrics, 1997. Proceedings ICT '97*; 1997; pp 481–484.
- (36) Perumal, S.; Roychowdhury, S.; Biswas, K. High Performance Thermoelectric Materials and Devices Based on GeTe. *J. Mater. Chem. C* **2016**, *4* (32), 7520–7536.
- (37) Lee, J. K.; Oh, M. W.; Kim, B. S.; Min, B. K.; Lee, H. W.; Park, S. D. Influence of Mn on Crystal Structure and Thermoelectric Properties of GeTe Compounds. *Electron. Mater. Lett.* **2014**, *10* (4), 813–817.
- (38) Sootsman, J. R.; Kong, H.; Uher, C.; D'Angelo, J. J.; Wu, C.-I.; Hogan, T. P.; Caillat, T.; Kanatzidis, M. G. Large Enhancements in the Thermoelectric Power Factor of Bulk PbTe at High Temperature by Synergistic Nanostructuring. *Angew. Chemie Int. Ed.* **2008**, *47* (45), 8618–8622.
- (39) Zhang, L.; Wang, J.; Cheng, Z.; Sun, Q.; Li, Z.; Dou, S. Lead-Free SnTe-Based Thermoelectrics: Enhancement of Thermoelectric Performance by Doping with Gd/Ag. *J. Mater. Chem. A* **2016**, *4* (20), 7936–7942.
- (40) Inayat, S. B.; Rader, K. R.; Hussain, M. M. Nano-Materials Enabled Thermoelectricity from Window Glasses. *Sci Rep* **2012**, *2*.
- (41) Li, Y.; Li, D.; Qin, X.; Yang, X.; Liu, Y.; Zhang, J.; Dou, Y.; Song, C.; Xin, H. Enhanced Thermoelectric Performance through Carrier Scattering at Heterojunction Potentials in

- BiSbTe Based Composites with  $\text{Cu}_3\text{SbSe}_4$  Nano-inclusions. *J. Mater. Chem. C* **2015**, 3 (27), 7045–7052.
- (42) LaLonde, A. D.; Pei, Y.; Snyder, G. J. Reevaluation of  $\text{PbTe}_{1-x}\text{I}_x$  as High Performance N-Type Thermoelectric Material. *Energy Environ. Sci.* **2011**, 4 (6), 2090–2096.
- (43) Hsu, K. F.; Loo, S.; Guo, F.; Chen, W.; Dyck, J. S.; Uher, C.; Hogan, T.; Polychroniadis, E. K.; Kanatzidis, M. G. Cubic  $\text{AgPb}_m\text{SbTe}_{2+m}$ : Bulk Thermoelectric Materials with High Figure of Merit. *Science* **2004**, 303 (5659), 818–821.
- (44) Bali, A.; Wang, H.; Snyder, G. J.; Mallik, R. C. Thermoelectric Properties of Indium Doped  $\text{PbTe}_{1-y}\text{Se}_y$  Alloys. *J. Appl. Phys.* **2014**, 116 (3), 033707.





# **Chapter 4**

**Effect of Processing Route on the Thermoelectric Performance of**

**CuPb<sub>18</sub>SbTe<sub>20</sub>**





## 4.1 Introduction

Lead tellurides are one of the most studied and earliest known class of TE materials.<sup>1</sup> Several strategies, some of them mentioned earlier in Chapter 1, have successfully been employed on PbTe based compounds to maximize their performance. Most notably, Kanatzidis' group<sup>2</sup> made a breakthrough in 2004, when a material of composition  $\text{AgPb}_{18}\text{SbTe}_{20}$ , abbreviated as LAST (Lead-Antimony-Silver-Tellurium), reportedly exhibited a high  $zT \sim 2.2$  at 800 K. Independent studies based on different synthesis routes of this LAST alloy have reported consistently high  $zT$ s in the range of  $\sim 1.3 - 1.5$  at around 700 K.<sup>3-6</sup> Various explanations for the very high  $zT$  of LAST alloys have been proposed: (i) the presence of coherent, endotaxially embedded nanoscopic inhomogeneity or nanodots (rich in Ag and Sb) in the PbTe matrix and/or modulated nanostructures and atomic ordering;<sup>2,7-11</sup> and (ii) to the presence of resonance states in the electronic band structure of bulk PbTe when Ag and Sb partially substitute for Pb and/or sizable band-gap widening caused by nanodopant induced lattice strains.<sup>12-14</sup>

Spark Plasma Sintering (SPS), involving direct Joule heating of electrically conductive dies (usually graphite), has been widely used to produce nanostructured materials, especially for thermoelectrics.<sup>15,16</sup> More recently, a novel sintering process called 'Flash-SPS', a derivative of the flash and SPS sintering techniques, has generated a lot of interest as it has been shown to improve the thermoelectric performance of Mg-Si based materials.<sup>17</sup> During SPS, the heating rate typically used is  $\sim 100$  °C/min, whereas the flash technique employs thermal runaway to achieve ultra-fast sintering with heating rate as high as  $\sim 10,000$  °C/min, producing dense materials in a matter of few seconds.<sup>18-20</sup> An additional advantage of the flash-SPS method is that no preheating is required when conducting samples are used. Though flash sintering has been used predominantly to process high temperature ceramics like SiC,<sup>20,21</sup>  $\text{ZrO}_2$ ,<sup>18</sup>  $\text{ZrB}_2$ ,<sup>22</sup> it has not been tried on many thermoelectric materials. For this reason, the flash-SPS process, infact its variant 'Hybrid flash-SPS' was used in this work to prepare PbTe based materials. More details regarding this recently developed 'Hybrid flash-SPS' technique (F. Gucci *et al.*<sup>23</sup>) are provided in the materials and methods section (synthesis part).

Building on the work by Kanatzidis *et al.*,<sup>2</sup> several papers have been published on replacing one or more of the elements in LAST alloys in an attempt to improve  $zT$ , such as substituting K for Ag to make  $n$ -type  $\text{K}_{1-x}\text{Pb}_{m+\delta}\text{Sb}_{1+\gamma}\text{Te}_{m+2}$  ( $zT \sim 1.6$  at 750 K),<sup>24</sup> Na for Ag to make  $p$ -type  $\text{Na}_{1-x}\text{Pb}_m\text{Sb}_y\text{Te}_{m+2}$  ( $zT \sim 1.7$  at 650 K),<sup>25</sup> La for Sb to make  $n$ -type  $\text{Ag}_n\text{Pb}_{1-x}\text{La}_x\text{Te}$  ( $zT \sim 1.2$  at 720 K),<sup>26</sup> Bi for Sb to make  $n$ -type  $\text{AgPb}_m\text{BiTe}_{m+2}$  ( $zT \sim 0.5$  at 650 K),<sup>27</sup> and Cl codoped with Se for Te to make  $n$ -type

$\text{AgPb}_m\text{SbSe}_{(m+2)-x}\text{Cl}_x$  ( $zT \sim 1.3$  at 873 K).<sup>28</sup> However, one obvious substitution has not yet been investigated, replacing Ag with chemically similar coinage metals like Cu or Au. Cu substitution is particularly interesting due to its much lower cost.

This chapter presents a comparison between the thermoelectric properties of nanostructured LAST alloys (as reported by Kanatzidis *et al.*<sup>2</sup>) and those of its Cu counterpart, *i.e.*,  $\text{CuPb}_{18}\text{SbTe}_{20}$ , examining experimental and theoretical aspects. For a more complete understanding on the effect of synthesis conditions on the thermoelectric properties of  $\text{CuPb}_{18}\text{SbTe}_{20}$ , samples were synthesized by many different routes, namely: (i) slow cooling of the melt; (ii) rapid quenching; (iii) Spark Plasma Sintering; and (iv) Hybrid flash-SPS. Additionally, first-principles calculations were carried out in order to understand the differences in the physical properties and electronic band structures of  $\text{AgPb}_{18}\text{SbTe}_{20}$  and  $\text{CuPb}_{18}\text{SbTe}_{20}$ . DFT calculations were also extended to the gold clusters ( $\text{AuPb}_{18}\text{SbTe}_{20}$ ) to convey a comprehensive picture of the influence of group-11 transition metals on the thermoelectric behavior of  $\text{MPb}_{18}\text{SbTe}_{20}$  ( $M = \text{Cu, Ag, Au}$ ).

## 4.2 Materials and Methods

### 4.2.1 Reagents

Pb (Strem Chemicals, 5N), Sb (Alfa Aesar, 5N), Cu (Alfa Aesar, 5N) and Te (JGI, 5N) were used for synthesis without any further purification.

### 4.2.2 Synthesis

In this work, several different processing routes were investigated, however, the first step (synthesis) was common to all of the processing routes. Samples of  $\text{CuPb}_{18}\text{SbTe}_{20}$  were synthesized using the vacuum-sealed tube melt processing. Stoichiometric amounts of the starting elements of Cu, Pb, Sb and Te were introduced into a silica tube. The tube was prepared by cleaning with hydrofluoric (HF) acid and distilled water, then dried under vacuum. The ampules were sealed under a vacuum of  $10^{-6}$  Torr, then placed in a rocking furnace and slowly heated to 1223 K over a period of 12 hours, then held at that temperature for 15 hours. Four different batches of samples were prepared, the first two were produced directly from the molten material, followed by: (i) cooling the melt to room temperature over a period of 18 hours (samples denoted as 'SS'); (ii) rapidly quenching the tube in water, followed by annealing at 973 K for 8 hours (denoted as 'MQ'). The other two batches

used the material produced by method (i), which was crushed and milled. The powders were then (iii) consolidated by Spark Plasma sintering, SPS (FCT Systeme GmbH) at 673 K (heating rate  $\sim 80$  °C/min) for 5 mins (holding time) under an axial pressure of 85 MPa; and (iv) consolidated by 'Hybrid' Flash-SPS processing, where the powders were sintered at 800 K with no holding time and a heating rate of  $\sim 10,000$  °C/min (heated from 293 – 800 K in 3 seconds) under an axial pressure of 80 MPa. Typically during a Flash-SPS process, the green compact was sandwiched between two graphite punches without a die and inserted in between the pistons of the SPS furnace.<sup>17</sup> But the 'Hybrid Flash-SPS' processing route is a variant of the originally developed Flash-SPS method, involving the use of a thin, low thermal inertia metal die to contain the TE powder during sintering.<sup>23</sup> The schematics of the experimental set-up and the current flow paths for SPS (graphite punches and die), Flash-SPS (graphite punches and no die) and Hybrid Flash-SPS (graphite punches and a thin walled stainless steel die) configurations are depicted in Figure 4.1. Additional information are provided in Table 4.1. Highly dense disc-shaped pellets were obtained with theoretical densities of 100% for SPS and  $\sim 98\%$  for Hybrid Flash-SPS. The obtained ingots and sintered discs were cut and polished to the required shapes and dimensions for various thermoelectric measurements.

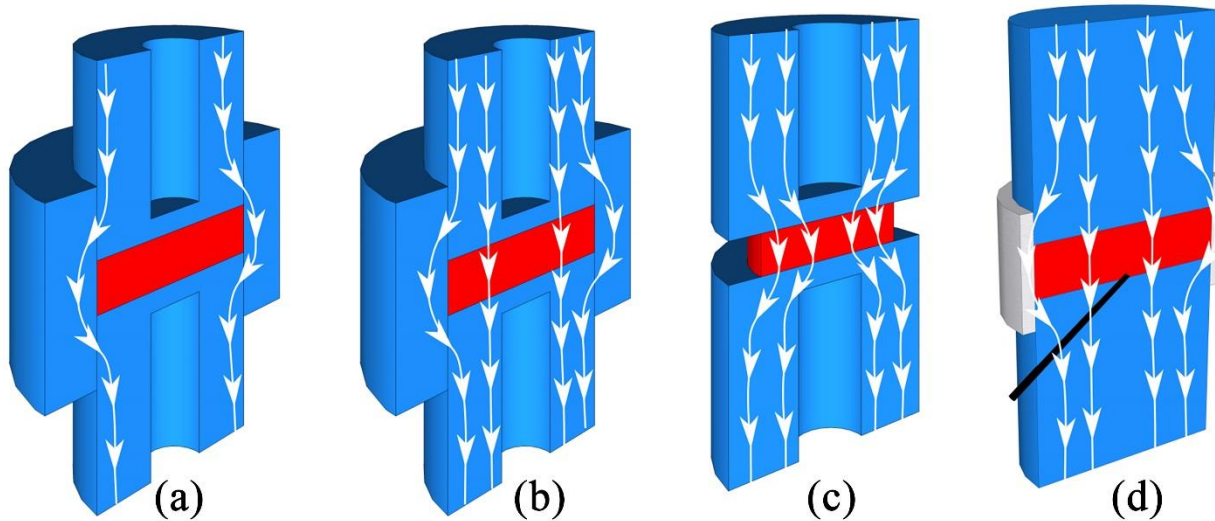


**Figure 4.1** Flow of current in different sintering configurations - (a, b) In SPS set-up (with graphite punches and die) for high and low resistive samples, (c) Flash-SPS (graphite punches and no die), and (d) Hybrid Flash-SPS (graphite punches and a thin walled stainless steel die) configurations. Additional details pertaining to each configuration are presented in Table 4.1.

**Table 4.1** Details pertaining to different sintering configurations (as observed in Figure 4.1).

Configurations	Figure (a)	Figure (b)	Figure (c)	Figure (d)
Description / Notation	SPS, graphite punches and die	SPS, graphite punches and die	Flash-SPS, graphite punches and no die	Hybrid Flash-SPS, graphite punches and a <u>thin walled stainless steel die</u>
Sample Resistivity	> 100 $\mu\Omega\text{m}$	< 10 $\mu\Omega\text{m}$	< 10 $\mu\Omega\text{m}$	< 10 $\mu\Omega\text{m}$
Sample Current Density	< 10 A/cm <sup>2</sup>	10 – 400 A/cm <sup>2</sup>	> 400 A/cm <sup>2</sup>	> 400 A/cm <sup>2</sup>
Typical Heating Rate	~ 100 °C/min		~ 10,000 °C/min	

The results presented in this chapter as ‘flash’ are achieved by using configuration (d) – ‘Hybrid Flash-SPS’ processing.

### 4.2.3 Computational Procedures

Density functional theory (DFT) geometry optimizations of  $\text{MPb}_{18}\text{SbTe}_{20}$  (M = Cu, Ag, Au) were carried out with the *CASTEP16.1*<sup>29</sup> code using the generalized gradient approximation (GGA) in the parameterization of PBE functional.<sup>30</sup> In order to simulate a stoichiometry relevant to  $\text{MPb}_{18}\text{SbTe}_{20}$  compounds, a supercell was considered from the cubic cell of the PbTe structure. Several supercells were tested and a 1 x 1 x 5 supercell was chosen, since it was the simplest supercell that correctly predicted semiconducting behavior and was the most stable one among the supercells that were considered. In this supercell, the Sb atom lies at the origin, whereas the group-11 metal lies at the next nearest neighboring site. Previous theoretical studies demonstrated that the Ag-Sb pair stabilizes the structure when it forms the nearest neighbor in the PbTe matrix.<sup>14</sup> Therefore, M and Sb atoms were located in the same layer normal to the [0 0 1] direction, and separated by five Pb layers. Cell parameters and atomic positions were both relaxed. All ultra-soft pseudopotentials were generated using the OTF generator included in the program. The cut-off energy for plane-waves was set at 500 eV. The electronic wave function was sampled with 110 *k*-points in the first Brillouin zone using the Monkhorst-Pack method.<sup>31</sup> For the electronic band structures, the full-potential linearized augmented plane wave (FLAPW) approach was used, as implemented in the *WIEN2K* code.<sup>32</sup> Since

GGA exchange-correlation functionals are known to underestimate experimental band gaps, the modified Becke-Johnson (mBJ) functional proposed by Tran and Blaha was utilized.<sup>33</sup> This functional yields band gaps with an accuracy similar to hybrid functional or GW methods, but at a considerably reduced computational effort. A plane wave cut-off corresponding to  $R_{\text{MT}}K_{\text{max}} = 7$  was used. The radial wave functions inside the non-overlapping muffin-tin spheres were expanded up to  $l_{\text{max}} = 12$ . The charge density was Fourier expanded up to  $G_{\text{max}} = 12 \text{ \AA}^{-1}$ . Total energy convergence was achieved with a Brillouin zone (BZ) integration mesh of 500  $k$ -points.

The carrier effective mass ( $m^*$ ) was computed for each sample using a single parabolic band model<sup>34,35</sup> and the measured room temperature Seebeck coefficient ( $S$ ) and carrier concentration ( $n$ ). The chemical potential ( $\mu$ ) was estimated using equation (4.1) with  $\lambda = 0$  (acoustic-phonon scattering), where  $F_j(\mu)$  is the Fermi integrals given by equation (4.2). The hole effective mass can then be determined from equation (4.3), as given below,

$$S = \frac{k_B}{e} \left\{ \frac{(2 + \lambda)F_{1+\lambda}(\mu)}{(1 + \lambda)F_{\lambda}(\mu)} - \mu \right\} \quad (4.1)$$

$$F_j(\mu) = \int_0^{\infty} \frac{\xi^j d\xi}{1 + e^{(\xi - \mu)}} \quad (4.2)$$

$$m^* = \frac{\hbar^2}{2k_B T} \left[ \frac{n}{4\pi F_{1/2}(\mu)} \right]^{2/3} \quad (4.3)$$

Transport properties were computed using a semi-classical approach. The electronic transport coefficients for  $\text{MPb}_{18}\text{SbTe}_{20}$  ( $M = \text{Cu, Ag, Au}$ ) were calculated using the Boltzmann Transport Equation (BTE) and the constant scattering time and the rigid band structure approximation,<sup>36,37</sup> as implemented in the *BoltzTrap-1.2.5* code.<sup>38</sup> 5000  $k$ -points were used in the BZ to compute the band derivatives for the transport calculations.

## 4.3 Results and Discussion

### 4.3.1 Structural Analysis

Powder XRD patterns of all the samples of  $\text{CuPb}_{18}\text{SbTe}_{20}$  are shown in Figure 4.2. Sharp peaks indicate the polycrystalline nature of the phases. The majority of the patterns were consistent with the cubic NaCl-type PbTe structure ( $Fm-3m$ ). In the case of the slow cooled sample (SS), a few minor peaks from secondary phases of  $\text{Sb}_2\text{Te}_3$  (trigonal,  $R-3m$ ) and  $\text{Cu}_2\text{Te}$  (hexagonal,  $P3m1$ ) were present. The presence of these weak secondary reflections can be attributed to the low solubility of Sb and Cu

in  $\text{PbTe}$ .<sup>39-41</sup> The absence of any secondary phase in the SPS and the flash samples shows that the equilibrium solubility can be exceeded by rapid cooling.

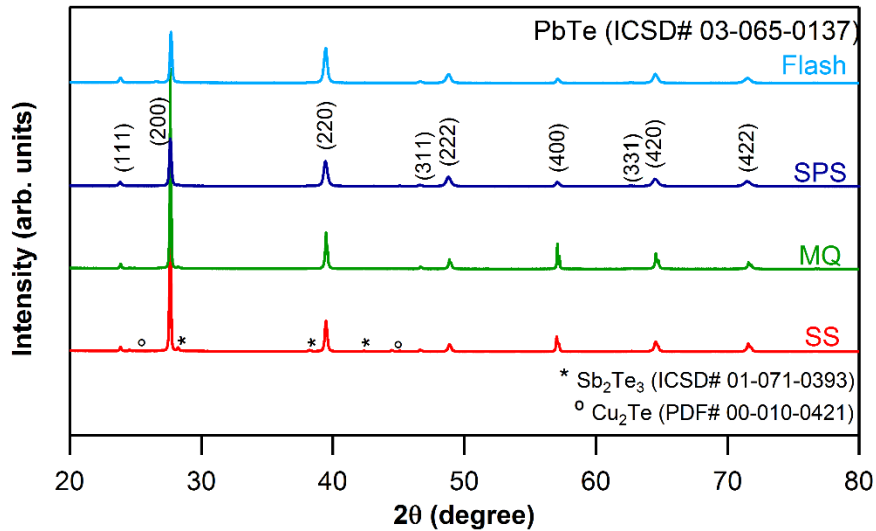


**Figure 4.2** XRD patterns for different  $\text{CuPb}_{18}\text{SbTe}_{20}$  samples. For convenience, the Hybrid Flash-SPS sample is simply referred as 'flash' in all the figure captions in this chapter.

The lattice parameter values for all the samples are given in Table 4.2. The Cu-substituted samples ( $\text{CuPb}_{18}\text{SbTe}_{20}$ ) had smaller lattice parameter values compared to the literature on  $\text{AgPb}_{18}\text{SbTe}_{20}$ . This is unsurprising given the smaller atomic radius of Cu compared to Ag.

**Table 4.2** Lattice parameter values for the samples of composition  $\text{CuPb}_{18}\text{SbTe}_{20}$  prepared by different synthesis routes and  $\text{AgPb}_{18}\text{SbTe}_{20}$ .

Composition	Synthesis Route	Sample Notation	Lattice parameter, $a$ (Å)
$\text{CuPb}_{18}\text{SbTe}_{20}$	Slow cooling	SS	6.4525(8)
	Melt quenching	MQ	6.4499(5)
	Spark Plasma Sintering	SPS	6.4542(3)
	Hybrid Flash-Spark Plasma Sintering	Hybrid Flash-SPS (in text) or 'Flash' (in figures)	6.4536(4)
$\text{AgPb}_{18}\text{SbTe}_{20}$	Any synthesis route	LAST	6.46 <sup>27</sup> , 6.54 <sup>11</sup>

### 4.3.2 Thermal Transport Properties

The temperature-dependent total thermal conductivity ( $\kappa_{\text{tot}}$ ) is presented in Figure 4.3.a. All of the  $\text{CuPb}_{18}\text{SbTe}_{20}$  samples showed relatively similar thermal conductivity, with strong negative temperature dependence. The copper substitution altered very little the thermal conductivity compared to  $\text{AgPb}_{18}\text{SbTe}_{20}$ ,<sup>2</sup> however, there were some differences due to the different synthesis routes.

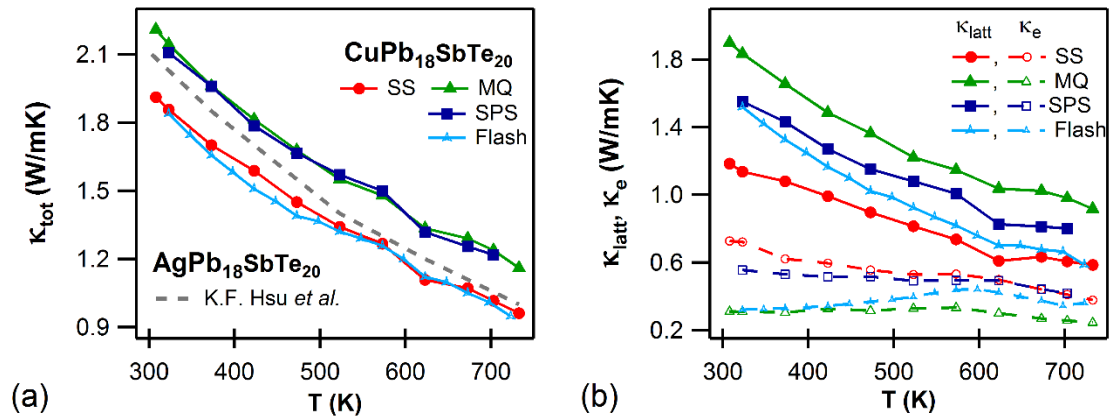


**Figure 4.3** Thermal transport properties - (a) comparison of the total thermal conductivities,  $\kappa_{\text{tot}}$  of different  $\text{CuPb}_{18}\text{SbTe}_{20}$  samples vs  $\text{AgPb}_{18}\text{SbTe}_{20}$  (b) lattice,  $\kappa_{\text{latt}}$  and electronic,  $\kappa_e$  contributions to thermal transport of different  $\text{CuPb}_{18}\text{SbTe}_{20}$  samples. The solid lines in the Figure 4.3.b represent  $\kappa_{\text{latt}}$  and the dashed lines represent  $\kappa_e$ .

The calculated temperature-dependent Lorenz numbers for all the samples were in the range of  $1.68 \times 10^{-8}$  to  $1.97 \times 10^{-8} \text{ W}\Omega\text{K}^{-2}$  (Annexure 4, Figure A4.4) and are lower than the metallic limit of  $2.45 \times 10^{-8} \text{ W}\Omega\text{K}^{-2}$ . The  $\text{CuPb}_{18}\text{SbTe}_{20}$  samples exhibited a low lattice thermal contribution of  $< 1 \text{ W/mK}$  at high temperatures (above 650 K), as shown in Figure 4.3.b.  $\kappa_{\text{latt}}$  for the slow cooled (SS) sample and the sintered samples (both SPS and flash) were somewhat lower than for the sample prepared by rapid quenching of the melt (MQ). Both the slow cooled (SS) and the flash sintered samples demonstrated an ultra-low  $\kappa_{\text{latt}} \sim 0.58 \text{ W/mK}$  at 700 K, which is comparable with literature values of LAST alloys prepared by different techniques.<sup>4,6,27</sup> The low  $\kappa_{\text{latt}}$  values of  $\text{AgPb}_{18}\text{SbTe}_{20}$  in the literature were widely reported to be due to the effect of phonon scattering. The scattering defects have been hypothesized to be either the presence of strain fields or endotaxially embedded nanodots (rich in Ag and Sb) in the PbTe matrix. These precipitates are strongly dependent on the annealing



conditions and synthesis routes used.<sup>2,7-11</sup> To shed some light on the reasons for the origin of ultra-low  $\kappa_{\text{latt}}$  in  $\text{CuPb}_{18}\text{SbTe}_{20}$  samples, a detailed TEM analysis was carried out to examine their nanostructure. The slow cooled (SS) sample was chosen for the TEM study, as it exhibits the lowest  $\kappa_{\text{latt}}$  in the entire temperature range from 300 – 725 K.

### 4.3.3 Nano and Microstructural Investigation

Figure 4.4.a is a typical low-resolution image of  $\text{CuPb}_{18}\text{SbTe}_{20}$  (SS), and it shows a distribution of Cu-rich nanoprecipitates with a uniform size range of 20-30 nm in the PbTe matrix. Besides these nano-inclusions, there was also a high number density of dislocations (Figure 4.4.b), which are known to scatter phonons via distinct mechanisms.<sup>42</sup> These nanoscale artifacts obviously generate constraints and deformation of the PbTe lattice, as seen from the high contrast image in Figure 4.4.c. Each micro/nano scale feature can potentially scatter different frequency heat-carrying phonons. For instance, atomic-scale solid-solution point defects scatter short wavelength phonons with a mean free path (MFP) of less than 5 nm, nanoscale precipitates scatter medium MFP phonons between 5 – 100 nm, and mesoscale grain structures scatter long MFP phonons of 0.1 – 1.0  $\mu\text{m}$ .<sup>43</sup> At room temperature, 86% of  $\kappa_{\text{latt}}$  of PbTe is found to be contributed by phonon modes with MFP of less than 100 nm and their contribution is increased to 93% at 600 K.<sup>44</sup> In  $\text{CuPb}_{18}\text{SbTe}_{20}$  (SS), the Cu-rich nanoprecipitates (20 - 30 nm) are to likely dominate phonon scattering due to the large mass difference between the precipitate and the matrix, especially targeting the medium wavelength phonons.<sup>43,45</sup> The SAED pattern oriented along the  $\{-110\}$  plane of the lattice, with an aperture including reflections from the precipitates and the matrix region, as shown in Figure 4.4.d, was indexed based on a cubic rock-salt PbTe structure. The exact composition of the individual precipitates could not be determined owing to their overlap with the matrix. Figures 4.4.e and 4.4.f suggested the presence of different kinds of precipitate-matrix interface (both coherent and incoherent interfaces) in this sample. Except for the presence of weak reflections from the Cu-rich precipitates in the aperture for diffraction, no extra reflections or split spots were observed, suggesting an endotaxial arrangement of the precipitates within the matrix.<sup>46,47</sup> The high resolution image along the  $\langle 002 \rangle$  direction, as in Figure 4.4.e, shows a coherent interface (no disorder) between the nano-inclusion and the matrix. But in some other regions (Figure 4.4.f), not much noticeable high magnification contrasts from the precipitates or their strain field was observed, so it is possible that the precipitates might also have a random orientation. The dark contrast inclusion (Figure 4.4.f) clearly showed two domains – the one which showed Moiré fringes (upper domain, noted as 'i') and

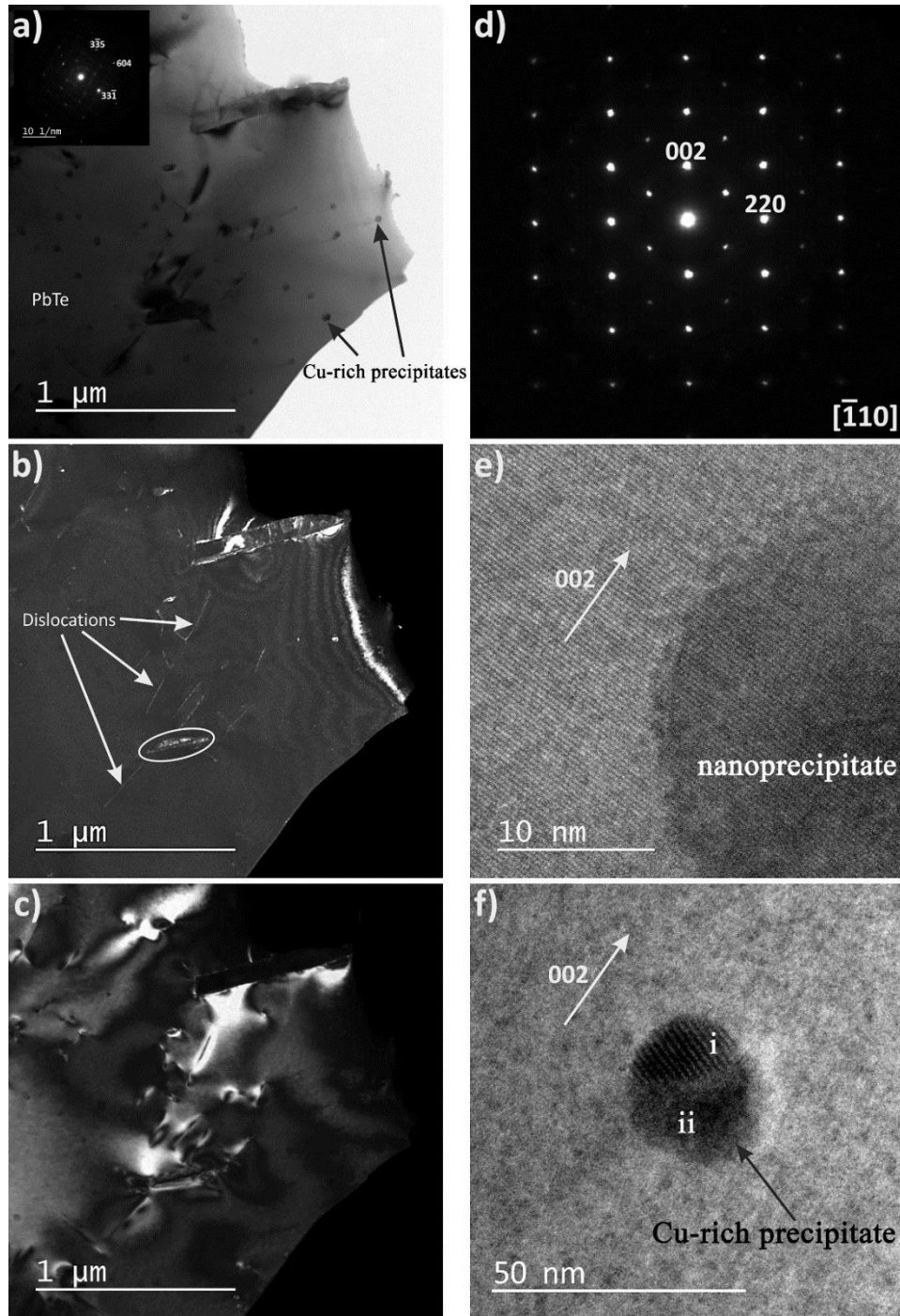


**Figure 4.4** a) Bright Field (BF) image of  $\text{CuPb}_{18}\text{SbTe}_{20}$  (SS) thin sample. Inset shows the diffraction pattern, b) Dark Field (DF) image made with the  $\langle 3-35 \rangle$  reflection depicting the dislocations, c) DF image made with the  $\langle 33-1 \rangle$  reflection, d) Diffraction pattern along the  $[-110]$  zone axis, e) High magnification image showing the interface between the PbTe matrix and a Cu-rich nano-inclusion. f) High magnification image of the nanoprecipitate showing Moiré fringes in the upper part of the dark contrast domain (marked as i).

the other which did not present any particular contrast (lower domain, noted as 'ii'). Moiré artifacts were observed at the interface (incoherent) as some of the precipitates were not oriented in the same  $\langle 002 \rangle$  direction of the PbTe lattice. These fringes were formed at the interface between two sets of lattice planes (overlap of matrix and nano-scale precipitates). A strong Moiré pattern, like that seen in Figure 4.4.f, required the two lattices to have a small relative rotating angle and very similar periodicity,<sup>48</sup> which provides sufficient atomic strains to scatter the heat carrying phonons. Hence it is clear that the medium mean free path phonons, the dominant contributor to the lattice thermal conductivity, are scattered by the nanoscale dislocations together with the high density of Cu-rich nano-inclusions.

The high number of nanoprecipitate-matrix interfaces produces an effective barrier to heat carrying phonon transport in the bulk sample.<sup>43</sup> Inhomogeneities within the matrix effectively reduce the lattice contribution, particularly when there is atomic reorganization to form thermodynamically stable nanostructures.<sup>42</sup> All these factors contributed for the  $\text{CuPb}_{18}\text{SbTe}_{20}$  sample prepared by slow cooling for manifesting an ultra-low  $\kappa_{\text{latt}}$ . The same can also be said for the relatively low  $\kappa_{\text{latt}}$  of the sintered samples, as current assisted sintering is widely known to produce nanostructured materials.<sup>15,49,50</sup> However, melt quenching normally suppresses the formation of nano-precipitates. This is because there is typically insufficient time for atoms of any species to diffuse towards a nucleation point before the material has cooled enough (diffusion is too slow). This explains why the MQ sample had the highest lattice thermal transport (Figure 4.3.b) because it has the least nano-precipitates.

Though the size of the precipitates, type of precipitate-matrix interfaces, and other nanoscale features for  $\text{CuPb}_{18}\text{SbTe}_{20}$  reported in this work are different from those reported for  $\text{AgPb}_{18}\text{SbTe}_{20}$  by Kanatzidis *et al.*,<sup>2,7,12,27</sup> the resulting thermal properties are very similar. This implies that one of these mechanisms could dominate the behavior, the others being far less important.

On the basis of the processing route, the  $\text{CuPb}_{18}\text{SbTe}_{20}$  samples also had notable differences in microstructure as well as nanostructure. In fact, the different microstructures clearly explain the difference in lattice conductivity between the hybrid flash-SPS sample and the conventional SPS sample (Figure 4.3.b). The microstructure of the SPS sample (Figure 4.5.a) shows a transgranular failure with large grains (100  $\mu\text{m}$ ) and no porosity, whereas the microstructure of the hybrid flash-SPS sample (Figure 4.5b, c) contains a large number of smaller grains (1 - 10  $\mu\text{m}$ ) surrounding larger grains (50  $\mu\text{m}$ ), with porosity between the smaller grains. The ultra-fast sintering rate helped to reduce the grain growth during flash processing, at the expense of some micro-porosity. Reducing the grain size enhances the boundary scattering of heat carrying phonons at the intergrain region.

Usually, the nanostructures produced by conventional processing techniques can scatter the majority of the short and medium MPF phonons, but a notable fraction of the remaining phonons (long MFP phonons) are not scattered. The mesoscale grain structures obtained by hybrid flash-SPS processing can also scatter those long wavelength phonons. Thus hybrid flash-SPS processing produced a ‘multi-scale hierarchical architectures’ (panoscopic approach),<sup>43</sup> which can scatter a broader spectrum of heat carrying phonons. This, along with the presence of micro-voids in their microstructure helps reducing the thermal conductivity of flash sintered sample.

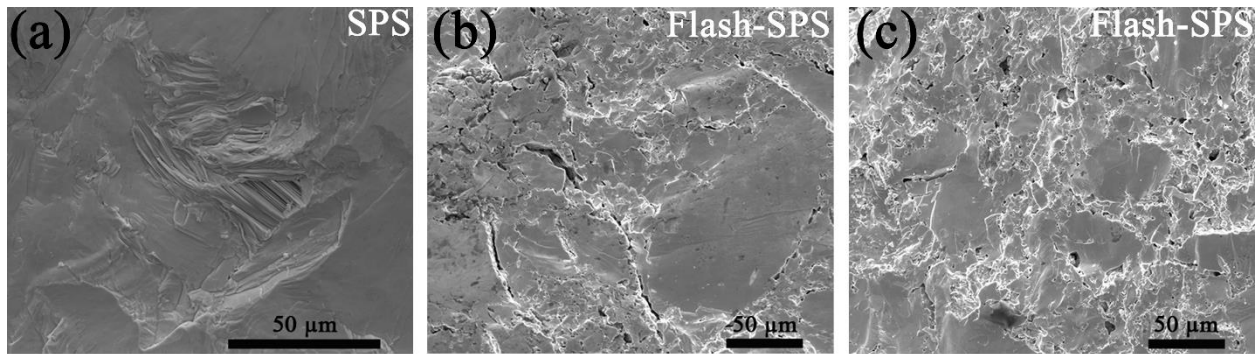


**Figure 4.5** SEM images showing the microstructures at the fractured surface of (a) SPS sample with larger grains, (b, c) hybrid flash-SPS sample showing micro-porous voids and a mixture of larger and smaller grains.

#### 4.3.4 Electrical Transport Properties

The results from the Hall measurement tabulating carrier concentration,  $n$ , and mobility,  $\mu$ , are presented in Table 4.3. For all of the samples, including the literature on  $\text{AgPb}_{18}\text{SbTe}_{20}$ , the Hall voltage was negative, meaning electrons were the major charge carriers ( $n$ -type).

The electrical transport properties are presented in Figure 4.6. The electrical conductivity of the Cu-doped samples were almost comparable with the Ag-doped LAST alloys (Figure 4.6.a), especially at higher temperatures as the Cu samples were less temperature dependent. At room temperature, the SS and SPS samples had higher  $\sigma$  compared to the MQ sample due to their higher charge carrier mobilities. The higher  $\sigma$  might also have been due to additional contributions from the more conductive secondary phases, especially in the SS sample. The transport properties of the constituent phases in the SS sample are tabulated in Annexure 4 (Table A4.1). The electrical and thermal transport are also known to undergo a significant change due to the nanoscale precipitation.<sup>42,51</sup> Due to its low charge carrier density, the hybrid flash-SPS sample exhibited a lower

$\sigma$ . Due to ultra-fast heating and short processing time during hybrid-flash SPS, there is not much sufficient time for the sample to recrystallize and the dopants may not be evenly distributed and possibly might have moved from their lattice positions. Such changes in the electronic crystal structural arrangements might affect the charge carrier density. More in-depth studies are required to understand the mechanisms and the structural changes that happens during flash sintering. It must be noted that the carrier mobility was not significantly affected by flash processing (Table 4.3). In the MQ sample, the significant drop in electron mobility could be explained by alloy scattering;<sup>52</sup> the electrons are scattered by the lattice distortions produced by the solid-solution atoms. The MQ sample had the fewest precipitates, so it must have had most solute atoms in the lattice. Though the carrier concentration was comparably high, the low carrier mobility caused the MQ sample to exhibit low  $\sigma$ . This explains the low  $\kappa_e$  value for MQ sample, as  $\kappa_e$  was calculated from  $\sigma$ .

**Table 4.3** Hall measurement results (at ~300 K) of carrier concentration, mobility, and computed effective mass for MPb<sub>18</sub>SbTe<sub>20</sub> (M = Cu, Ag) samples.

Sample	Carrier Concentration, $n$ (cm <sup>-3</sup> )	Carrier Mobility, $\mu_c$ (cm <sup>2</sup> V <sup>-1</sup> s <sup>-1</sup> )	Effective mass, $m^*$ ( $m_e$ )
SS	1.75 x 10 <sup>19</sup>	695.85	0.30
MQ	2.32 x 10 <sup>19</sup>	180.31	0.41
SPS	1.51 x 10 <sup>19</sup>	523.54	0.39
Hybrid Flash-SPS	0.58 x 10 <sup>19</sup>	520.89	0.24
LAST (Han <i>et al.</i> <sup>27</sup> )	0.54 x 10 <sup>19</sup>	778	0.24

The continuous increase of the Seebeck coefficient for CuPb<sub>18</sub>SbTe<sub>20</sub>, as shown in Figure 4.6.b, and the monotonic decrease in  $\sigma$  with increasing temperature suggests degenerate semiconducting behavior. The negative Seebeck coefficient of all the samples confirmed that  $n$ -type charge carriers dominated. The  $S$ -values were coherent with the carrier densities obtained from the Hall measurement, *i.e.*, congruent with  $S \propto 1/n$  relation. The only exception to this relation was the MQ sample, however such anomalous changes in the carrier density are difficult to explain and have been observed in few such materials.<sup>53-55</sup> There was no significant variation in  $S$ -values between the samples of CuPb<sub>18</sub>SbTe<sub>20</sub> prepared by SS, MQ and SPS. But the thermopower of the flash sample fares well compared to the other synthesis routes and it reaches a maximum thermopower of ~ -200  $\mu$ V/K at 700 K. The low  $\sigma$  of MQ sample affected considerably its thermoelectric power factor, as shown in

Figure 4.6.d. At temperatures  $> 450$  K, the flash sample outperformed the others in power factor values. It seems likely that the hybrid flash-SPS sintering process helps to achieve a better trade-off between  $\sigma$  and  $S$ , as well as optimizing the charge carrier density and mobility. An intriguing aspect is that the  $S$ -values for  $\text{CuPb}_{18}\text{SbTe}_{20}$  were much lower (almost 50% reduction at high temperature) than those for its Ag counterpart, *i.e.*,  $\text{AgPb}_{18}\text{SbTe}_{20}$ , as illustrated in Figure 4.6.c. In order to understand the origin of the huge difference in  $S$ -values between  $\text{CuPb}_{18}\text{SbTe}_{20}$  and  $\text{AgPb}_{18}\text{SbTe}_{20}$ , despite both compositions having comparable electrical and thermal conductivities, DFT calculations were performed to compare their band structures to get a clearer picture.

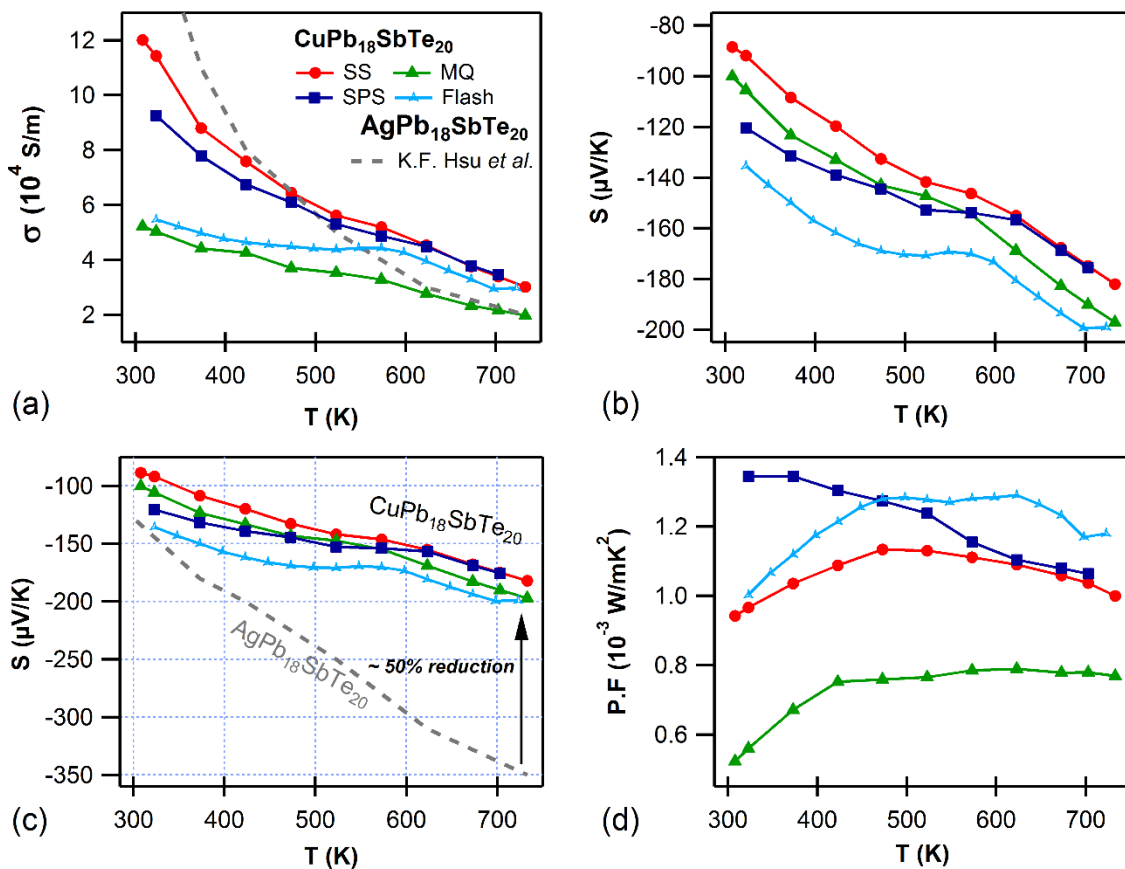


**Figure 4.6** Temperature-dependent electrical transport properties for  $\text{CuPb}_{18}\text{SbTe}_{20}$  prepared by different synthesis routes - (a) electrical conductivity ( $\sigma$ ), (b) Seebeck coefficient ( $S$ ), (c) comparison of thermopower with  $\text{AgPb}_{18}\text{SbTe}_{20}$ , and (d) Power factor ( $\text{PF} = S^2\sigma$ ). Color code legend in (a) applies to all the plots here.

### 4.3.5 Investigation of Electronic Band Structures

The band structures of the  $\text{MPb}_{18}\text{SbTe}_{20}$  ( $M = \text{Ag}, \text{Cu}$ ) compounds along the high symmetry lines of the Brillouin zone (supercell) are shown in Figure 4.7. Both compounds were computed to be semiconductor in character and were almost identical. They both exhibited a direct energy band gap. This energy band gap ( $E_g$ ) between the valence and the conduction bands was much smaller for  $\text{CuPb}_{18}\text{SbTe}_{20}$  (about 0.02 eV) when compared to that of  $\text{AgPb}_{18}\text{SbTe}_{20}$  (0.1 eV). The computed band structure and the  $E_g$  value for the LAST alloy are in agreement with the literature.<sup>27</sup> Goldsmid and Sharp<sup>56</sup> derived an approximate expression for the maximum thermopower of a band material,  $S_{\text{max}} \approx E_g/2eT_{\text{max}}$ , where  $e$  is the elemental charge and  $T_{\text{max}}$  is the absolute temperature where the maximum thermopower is observed. According to this relation, the Seebeck coefficient of a semiconducting compound varies as the band gap, and this explains the reason for a decreased thermopower for  $\text{Cu}_{18}\text{SbTe}_{20}$  ( $E_g \sim 0.02$  eV) when compared to  $\text{AgPb}_{18}\text{SbTe}_{20}$  ( $E_g \sim 0.1$  eV). The energy differences between the heavy and light bands were lower in  $\text{Cu}_{18}\text{SbTe}_{20}$  (Figure 4.7), and this explains the reason for higher effective masses (Table 4.3) for  $\text{Cu}_{18}\text{SbTe}_{20}$  when compared to  $\text{AgPb}_{18}\text{SbTe}_{20}$ .

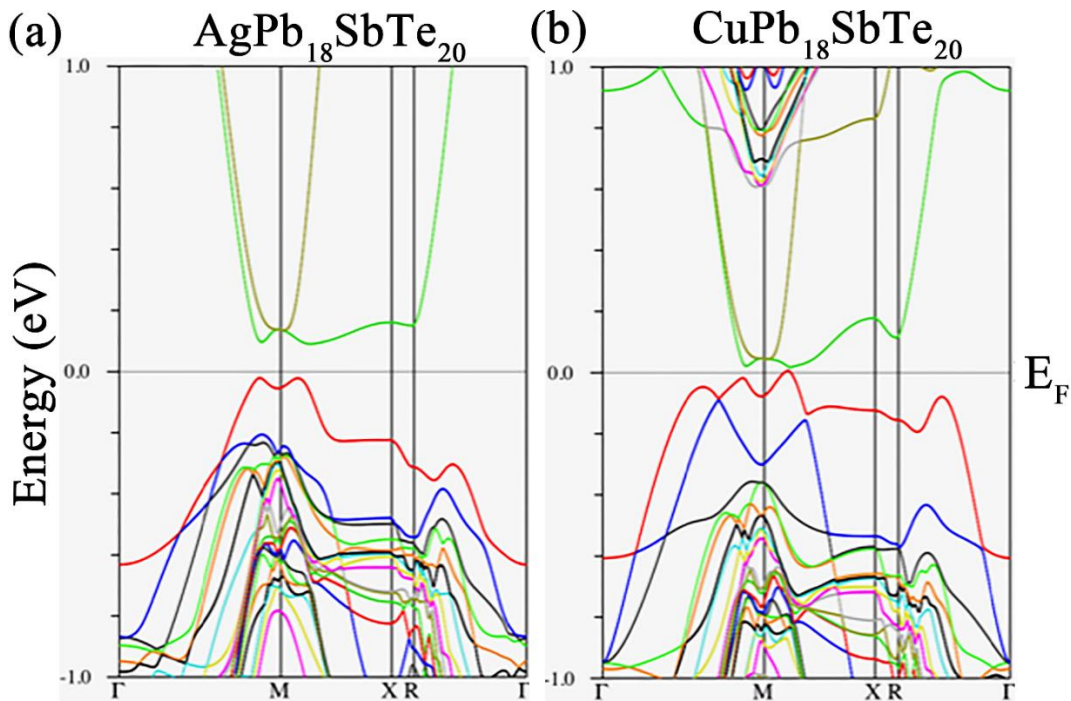


**Figure 4.7** Electronic band structures computed for  $\text{MPb}_{18}\text{SbTe}_{20}$  ( $M = \text{Cu}, \text{Ag}$ ). To compare the band structures, the same supercell was considered. Coordinates of high symmetry  $k$ -points:  $\Gamma = (0, 0, 0)$ ,  $M = (\frac{1}{2}, \frac{1}{2}, 0)$ ,  $X = (0, \frac{1}{2}, 0)$ , and  $R = (0, \frac{1}{2}, \frac{1}{2})$ .

Isoelectronic  $\text{MPb}_{18}\text{SbTe}_{20}$  ( $M = \text{Cu}, \text{Ag}, \text{Au}$ ) compounds were studied in silico. The calculated thermopower (at 300 K and 800 K) as a function of the chemical potential ( $\mu$ ) for  $\text{MPb}_{18}\text{SbTe}_{20}$  ( $M = \text{Cu}, \text{Ag}, \text{Au}$ ) is sketched in Figure 4.8. The computed Seebeck coefficient, at both lower and higher temperatures, for  $\text{CuPb}_{18}\text{SbTe}_{20}$  was lower than for  $\text{AgPb}_{18}\text{SbTe}_{20}$ , consistent with the findings from their band structures (Figure 4.7) and their experimental results (Figure 4.6.c). To complete the comparison on the coinage series, the computation of the transport properties were extended to the gold analogue as well ( $\text{AuPb}_{18}\text{SbTe}_{20}$ ). For this purpose, the same supercell was considered with Au clusters, as like Cu and Ag. It is noteworthy to mention that, irrespective of the carrier concentration, the Seebeck coefficient was higher for  $\text{AgPb}_{18}\text{SbTe}_{20}$  (at both lower and higher temperatures) compared to its gold and copper congeners, as depicted in Figure 4.8.

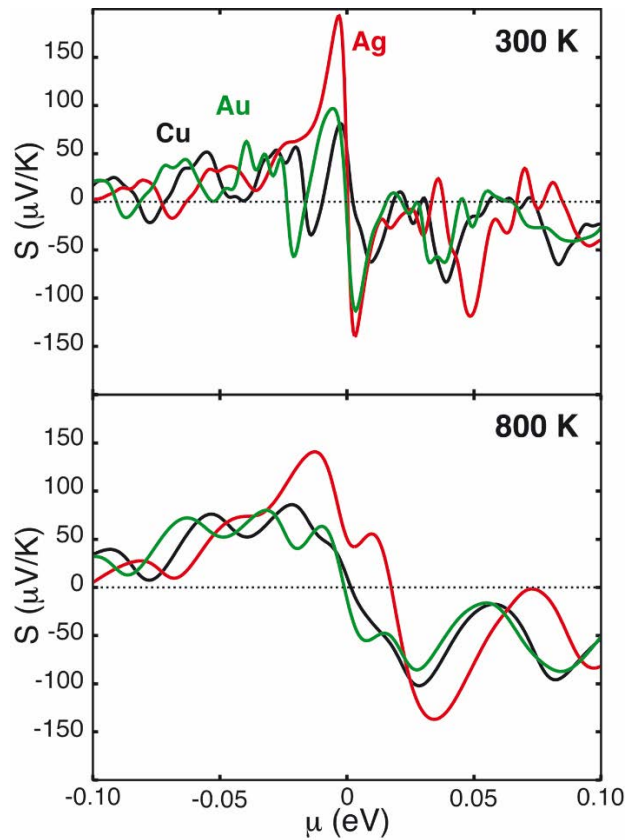


**Figure 4.8** Thermopower as a function of the chemical potential ( $\mu$ ) computed at 300 K (top) and 800 K (bottom) for  $\text{MPb}_{18}\text{SbTe}_{20}$  ( $M = \text{Cu}, \text{Ag}, \text{Au}$ ) models.



### 4.3.6 Thermoelectric Figure of Merit, $zT$

The thermoelectric figure of merit,  $zT$  as a function of temperature is shown in Figure 4.9. The maximum  $zT$  achieved for  $\text{CuPb}_{18}\text{SbTe}_{20}$  is  $\sim 0.9$  at 723 K from the hybrid flash-SPS sample, followed by the SS sample with  $zT \sim 0.8$  at 723 K, while the SPS and MQ samples had slightly lower  $zT$  values of  $\sim 0.6$  at 700 K and  $\sim 0.5$  at 723 K, respectively. The higher  $zT$  for the hybrid flash-SPS samples was due to the increased power factor and decreased thermal conductivity.

It is established that higher the ratio of the carrier mobility to lattice thermal conductivity, the greater the  $zT$ .<sup>57</sup> Normally, there is a trade-off when alloying a material. The lattice thermal conductivity is decreased due to scattering from impurities, but that also reduces the carrier mobility, meaning limited change in  $zT$ . An improvement in  $zT$  for an alloy system occurs only when  $\kappa_{\text{latt}}$  is reduced by a significant factor with little or no degradation of  $\mu$ . The slow cooled sample (SS) and conventional SPS sample exhibit higher  $\mu/\kappa_{\text{latt}}$  ratio, thanks to their precipitate scattering, however their higher carrier concentration reduces their thermopower significantly. But with the hybrid flash-SPS sintering process, we have demonstrated that it is possible to optimize the charge carrier density, and at the same time benefit from the decreased lattice thermal conductivity without significantly affecting the carrier mobility (*i.e.*, higher  $\mu/\kappa_{\text{latt}}$  ratio). Moving forward, the flash technique can potentially be used as a strategic processing route to decouple electrical and thermal transport properties to produce high  $zT$  materials.

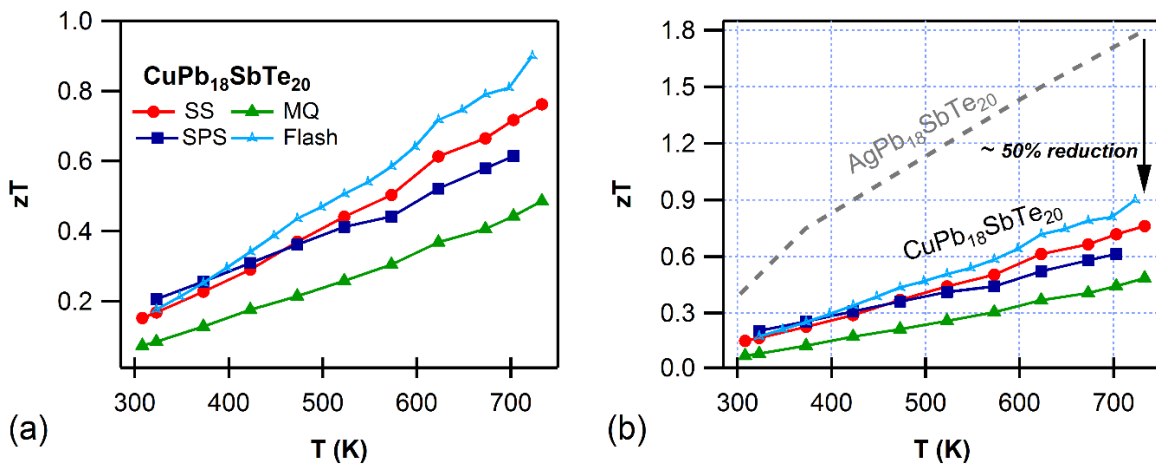


**Figure 4.9** Temperature-dependent thermoelectric figure of merit,  $zT$  – (a) for  $\text{CuPb}_{18}\text{SbTe}_{20}$  samples that were prepared by different synthesis routes, (b) for different  $\text{CuPb}_{18}\text{SbTe}_{20}$  samples vs  $\text{AgPb}_{18}\text{SbTe}_{20}$ .

In any case, the larger picture is that, irrespective of the route of synthesis,  $\text{AgPb}_{18}\text{SbTe}_{20}$  exhibits much higher  $zT$  compared to its Cu-counterpart that is reported in this chapter. The  $zT$  of  $\text{CuPb}_{18}\text{SbTe}_{20}$  at higher temperatures ( $> 700$  K) is more than 50% lower than the  $zT$  of LAST-18 composition, as illustrated in Figure 4.9.b. Such a disparity in  $zT$  is primarily ascribed to differing power factor values, caused primarily by the Seebeck coefficient. Our theoretical analysis, described earlier in this chapter, clearly reveals the rationale for the origin of divergence in the Seebeck coefficient values for  $\text{CuPb}_{18}\text{SbTe}_{20}$  and  $\text{AgPb}_{18}\text{SbTe}_{20}$ .

#### 4.4 Conclusion

In this chapter, we systematically investigated four different routes of synthesizing crystalline samples of  $\text{CuPb}_{18}\text{SbTe}_{20}$ . The thermoelectric properties of the different  $\text{CuPb}_{18}\text{SbTe}_{20}$  samples were compared with their well-studied Ag counterpart, *i.e.*,  $\text{AgPb}_{18}\text{SbTe}_{20}$ . Replacement of Ag by Cu in LAST alloys, despite the differences in their nanoscale architectures, did not significantly affect their thermal conductivity.  $\text{CuPb}_{18}\text{SbTe}_{20}$  exhibited  $\kappa_{\text{tot}}$  values of less than 1.2 W/mK at  $T > 700$  K, comparable with that of  $\text{AgPb}_{18}\text{SbTe}_{20}$ . In particular, both the slow cooled sample and the hybrid flash sintered sample had an ultra-low  $\kappa_{\text{latt}}$  of  $\sim 0.58$  W/mK at 723 K, primarily due to phonon scattering that arose from the presence of nanoscale dislocations together with a high density of Cu-rich nano-inclusions in the SS sample and reduced grain growth (meso-structuring) and porosity of the flash sintered sample. In addition, the electrical conductivities of the  $\text{CuPb}_{18}\text{SbTe}_{20}$  samples were also comparable with that of their Ag counterpart. Hybrid Flash-SPS processing provided a way to achieve a better trade-off between the transport properties by decreasing the carrier concentration and  $\kappa_{\text{latt}}$  without degrading the carrier mobility, thus enabling a higher  $zT \sim 0.9$  at 723 K. However, the replacement of Ag with Cu was found to be detrimental to the overall thermoelectric figure of merit, as the  $zT$  values of  $\text{CuPb}_{18}\text{SbTe}_{20}$ , irrespective of the route of synthesis, were drastically reduced when compared with  $\text{AgPb}_{18}\text{SbTe}_{20}$ . This stems foremost from the fact that the Seebeck coefficient values of  $\text{CuPb}_{18}\text{SbTe}_{20}$  were almost 50% lower than that of  $\text{AgPb}_{18}\text{SbTe}_{20}$ , especially at higher temperatures. The electronic transport coefficients for  $\text{MPb}_{18}\text{SbTe}_{20}$  ( $M = \text{Cu, Ag and Au}$ ) calculated within the Boltzmann transport equation at 300 K and 800 K, also reveal that the thermopower of Ag-doped material outshines that of the Au or Cu-doped ones, consistent with the experimental findings. With the aid of first-principles calculations, we have demonstrated that replacement by isovalent Cu for Ag in LAST alloys significantly modify their electronic band structure by decreasing the energy band gap, which unraveled the rationale for their decreased thermopower.

➤ **Adaptation**

The results presented in this chapter have been published in *Inorganic Chemistry* (ACS). Hence, this chapter is an adaptation from that publication – **B. Srinivasan *et al.*, *Inorg. Chem.* 2018, 57, 12976–12986.**

➤ **Author Contributions**

B.S conceived the project, designed and performed experiments, analyzed the results and wrote the journal manuscript. The hybrid flash-SPS experiments were carried out by B.S during his secondment activity at Nanoforce, London. Francesco Gucci and Dr. Theo Saunders supported B.S during those flash experiments. The DFT computations were performed by Dr. Bruno Fontaine and Prof. Régis Gautier (ISCR Rennes).

## References

- (1) LaLonde, A. D.; Pei, Y.; Wang, H.; Jeffrey Snyder, G. Lead Telluride Alloy Thermoelectrics. *Mater. Today* **2011**, 14 (11), 526–532.
- (2) Hsu, K. F.; Loo, S.; Guo, F.; Chen, W.; Dyck, J. S.; Uher, C.; Hogan, T.; Polychroniadis, E. K.; Kanatzidis, M. G. Cubic  $\text{AgPb}_m\text{SbTe}_{2+m}$ : Bulk Thermoelectric Materials with High Figure of Merit. *Science* **2004**, 303 (5659), 818–821.
- (3) Wang, H.; Li, J.-F.; Nan, C.-W.; Zhou, M.; Liu, W.; Zhang, B.-P.; Kita, T. High-Performance  $\text{Ag}_{0.8}\text{Pb}_{18+x}\text{SbTe}_{20}$  Thermoelectric Bulk Materials Fabricated by Mechanical Alloying and Spark Plasma Sintering. *Appl. Phys. Lett.* **2006**, 88 (9), 092104.
- (4) Zhou, M.; Li, J.-F.; Kita, T. Nanostructured  $\text{AgPb}_m\text{SbTe}_{m+2}$  System Bulk Materials with Enhanced Thermoelectric Performance. *J. Am. Chem. Soc.* **2008**, 130 (13), 4527–4532.
- (5) Kanatzidis, M. G. Nanostructured Thermoelectrics: The New Paradigm? *Chem. Mater.* **2010**, 22 (3), 648–659.
- (6) Pei, J.; Zhang, B.-P.; Li, J.-F.; Liang, D.-D. Maximizing Thermoelectric Performance of  $\text{AgPb}_m\text{SbTe}_{m+2}$  by Optimizing Spark Plasma Sintering Temperature. *J. Alloys Compd.* **2017**.
- (7) Cook, B. A.; Kramer, M. J.; Harringa, J. L.; Han, M.-K.; Chung, D.-Y.; Kanatzidis, M. G. Analysis of Nanostructuring in High Figure-of-Merit  $\text{Ag}_{1-x}\text{Pb}_m\text{SbTe}_{2+m}$  Thermoelectric Materials. *Adv. Funct. Mater.* **2009**, 19 (8), 1254–1259.

- (8) Quarez, E.; Hsu, K.-F.; Pcionek, R.; Frangis, N.; Polychroniadis, E. K.; Kanatzidis, M. G. Nanostructuring, Compositional Fluctuations, and Atomic Ordering in the Thermoelectric Materials  $\text{AgPb}_m\text{SbTe}_{2+m}$ . The Myth of Solid Solutions. *J. Am. Chem. Soc.* **2005**, *127* (25), 9177–9190.
- (9) Ke, X.; Chen, C.; Yang, J.; Wu, L.; Zhou, J.; Li, Q.; Zhu, Y.; Kent, P. R. C. Microstructure and a Nucleation Mechanism for Nanoprecipitates in  $\text{PbTe} - \text{AgSbTe}_2$ . *Phys. Rev. Lett.* **2009**, *103* (14), 145502.
- (10) Perlt, S.; Höche, T.; Dadda, J.; Müller, E.; Bauer Pereira, P.; Hermann, R.; Sarahan, M.; Pippel, E.; Brydson, R. Microstructure Analyses and Thermoelectric Properties of  $\text{Ag}_{1-x}\text{Pb}_{18}\text{Sb}_{1+y}\text{Te}_{20}$ . *J. Solid State Chem.* **2012**, *193*, 58–63.
- (11) Arachchige, I. U.; Wu, J.; Dravid, V. P.; Kanatzidis, M. G. Nanocrystals of the Quaternary Thermoelectric Materials:  $\text{AgPb}_m\text{SbTe}_{m+2}$  ( $m = 1-18$ ): Phase-Segregated or Solid Solutions? *Adv. Mater.* **2008**, *20* (19), 3638–3642.
- (12) Bilc, D.; Mahanti, S. D.; Quarez, E.; Hsu, K.-F.; Pcionek, R.; Kanatzidis, M. G. Resonant States in the Electronic Structure of the High Performance Thermoelectrics  $\text{AgPb}_m\text{SbTe}_{2+m}$ : The Role of Ag-Sb Microstructures. *Phys. Rev. Lett.* **2004**, *93* (14), 146403.
- (13) Zhang, Y.; Ke, X.; Chen, C.; Yang, J.; Kent, P. R. C. Nanodopant-Induced Band Modulation in  $\text{AgPb}_m\text{SbTe}_{2+m}$ -Type Thermoelectrics. *Phys. Rev. Lett.* **2011**, *106* (20), 206601.
- (14) Hazama, H.; Mizutani, U.; Asahi, R. First-Principles Calculations of Ag-Sb Nanodot Formation in Thermoelectric  $\text{AgPb}_m\text{SbTe}_{2+m}$  ( $M=6,14,30$ ). *Phys. Rev. B* **2006**, *73* (11), 115108.
- (15) Biswas, K.; He, J.; Blum, I. D.; Wu, C.-I.; Hogan, T. P.; Seidman, D. N.; Dravid, V. P.; Kanatzidis, M. G. High-Performance Bulk Thermoelectrics with All-Scale Hierarchical Architectures. *Nature* **2012**, *489* (7416), 414–418.
- (16) Chen, Z.-G.; Han, G.; Yang, L.; Cheng, L.; Zou, J. Nanostructured Thermoelectric Materials: Current Research and Future Challenge. *Prog. Nat. Sci. Mater. Int.* **2012**, *22* (6), 535–549.
- (17) Du, B.; Gucci, F.; Porwal, H.; Grasso, S.; Mahajan, A.; Reece, M. J. Flash Spark Plasma Sintering of Magnesium Silicide Stannide with Improved Thermoelectric Properties. *J. Mater. Chem. C* **2017**, *5* (6), 1514–1521.
- (18) Cologna Marco; Rashkova Boriana; Raj Rishi. Flash Sintering of Nanograin Zirconia in  $<5$  s at  $850^\circ\text{C}$ . *J. Am. Ceram. Soc.* **2010**, *93* (11), 3556–3559.
- (19) Yu, M.; Grasso, S.; Mckinnon, R.; Saunders, T.; Reece, M. J. Review of Flash Sintering: Materials, Mechanisms and Modelling. *Adv. Appl. Ceram.* **2017**, *116* (1), 24–60.

- (20) Olevsky, E. A.; Roling, S. M.; Maximenko, A. L. Flash (Ultra-Rapid) Spark-Plasma Sintering of Silicon Carbide. *Sci. Rep.* **2016**, *6*, 33408.
- (21) Grasso, S.; Kim, E.-Y.; Saunders, T.; Yu, M.; Tudball, A.; Choi, S.-H.; Reece, M. Ultra-Rapid Crystal Growth of Textured SiC Using Flash Spark Plasma Sintering Route. *Cryst. Growth Des.* **2016**, *16* (4), 2317–2321.
- (22) Grasso Salvatore; Saunders Theo; Porwal Harshit; Cedillos-Barraza Omar; Jayaseelan Daniel Doni; Lee William E.; Reece Mike John; Fahrenholtz W. Flash Spark Plasma Sintering (FSPS) of Pure  $\text{ZrB}_2$ . *J. Am. Ceram. Soc.* **2014**, *97* (8), 2405–2408.
- (23) Gucci, F.; Saunders, T. G.; Reece, M. J. In-Situ Synthesis of n-Type Unfilled Skutterudite with Reduced Thermal Conductivity by Hybrid Flash-Spark Plasma Sintering. *Scr. Mater.* **2018**, *157*, 58–61.
- (24) Poudeu, P. F. P.; Guéguen, A.; Wu, C.-I.; Hogan, T.; Kanatzidis, M. G. High Figure of Merit in Nanostructured N-Type  $\text{KPb}_m\text{SbTe}_{m+2}$  Thermoelectric Materials. *Chem. Mater.* **2010**, *22* (3), 1046–1053.
- (25) Poudeu, P. F. P.; D'Angelo, J.; Downey, A. D.; Short, J. L.; Hogan, T. P.; Kanatzidis, M. G. High Thermoelectric Figure of Merit and Nanostructuring in Bulk P-Type  $\text{Na}_{1-x}\text{Pb}_m\text{Sb}_y\text{Te}_{m+2}$ . *Angew. Chem. Int. Ed.* **2006**, *45* (23), 3835–3839.
- (26) Ahn, K.; Li, C.; Uher, C.; Kanatzidis, M. G. Improvement in the Thermoelectric Figure of Merit by La/Ag Cosubstitution in PbTe. *Chem. Mater.* **2009**, *21* (7), 1361–1367.
- (27) Han, M.-K.; Hoang, K.; Kong, H.; Pcionek, R.; Uher, C.; Paraskevopoulos, K. M.; Mahanti, S. D.; Kanatzidis, M. G. Substitution of Bi for Sb and Its Role in the Thermoelectric Properties and Nanostructuring in  $\text{Ag}_{1-x}\text{Pb}_{18}\text{MTe}_{20}$  (M = Bi, Sb) ( $x = 0, 0.14, 0.3$ ). *Chem. Mater.* **2008**, *20* (10), 3512–3520.
- (28) Qian Zhang, Y. L. Increased Thermoelectric Performance by Cl Doping in Nanostructured  $\text{AgPb}_{18}\text{SbSe}_{20-x}\text{Cl}_x$ . *Nano Energy* **2013**, *2* (6), 1121–1127.
- (29) Clark, S. J.; Segall, M. D.; Pickard, C. J.; Hasnip, P. J.; Probert, M. I. J.; Refson, K.; Payne, M. C. First Principles Methods Using CASTEP. *Z. Für Krist. - Cryst. Mater.* **2009**, *220* (5/6), 567–570.
- (30) Perdew, J. P.; Burke, K.; Ernzerhof, M. Generalized Gradient Approximation Made Simple. *Phys. Rev. Lett.* **1996**, *77* (18), 3865–3868.
- (31) Monkhorst, H. J.; Pack, J. D. Special Points for Brillouin-Zone Integrations. *Phys. Rev. B* **1976**, *13* (12), 5188–5192.

- (32) Blaha, P.; Schwarz, K.; Madsen, G.; Kvasnicka, D.; Luitz, J. *WIEN2K: An Augmented Plane Wave plus Local Orbitals Program for Calculating Crystal Properties*; Karlheinz Schwarz, Techn. Universität Wien, Austria: Wien, Austria, 2001.
- (33) Tran, F.; Blaha, P.; Schwarz, K. Band Gap Calculations with Becke–Johnson Exchange Potential. *J. Phys. Condens. Matter* **2007**, *19* (19), 196208.
- (34) May, A. F.; Toberer, E. S.; Saramat, A.; Snyder, G. J. Characterization and Analysis of Thermoelectric Transport in N-Type Ba<sub>8</sub>Ga<sub>16-x</sub>Ge<sub>30+x</sub>. *Phys. Rev. B* **2009**, *80* (12), 125205.
- (35) Toberer, E. S.; Zevalkink, A.; Crisosto, N.; Snyder, G. J. The Zintl Compound Ca<sub>5</sub>Al<sub>2</sub>Sb<sub>6</sub> for Low-Cost Thermoelectric Power Generation. *Adv. Funct. Mater.* **2010**, *20* (24), 4375–4380.
- (36) Scheidemantel, T. J.; Ambrosch-Draxl, C.; Thonhauser, T.; Badding, J. V.; Sofo, J. O. Transport Coefficients from First-Principles Calculations. *Phys. Rev. B* **2003**, *68* (12), 125210.
- (37) Madsen, G. K. H. Automated Search for New Thermoelectric Materials: The Case of LiZnSb. *J. Am. Chem. Soc.* **2006**, *128* (37), 12140–12146.
- (38) Madsen, G. K. H.; Singh, D. J. BoltzTraP. A Code for Calculating Band-Structure Dependent Quantities. *Comput. Phys. Commun.* **2006**, *175* (1), 67–71.
- (39) Li, C. C.; Drymiotis, F.; Liao, L. L.; Hung, H. T.; Ke, J. H.; Liu, C. K.; Kao, C. R.; Snyder, G. J. Interfacial Reactions between PbTe-Based Thermoelectric Materials and Cu and Ag Bonding Materials. *J. Mater. Chem. C* **2015**, *3* (40), 10590–10596.
- (40) Srinivasan, B.; Gucci, F.; Boussard-Pledel, C.; Chevire, F.; Reece, M. J.; Tricot, S.; Calvez, L.; Bureau, B. Enhancement in Thermoelectric Performance of N-Type Pb-Deficit Pb-Sb-Te Alloys. *J. Alloys Compd.* **2017**, *729*, 198–202.
- (41) Dow, H. S.; Oh, M. W.; Kim, B. S.; Park, S. D.; Min, B. K.; Lee, H. W.; Wee, D. M. Effect of Ag or Sb Addition on the Thermoelectric Properties of PbTe. *J. Appl. Phys.* **2010**, *108* (11), 113709.
- (42) He, J.; Kanatzidis, M. G.; Dravid, V. P. High Performance Bulk Thermoelectrics via a Panoscopic Approach. *Mater. Today* **2013**, *16* (5), 166–176.
- (43) Zhao, L.-D.; Dravid, V. P.; Kanatzidis, M. G. The Panoscopic Approach to High Performance Thermoelectrics. *Energy Environ. Sci.* **2013**, *7* (1), 251–268.
- (44) Qiu, B.; Bao, H.; Zhang, G.; Wu, Y.; Ruan, X. Molecular Dynamics Simulations of Lattice Thermal Conductivity and Spectral Phonon Mean Free Path of PbTe: Bulk and Nanostructures. *Comput. Mater. Sci.* **2012**, *53* (1), 278–285.
- (45) Zhang, L.; Wang, J.; Cheng, Z.; Sun, Q.; Li, Z.; Dou, S. Lead-Free SnTe-Based Thermoelectrics: Enhancement of Thermoelectric Performance by Doping with Gd/Ag. *J. Mater. Chem. A* **2016**, *4* (20), 7936–7942.

- (46) Biswas, K.; He, J.; Zhang, Q.; Wang, G.; Uher, C.; Dravid, V. P.; Kanatzidis, M. G. Strained Endotaxial Nanostructures with High Thermoelectric Figure of Merit. *Nat. Chem.* **2011**, *3* (2), 160–166.
- (47) Jood, P.; Ohta, M.; Kunii, M.; Hu, X.; Nishiata, H.; Yamamoto, A.; Kanatzidis, M. G. Enhanced Average Thermoelectric Figure of Merit of N-Type PbTe<sub>1-x</sub>I<sub>x</sub>-MgTe. *J. Mater. Chem. C* **2015**, *3* (40), 10401–10408.
- (48) Lo, S.-H.; He, J.; Biswas, K.; Kanatzidis, M. G.; Dravid, V. P. Phonon Scattering and Thermal Conductivity in P-Type Nanostructured PbTe-BaTe Bulk Thermoelectric Materials. *Adv. Funct. Mater.* **2012**, *22* (24), 5175–5184.
- (49) Li, Z.-Y.; Li, J.-F. Fine-Grained and Nanostructured AgPb<sub>m</sub>SbTe<sub>m+2</sub> Alloys with High Thermoelectric Figure of Merit at Medium Temperature. *Adv. Energy Mater.* **2014**, *4* (2), 300937.
- (50) Ning, H.; Mastrorillo, G. D.; Grasso, S.; Du, B.; Mori, T.; Hu, C.; Xu, Y.; Simpson, K.; Maizza, G.; Reece, M. J. Enhanced Thermoelectric Performance of Porous Magnesium Tin Silicide Prepared Using Pressure-Less Spark Plasma Sintering. *J. Mater. Chem. A* **2015**, *3* (33), 17426–17432.
- (51) Girard, S. N.; Schmidt-Rohr, K.; Chasapis, T. C.; Hatzikraniotis, E.; Njegic, B.; Levin, E. M.; Rawal, A.; Paraskevopoulos, K. M.; Kanatzidis, M. G. Analysis of Phase Separation in High Performance PbTe–PbS Thermoelectric Materials. *Adv. Funct. Mater.* **2013**, *23* (6), 747–757.
- (52) Wang, H.; LaLonde, A. D.; Pei, Y.; Snyder, G. J. The Criteria for Beneficial Disorder in Thermoelectric Solid Solutions. *Adv. Funct. Mater.* **2013**, *23* (12), 1586–1596.
- (53) Al Rahal Al Orabi, R.; Mecholsky, N. A.; Hwang, J.; Kim, W.; Rhyee, J.-S.; Wee, D.; Fornari, M. Band Degeneracy, Low Thermal Conductivity, and High Thermoelectric Figure of Merit in SnTe–CaTe Alloys. *Chem. Mater.* **2016**, *28* (1), 376–384.
- (54) Tan, G.; Shi, F.; Doak, J. W.; Sun, H.; Zhao, L.-D.; Wang, P.; Uher, C.; Wolverton, C.; Dravid, V. P.; Kanatzidis, M. G. Extraordinary Role of Hg in Enhancing the Thermoelectric Performance of P-Type SnTe. *Energy Environ. Sci.* **2014**, *8* (1), 267–277.
- (55) Tan, G.; Zhao, L.-D.; Shi, F.; Doak, J. W.; Lo, S.-H.; Sun, H.; Wolverton, C.; Dravid, V. P.; Uher, C.; Kanatzidis, M. G. High Thermoelectric Performance of P-Type SnTe via a Synergistic Band Engineering and Nanostructuring Approach. *J. Am. Chem. Soc.* **2014**, *136* (19), 7006–7017.
- (56) Goldsmid, H. J.; Sharp, J. W. Estimation of the Thermal Band Gap of a Semiconductor from Seebeck Measurements. *J. Electron. Mater.* **1999**, *28* (7), 869–872.

- (57) Wang, J. L.; Wang, H.; Snyder, G. J.; Zhang, X.; Ni, Z. H.; Chen, Y. F. Characteristics of Lattice Thermal Conductivity and Carrier Mobility of Undoped PbSe-PbS Solid Solutions. *J. Phys. Appl. Phys.* **2013**, *46* (40), 405301.





# **Chapter 5**

**Enhancement in Thermoelectric Performance of *n*-type**

**Pb-deficit Pb-Sb-Te Alloys**



## 5.1 Introduction

Advances in recent times show that it is feasible to enhance thermoelectric figure of merit,  $zT$  by a number of approaches,<sup>1-4</sup> many of which are listed in Chapter 1. One such approach is the so called ‘solid solution alloying’, which enables acoustic phonon scattering leading to a decreased lattice thermal conductivity,  $\kappa_{\text{latt}}$ .<sup>5-10</sup> Among several kinds of thermoelectric materials, PbTe has demonstrated a relatively high  $zT$  value ( $zT > 1$ ) at mid-temperature ranges and is one of the most studied material<sup>11</sup> with an array of alloying materials and strategies to optimize its carrier concentration,<sup>12,13</sup> manipulate its band structure<sup>14-19</sup> and to achieve nanostructuring.<sup>6,20-26</sup>

Our investigation of the thermoelectric properties of Pb-deficit  $\text{Pb}_{0.98-x}\text{Sb}_x\text{Te}$  system was motivated by a past study on the *n*-type Pb-deficit  $\text{Pb}_{0.96}\text{Sb}_{0.02}\text{Te}_{1-x}\text{Se}_x$  bulk materials, where a strong reduction of  $\kappa_{\text{latt}}$  and an enhanced  $zT$  was reported.<sup>27</sup> Improvising on that work, where the Sb content was kept fixed while the Se content was varied, herein we try to understand the effect of variation of Sb content on the thermoelectric properties of Se-free Pb-deficit  $\text{Pb}_{0.98-x}\text{Sb}_x\text{Te}$  materials and to compare the performance of these Pb-deficit samples with that of previously reported pristine (stoichiometric)  $\text{Pb}_{1-x}\text{Sb}_x\text{Te}$  compositions.<sup>28</sup> The motivation for this work, also stems from the results from Snyder’s group (Jet Propulsion Laboratory), where they have successfully optimized the thermoelectric performance in La-deficit  $\text{La}_{3-x}\text{Te}_4$  compounds by tuning their cation vacancies (*i.e.*, by the control of carrier concentrations).<sup>29-31</sup> Though several works have been done in the past to exploit the thermoelectric phenomenon in PbTe based alloys, including Sb doped PbTe, not much information is available on the Sb doped, Pb deficient composition ( $\text{Pb}_{0.98}\text{Te}$ ). The choice of Sb was also motivated by the ab-initio calculations of the effect of Sb impurities on the electronic structure of PbTe, which pointed to the presence of resonance states at the bottom of the conduction band and a possible enhancement of the Seebeck coefficient for optimal Sb concentration.<sup>17</sup> Moreover, given the low solubility of Sb in the PbTe lattice,<sup>28</sup> we anticipated a phase separation upon cooling with formation of Sb precipitates embedded in a PbTe matrix. Such precipitates could play a key role in reducing the lattice thermal conductivity through the scattering of mid-wavelength to long wavelength phonons, as they provide an additional phonon scattering mechanism over and above the standard point defect scattering mechanism that typically governs solid solutions.

In this chapter, we report a significant improvement in the thermoelectric performance of Pb-deficit  $\text{Pb}_{0.98-x}\text{Sb}_x\text{Te}$  ( $x = 0.01 - 0.12$ ) samples, when compared to their stoichiometric counterparts, *i.e.*,  $\text{Pb}_{1-x}\text{Sb}_x\text{Te}$ , where is no Pb-deficiency.

## 5.2 Materials and Methods

### 5.2.1 Reagents

Pb (Strem Chemicals, 5N), Sb (Alfa Aesar, 5N), and Te (JGI, 5N) were used for synthesis without any further purification.

### 5.2.2 Synthesis

The samples of  $\text{Pb}_{0.98-x}\text{Sb}_x\text{Te}$  ( $x = 0.01 - 0.12$ ) were synthesized by vacuum sealed-tube melt processing. The ampules with appropriate stoichiometric amounts of high purity starting elements (Pb, Sb and Te) were sealed under a vacuum of  $10^{-6}$  Torr, then placed in a rocking furnace and slowly heated up to 1223 K over a period of 12 hours, then held at that temperature for 12 hours and slowly cooled down to room temperature over 24 hours. The obtained ingots were cut and polished to required shapes and dimensions for various thermoelectric measurements.

## 5.3 Results and Discussion

### 5.3.1 Structural Analysis

Powder XRD patterns of all of the samples are presented in Figure 5.1.a. Sharp peaks indicate the crystalline nature of the phases.

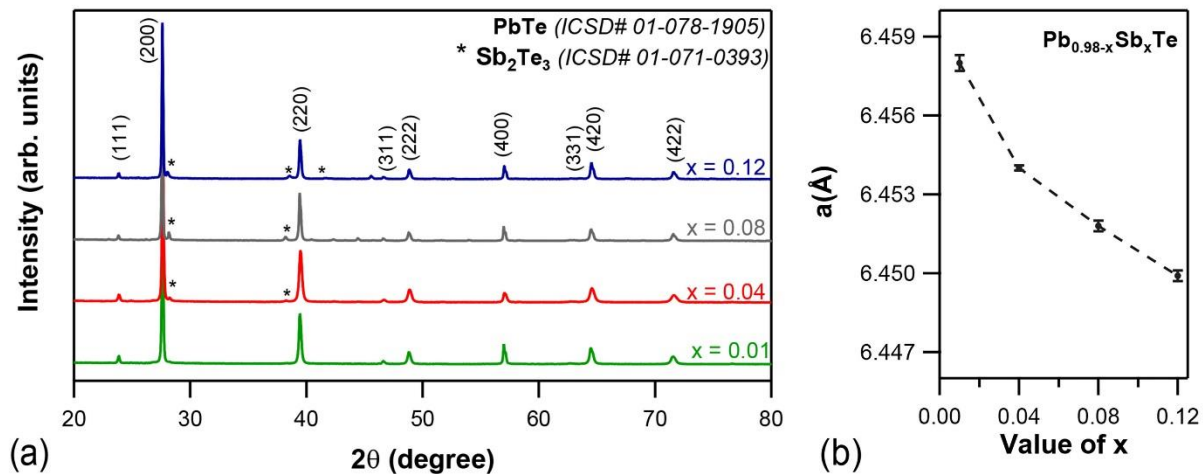


**Figure 5.1** (a) PXRD patterns for  $\text{Pb}_{0.98-x}\text{Sb}_x\text{Te}$  ( $x = 0.01 - 0.12$ ) samples, (b) Lattice parameter,  $a$ , as a function of Sb content.

The main peaks could be indexed to a cubic PbTe phase (ICSD# 01-078-1905).  $\text{Sb}_2\text{Te}_3$  secondary phase was also observed at higher concentrations of the dopant ( $\geq 4$  mol% Sb), indicating a low solubility limit for Sb in PbTe, which is in agreement with the previous reports.<sup>28</sup> Still, the decrease of lattice parameter with Sb content, as shown in Figure 5.1.b, suggests some substitution of smaller  $\text{Sb}^{3+}$  atoms ( $\sim 1.45 \text{ \AA}$ ) for larger  $\text{Pb}^{2+}$  atoms ( $\sim 1.8 \text{ \AA}$ ). The non-linear evolution of the lattice parameter at higher Sb contents indicates that Sb is not fully substituted for Pb in the whole composition range, confirming its low solubility in PbTe.

In the upcoming the sections of this chapter, the Pb-deficit  $\text{Pb}_{0.98-x}\text{Sb}_x\text{Te}$  ( $x = 0.01 - 0.12$ ) samples are shortly denoted as PST-*x*, as listed in Table 5.1.

**Table 5.1** Sample compositions and their notations.

<b><math>\text{Pb}_{0.98-x}\text{Sb}_x\text{Te}</math></b>	<b>Sample</b>
<b>Value of <i>x</i></b>	<b>Acronym</b>
0.01	PST-01
0.04	PST-04
0.08	PST-08
0.12	PST-12

### 5.3.2 Microstructural Analysis

Microstructural data obtained from SEM-EDX analysis are in agreement with the XRD results. SEM images, as in Figure 5.2 and 5.3, portrayed the presence of two distinct regions. On the basis of EDX analysis, the bright region was found to be PbTe phase (major phase) and the dark region to be  $\text{Sb}_2\text{Te}_3$  phase (secondary phase). It must be mentioned that both PbTe and  $\text{Sb}_2\text{Te}_3$  phases contained traces of Sb ( $\sim 3$  at%) and Pb ( $\sim 8$  at%) respectively. This clearly indicates that the solubilities of Sb in PbTe and Pb in  $\text{Sb}_2\text{Te}_3$  are quite limited.

SEM images, as in Figure 5.2, shows the evolution or growth of the secondary phase ( $\text{Sb}_2\text{Te}_3$ ) in the Pb-deficit  $\text{Pb}_{0.98-x}\text{Sb}_x\text{Te}$  ( $x = 0.01, 0.08$  and  $0.12$ ) composition. The microstructure of PST-01, which has the least Sb content (0.01%), shows just a few tiny region of  $\text{Sb}_2\text{Te}_3$  (dark region) that are sparingly distributed in the PbTe matrix (bright region). With the addition of more Sb content to the composition, this  $\text{Sb}_2\text{Te}_3$  secondary phase grows and becomes more dominant. The microstructure

of PST-08 and PST-12, as in Figures 5.2.b and 5.2.c respectively, have more dark domains of  $Sb_2Te_3$  phase, which are embedded within the PbTe matrix.

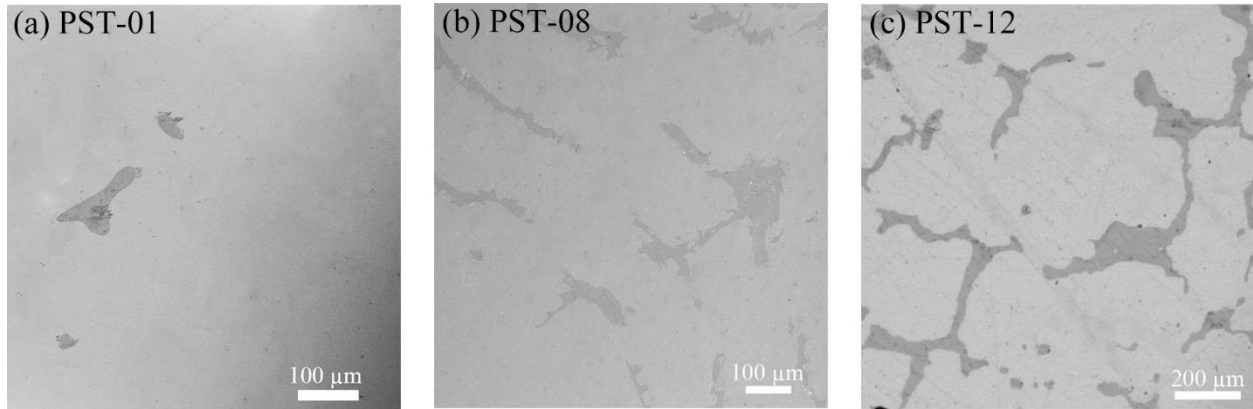


**Figure 5.2** SEM images showing the growth or evolution of  $Sb_2Te_3$  phase in Pb-deficit  $Pb_{0.98-x}Sb_xTe$  ( $x = 0.01, 0.08$  and  $0.12$ ) composition.

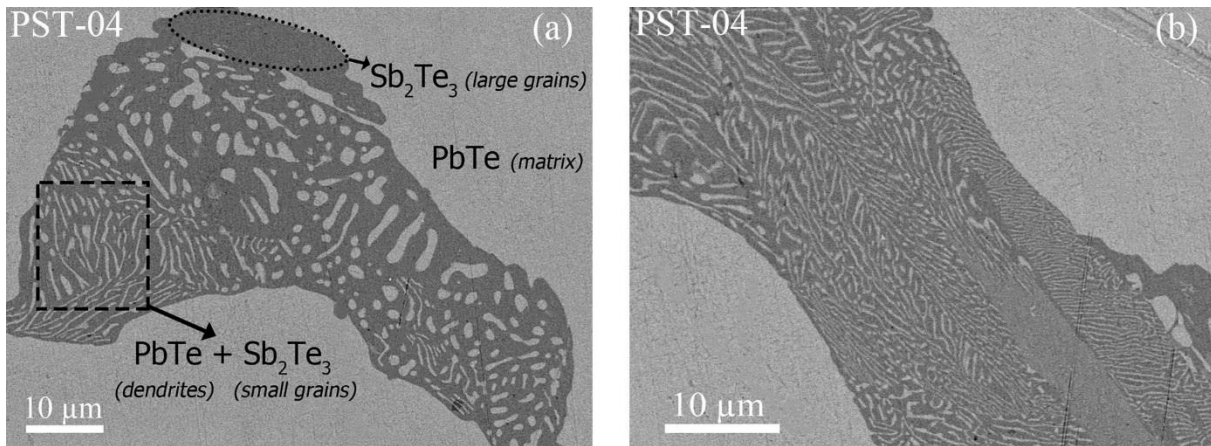


**Figure 5.3** Magnified SEM images of PST-04 sample showing, (a) different domains corresponding to PbTe and  $Sb_2Te_3$  phases, and (b) lamellar growth regions.

The high resolution SEM images for PST-04, as in Figure 5.3, show an intriguing microstructure. In the sea of PbTe matrix, found are the sub-micrometer layers of PbTe and  $Sb_2Te_3$  phases with a lamellar composite microstructure. PbTe phase exhibits a range of microstructural morphologies ranging from globular to dendritic. The  $Sb_2Te_3$  exhibits a bimodal grain size distribution with large and small grained regions. Crystallization of  $Sb_2Te_3$  from the melt results in these large crystals, as shown in Figure 5.3.a by a dotted ellipsoid. The dashed rectangle in Figure 5.3.a shows the dendrites (or platelets) of PbTe within the  $Sb_2Te_3$  crystallite region. Figure 5.3.b

shows a vast lamellar growth region. The different lamellar spacing in different domains can be due to the differences in orientation of individual grains. But it has been reported that such sub-micrometer scale lamellar spacing, growth direction and hence orientation can be controlled via tuning of crystallization conditions like adjusting the time and/or temperature of the transformation process, or by employing heterogeneous nucleation sites.<sup>32,33</sup> Earlier studies carried out on the solidification processes of Pb-Sb-Te alloys had reported such similar microstructures with colonies of lamellar nucleation and growth.<sup>34,35</sup>

The lamellar growth-type microstructure was observed only for PST-04 (Figure 5.3), while PST-08 and PST-12 (Figures 5.2.b and 5.2.c) showed completely grown  $\text{Sb}_2\text{Te}_3$  crystals (larger grain size). From the above microstructural investigation, it seems that  $\text{PbTe-Sb}_2\text{Te}_3$  forms what looks like a binary eutectic, atleast for the lower Sb content.

### 5.3.3 Thermoelectric Properties

The results from Hall measurements tabulating carrier concentration ( $n$ ) and mobility ( $\mu$ ) are presented in Table 5.2. As the Hall voltage was negative in all these samples, electrons are the major charge carriers (*n*-type).

**Table 5.2** Hall measurement results (at 300 K) of carrier concentration,  $n$  and mobility,  $\mu$  for  $\text{Pb}_{0.98-x}\text{Sb}_x\text{Te}$  ( $x = 0.01 - 0.12$ ) samples.

Sample Notation	Carrier concentration, $n$ ( $10^{-19} \text{ cm}^{-3}$ )	Mobility, $\mu$ ( $\text{cm}^2\text{V}^{-1}\text{s}^{-1}$ )
PST-01	0.38	330.9
PST-04	1.99	677.45
PST-08	1.36	518.84
PST-12	3.65	317.34

The electrical transport properties of the different compositions are presented in Figure 5.4 (a) and (b). The negative Seebeck coefficients confirm the *n*-type charge carriers in the samples. The linear increase of the absolute Seebeck coefficient and the monotonic decrease in electrical conductivity with increasing temperature suggests degenerate semiconducting behavior for most of the samples.<sup>36-38</sup> These tendencies, expected due to a slight loss of degeneracy at elevated



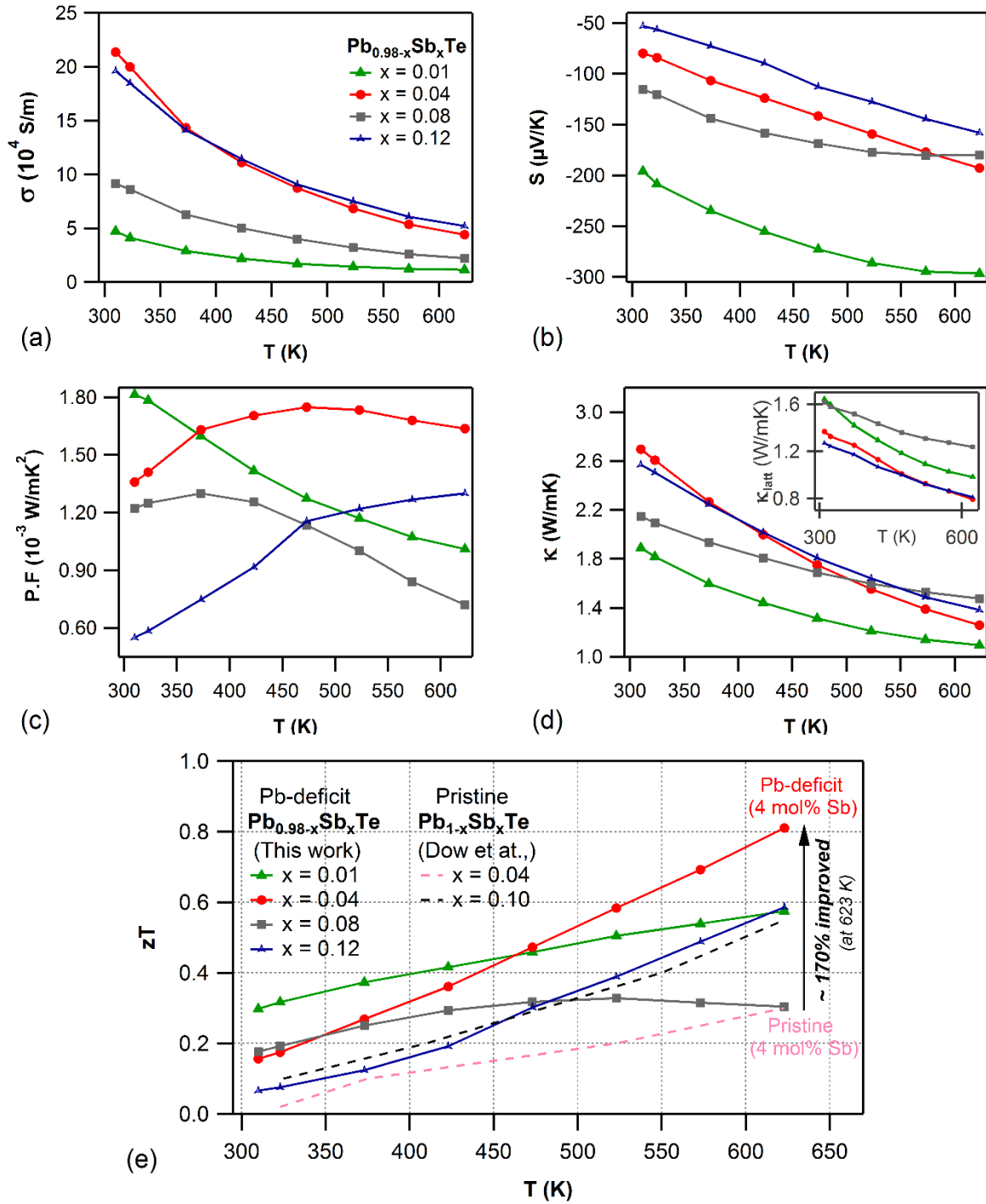


**Figure 5.4** Temperature dependent transport properties – (a) Electrical conductivity,  $\sigma$ ; (b) Seebeck coefficient,  $S$ ; (c) Power Factor, P.F; (d) Total thermal conductivity,  $\kappa$  and Lattice thermal conductivity,  $\kappa_{\text{latt}}$  in the insert; and (e) Figure of merit,  $zT$ .

temperatures,<sup>13</sup> allow the assumption of single band conduction behavior for these samples within the values of carrier density and temperature ranges studied. The carrier density did not follow any specific trend, and such anomalous changes, which are difficult to explain have been reported for other such self-compensated compositions.<sup>39,40</sup> It must also be noted that the carrier densities for these Pb-deficit  $\text{Pb}_{0.98-x}\text{Sb}_x\text{Te}$  compositions are almost one order of magnitude higher than undoped PbTe ( $n \sim 1.11 \times 10^{18} \text{ cm}^{-3}$ ),<sup>13</sup> due to the aliovalent donor doping of  $\text{Sb}^{3+}$  in the  $\text{Pb}^{2+}$  sub-lattices of PbTe, which also explains the reason for increased  $\sigma$  with Sb content. The carrier densities of these Pb-deficit samples are not much different from their stoichiometric counterparts.<sup>28</sup> Interestingly, Sb is known to be an amphoteric dopant depending on its lattice position,<sup>41</sup> which means that in Te-rich PbTe, Sb substitutes for Pb (donor) and in Pb-rich PbTe, Sb substitutes for Te (acceptor). Despite PST-12 having twice the carrier concentration values of PST-08, its carrier charge mobility was reduced by half and this cumulative effect is observed in Figure. 5.4.a, where the  $\sigma$  of both these samples are almost the same.

The *S*-value for these samples at room temperature were in the range of -50 to -200  $\mu\text{V}/\text{K}$ , while at 623 K it reached a maximum of -300  $\mu\text{V}/\text{K}$  for PST-01 and -193  $\mu\text{V}/\text{K}$  for PST-04. The Seebeck results are coherent (inverse proportionality) with the carrier densities obtained by Hall measurements. The thermoelectric power factor,  $\text{P.F} = S^2\sigma$ , as shown in Figure 5.4.c, reaches more than  $1.7 \times 10^{-3} \text{ W}/\text{mK}^2$  at mid-temperature ranges for PST-04, which is on par with other PbTe based materials.<sup>12</sup> The power factor did not vary much beyond 500 K for PST-04 and PST-12, whereas the power factor slumped continuously for PST-01 and PST-08, just like in LAST alloys.<sup>15</sup> The reduction in mobility with increasing Sb content can be attributed to the dopant scattering, arising due to solid solution alloying. PST-04 has an increased carrier mobility, possibly arising from its interesting microstructure (with lamellar growth domains and different grain sizes), as shown in Figure 5.3. The transport properties of the constituent phases (PbTe and  $\text{Sb}_2\text{Te}_3$ ) are tabulated in Annexure 4 (Table A4.1).

The total thermal conductivity of the PST samples and its lattice contributions are presented in Figure 5.4.d. At room temperature, the  $\kappa$  value for the samples varied from 1.9 to 2.9  $\text{W}/\text{mK}$  and the values dropped to lower than 1.5 at 623 K. The lowest value of  $\kappa$  was exhibited by PST-01 (1.1  $\text{W}/\text{mK}$ ), followed by PST-04 (1.25  $\text{W}/\text{mK}$ ), which are lower than other well-known *n*-type PbTe based high performance materials ( $\kappa < 1.5 \text{ W}/\text{mK}$ ) with the similar carrier concentration values.<sup>13</sup> This can be due to the increased disorder created by Sb doping in the self-deficit PbTe lattice, leading to a decreased lattice contribution. Moreover, as reported by Zhu *et al.*,<sup>42</sup> there is also an increase of anharmonic coupling between heat carrying phonons, causing their mutual scattering with

increasing temperature. For PST-04 and PST-12 samples, an ultra-low  $\kappa_{\text{latt}} \sim 0.8$  W/mK was achieved at 623 K, competing well with state-of-the-art TE materials ( $\kappa_{\text{latt}} < 1$  W/mK). At the same temperature (623 K), a much higher  $\kappa_{\text{latt}} \sim 1.5$  W/mK was reported for the stoichiometric  $\text{Pb}_{1-x}\text{Sb}_x\text{Te}$  (for  $x = 0.04$ ) sample.<sup>28</sup>

A plot of the temperature dependent thermoelectric figure of merit,  $zT$  is presented in Figure 5.4.e. In Pb-deficit compositions, the highest  $zT$  of  $\sim 0.81$  was achieved at 623 K for the 4 mol% Sb containing sample. Both the 1 mol% and 12 mol% Sb containing samples exhibited  $zT$  of  $\sim 0.6$  at 623 K. The  $zT$  values of these self-deficit  $\text{Pb}_{0.98-x}\text{Sb}_x\text{Te}$  compositions are much higher than the values for stoichiometric  $\text{Pb}_{1-x}\text{Sb}_x\text{Te}$  compositions reported by Dow *et al.*<sup>28</sup> For instance, the 4 mol% Sb containing Pb-deficit sample with the nominal composition  $\text{Pb}_{0.94}\text{Sb}_{0.04}\text{Te}$  exhibited  $zT \sim 0.81$  at 623 K. While it was reported that, for the same dopant concentration in stoichiometric composition ( $\text{Pb}_{0.96}\text{Sb}_{0.04}\text{Te}$ ), the  $zT$  obtained was only  $\sim 0.3$  at the same temperature.<sup>28</sup> In the case of stoichiometric compositions, the highest value of  $zT$  obtained at 623 K was only  $\sim 0.5$  for  $\text{Pb}_{0.9}\text{Sb}_{0.1}\text{Te}$ , which then reached a maximum of  $\sim 0.6$  at 723 K.

The better TE performance of Pb-deficit samples is due to their better electrical conductivity and lower thermal conductivity when compared to pristine  $\text{Pb}_{1-x}\text{Sb}_x\text{Te}$ .<sup>28</sup> This reduction in  $\kappa$  for self-deficient samples can arise from phonon-scattering at the vacancies, which act as point-defects and suppresses the lattice thermal conductivity by about 90%, when compared with stoichiometric  $\text{Pb}_{1-x}\text{Sb}_x\text{Te}$ .<sup>28</sup> Moreover, the reduced lattice contribution in Pb-deficit PST-04 can also be attributed to its unique microstructure, where the grain size of the precipitates are much lower (and hence better phonon scattering) compared to other compositions.

A high temperature extrapolation of the linear temperature dependence  $zT$  plot of Pb-deficit PST-04 sample ( $\text{Pb}_{0.94}\text{Sb}_{0.04}\text{Te}$ ) indicates a possible  $zT \sim 1.3$  at 850 K.

In future, it may be interesting to study the transport properties of the  $\text{Pb}_{0.94-x}\text{Sb}_{0.04}\text{Te}$  alloy system by varying their cation vacancies ( $x$ ), which may provide a slight valence imbalance in the nominally valence balanced compound.<sup>44</sup> Such carrier optimizations were found to be extremely effective in the very recently reported work (April 2018) on  $\text{Pr}_{3-x}\text{Te}_4$  (from the Jet Propulsion Laboratory), where a high  $zT \sim 1.7$  at 1200 K was achieved for  $\text{Pr}_{2.74}\text{Te}_4$  compound,<sup>45,46</sup> which is a remarkable improvement when compared to the stoichiometric  $\text{Pr}_3\text{Te}_4$  compound ( $zT$  is only  $\sim 0.3$  at 1200 K for stoichiometric  $\text{Pr}_3\text{Te}_4$ ).

## 5.4 Conclusion

To summarize, the crystalline ingots of  $\text{Pb}_{0.98-x}\text{Sb}_x\text{Te}$  were obtained by vacuum sealed-tube melt processing. Reduction in the lattice parameter confirmed the aliovalent donor substitution of  $\text{Sb}^{3+}$  for  $\text{Pb}^{2+}$  in PbTe, but the solubility limit was found to be minimum. These Sb-doped, Pb-deficit, *n*-type samples exhibited high carrier densities ( $\sim 10^{19} \text{ cm}^{-3}$ ). The thermal conductivities were significantly reduced due to the phonon scattering at the vacancies of these Pb-deficit samples. The combination of ultra-low  $\kappa_{\text{latt}} \sim 0.8 \text{ W/mK}$  and power factors in excess of  $1.5 \times 10^{-3} \text{ W/mK}^2$  at around 600 K, for 4 mol% Sb alloying, markedly enhanced the  $zT$  from  $\sim 0.3$  in pristine samples ( $\text{Pb}_{1-x}\text{Sb}_x\text{Te}$ ) to  $\sim 0.81$  in Pb-deficit ( $\text{Pb}_{0.98-x}\text{Sb}_x\text{Te}$ ) samples, an improvement by 170%.

### ➤ **Adaptation**

The results presented in this chapter have been published in the Journal of Alloys and Compounds (Elsevier). Hence, this chapter is an adaptation from that publication – **B. Srinivasan *et al.*, J. Alloys Compd. 2017, 729, 198 – 202.**

### ➤ **Author Contributions**

B.S conceived the project, designed and performed experiments, analyzed the results and wrote the journal manuscript.

## References

- (1) Sootsman, J. R.; Chung, D. Y.; Kanatzidis, M. G. New and Old Concepts in Thermoelectric Materials. *Angew. Chem. Int. Ed.* **2009**, *48* (46), 8616–8639.
- (2) Vaquero, P.; Powell, A. V. Recent Developments in Nanostructured Materials for High-Performance Thermoelectrics. *J. Mater. Chem.* **2010**, *20* (43), 9577–9584.
- (3) Dresselhaus, M. S.; Chen, G.; Tang, M. Y.; Yang, R. G.; Lee, H.; Wang, D. Z.; Ren, Z. F.; Fleurial, J.-P.; Gogna, P. New Directions for Low-Dimensional Thermoelectric Materials. *Adv. Mater.* **2007**, *19* (8), 1043–1053.
- (4) Chen, Z.-G.; Han, G.; Yang, L.; Cheng, L.; Zou, J. Nanostructured Thermoelectric Materials: Current Research and Future Challenge. *Prog. Nat. Sci. Mater. Int.* **2012**, *22* (6), 535–549.

- (5) Wang, H.; LaLonde, A. D.; Pei, Y.; Snyder, G. J. The Criteria for Beneficial Disorder in Thermoelectric Solid Solutions. *Adv. Funct. Mater.* **2013**, *23* (12), 1586–1596.
- (6) Lo, S.-H.; He, J.; Biswas, K.; Kanatzidis, M. G.; Dravid, V. P. Phonon Scattering and Thermal Conductivity in P-Type Nanostructured PbTe-BaTe Bulk Thermoelectric Materials. *Adv. Funct. Mater.* **2012**, *22* (24), 5175–5184.
- (7) Ohta, M.; Biswas, K.; Lo, S.-H.; He, J.; Chung, D. Y.; Dravid, V. P.; Kanatzidis, M. G. Enhancement of Thermoelectric Figure of Merit by the Insertion of MgTe Nanostructures in P-Type PbTe Doped with Na<sub>2</sub>Te. *Adv. Energy Mater.* **2012**, *2* (9), 1117–1123.
- (8) Thermoelectric Properties of In and I Doped PbTe. *J. Appl. Phys.* **2016**, *120* (17), 175101.
- (9) Samanta, M.; Biswas, K. Low Thermal Conductivity and High Thermoelectric Performance in (GeTe)<sub>1-2x</sub>(GeSe)<sub>x</sub>(GeS)<sub>x</sub>: Competition between Solid Solution and Phase Separation. *J. Am. Chem. Soc.* **2017**, *139* (27), 9382–9391.
- (10) Jana, M. K.; Pal, K.; Warankar, A.; Mandal, P.; Waghmare, U. V.; Biswas, K. Intrinsic Rattler-Induced Low Thermal Conductivity in Zintl Type TlInTe<sub>2</sub>. *J. Am. Chem. Soc.* **2017**, *139* (12), 4350–4353.
- (11) LaLonde, A. D.; Pei, Y.; Wang, H.; Jeffrey Snyder, G. Lead Telluride Alloy Thermoelectrics. *Mater. Today* **2011**, *14* (11), 526–532.
- (12) Pei, Y.; Gibbs, Z. M.; Gloskovskii, A.; Balke, B.; Zeier, W. G.; Snyder, G. J. Optimum Carrier Concentration in N-Type PbTe Thermoelectrics. *Adv. Energy Mater.* **2014**, *4* (13), 1400486.
- (13) LaLonde, A. D.; Pei, Y.; Snyder, G. J. Reevaluation of PbTe<sub>1-x</sub>I<sub>x</sub> as High Performance N-Type Thermoelectric Material. *Energy Environ. Sci.* **2011**, *4* (6), 2090–2096.
- (14) Heremans, J. P.; Jovovic, V.; Toberer, E. S.; Saramat, A.; Kurosaki, K.; Charoenphakdee, A.; Yamanaka, S.; Snyder, G. J. Enhancement of Thermoelectric Efficiency in PbTe by Distortion of the Electronic Density of States. *Science* **2008**, *321* (5888), 554–557.
- (15) Han, M.-K.; Hoang, K.; Kong, H.; Pcionek, R.; Uher, C.; Paraskevopoulos, K. M.; Mahanti, S. D.; Kanatzidis, M. G. Substitution of Bi for Sb and Its Role in the Thermoelectric Properties and Nanostructuring in Ag<sub>1-x</sub>Pb<sub>18</sub>MTe<sub>20</sub> (M = Bi, Sb) (x = 0, 0.14, 0.3). *Chem. Mater.* **2008**, *20* (10), 3512–3520.
- (16) Pei, Y.; Shi, X.; LaLonde, A.; Wang, H.; Chen, L.; Snyder, G. J. Convergence of Electronic Bands for High Performance Bulk Thermoelectrics. *Nature* **2011**, *473* (7345), 66–69.
- (17) Bilc, D.; Mahanti, S. D.; Quarez, E.; Hsu, K.-F.; Pcionek, R.; Kanatzidis, M. G. Resonant States in the Electronic Structure of the High Performance Thermoelectrics AgPb<sub>m</sub>SbTe<sub>2+m</sub>: The Role of Ag-Sb Microstructures. *Phys. Rev. Lett.* **2004**, *93* (14), 146403.

- (18) Zhang, Q.; Cao, F.; Liu, W.; Lukas, K.; Yu, B.; Chen, S.; Opeil, C.; Broido, D.; Chen, G.; Ren, Z. Heavy Doping and Band Engineering by Potassium to Improve the Thermoelectric Figure of Merit in P-Type PbTe, PbSe, and PbTe<sub>1-y</sub>Se<sub>y</sub>. *J. Am. Chem. Soc.* **2012**, *134* (24), 10031–10038.
- (19) Roychowdhury, S.; Shenoy, U. S.; Waghmare, U. V.; Biswas, K. Tailoring of Electronic Structure and Thermoelectric Properties of a Topological Crystalline Insulator by Chemical Doping. *Angew. Chem. Int. Ed.* **2015**, *54* (50), 15241–15245.
- (20) Zhao, L. D.; Wu, H. J.; Hao, S. Q.; Wu, C. I.; Zhou, X. Y.; Biswas, K.; He, J. Q.; Hogan, T. P.; Uher, C.; Wolverton, C.; et al. All-Scale Hierarchical Thermoelectrics: MgTe in PbTe Facilitates Valence Band Convergence and Suppresses Bipolar Thermal Transport for High Performance. *Energy Environ. Sci.* **2013**, *6* (11), 3346–3355.
- (21) Jood, P.; Ohta, M.; Kunii, M.; Hu, X.; Nishiate, H.; Yamamoto, A.; Kanatzidis, M. G. Enhanced Average Thermoelectric Figure of Merit of N-Type PbTe<sub>1-x</sub>I<sub>x</sub>-MgTe. *J. Mater. Chem. C* **2015**, *3* (40), 10401–10408.
- (22) Tan, G.; Shi, F.; Hao, S.; Zhao, L.-D.; Chi, H.; Zhang, X.; Uher, C.; Wolverton, C.; Dravid, V. P.; Kanatzidis, M. G. Non-Equilibrium Processing Leads to Record High Thermoelectric Figure of Merit in PbTe–SrTe. *Nat. Commun.* **2016**, *7*, 12167.
- (23) Ahn, K.; Biswas, K.; He, J.; Chung, I.; Dravid, V.; Kanatzidis, M. G. Enhanced Thermoelectric Properties of P-Type Nanostructured PbTe–MTe (M = Cd, Hg) Materials. *Energy Environ. Sci.* **2013**, *6* (5), 1529–1537.
- (24) Li, Z.-Y.; Li, J.-F. Fine-Grained and Nanostructured AgPb<sub>m</sub>SbTe<sub>m+2</sub> Alloys with High Thermoelectric Figure of Merit at Medium Temperature. *Adv. Energy Mater.* **2014**, *4* (2), 300937.
- (25) Poudeu, P. F. P.; D'Angelo, J.; Downey, A. D.; Short, J. L.; Hogan, T. P.; Kanatzidis, M. G. High Thermoelectric Figure of Merit and Nanostructuring in Bulk P-Type Na<sub>1-x</sub>Pb<sub>m</sub>Sb<sub>y</sub>Te<sub>m+2</sub>. *Angew. Chem. Int. Ed.* **2006**, *45* (23), 3835–3839.
- (26) Sootsman, J. R.; Kong, H.; Uher, C.; D'Angelo, J. J.; Wu, C.-I.; Hogan, T. P.; Caillat, T.; Kanatzidis, M. G. Large Enhancements in the Thermoelectric Power Factor of Bulk PbTe at High Temperature by Synergistic Nanostructuring. *Angew. Chem. Int. Ed.* **2008**, *47* (45), 8618–8622.
- (27) Poudeu, P. F. P.; D'Angelo, J.; Kong, H.; Downey, A.; Short, J. L.; Pcionek, R.; Hogan, T. P.; Uher, C.; Kanatzidis, M. G. Nanostructures versus Solid Solutions: Low Lattice Thermal Conductivity and Enhanced Thermoelectric Figure of Merit in Pb<sub>9.6</sub>Sb<sub>0.2</sub>Te<sub>10-x</sub>Se<sub>x</sub> Bulk Materials. *J. Am. Chem. Soc.* **2006**, *128* (44), 14347–14355.

- (28) Dow, H. S.; Oh, M. W.; Kim, B. S.; Park, S. D.; Min, B. K.; Lee, H. W.; Wee, D. M. Effect of Ag or Sb Addition on the Thermoelectric Properties of PbTe. *J. Appl. Phys.* **2010**, *108* (11), 113709.
- (29) May, A. F.; Fleurial, J.-P.; Snyder, G. J. Optimizing Thermoelectric Efficiency in  $\text{La}_{3-x}\text{Te}_4$  via Yb Substitution. *Chem. Mater.* **2010**, *22* (9), 2995–2999.
- (30) May, A. F.; Fleurial, J.-P.; Snyder, G. J. Thermoelectric Performance of Lanthanum Telluride Produced via Mechanical Alloying. *Phys. Rev. B* **2008**, *78* (12), 125205.
- (31) May, A. F. High-Temperature Transport in Lanthanum Telluride and Other Modern Thermoelectric Materials. PhD Thesis, California Institute of Technology, 2010.
- (32) Ikeda, T.; Collins, L. A.; Ravi, V. A.; Gascoin, F. S.; Haile, S. M.; Snyder, G. J. Self-Assembled Nanometer Lamellae of Thermoelectric PbTe and  $\text{Sb}_2\text{Te}_3$  with Epitaxy-like Interfaces. *Chem. Mater.* **2007**, *19* (4), 763–767.
- (33) Ikeda, T.; Ravi, V. A.; Collins, L. A.; Haile, S. M.; Snyder, G. J. Development and Evolution of Nanostructure in Bulk Thermoelectric Pb-Te-Sb Alloys. *J. Electron. Mater.* **2007**, *36* (7), 716–720.
- (34) Ikeda, T.; Ravi, V.; Collins, L. A.; Haile, S. M.; Snyder, G. J. Development of Nanostructures in Thermoelectric Pb-Te-Sb Alloys. In *2006 25th International Conference on Thermoelectrics*; 2006; pp 172–175.
- (35) Ikeda, T.; Haile, S. M.; Ravi, V. A.; Azizgolshani, H.; Gascoin, F.; Snyder, G. J. Solidification Processing of Alloys in the Pseudo-Binary PbTe– $\text{Sb}_2\text{Te}_3$  System. *Acta Mater.* **2007**, *55* (4), 1227–1239.
- (36) Srinivasan, B.; Boussard-Pledel, C.; Dorcet, V.; Samanta, M.; Biswas, K.; Lefèvre, R.; Gascoin, F.; Chevire, F.; Tricot, S.; Reece, M.; et al. Thermoelectric Properties of Highly-Crystallized Ge-Te-Se Glasses Doped with Cu/Bi. *Materials* **2017**, *10* (4), 328.
- (37) Perumal, S.; Roychowdhury, S.; Negi, D. S.; Datta, R.; Biswas, K. High Thermoelectric Performance and Enhanced Mechanical Stability of P-Type  $\text{Ge}_{1-x}\text{Sb}_x\text{Te}$ . *Chem. Mater.* **2015**, *27* (20), 7171–7178.
- (38) Srinivasan, B.; Cui, S.; Prestipino, C.; Gellé, A.; Boussard-Pledel, C.; Ababou-Girard, S.; Trapananti, A.; Bureau, B.; Di Matteo, S. Possible Mechanism for Hole Conductivity in Cu-As-Te Thermoelectric Glasses: A XANES and EXAFS Study. *J. Phys. Chem. C* **2017**, *121* (26), 14045–14050.
- (39) Banik, A.; Shenoy, U. S.; Anand, S.; Waghmare, U. V.; Biswas, K. Mg Alloying in SnTe Facilitates Valence Band Convergence and Optimizes Thermoelectric Properties. *Chem. Mater.* **2015**, *27* (2), 581–587.

- (40) Al Rahal Al Orabi, R.; Mecholsky, N. A.; Hwang, J.; Kim, W.; Rhyee, J.-S.; Wee, D.; Fornari, M. Band Degeneracy, Low Thermal Conductivity, and High Thermoelectric Figure of Merit in SnTe–CaTe Alloys. *Chem. Mater.* **2016**, *28* (1), 376–384.
- (41) Jaworski, C. M.; Tobola, J.; Levin, E. M.; Schmidt-Rohr, K.; Heremans, J. P. Antimony as an Amphoteric Dopant in Lead Telluride. *Phys. Rev. B* **2009**, *80* (12), 125208.
- (42) Zhu, P.; Imai, Y.; Isoda, Y.; Shinohara, Y.; Jia, X.; Zou, G. Carrier-Concentration-Dependent Transport and Thermoelectric Properties of PbTe Doped with Sb<sub>2</sub>Te<sub>3</sub>. *Mater. Trans.* **2005**, *46* (12), 2690–2693.
- (43) Zhu, P.; Imai, Y.; Isoda, Y.; Shinohara, Y.; Jia, X.; Zou, G. Enhanced Thermoelectric Properties of PbTe Alloyed with Sb<sub>2</sub>Te<sub>3</sub>. *J. Phys. Condens. Matter* **2005**, *17* (46), 7319.
- (44) Toberer, E. S.; May, A. F.; Snyder, G. J. Zintl Chemistry for Designing High Efficiency Thermoelectric Materials. *Chem. Mater.* **2010**, *22* (3), 624–634.
- (45) Cheikh, D.; Hogan, B. E.; Vo, T.; Allmen, P. V.; Lee, K.; Smiadak, D. M.; Zevalkink, A.; Dunn, B. S.; Fleurial, J.-P.; Bux, S. K. Praseodymium Telluride: A High-Temperature, High-ZT Thermoelectric Material. *Joule* **2018**, *2* (4), 698–709.
- (46) Kanatzidis, M. G. Pr<sub>3-x</sub>Te<sub>4</sub>: Boost in ZT from Spike at the Fermi Level, but Not before a Good Synthesis. *Joule* **2018**, *2* (4), 583–584.





# **Chapter 6**

**Coinage Metal Insertion on the Thermoelectric Properties of GeTe**

**Solid-State Solutions**



## 6.1 Introduction

Amongst the state-of-the-art thermoelectric materials, the extensively studied PbTe based materials are limited by their toxicity for any practical applications, despite their high figure of merit,  $zT$ . Recently, GeTe based materials have emerged as a clear alternative choice.  $\text{Ge}_{0.87}\text{Pb}_{0.13}\text{Te}$  with/without doping of 3 mol%  $\text{Bi}_2\text{Te}_3$  have reportedly shown an impressive  $zT \sim 2$  in the temperature range 700-773 K due to thermodynamically driven phase segregations and band convergence caused by the donor dopant capability of Bi and Pb.<sup>1-4</sup> However, the concentration of Pb is still quite high (hazardous) in these materials. High  $zT$  values around 750 K have been attained by simple solid-state substitution of Ge in GeTe by 10 mol% Sb ( $zT \sim 1.8$ ),<sup>5</sup> 6 mol% Bi ( $zT \sim 1.3$ ),<sup>6</sup> 5 mol% Mn ( $zT \sim 1.3$ ),<sup>7</sup> 2.5 mol% Sn + 2.5 mol% Pb ( $zT \sim 1.2$ )<sup>8</sup> and 2 mol% In ( $zT \sim 1.3$ ).<sup>9</sup>

Other well established classes of high performance materials involving carrier and phonon engineering of GeTe are the so-called TAGS alloys with composition  $(\text{GeTe})_x(\text{AgSbTe}_2)_{1-x}$  exhibiting  $zT$  values of more than 1.<sup>10-13</sup> Similar values of  $zT$  at mid-temperature ranges (600-800 K) were achieved for different isovalent substitution of TAGS, *e.g.*, substitution of  $\text{Ag}^+$  by  $\text{Li}^+$ ,<sup>14</sup>  $\text{Sb}^{3+}$  by  $\text{In}^{3+}$ ,<sup>15</sup>  $\text{Ge}^{2+}$  by  $\text{Sn}^{2+}$ ,<sup>16</sup> and aliovalent substitution of  $\text{Ge}^{2+}$  by  $\text{Dy}^{+3}$ .<sup>17</sup> Sb and Ag are the principle dopants in TAGS. Several studies have clearly explained the structure and thermoelectric properties of the Ge-Sb-Te system, to emphasize the role of Sb in GeTe,<sup>5,18,19</sup> but not much information is available for the Ge-Ag-Te system. Very recently, Levin<sup>20</sup> reported some interesting findings by correlating variations of the Seebeck coefficient with <sup>125</sup>Te-NMR results on GeTe based materials, where a small concentration of Ge was substituted by Ag and/or Sb. However, there have been no reports on the complete thermoelectric properties ( $zT$  calculations) of  $\text{Ge}_{1-x}\text{Ag}_x\text{Te}$  ( $0 \leq x \leq 0.1$ ) compounds.

The crystal structure of GeTe-based compounds undergoes a second-order phase transition from rhombohedral symmetry (low temperature phase) to cubic symmetry (high temperature phase) at around 700 K.<sup>4,12</sup> Some previous theoretical calculations of density-functional theory (DFT) type carried out on pristine GeTe suggest the presence of a large number of Ge vacancies leading to high concentration of holes in the valence band,<sup>21</sup> and the displacement of Ge and Te atoms as the main reason for the structural transition.<sup>22</sup> Hoang *et al.*<sup>23</sup> performed first-principles calculations by assuming a rock-salt NaCl-structure for GeTe to provide some insights on the role of dopants in TAGS alloys. But the band structure calculations on the rhombohedral phase (below 700 K) of GeTe have not been exploited until recently.<sup>24</sup> The goal of this chapter is to exclusively elucidate the effects of partially replacing Ge by coinage metals ( $M = \text{Cu}, \text{Ag}$  and  $\text{Au}$ ) on the electronic band structure, density of state and electrical and thermal transport properties of the rhombohedral  $\text{Ge}_{1-x}\text{M}_x\text{Te}$  system.

## 6.2 Materials and Methods

### 6.2.1 Reagents

Ge (Umicore, 5N), Te (JGI, 5N) and Ag (Alfa Aesar, 5N) were used for synthesis without involving any further purification process.

### 6.2.2 Synthesis

Samples of  $\text{Ge}_{1-x}\text{Ag}_x\text{Te}$  ( $x = 0.00-0.06$ ) solid-state solutions were synthesized using the vacuum-sealed tube melt processing. Appropriate stoichiometric amounts of the starting elements of Ge, Ag and Te were introduced into a silica tube that had previously been cleaned with hydrofluoric (HF) acid, rinsed with distilled water and dried under vacuum. The ampules were sealed under a vacuum of  $10^{-6}$  Torr, then placed in a rocking furnace and slowly heated up to 1000 °C over a period of 12 hours, then held at that temperature for 15 hours and slowly cooled down to room temperature over 12 hours. The obtained ingots were cut and polished to required shapes and dimensions for various thermoelectric measurements.

### 6.2.3 Computational Procedures

DFT geometry optimizations of  $\text{M}_x\text{Ge}_{1-x}\text{Te}$  ( $x = 0.00, 0.042$ ;  $\text{M} = \text{Cu, Ag, Au}$ ) were carried out with the *CASTEP16.1*<sup>25</sup> code using the generalized gradient approximation Perdew-Burke-Ernzerhof (GGA PBE) functional.<sup>26</sup> Dispersion corrections were added in the calculations within the scheme proposed by Tkatchenko and Scheffler.<sup>27</sup> In order to model the crystal structure of  $\text{M}_{0.042}\text{Ge}_{0.958}\text{Te}$ , a supercell ( $2 \times 2 \times 2$ ) was built from the hexagonal cell of GeTe. The  $P-3m1$  (No. 164) space group was considered for both  $\text{M}_x\text{Ge}_{1-x}\text{Te}$  models ( $x = 0.00, 0.042$ ). Cell parameters and atomic positions of  $\text{M}_{0.042}\text{Ge}_{0.958}\text{Te}$  were both relaxed. All ultra-soft pseudopotentials were generated using the OTF\_ultrasoftpseudopotential generator included in the program. The cut-off energy for plane-waves was set at 500 eV. The electronic wave function was sampled with 110  $k$ -points in the first Brillouin zone using the Monkhorst-Pack method.<sup>28</sup> For the electronic band structures, we used the full-potential linearized augmented plane wave (FLAPW) approach, as implemented in the *WIEN2K* code.<sup>29</sup> For comparison, the band structure of GeTe was computed using the same unit cell and space group as  $\text{M}_{0.042}\text{Ge}_{0.958}\text{Te}$ . A plane wave cut-off corresponding to  $R_{\text{MT}}K_{\text{max}} = 7$  was used. The radial wave

functions inside the non-overlapping muffin-tin spheres were expanded up to  $l_{\max} = 12$ . The charge density was Fourier expanded up to  $G_{\max} = 12 \text{ \AA}^{-1}$ . Total energy convergence was achieved with a Brillouin zone (BZ) integration mesh of 500  $k$ -points.

The carrier effective mass ( $m^*$ ) was computed for each sample using a single parabolic band model<sup>30,31</sup> and the measured room temperature Seebeck coefficient ( $S$ ) and carrier concentration ( $n$ ). Detailed procedure was provided in Chapter 4.

The electronic transport coefficients for  $M_x\text{Ge}_{1-x}\text{Te}$  ( $M = \text{Cu, Ag, Au}; x = 0.04$ ) were calculated within the Boltzmann Transport Equation (BTE) with constant relaxation time for the electrons ( $\tau$ ) and a rigid band structure approximation,<sup>32,33</sup> as implemented in the *BoltzTrap-1.2.5* code.<sup>34</sup> 10,000  $k$ -points in the BZ were used to compute the band derivatives and the density of states for the transport calculations.

## 6.3 Results and Discussion

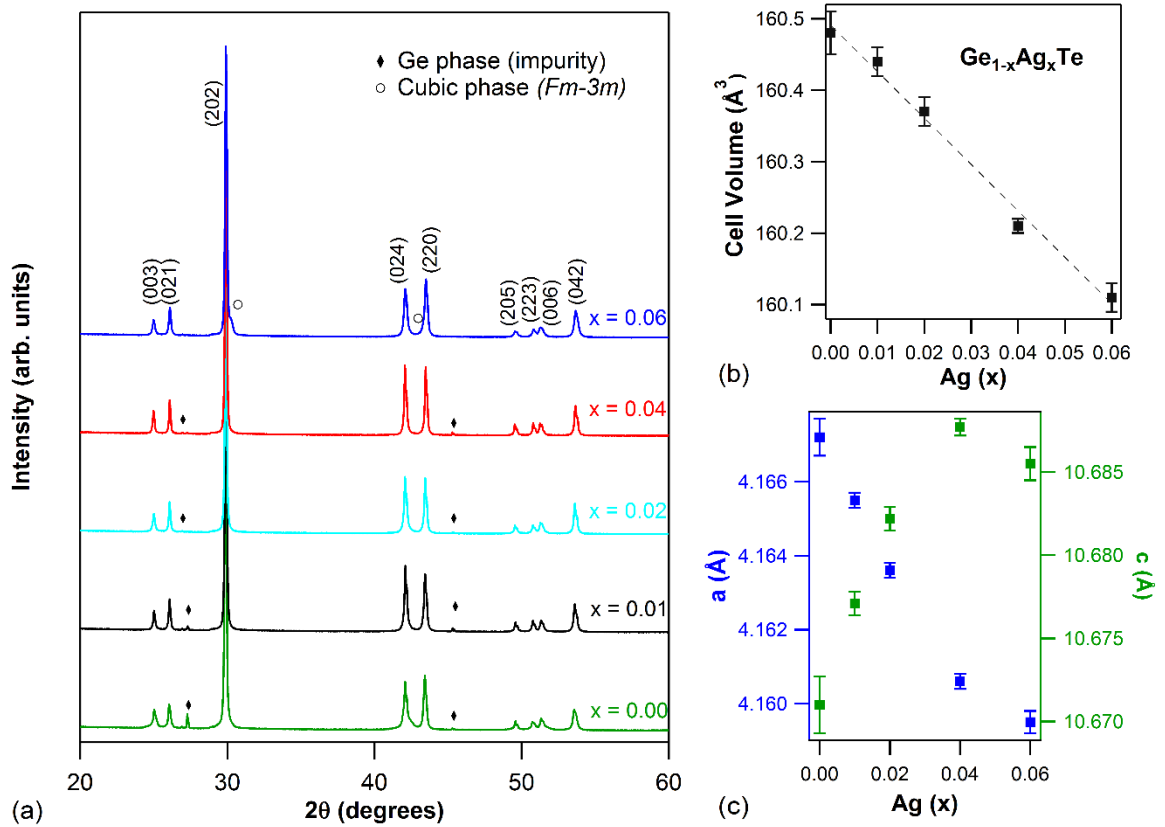
### 6.3.1 Structural Analysis

Figure 6.1.a shows the room temperature XRD pattern of all the  $\text{Ge}_{1-x}\text{Ag}_x\text{Te}$  ( $x = 0.00, 0.01, 0.02, 0.04$  and  $0.06$ ) samples. Sharp reflections indicate the crystalline nature of the synthesized ingots. All the main reflections could be indexed based on a rhombohedral GeTe phase (PDF#47-1079,  $R3m$  space group). Minor reflections of Ge-rich secondary phase (or impurities) could be detected in some samples. The rhombohedral phase was further confirmed by the presence of double reflections<sup>1,5</sup> [(024) and (220)] in the range of  $2\theta$  values between  $41^\circ$  to  $44^\circ$ . As shown in Figure 6.1.c, a progressive evolution of the lattice parameters  $a$  (decreasing trend) and  $c$  (increasing trend) was observed upon increasing Ag content, leading to a continuous decrease of the hexagonal cell volume, as illustrated in Figure 6.1.b. The linear evolution in the lattice parameters for  $x = 0.00 - 0.04$  followed the solid-solution Vegard's law, as Ag was progressively incorporated into the GeTe crystal structure.

In our experimental conditions, the maximum solubility of silver in the rhombohedral GeTe phase appeared to be between 4 and 6 mol%, as a cubic phase ( $Fm-3m$  space group;  $a = 5.9118(9) \text{ \AA}$ ) started to appear for values of  $x \geq 0.06$ . This secondary cubic phase was identified as (Ag,Ge)Te, as the estimated lattice parameter is smaller than that of undoped cubic GeTe ( $a = 6.02 \text{ \AA}$ ).<sup>12,35</sup>

Microscopic data, as shown in SEM images in Figure 6.2, also supported the PXRD results. Few traces of secondary Ge phases or impurities (dark region) were sparingly distributed in the main

phase, *i.e.*, in the GeTe matrix (bright region). The formation of these minor proportion of secondary Ge-inclusions are quite commonly observed in GeTe based materials at several instances.<sup>36,37</sup>



**Figure 6.1** (a) Powder XRD patterns for  $Ge_{1-x}Ag_xTe$  samples, (b) hexagonal cell volume vs. Ag concentration, and (c) evolution of  $a$  and  $c$  lattice parameters with Ag content.

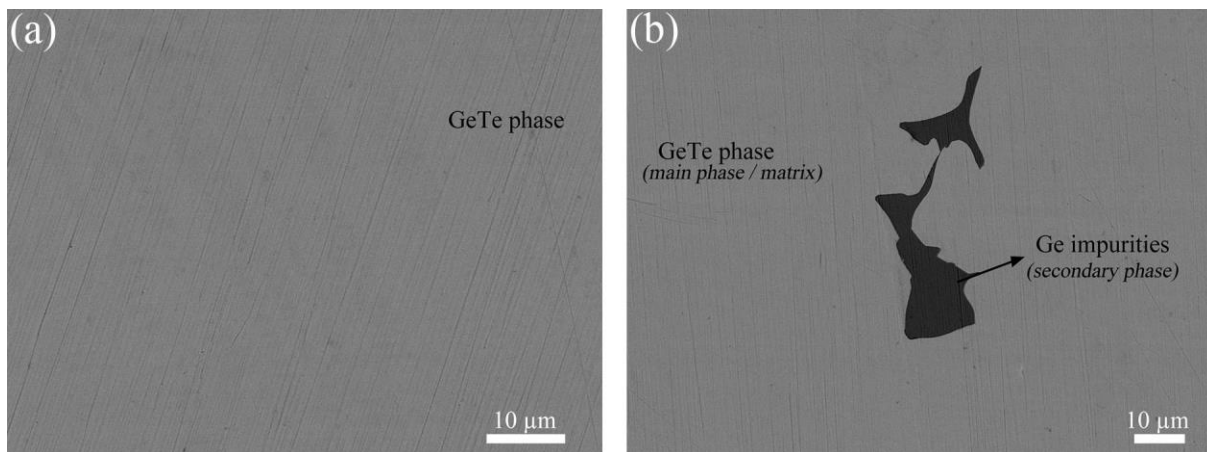


**Figure 6.2** SEM images of  $Ge_{0.99}Ag_{0.01}Te$  showing predominantly the GeTe (main) phase and few secondary Ge inclusions (consistent with the PXR results).

The electrical and thermal transport properties of  $\text{Ge}_{1-x}\text{Ag}_x\text{Te}$  samples for the values of  $x = 0.00$  and  $0.02$  are pretty much close to  $x = 0.01$ . Hence, for better visibility, only values of  $x = 0.01$ ,  $0.04$  and  $0.06$  are depicted in the forthcoming graphs and sections in this chapter.

### 6.3.2 Electrical Transport Properties

The room temperature values of carrier concentration ( $n$ ) and mobility ( $\mu$ ) obtained from Hall measurements are reported in Table 6.1

**Table 6.1** Hall measurement results (at  $\sim 300$  K) of carrier concentration, mobility, and computed effective mass for  $\text{Ge}_{1-x}\text{Ag}_x\text{Te}$  samples.

$x$	Carrier Concentration, $n$ ( $\text{cm}^{-3}$ )	Mobility, $\mu$ ( $\text{cm}^2\text{V}^{-1}\text{s}^{-1}$ )	Effective mass, $m^*$
0.01	$1.39 \times 10^{21}$	31.7	$1.84m_e$
0.04	$2.74 \times 10^{21}$	13.7	$2.90m_e$
0.06	$2.52 \times 10^{22}$	1.89	$12.7m_e$

Holes were the major charge carriers ( $p$ -type), as the Hall voltage was positive in these samples. The carrier concentration value at room temperature increased with increasing Ag content, due to the aliovalent  $\text{Ag}^+$  at the  $\text{Ge}^{2+}$  site in GeTe, which seems to give rise to extra mobile holes in the system. In pristine GeTe, the Ge vacancy has very low formation energy and is the most easily formed intrinsic defect.<sup>20,21</sup> The addition of Ag to GeTe can further decrease this vacancy formation energy, thereby leading to a large density of carrier concentrations. The temperature-dependent electrical transport properties of  $\text{Ge}_{1-x}\text{Ag}_x\text{Te}$  are shown in Figure 6.3. The electrical conductivity of all the samples decreased with increasing temperature (Figure 6.3.a), which is the archetypal behavior of degenerate semi-conductors.<sup>5,6,38,39</sup> As expected, the room temperature hole mobility ( $\mu$ ) decreased with the increase in Ag concentration (Table 6.1) due to an alloy scattering mechanism, which usually comes into picture in such a case of doping.<sup>1,38,40</sup> Besides alloy scattering, the low  $\mu$  in  $\text{Ge}_{0.94}\text{Ag}_{0.06}\text{Te}$  could also be attributed to the presence of an additional cubic phase.



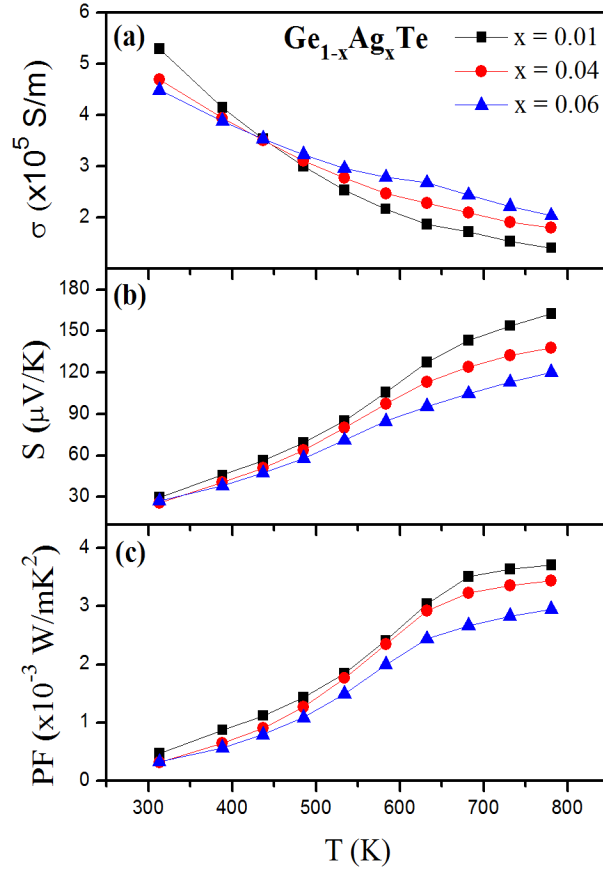


**Figure 6.3** Temperature-dependent (a) electrical conductivity ( $\sigma$ ), (b) Seebeck coefficient, ( $S$ ), (c) Power factor ( $\text{PF} = S^2\sigma$ ) of  $\text{Ge}_{1-x}\text{Ag}_x\text{Te}$  ( $x = 0.01-0.06$ ) solid-state solutions.

Figure 6.3.b shows the temperature-dependent Seebeck coefficient results.  $S$ -values being positive for all the composition over the entire temperature range, indicates  $p$ -type charge carriers, which is consistent with the Hall measurement results. The thermopowers of  $\text{Ge}_{1-x}\text{Ag}_x\text{Te}$  show a steadily increasing trend with temperature. With increasing Ag content, the change in  $S$ -values at room temperature was not much evident, but they decreased significantly with increasing temperature. At 773 K, the  $S$ -value for  $\text{Ge}_{0.99}\text{Ag}_{0.01}\text{Te}$  was  $\sim 163 \mu\text{V/K}$ . It reduced to  $\sim 120 \mu\text{V/K}$  for  $\text{Ge}_{0.94}\text{Ag}_{0.06}\text{Te}$  at the same temperature. It is understood that the doping of Ag in GeTe decreases the  $S$  value, as it drastically inflates the free carrier concentration.

Mention must be made on the fact that the presence of minor proportion of secondary Ge phases (impurities) in the samples of  $\text{Ge}_{1-x}\text{Ag}_x\text{Te}$  ( $x = 0.01$  to  $0.04$ ) has no significant impact on its thermoelectric properties.<sup>4,5,9</sup>

The temperature dependence of the power factors ( $S^2\sigma$ ) for  $\text{Ge}_{1-x}\text{Ag}_x\text{Te}$  are depicted in Figure 6.3.c. The sample with  $x = 0.01$  showed a power factor value of  $\sim 0.47 \times 10^{-3} \text{ W/mK}^2$  at 310 K, which

raised to  $\sim 3.7 \times 10^{-3} \text{ W/mK}^2$  at 773 K, whereas the sample with  $x = 0.06$  exhibited a lower power factor values of  $\sim 0.3 \times 10^{-3} \text{ W/mK}^2$  at 310 K and  $\sim 2.9 \times 10^{-3} \text{ W/mK}^2$  at 773 K. Reduction of Seebeck coefficient with Ag content due to local electron imbalance considerably affected the thermoelectric power factor.

### 6.3.3 Investigation of Electronic Band Structures and Density of States

The computed effective masses of  $\text{Ge}_{1-x}\text{Ag}_x\text{Te}$  samples are listed in Table 6.1. The values of  $m^*$  given here are only an estimate, as the calculation considers only a single parabolic band for simplicity. Accurate evaluation of  $m^*$  for GeTe based materials is quite complex, as their conduction band structures are not only anisotropic (different along transverse and longitudinal directions) and non-parabolic, but also have a unique corrugated structure in the doping range near the band edges, which cannot be covered in the parabolic band models.<sup>41</sup>  $m^*$  increased gradually from  $1.84m_e$  to  $12.7m_e$  ( $m_e$  is the free electron mass) with increasing Ag concentration from 0 to 6 % (Table 6.1).

In order to study the effect of germanium substitution with silver in rhombohedral GeTe (r-GeTe), DFT calculations were carried out on  $\text{Ag}_{0.042}\text{Ge}_{0.958}\text{Te}$  model structure (as it is close to the experimental composition). Previous computational studies on amorphous and cubic GeTe (c-GeTe) showed that the formation energy (to form a defect) becomes lower when Ag atoms replace Ge ones.<sup>42,43</sup> The DOS computed for r-GeTe and  $\text{Ag}_{0.042}\text{Ge}_{0.958}\text{Te}$  are sketched in Figure 6.4.

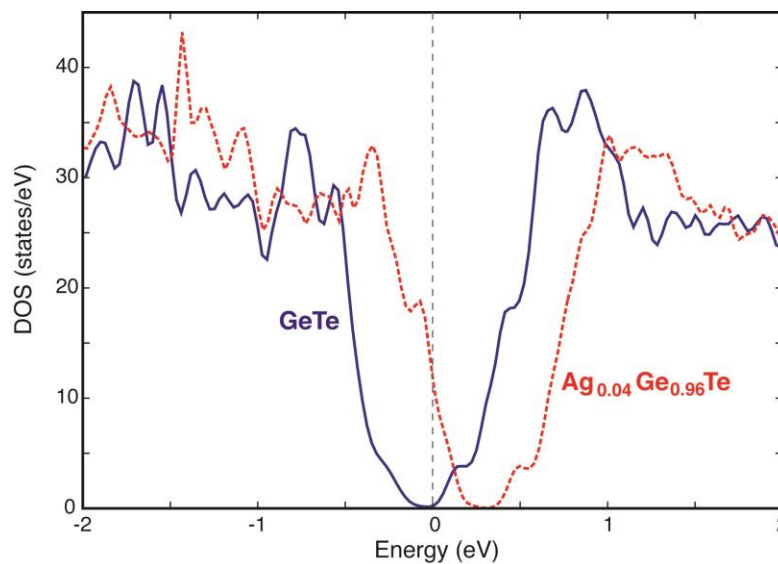


**Figure 6.4.** Computed DOS for r-GeTe and  $\text{Ag}_{0.04}\text{Ge}_{0.96}\text{Te}$  models. The Fermi energy level is set at 0 eV.

Substituting divalent Ge with monovalent Ag decreased the number of electrons and, assuming a rigid band model, shifted the Fermi level downwards. Therefore, the DOS at the Fermi level significantly increased, which is in agreement with the enhancement of charge carrier density upon increase of the silver vs. germanium ratio in the solid solution. According to the Boltzmann equation, the carrier concentration and the Seebeck coefficient have an inverse relationship, so an improvement in one will result in a degradation of the other. This is consistent with the decrease of the Seebeck coefficient measured with the increase of silver content. Kanatzidis *et al.* showed that the electronic structure of *c*-GeTe is perturbed by impurities in the concentration range of 1%.<sup>23</sup> As observed in Figure 6.5, upon substitution of Ge with Ag in *r*-GeTe, band degeneracy at the valence band maximum (VBM) and conduction band minimum (CBM) of the host material was removed and band splitting occurred in the presence of silver in GeTe. In the band structure of the  $\text{Ag}_{0.042}\text{Ge}_{0.958}\text{Te}$  model compound (Figure 6.5.b), the Fermi level lies almost at the top of the valence band. This reinforces the decrease of the Seebeck coefficient with Ag content.

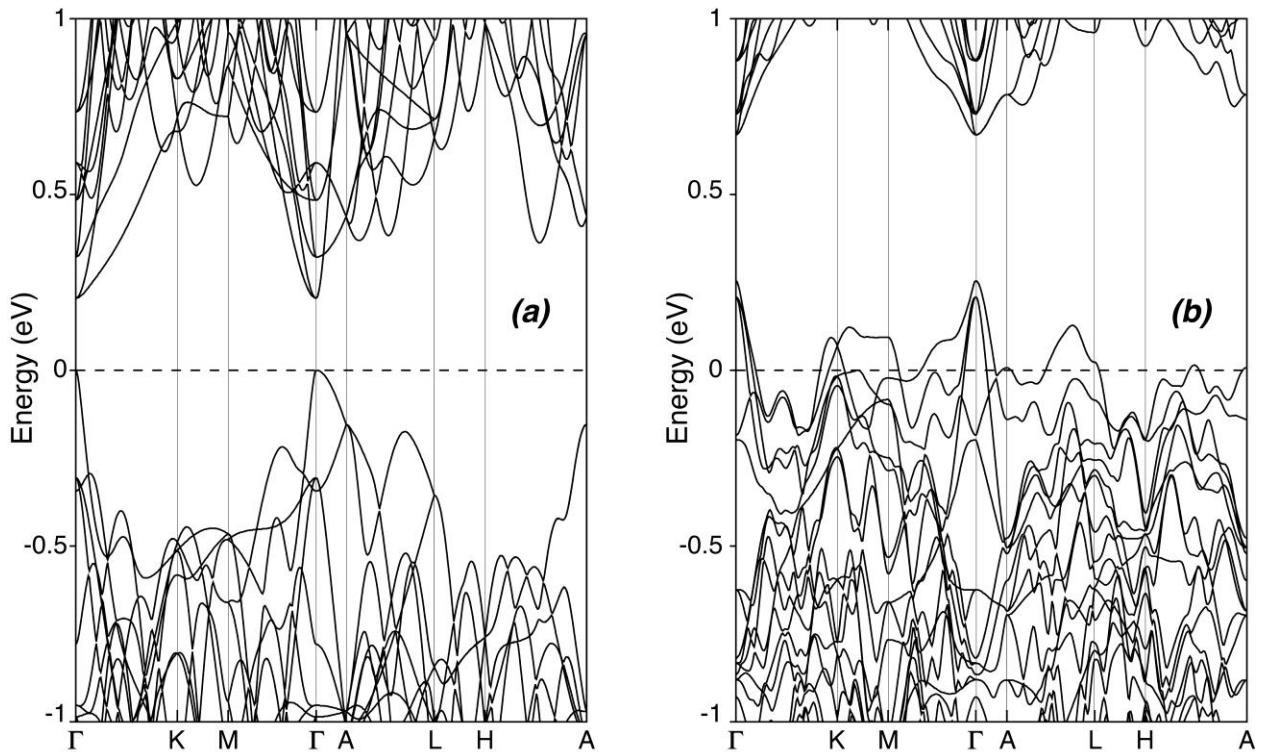


**Figure 6.5** Electronic band structures of pristine *r*-GeTe (a) and  $\text{Ag}_{0.042}\text{Ge}_{0.958}\text{Te}$  (b). In order to compare the band structures, the same supercell has been considered for *r*-GeTe.

The gradual increase of  $m^*$  with increasing Ag concentration, as reported in Table 6.1, probably resulted from the increasing contribution of several hole pockets in the valence band of  $\text{Ag}_{0.042}\text{Ge}_{0.958}\text{Te}$ , as expected from its band structure. Isoelectronic  $\text{M}_{0.042}\text{Ge}_{0.958}\text{Te}$  ( $\text{M} = \text{Cu}, \text{Au}$ ) compounds were studied in silico. As for the silver analog, substitution of one Ge by a group-11 transition metal hardly modified the crystal structure of r-GeTe. DOS of  $\text{Cu}_{0.042}\text{Ge}_{0.958}\text{Te}$  and  $\text{Au}_{0.042}\text{Ge}_{0.958}\text{Te}$  models (Annexure 6, Figure A6.3) looked very similar to that of the silver analogue shown in Figure 6.4. In order to evaluate the impact of Ge substitution with group-11 elements, the electronic part of the transport properties was computed using a semi-classical approach. The Seebeck coefficient as a function of the chemical potential is shown in Figure 6.6. Irrespective of the carrier concentration, the Seebeck coefficient was found to be higher for silver-doped GeTe when compared to its gold and copper congeners. This is consistent with the DOS of  $\text{M}_{0.042}\text{Ge}_{0.958}\text{Te}$  ( $\text{M} = \text{Cu}, \text{Ag}, \text{Au}$ ), as sketched in Annexure 6 (Figure A6.3).

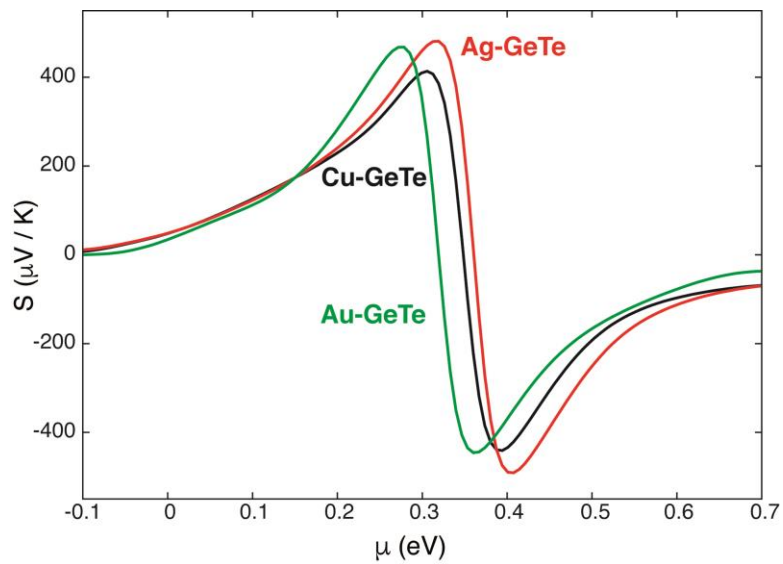


**Figure 6.6** Seebeck coefficient as a function of the chemical potential ( $\mu$ ), computed at 300 K for  $\text{M}_{0.042}\text{Ge}_{0.958}\text{Te}$  ( $\text{M} = \text{Cu}, \text{Ag}, \text{Au}$ ) using a semi-classical approach.

### 6.3.4 Thermal Transport Properties and Figure of Merit

The temperature-dependent total thermal conductivity  $\kappa_{\text{total}}$  is presented in Figure 6.7.a. At 773 K, the  $\kappa_{\text{total}}$  value for  $\text{Ge}_{0.99}\text{Ag}_{0.01}\text{Te}$  was  $\sim 3.05$  W/mK and with addition of more Ag, it increased to  $\sim 4.02$  W/mK for  $\text{Ge}_{0.94}\text{Ag}_{0.06}\text{Te}$ . It is to be noted that the  $\kappa_{\text{total}}$  value for  $\text{Ge}_{0.99}\text{Ag}_{0.01}\text{Te}$  decreased till 673 K and then marginally increased. Such a change of trend was observed for other GeTe based

materials, which was ascribed to the second-order phase transition from rhombohedral to cubic phase.<sup>1,4,5,7,12</sup> This transition temperature decreases from 673 K to 573 K with increase in Ag content from 1 to 6 mol%.

To better understand the impacts of Ag on the thermal transport properties of GeTe, the contributions from electronic and lattice parts were calculated. The calculated temperature dependent Lorenz number ( $L$ ) for all the samples were in the range of  $2.3 \times 10^{-8}$  to  $1.75 \times 10^{-8} \text{ W}\Omega\text{K}^{-2}$  and was lower than the metallic limit of  $2.45 \times 10^{-8} \text{ W}\Omega\text{K}^{-2}$  (Annexure 6, Figure A6.2).

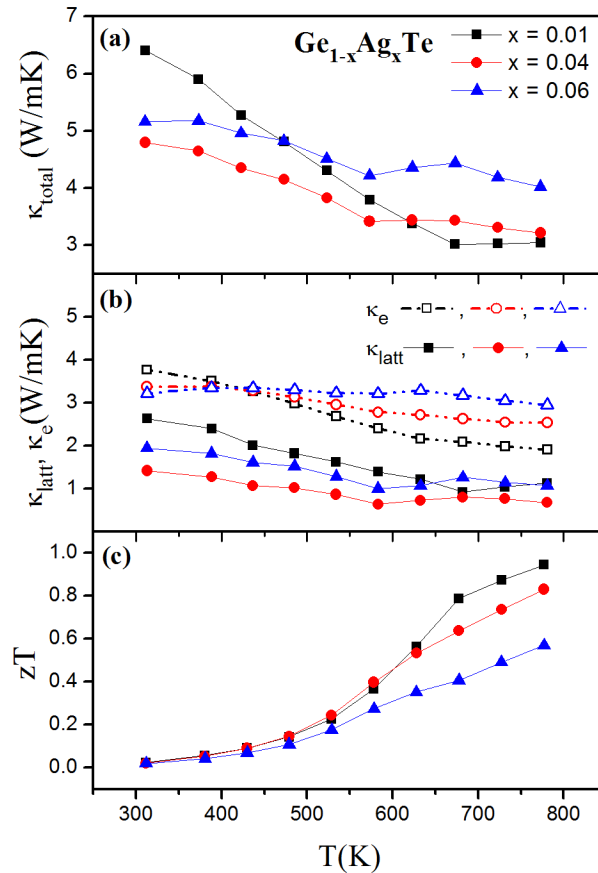


**Figure 6.7** Temperature-dependent (a) total thermal conductivity ( $\kappa_{\text{total}}$ ), (b) lattice ( $\kappa_{\text{latt}}$ ) and electronic ( $\kappa_e$ ) thermal conductivities, (c)  $zT$  for  $\text{Ge}_{1-x}\text{Ag}_x\text{Te}$  ( $x = 0.01-0.06$ ) solid-state solutions.

The lattice and electronic thermal conductivities are plotted in Figure 6.7.b. As it can be seen, the lattice contribution is relatively low compared to the electronic contribution, and at higher temperatures  $\kappa_{\text{latt}}$  is in the order of  $\sim 1 \text{ W/mK}$ , analogous with that of other high performance GeTe based materials<sup>1,4-8,19,44-46</sup> and other state-of-the-art thermoelectric materials like PbTe<sup>39,47-59</sup> and SnTe.<sup>60-65</sup> Ag substitution helps reducing this lattice contribution, presumably because of increased

alloy scattering and phonon interfacial scattering at the grain boundaries. It is in fact the electronic part that affected the total thermal conductivity. At 773 K,  $\kappa_e$  increased conspicuously with Ag doping, thereby contributing to the substantial raise in  $\kappa_{\text{total}}$ . More metallic behavior of Ag unfavorably affected the thermal conductivity of GeTe solid-state solutions.

The thermoelectric figure of merit as a function of temperature, calculated from the electrical transport and thermal conductivity data, is shown in Figure 6.7.c. The maximum  $zT$  achieved is  $\sim 0.95$  at 773 K for  $\text{Ge}_{0.99}\text{Ag}_{0.01}\text{Te}$ , which is almost the same as pristine GeTe.<sup>12</sup>  $zT$  reduced to  $\sim 0.57$  at 773 K for  $\text{Ge}_{0.94}\text{Ag}_{0.06}\text{Te}$ . Ag insertion subsided the thermoelectric performance in GeTe mainly due to reduced Seebeck coefficient, arising due to proliferation of the hole concentration.

The study highlights the limits in doping just a coinage metal to GeTe and explains why Ag + Sb pair substituted  $\text{Ag}_x\text{Sb}_x\text{Ge}_{50-2x}\text{Te}_{50}$  (TAGS) exhibits exceptional thermoelectric properties, as the opposing effects of excess hole concentration created by Ag (acceptor) insertion is compensated by Sb (donor dopant).

## 6.4 Conclusion

The crystalline ingots of  $\text{Ge}_{1-x}\text{Ag}_x\text{Te}$  ( $x = 0.00 - 0.06$ ) have been synthesized by vacuum-sealed tube melt processing. The solubility of Ag in r-GeTe was found to be less than 6%. Substitution of Ge by Ag profoundly affected the electronic and thermal transport properties of r-GeTe: (i) it proliferated the charge carrier density due to the aliovalent  $\text{Ag}^+$  and the reduction in Ge vacancy formation energy, (ii) it lowered the Fermi level which lies almost at the top of the valence band, affecting the Seebeck coefficient, (iii) it led to a loss of band degeneracy, (iv) it also led to a surge in the contribution of several hole pockets in the valence band, thus increasing the effective mass, and (v) it caused a decrease of the lattice thermal conductivity due to alloy scattering, contributing to reduced mobility, but an increase of the electronic thermal conductivity.  $\text{Ge}_{1-x}\text{Ag}_x\text{Te}$  ( $x \leq 0.04$ ) exhibited a mean  $zT \sim 0.85$  at 773 K. First-principles calculations carried out on GeTe substituted with other coinage metals (Cu, Au), demonstrate that silver doped solid solutions exhibit higher thermopower compared to the others. The multiple factors presented in this work demonstrate that substitution by just a coinage metal is not the best choice of a dopant for achieving high  $zT$  in GeTe-based thermoelectric materials, and reiterates the need for pair substitution, as like in TAGS where silver and antimony substitute for germanium, to enhance the thermoelectric performance of GeTe.

➤ **Adaptation**

The results presented in this chapter have been published in the Journal of Physical Chemistry C (ACS). Hence, this chapter is an adaptation from that publication – **B. Srinivasan et al., J. Phys. Chem. 2018, 122, 227–235.**

➤ **Author Contributions**

B.S conceived the project, designed and performed experiments, analyzed the results and wrote the journal manuscript. The DFT computations were performed by Prof. Régis Gautier and Dr. Bruno Fontaine (ISCR Rennes).

## References

- (1) Gelbstein, Y.; Davidow, J. Highly Efficient Functional  $\text{Ge}_x\text{Pb}_{1-x}\text{Te}$  Based Thermoelectric Alloys. *Phys. Chem. Chem. Phys.* **2014**, *16* (37), 20120–20126.
- (2) Gelbstein, Y.; Davidow, J.; Girard, S. N.; Chung, D. Y.; Kanatzidis, M. Controlling Metallurgical Phase Separation Reactions of the  $\text{Ge}_{0.87}\text{Pb}_{0.13}\text{Te}$  Alloy for High Thermoelectric Performance. *Adv. Energy Mater.* **2013**, *3* (6), 815–820.
- (3) Hazan, E.; Ben-Yehuda, O.; Madar, N.; Gelbstein, Y. Functional Graded Germanium–Lead Chalcogenide-Based Thermoelectric Module for Renewable Energy Applications. *Adv. Energy Mater.* **2015**, *5* (11), 1500272.
- (4) Wu, D.; Zhao, L.-D.; Hao, S.; Jiang, Q.; Zheng, F.; Doak, J. W.; Wu, H.; Chi, H.; Gelbstein, Y.; Uher, C.; et al. Origin of the High Performance in GeTe-Based Thermoelectric Materials upon  $\text{Bi}_2\text{Te}_3$  Doping. *J. Am. Chem. Soc.* **2014**, *136* (32), 11412–11419.
- (5) Perumal, S.; Roychowdhury, S.; Negi, D. S.; Datta, R.; Biswas, K. High Thermoelectric Performance and Enhanced Mechanical Stability of P-Type  $\text{Ge}_{1-x}\text{Sb}_x\text{Te}$ . *Chem. Mater.* **2015**, *27* (20), 7171–7178.
- (6) Perumal, S.; Roychowdhury, S.; Biswas, K. Reduction of Thermal Conductivity through Nanostructuring Enhances the Thermoelectric Figure of Merit in  $\text{Ge}_{1-x}\text{Bi}_x\text{Te}$ . *Inorg. Chem. Front.* **2016**, *3* (1), 125–132.

- (7) Lee, J. K.; Oh, M. W.; Kim, B. S.; Min, B. K.; Lee, H. W.; Park, S. D. Influence of Mn on Crystal Structure and Thermoelectric Properties of GeTe Compounds. *Electron. Mater. Lett.* **2014**, *10* (4), 813–817.
- (8) Gelbstein, Y.; Dado, B.; Ben-Yehuda, O.; Sadia, Y.; Dashevsky, Z.; Dariel, M. P. High Thermoelectric Figure of Merit and Nanostructuring in Bulk P-Type  $\text{Ge}_x(\text{Sn}_y\text{Pb}_{1-y})_{1-x}\text{Te}$  Alloys Following a Spinodal Decomposition Reaction. *Chem. Mater.* **2010**, *22* (3), 1054–1058.
- (9) Wu, L.; Li, X.; Wang, S.; Zhang, T.; Yang, J.; Zhang, W.; Chen, L.; Yang, J. Resonant Level-Induced High Thermoelectric Response in Indium-Doped GeTe. *NPG Asia Mater.* **2017**, *9* (1), e343.
- (10) Yang, S. H.; Zhu, T. J.; Sun, T.; He, J.; Zhang, S. N.; Zhao, X. B. Nanostructures in High-Performance  $(\text{GeTe})_x(\text{AgSbTe}_2)_{100-x}$  Thermoelectric Materials. *Nanotechnology* **2008**, *19* (24), 245707.
- (11) Cook, B. A.; Kramer, M. J.; Wei, X.; Haringa, J. L.; Levin, E. M. Nature of the Cubic to Rhombohedral Structural Transformation in  $(\text{AgSbTe}_2)_{15}(\text{GeTe})_{85}$  Thermoelectric Material. *J. Appl. Phys.* **2007**, *101* (5), 053715.
- (12) Perumal, S.; Roychowdhury, S.; Biswas, K. High Performance Thermoelectric Materials and Devices Based on GeTe. *J. Mater. Chem. C* **2016**, *4* (32), 7520–7536.
- (13) Rosi, F. D.; Dismukes, J. P.; Hockings, E. F. Semiconductor Materials for Thermoelectric Power Generation up to 700 °C. *Electr. Eng.* **1960**, *79* (6), 450–459.
- (14) Schröder, T.; Schwarzmüller, S.; Stiewe, C.; de Boor, J.; Hölzel, M.; Oeckler, O. The Solid Solution Series  $(\text{GeTe})_x(\text{LiSbTe}_2)_2$  ( $1 \leq x \leq 11$ ) and the Thermoelectric Properties of  $(\text{GeTe})_{11}(\text{LiSbTe}_2)_2$ . *Inorg. Chem.* **2013**, *52* (19), 11288–11294.
- (15) Schröder, T.; Rosenthal, T.; Giesbrecht, N.; Maier, S.; Scheidt, E.-W.; Scherer, W.; Snyder, G. J.; Schnick, W.; Oeckler, O. TAGS-Related Indium Compounds and Their Thermoelectric Properties – the Solid Solution Series  $(\text{GeTe})_x\text{AgIn}_y\text{Sb}_{1-y}\text{Te}_2$  ( $x = 1-12$ ;  $y = 0.5$  and  $1$ ). *J. Mater. Chem. A* **2014**, *2* (18), 6384–6395.
- (16) Shi, X.; Salvador, J. R.; Yang, J.; Wang, H. Prospective Thermoelectric Materials:  $(\text{AgSbTe}_2)_{100-x}(\text{SnTe})_x$  Quaternary System ( $x = 80, 85, 90,$  and  $95$ ). *Sci. Adv. Mater.* **2011**, *3* (4), 667–671.
- (17) Levin, E. M.; Hanus, R.; Hanson, M.; Straszheim, W. E.; Schmidt-Rohr, K. Thermoelectric Properties of  $\text{Ag}_2\text{Sb}_2\text{Ge}_{46-x}\text{Dy}_x\text{Te}_{50}$  Alloys with High Power Factor. *Phys. Status Solidi A* **2013**, *210* (12), 2628–2637.
- (18) Fahrnbauer, F.; Souchay, D.; Wagner, G.; Oeckler, O. High Thermoelectric Figure of Merit Values of Germanium Antimony Tellurides with Kinetically Stable Cobalt Germanide Precipitates. *J. Am. Chem. Soc.* **2015**, *137* (39), 12633–12638.



- (19) Rosenthal, T.; Schneider, M. N.; Stiewe, C.; Döblinger, M.; Oeckler, O. Real Structure and Thermoelectric Properties of GeTe-Rich Germanium Antimony Tellurides. *Chem. Mater.* **2011**, *23* (19), 4349–4356.
- (20) Levin, E. M. Effects of Ge Substitution in GeTe by Ag or Sb on the Seebeck Coefficient and Carrier Concentration Derived from  $^{125}\text{Te}$  NMR. *Phys. Rev. B* **2016**, *93* (4), 045209.
- (21) Edwards, A. H.; Pineda, A. C.; Schultz, P. A.; Martin, M. G.; Thompson, A. P.; Hjalmarsen, H. P.; Umrigar, C. J. Electronic Structure of Intrinsic Defects in Crystalline Germanium Telluride. *Phys. Rev. B* **2006**, *73* (4), 045210.
- (22) Rabe, K. M.; Joannopoulos, J. D. Theory of the Structural Phase Transition of GeTe. *Phys. Rev. B* **1987**, *36* (12), 6631–6639.
- (23) Hoang, K.; Mahanti, S. D.; Kanatzidis, M. G. Impurity Clustering and Impurity-Induced Bands in PbTe-, SnTe-, and GeTe-Based Bulk Thermoelectrics. *Phys. Rev. B* **2010**, *81* (11), 115106.
- (24) Li, J.; Chen, Z.; Zhang, X.; Sun, Y.; Yang, J.; Pei, Y. Electronic Origin of the High Thermoelectric Performance of GeTe among the P-Type Group IV Monotellurides. *NPG Asia Mater.* **2017**, *9* (3), e353.
- (25) Clark, S. J.; Segall, M. D.; Pickard, C. J.; Hasnip, P. J.; Probert, M. I. J.; Refson, K.; Payne, M. C. First Principles Methods Using CASTEP. *Z. Für Krist. - Cryst. Mater.* **2009**, *220* (5/6), 567–570.
- (26) Perdew, J. P.; Burke, K.; Ernzerhof, M. Generalized Gradient Approximation Made Simple. *Phys. Rev. Lett.* **1996**, *77* (18), 3865–3868.
- (27) Tkatchenko, A.; Scheffler, M. Accurate Molecular Van Der Waals Interactions from Ground-State Electron Density and Free-Atom Reference Data. *Phys. Rev. Lett.* **2009**, *102* (7), 073005.
- (28) Monkhorst, H. J.; Pack, J. D. Special Points for Brillouin-Zone Integrations. *Phys. Rev. B* **1976**, *13* (12), 5188–5192.
- (29) Blaha, P.; Schwarz, K.; Madsen, G.; Kvasnicka, D.; Luitz, J. *WIEN2K: An Augmented Plane Wave plus Local Orbitals Program for Calculating Crystal Properties*; Karlheinz Schwarz, Techn. Universität Wien, Austria: Wien, Austria, 2001.
- (30) May, A. F.; Toberer, E. S.; Saramat, A.; Snyder, G. J. Characterization and Analysis of Thermoelectric Transport in N-Type  $\text{Ba}_8\text{Ga}_{16-x}\text{Ge}_{30+x}$ . *Phys. Rev. B* **2009**, *80* (12), 125205.
- (31) Toberer, E. S.; Zevalkink, A.; Crisosto, N.; Snyder, G. J. The Zintl Compound  $\text{Ca}_5\text{Al}_2\text{Sb}_6$  for Low-Cost Thermoelectric Power Generation. *Adv. Funct. Mater.* **2010**, *20* (24), 4375–4380.
- (32) Scheidemantel, T. J.; Ambrosch-Draxl, C.; Thonhauser, T.; Badding, J. V.; Sofo, J. O. Transport Coefficients from First-Principles Calculations. *Phys. Rev. B* **2003**, *68* (12), 125210.

- (33) Madsen, G. K. H. Automated Search for New Thermoelectric Materials: The Case of LiZnSb. *J. Am. Chem. Soc.* **2006**, *128* (37), 12140–12146.
- (34) Madsen, G. K. H.; Singh, D. J. BoltzTraP. A Code for Calculating Band-Structure Dependent Quantities. *Comput. Phys. Commun.* **2006**, *175* (1), 67–71.
- (35) Wiedemeier, H.; Siemers, P. A. The Temperature—Composition Phase Diagram of the GeSe—GeTe System. In *Modern High Temperature Science*; Margrave, J. L., Ed.; Humana Press, 1984; pp 395–408.
- (36) Levin, E. M.; Besser, M. F.; Hanus, R. Electronic and Thermal Transport in GeTe: A Versatile Base for Thermoelectric Materials. *J. Appl. Phys.* **2013**, *114* (8), 083713.
- (37) Perumal, S.; Bellare, P.; Shenoy, U. S.; Waghmare, U. V.; Biswas, K. Low Thermal Conductivity and High Thermoelectric Performance in Sb and Bi Codoped GeTe: Complementary Effect of Band Convergence and Nanostructuring. *Chem. Mater.* **2017**, *29* (24), 10426–10435.
- (38) Srinivasan, B.; Boussard-Pledel, C.; Dorcet, V.; Samanta, M.; Biswas, K.; Lefèvre, R.; Gascoin, F.; Chevirié, F.; Tricot, S.; Reece, M.; et al. Thermoelectric Properties of Highly-Crystallized Ge-Te-Se Glasses Doped with Cu/Bi. *Materials* **2017**, *10* (4), 328.
- (39) LaLonde, A. D.; Pei, Y.; Snyder, G. J. Reevaluation of  $\text{PbTe}_{1-x}\text{I}_x$  as High Performance N-Type Thermoelectric Material. *Energy Environ. Sci.* **2011**, *4* (6), 2090–2096.
- (40) Wang, H.; LaLonde, A. D.; Pei, Y.; Snyder, G. J. The Criteria for Beneficial Disorder in Thermoelectric Solid Solutions. *Adv. Funct. Mater.* **2013**, *23* (12), 1586–1596.
- (41) Chen, X.; Parker, D.; Singh, D. J. Importance of Non-Parabolic Band Effects in the Thermoelectric Properties of Semiconductors. *Sci. Rep.* **2013**, *3*, 3168.
- (42) Xu, L.; Li, Y.; Yu, N. N.; Zhong, Y. P.; Miao, X. S. Local Order Origin of Thermal Stability Enhancement in Amorphous Ag Doping GeTe. *Appl. Phys. Lett.* **2015**, *106* (3), 031904.
- (43) Bruns, G.; Merkelbach, P.; Schlockermann, C.; Salinga, M.; Wuttig, M.; Happ, T. D.; Philipp, J. B.; Kund, M. Nanosecond Switching in GeTe Phase Change Memory Cells. *Appl. Phys. Lett.* **2009**, *95* (4), 043108.
- (44) Davidow, J.; Gelbstein, Y. A Comparison Between the Mechanical and Thermoelectric Properties of Three Highly Efficient P-Type GeTe-Rich Compositions: TAGS-80, TAGS-85, and 3%  $\text{Bi}_2\text{Te}_3$ -Doped  $\text{Ge}_{0.87}\text{Pb}_{0.13}\text{Te}$ . *J. Electron. Mater.* **2013**, *42* (7), 1542–1549.
- (45) Schröder, T.; Rosenthal, T.; Giesbrecht, N.; Nentwig, M.; Maier, S.; Wang, H.; Snyder, G. J.; Oeckler, O. Nanostructures in Te/Sb/Ge/Ag (TAGS) Thermoelectric Materials Induced by Phase Transitions Associated with Vacancy Ordering. *Inorg. Chem.* **2014**, *53* (14), 7722–7729.

- (46) Welzmler, S.; Rosenthal, T.; Ganter, P.; Neudert, L.; Fahrnbauer, F.; Urban, P.; Stiewe, C.; Boor, J. de; Oeckler, O. Layered Germanium Tin Antimony Tellurides: Element Distribution, Nanostructures and Thermoelectric Properties. *Dalton Trans.* **2014**, 43 (27), 10529–10540.
- (47) Bali, A.; Wang, H.; Snyder, G. J.; Mallik, R. C. Thermoelectric Properties of Indium Doped PbTe<sub>1-y</sub>Se<sub>y</sub> Alloys. *J. Appl. Phys.* **2014**, 116 (3), 033707.
- (48) Zhang, Q.; Wang, H.; Zhang, Q.; Liu, W.; Yu, B.; Wang, H.; Wang, D.; Ni, G.; Chen, G.; Ren, Z. Effect of Silicon and Sodium on Thermoelectric Properties of Thallium-Doped Lead Telluride-Based Materials. *Nano Lett.* **2012**, 12 (5), 2324–2330.
- (49) Zhang, Q.; Wang, H.; Liu, W.; Wang, H.; Yu, B.; Zhang, Q.; Tian, Z.; Ni, G.; Lee, S.; Esfarjani, K.; et al. Enhancement of Thermoelectric Figure-of-Merit by Resonant States of Aluminium Doping in Lead Selenide. *Energy Environ. Sci.* **2012**, 5 (1), 5246–5251.
- (50) Yu, B.; Zhang, Q.; Wang, H.; Wang, X.; Wang, H.; Wang, D.; Wang, H.; Snyder, G. J.; Chen, G.; Ren, Z. F. Thermoelectric Property Studies on Thallium-Doped Lead Telluride Prepared by Ball Milling and Hot Pressing. *J. Appl. Phys.* **2010**, 108 (1), 016104.
- (51) Zhang, Q.; Cao, F.; Lukas, K.; Liu, W.; Esfarjani, K.; Opeil, C.; Broido, D.; Parker, D.; Singh, D. J.; Chen, G.; et al. Study of the Thermoelectric Properties of Lead Selenide Doped with Boron, Gallium, Indium, or Thallium. *J. Am. Chem. Soc.* **2012**, 134 (42), 17731–17738.
- (52) Zhang, Q.; Yang, S.; Zhang, Q.; Chen, S.; Liu, W.; Wang, H.; Tian, Z.; Broido, D.; Gang Chen; Ren, Z. Effect of Aluminum on the Thermoelectric Properties of Nanostructured PbTe. *Nanotechnology* **2013**, 24 (34), 345705.
- (53) Poudeu, P. F. P.; D'Angelo, J.; Kong, H.; Downey, A.; Short, J. L.; Pcionek, R.; Hogan, T. P.; Uher, C.; Kanatzidis, M. G. Nanostructures versus Solid Solutions: Low Lattice Thermal Conductivity and Enhanced Thermoelectric Figure of Merit in Pb<sub>9.6</sub>Sb<sub>0.2</sub>Te<sub>10-x</sub>Se<sub>x</sub> Bulk Materials. *J. Am. Chem. Soc.* **2006**, 128 (44), 14347–14355.
- (54) Poudeu, P. F. P.; D'Angelo, J.; Downey, A. D.; Short, J. L.; Hogan, T. P.; Kanatzidis, M. G. High Thermoelectric Figure of Merit and Nanostructuring in Bulk P-Type Na<sub>1-x</sub>Pb<sub>m</sub>Sb<sub>y</sub>Te<sub>m+2</sub>. *Angew. Chem. Int. Ed.* **2006**, 45 (23), 3835–3839.
- (55) Zhang, Q.; Cao, F.; Liu, W.; Lukas, K.; Yu, B.; Chen, S.; Opeil, C.; Broido, D.; Chen, G.; Ren, Z. Heavy Doping and Band Engineering by Potassium to Improve the Thermoelectric Figure of Merit in P-Type PbTe, PbSe, and PbTe<sub>1-y</sub>Se<sub>y</sub>. *J. Am. Chem. Soc.* **2012**, 134 (24), 10031–10038.
- (56) Ohta, M.; Biswas, K.; Lo, S.-H.; He, J.; Chung, D. Y.; Dravid, V. P.; Kanatzidis, M. G. Enhancement of Thermoelectric Figure of Merit by the Insertion of MgTe Nanostructures in P-Type PbTe Doped with Na<sub>2</sub>Te. *Adv. Energy Mater.* **2012**, 2 (9), 1117–1123.

- (57) Jood, P.; Ohta, M.; Kunii, M.; Hu, X.; Nishiata, H.; Yamamoto, A.; Kanatzidis, M. G. Enhanced Average Thermoelectric Figure of Merit of N-Type  $\text{PbTe}_{1-x}\text{I}_x\text{-MgTe}$ . *J. Mater. Chem. C* **2015**, *3* (40), 10401–10408.
- (58) Qian Zhang, Y. L. Increased Thermoelectric Performance by Cl Doping in Nanostructured  $\text{AgPb}_{18}\text{SbSe}_{20-x}\text{Cl}_x$ . *Nano Energy* **2013**, *2* (6), 1121–1127.
- (59) Wang, H.; Bahk, J.-H.; Kang, C.; Hwang, J.; Kim, K.; Kim, J.; Burke, P.; Bowers, J. E.; Gossard, A. C.; Shakouri, A.; et al. Right Sizes of Nano- and Microstructures for High-Performance and Rigid Bulk Thermoelectrics. *Proc. Natl. Acad. Sci.* **2014**, *111* (30), 10949–10954.
- (60) Zhang, L.; Wang, J.; Cheng, Z.; Sun, Q.; Li, Z.; Dou, S. Lead-Free SnTe-Based Thermoelectrics: Enhancement of Thermoelectric Performance by Doping with Gd/Ag. *J. Mater. Chem. A* **2016**, *4* (20), 7936–7942.
- (61) Banik, A.; Shenoy, U. S.; Anand, S.; Waghmare, U. V.; Biswas, K. Mg Alloying in SnTe Facilitates Valence Band Convergence and Optimizes Thermoelectric Properties. *Chem. Mater.* **2015**, *27* (2), 581–587.
- (62) Banik, A.; Biswas, K. AgI Alloying in SnTe Boosts the Thermoelectric Performance via Simultaneous Valence Band Convergence and Carrier Concentration Optimization. *J. Solid State Chem.* **2016**, *242*, Part 2, 43–49.
- (63) Banik, A.; Vishal, B.; Perumal, S.; Datta, R.; Biswas, K. The Origin of Low Thermal Conductivity in  $\text{Sn}_{1-x}\text{Sb}_x\text{Te}$ : Phonon Scattering via Layered Intergrowth Nanostructures. *Energy Environ. Sci.* **2016**, *9* (6), 2011–2019.
- (64) Al Rahal Al Orabi, R.; Mecholsky, N. A.; Hwang, J.; Kim, W.; Rhyee, J.-S.; Wee, D.; Fornari, M. Band Degeneracy, Low Thermal Conductivity, and High Thermoelectric Figure of Merit in SnTe–CaTe Alloys. *Chem. Mater.* **2016**, *28* (1), 376–384.
- (65) Zhang, Q.; Liao, B.; Lan, Y.; Lukas, K.; Liu, W.; Esfarjani, K.; Opeil, C.; Broido, D.; Chen, G.; Ren, Z. High Thermoelectric Performance by Resonant Dopant Indium in Nanostructured SnTe. *Proc. Natl. Acad. Sci.* **2013**, *110* (33), 13261–13266.



# **Chapter 7**

**Detrimental Effects of Doping Al and Ba on the Thermoelectric  
Performance of GeTe**



## 7.1 Introduction

GeTe based materials have emerged as a clear alternative choice to PbTe, as they have proven to exhibit higher performance ( $zT > 1$ ), if optimally doped with suitable elements.<sup>1</sup> Some of the strategies for GeTe-based materials to enhance the power factor ( $S^2\sigma$ ) and/or to suppress  $\kappa_{\text{latt}}$  were adopted on compositions such as GeTe-AgSbTe<sub>2</sub> (TAGS),<sup>2</sup> GeTe-LiSbTe<sub>2</sub>,<sup>3</sup> GeTe-AgInTe<sub>2</sub>,<sup>4</sup> GeTe-AgSbSe<sub>2</sub>,<sup>5</sup> (GeTe)<sub>n</sub>Sb<sub>2</sub>Te<sub>3</sub>,<sup>6</sup> Ge<sub>1-x</sub>Pb<sub>x</sub>Te,<sup>7</sup> Ge<sub>1-x</sub>Bi<sub>x</sub>Te,<sup>8</sup> (Bi<sub>2</sub>Te<sub>3</sub>)<sub>n</sub>Ge<sub>1-x</sub>Pb<sub>x</sub>Te,<sup>9</sup> Ge<sub>1-x</sub>In<sub>x</sub>Te,<sup>10</sup> GeTe<sub>1-x</sub>Se,<sup>11</sup> Ge<sub>1-x</sub>Sb<sub>x</sub>Te,<sup>12</sup> Ge<sub>1-x</sub>Ag<sub>x</sub>Te,<sup>13</sup> Ge<sub>1-x</sub>Mn<sub>x</sub>Te,<sup>14</sup> Ge<sub>1-x-y</sub>Sn<sub>x</sub>Pb<sub>y</sub>Te,<sup>15</sup> Ge<sub>1-x</sub>Sb<sub>x</sub>Te<sub>1-y</sub>Se<sub>y</sub>,<sup>16</sup> GeTe-GeSe-GeS,<sup>17</sup> Ge<sub>1-x-y</sub>Bi<sub>x</sub>Sb<sub>y</sub>Te,<sup>18</sup> Ge<sub>1-x-y</sub>Bi<sub>x</sub>In<sub>y</sub>Te,<sup>19</sup> and more recently Ge<sub>0.9-y</sub>Pb<sub>0.1</sub>Bi<sub>y</sub>Te.<sup>20</sup>

As the coinage metals (Cu, Ag, Au) did not help in improving the thermoelectric  $zT$  in GeTe (Chapter 6), we explored other elements, such as trivalent Al and divalent Ba as dopants for improving the thermoelectric performance of GeTe. In order to evaluate the suitability of Al and Ba as dopant in thermoelectric GeTe, we performed a systematic study on the thermoelectric properties of Ge<sub>1-x</sub>Al<sub>x</sub>Te ( $x = 0 - 0.08$ ) and Ge<sub>1-x</sub>Ba<sub>x</sub>Te ( $x = 0 - 0.06$ ) alloys processed by Spark Plasma Sintering. The results of those study on Al and Ba doped GeTe are presented in this Chapter 7.

The choice of Al is particularly interesting (studied both experimentally and theoretically), as its isoelectronic group-13 counterparts In and Ga, if doped in optimum concentration, have proved to strongly enhance the thermoelectric performance of GeTe.<sup>10,21</sup> The choice of using Ba as a dopant in GeTe was motivated from the work of Orabi *et al.*,<sup>22</sup> where they have shown an improved thermoelectric performance in Ca-doped SnTe.

## 7.2 Materials & Methods

### 7.2.1 Reagents

Ge (Umicore, 5N), Te (JGI, 5N), Al (Aldrich, 4N) and Ba (Sigma Aldrich, 2N) were used for synthesis without involving any further purification process.

### 7.2.2 Synthesis

The samples Ge<sub>1-x</sub>Al<sub>x</sub>Te ( $x = 0 - 0.08$ ) and Ge<sub>1-x</sub>Ba<sub>x</sub>Te ( $x = 0 - 0.06$ ) were synthesized by vacuum sealed-tube melt processing. Appropriate stoichiometric amounts of the starting elements of Ge, Ag and Te were introduced into a silica tube that had previously been cleaned with hydrofluoric



(HF) acid, rinsed with distilled water and dried under vacuum. The ampules were sealed under a vacuum of  $10^{-6}$  Torr, then placed in a rocking furnace and slowly heated up to 950 °C over a period of 12 hours, then held at that temperature for 12 hours and slowly cooled down to room temperature over 24 hours.

The obtained ingots were crushed into powder and consolidated by Spark Plasma sintering, SPS (FCT Systeme GmbH) at 773 K for 5 mins under an axial pressure of 60 MPa. The obtained sintered discs were cut and polished to required shapes and dimensions for various thermoelectric measurements.

### 7.2.3 Computational Procedures

Density Functional Theory (DFT) calculations were performed to understand the effect of doping on the electronic states. We used the projector-augmented-wave (PAW) approach<sup>23</sup> implemented in the Vienna ab initio simulation package (VASP).<sup>24</sup> Calculations were performed using generalized gradient approximation (GGA) for the exchange-correlation term parametrized by J. P. Perdew *et al.*<sup>25</sup> Spin orbit coupling was included in the computation.

As we were interested in high temperature behavior of doped GeTe, calculations were performed on the cubic structural models. Impurities were substituted to Ge atom in a  $4 \times 4 \times 4$  super-cell. In order to understand the effect of Al, the calculations were performed on  $\text{Al}_2\text{Ge}_{62}\text{Te}_{64}$  model (which is close to the experimental  $\text{Ge}_{0.97}\text{Al}_{0.03}\text{Te}$  composition). The distance between two Al atoms was 12.02 Å. For the irreducible cell, the Brillouin-zone integration was performed using a  $25 \times 25 \times 25$  Monkhorst-Pack  $k$ -mesh. For the super cell, we used a  $3 \times 3 \times 3$   $k$ -mesh for the atomic relaxation and a  $7 \times 7 \times 7$   $k$ -mesh for the electronic density of states (DOS) calculations.

## 7.3 Results & Discussion

### 7.3.1 Structural Analysis

The sharp reflections observed from XRD patterns for Al and Ba doped GeTe (Figure 7.1 and 7.2, respectively) indicate the crystalline nature of the phases. The main reflections in both cases could be indexed to the rhombohedral ( $R3m$ ) GeTe phase (PDF# 00-047-1079). The rhombohedral phase was further confirmed by the presence of double reflections  $[(0\ 2\ 4)$  and  $(2\ 2\ 0)]$  in the range of  $2\theta$  values between  $41^\circ$  and  $44^\circ$ . Minor proportion of Ge-rich secondary phase was also present, as

in agreement with the previous studies.<sup>13</sup> The  $\text{Al}_2\text{Te}_3$  secondary phase appeared at higher content of Al (for  $x > 0.04$ ). The solubility limit for Ba in GeTe was found to be minimum, as  $\text{Ba}_2\text{Ge}_2\text{Te}_5$  phase existed in all the samples. This is unsurprising given the larger atomic radii of Ba compared to that of Ge.

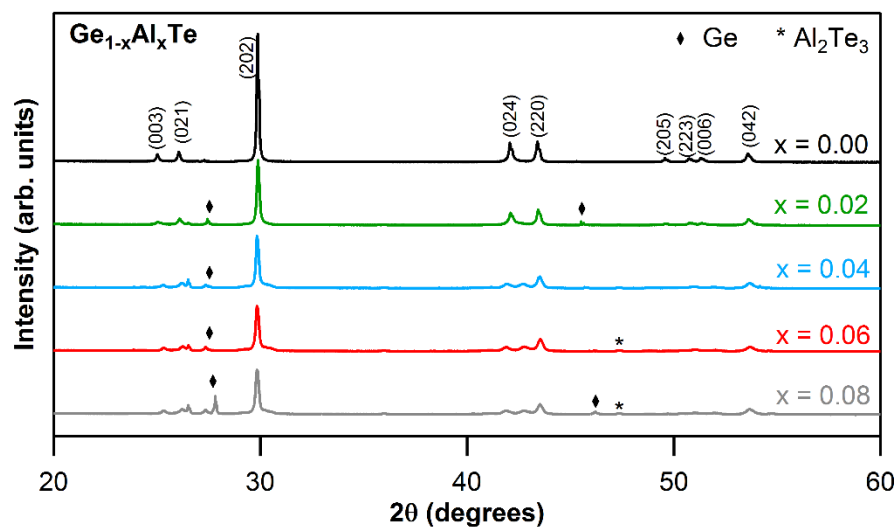


Figure 7.1 XRD patterns for  $\text{Ge}_{1-x}\text{Al}_x\text{Te}$  ( $x = 0.00 - 0.08$ ) system.

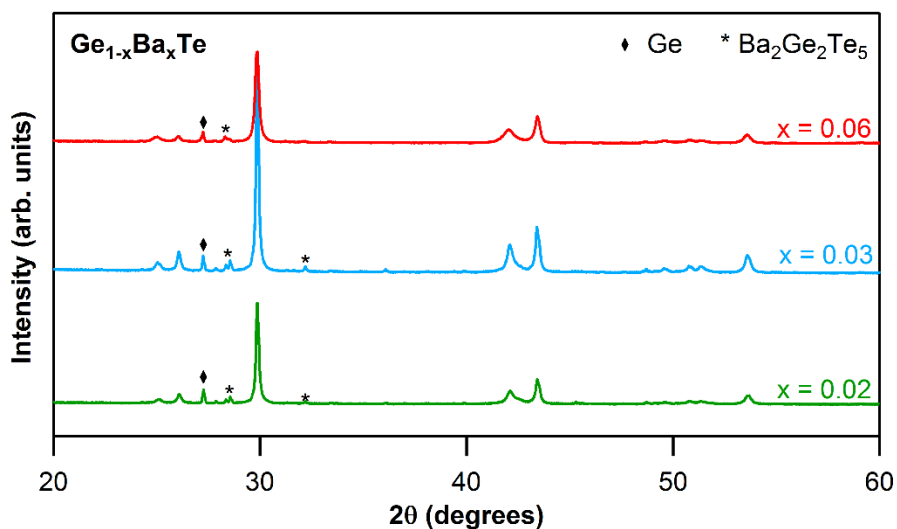


Figure 7.2 XRD patterns for  $\text{Ge}_{1-x}\text{Ba}_x\text{Te}$  ( $x = 0.02 - 0.06$ ) system.

### 7.3.2 Thermoelectric Properties of $\text{Ge}_{1-x}\text{Al}_x\text{Te}$ and $\text{Ge}_{1-x}\text{Ba}_x\text{Te}$ Systems

Results from Hall measurements tabulating carrier concentration ( $n$ ) and mobility ( $\mu$ ) are presented in Table 7.1. Holes are the major charge carriers ( $p$ -type), as the Hall voltage was found to be positive ( $p$ -type) in both  $\text{Ge}_{1-x}\text{Al}_x\text{Te}$  and  $\text{Ge}_{1-x}\text{Ba}_x\text{Te}$  systems. Doping Al to GeTe provides extra holes to the system, which is reflected in the enhancement in charge carrier density. This is in contrast to the effect observed in In and Ga (isoelectronic with Al) doped GeTe, where In and Ga decreased the hole concentration by filling up Ge vacancies.<sup>10,21</sup> On the other hand, the mobility reduction can be attributed to the alloy scattering mechanism arising from the doping of Al and Ba to GeTe.<sup>26</sup>

**Table 7.1** Hall measurement results (at  $\sim 300$  K) of carrier concentration ( $n$ ) and mobility ( $\mu$ ) for  $\text{Ge}_{1-x}\text{Al}_x\text{Te}$  ( $x = 0.00 - 0.08$ ) and  $\text{Ge}_{1-x}\text{Ba}_x\text{Te}$  ( $x = 0.00 - 0.06$ ) samples.

Sample	Carrier Concentration, $n$ ( $\text{cm}^{-3}$ )	Mobility, $\mu$ ( $\text{cm}^2\text{V}^{-1}\text{s}^{-1}$ )
GeTe	$9.08 \times 10^{20}$	57.0
$\text{Ge}_{0.98}\text{Al}_{0.02}\text{Te}$	$1.75 \times 10^{21}$	21.8
$\text{Ge}_{0.96}\text{Al}_{0.04}\text{Te}$	$2.88 \times 10^{21}$	10.6
$\text{Ge}_{0.94}\text{Al}_{0.06}\text{Te}$	$2.17 \times 10^{21}$	12.5
$\text{Ge}_{0.92}\text{Al}_{0.08}\text{Te}$	$3.01 \times 10^{21}$	8.8
$\text{Ge}_{0.98}\text{Ba}_{0.02}\text{Te}$	$9.78 \times 10^{20}$	28.2
$\text{Ge}_{0.97}\text{Ba}_{0.03}\text{Te}$	$9.06 \times 10^{20}$	33.6
$\text{Ge}_{0.94}\text{Ba}_{0.06}\text{Te}$	$1.62 \times 10^{21}$	16.2

Due to decreased mobility, the electrical conductivity at room temperature was decreased for both  $\text{Ge}_{1-x}\text{Al}_x\text{Te}$  (Figure 7.3.a) and  $\text{Ge}_{1-x}\text{Ba}_x\text{Te}$  (Figure 7.4.a) systems with respect to that of GeTe. However, this trend was reversed at higher temperatures (cross over point at  $\sim 450$  K) for Al doped GeTe (Figure 7.3.a). Such similar cases were reported for SnTe and PbTe based materials, and those cross over effects were attributed to the changes in the electronic band structure with increasing temperature.<sup>27,28</sup> The electrical conductivity of all the samples decreased with increasing temperature, which suggests a degenerate semi-conducting behavior. The positive Seebeck coefficient confirmed the  $p$ -type charge carriers in Al and Ba doped GeTe (Figure 7.3.b and 7.4.b), which was consistent with the Hall measurement results. The thermopowers of  $\text{Ge}_{1-x}\text{Al}_x\text{Te}$  and  $\text{Ge}_{1-x}\text{Ba}_x\text{Te}$  monotonically increased with temperature. With increasing Al and Ba content, the change in  $S$ -values at room temperature was not much evident, but they decreased significantly with increasing

temperature, when compared to pristine GeTe. Doping of Al and Ba to GeTe decreased the S-values, as it drastically inflated the hole carrier concentration. Consequently, the reduction of Seebeck coefficient with Al and Ba content also considerably affected the thermoelectric power factor (Figure 7.3.c and 7.4.c).

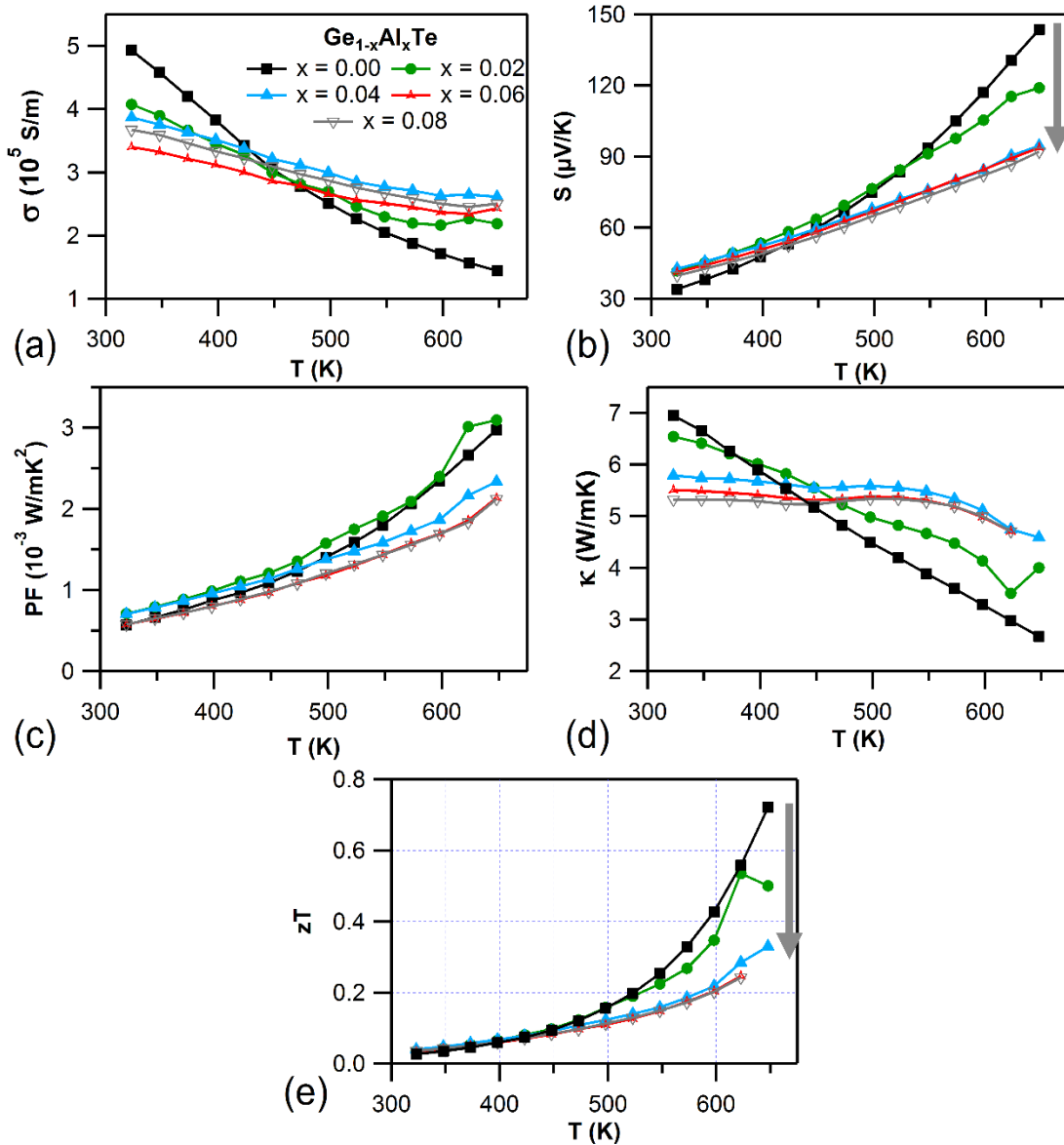


**Figure 7.3** Temperature-dependent (a) electrical conductivity ( $\sigma$ ), (b) Seebeck coefficient ( $S$ ), and (c) power factor ( $\text{PF} = S^2\sigma$ ), (d) total thermal conductivity ( $\kappa$ ), (e) figure of merit ( $zT$ ) for  $\text{Ge}_{1-x}\text{Al}_x\text{Te}$  ( $x = 0.00 - 0.08$ ) samples.

Finally, with Al and Ba doping, the total thermal conductivity decreased considerably at room temperature (Figure 7.3.d and 7.4.d). However, it remained almost constant with temperature for Al-doped GeTe. The decreased thermopower significantly affected the thermoelectric figure of merit,  $zT$  (Figures 7.3.e and 7.4.e), which plunged with dopant concentration.

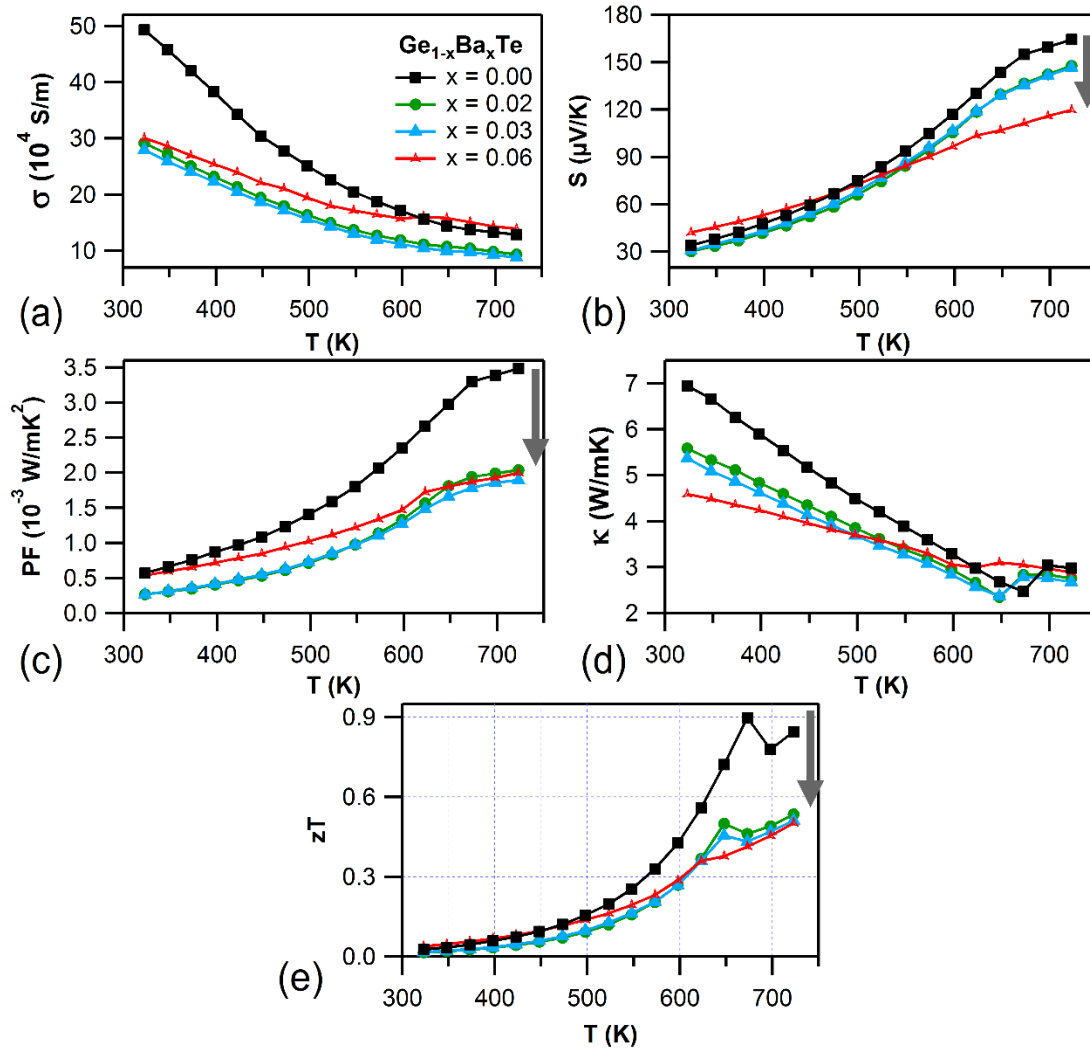


**Figure 7.4** Temperature-dependent (a) electrical conductivity ( $\sigma$ ), (b) Seebeck coefficient ( $S$ ), and (c) power factor ( $\text{PF} = S^2\sigma$ ), (d) total thermal conductivity ( $\kappa$ ), (e) figure of merit ( $zT$ ) for  $\text{Ge}_{1-x}\text{Ba}_x\text{Te}$  ( $x = 0.00 - 0.06$ ) samples.

### 7.3.3 Investigation of Electronic Band Structures and Density of States

To have a more cogent understanding on the detrimental effects of these dopants in GeTe, DFT calculations were performed. As we were interested in the high temperature domain for thermoelectric application, these DFT calculations were carried out on  $4 \times 4 \times 4$  supercells derived from the cubic structural arrangement of GeTe. The electronic DOS computed for the cubic models of pristine and Al doped GeTe ( $\text{Al}_2\text{Ge}_{62}\text{Te}_{64} \approx \text{Ge}_{0.97}\text{Al}_{0.03}\text{Te}$ ) are shown and compared in Figure 7.5.a. The Al-induced resonant states (distinctly indicated by a sharp hump) are present around the Fermi level, just like for its isoelectronic counterparts In and Ga.<sup>10,21</sup> In such a situation, the Seebeck coefficient is expected to increase, which is not the case with Al (Figure 7.3.b).

Since the DOS calculations yielded inconclusive evidence, electronic band structures were computed to decipher the role of Al in GeTe. The band structures are plotted in Figure 7.5 along some high symmetry lines of the cubic Brillouin zone (BZ). The energy difference between light and heavy hole valence bands ( $\Delta E_{L\Sigma}$ ) for undoped cubic  $\text{Ge}_{64}\text{Te}_{64}$  was found to be 64 meV, consistent with a recent report.<sup>29</sup> The flat and localized Al bands are located within the principal band gap (Figure 7.5.d). Al doping in GeTe increased the energy separation between the light hole and heavy hole valence bands to 179 meV (180% increment in  $\Delta E_{L\Sigma}$  when compared to pristine c-GeTe), thus disfavoring the band convergence. According to Mott's relationship, Seebeck coefficient strongly depends on the total DOS effective mass, which in fact is directly proportional to the product of  $N_v^{2/3}$  and the average DOS effective mass for each pocket ( $N_v$  is the number of degenerate carrier pockets).<sup>30</sup> For GeTe,  $N_v$  is 4 for the L band and it increases to 12 for the  $\Sigma$  band.<sup>12</sup> Hence by increasing the energy separation between L and  $\Sigma$  bands by doping of Al to GeTe, the contributions from the additional carriers (from  $\Sigma$  valence band) to electrical transport is lost, thus resulting in a significant reduction in the Seebeck coefficient.

For composition at  $x = 0.02$ , Al-doped GeTe exhibits a thermopower of  $\sim 110 \mu\text{V/K}$  at 623 K. For the same level of doping, the isoelectronic In-doped GeTe is known to exhibit a much higher thermopower of  $\sim 200 \mu\text{V/K}$  at the same temperature.<sup>10</sup>  $\Delta E_{L\Sigma}$  for the In-doped GeTe (for  $\text{InGe}_{63}\text{Te}_{64} \approx \text{Ge}_{0.98}\text{In}_{0.02}\text{Te}$  model) is calculated to be 95 meV, which is almost two times lower than the  $\Delta E_{L\Sigma}$  for Al-doped GeTe. The band structure plot for In-doped GeTe is provided in Annexure 7 (Figure A7.3). It must be noted that, even though the  $\Delta E_{L\Sigma}$  for In-doped GeTe is marginally higher than that of pristine GeTe, the presence of In-induced resonant states near the Fermi level has helped it to exhibit a superior thermopower compared to pristine GeTe. But for the Al-doped GeTe, the beneficial effect of the presence of Al-induced resonant states near the  $E_F$  is nullified and severely affected by the

extremely large energy separation between the light hole and heavy hole valence bands (179 meV). This explains the juxtaposition of high thermoelectric performance of  $\text{Ge}_{0.98}\text{In}_{0.02}\text{Te}$  and low thermoelectric performance of  $\text{Ge}_{0.98}\text{Al}_{0.02}\text{Te}$  (isoelectronic) compounds.

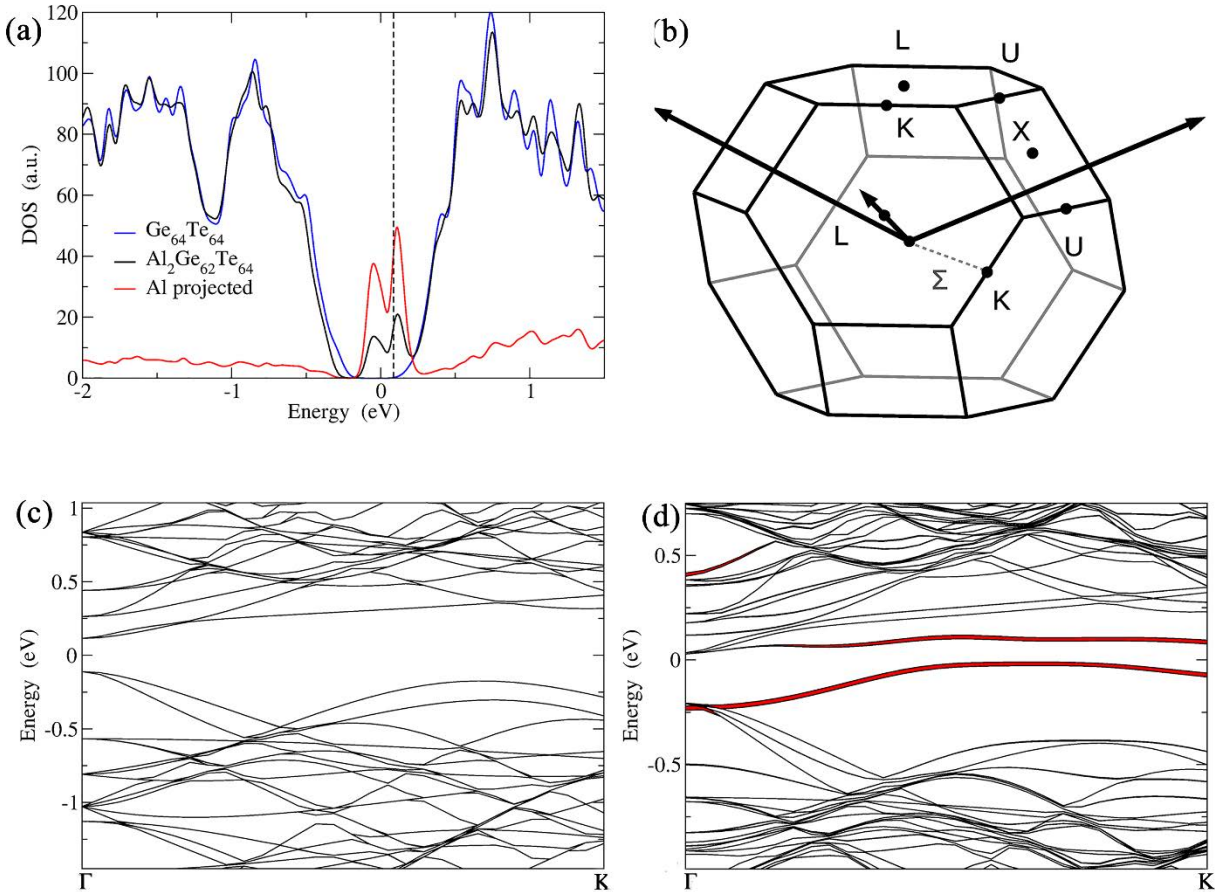


**Figure 7.5** (a) Calculated DOS for  $\text{Al}_2\text{Ge}_{62}\text{Te}_{64}$  ( $\text{Ge}_{0.97}\text{Al}_{0.03}\text{Te}$ ) model, which is compared with that of the pristine cubic phase  $\text{Ge}_{64}\text{Te}_{64}$  ( $c\text{-GeTe}$ ). The Fermi level ( $E_F$ ) of pristine  $c\text{-GeTe}$  is set arbitrarily at 0 eV. The dashed line represents the shifted Fermi level for the doped compositions. Additional Gaussian smearing of 25 meV was applied and the Al projected DOS is magnified for a better readability of the curves. (b) Brillouin zone of  $c\text{-GeTe}$ . Band structures for (c)  $c\text{-Ge}_{64}\text{Te}_{64}$  using a  $4 \times 4 \times 4$  supercell showing band folding in the  $\Gamma \rightarrow K$  ( $\Sigma$ ) direction, and (d)  $\text{Al}_2\text{Ge}_{62}\text{Te}_{64}$  ( $\text{Ge}_{0.97}\text{Al}_{0.03}\text{Te}$ ) highlighting Al projections. Line thickness is proportional to the projection of the wave function on the Al (in red) orbitals.

For the case of Ba doped GeTe, though the DFT results were inconclusive in portraying a clearer picture to explain the reduction in thermopower, it can be attributed to the presence of the

secondary phase ( $\text{Ba}_2\text{Ge}_2\text{Te}_5$ ). More in depth studies, like experiments to synthesize this  $\text{Ba}_2\text{Ge}_2\text{Te}_5$  phase and measure its transport properties (to estimate the role of contribution of that secondary phase to the overall thermoelectric behavior of the  $\text{Ge}_{1-x}\text{Ba}_x\text{Te}$  compound), are required to understand the causes for Ba doped GeTe to exhibit lower TE performance.

#### 7.4 Conclusion

The crystalline ingots of  $\text{Ge}_{1-x}\text{Al}_x\text{Te}$  ( $x = 0 - 0.08$ ) and  $\text{Ge}_{1-x}\text{Ba}_x\text{Te}$  ( $x = 0 - 0.06$ ) were prepared by the vacuum-sealed tube melting route, followed by Spark Plasma Sintering processing. Al and Ba are found to be not the best choice of dopants for GeTe, as they subside its thermoelectric performance. Al doping, unlike other isoelectronic group-13 elements (In and Ga), inflates the hole concentration and drastically increases the energy separation between light and heavy hole bands in GeTe, thus resulting in a reduced thermopower.

➤ **Adaptation**

The results presented in this chapter have been published in the special issue “*Advanced Glasses, Composites and Ceramics for High Growth Industries*” in Materials (MDPI). Hence, this chapter is an adaptation from that publication – **B. Srinivasan *et al.*, Materials, 2018, 11, 2237.**

➤ **Author Contributions**

B.S. designed and performed experiments, analyzed the results, and wrote the journal manuscript. B.S. also wrote the explanations pertaining to the theoretical (DFT) results. The DFT computations were performed by Dr. Alain Gellé (IPR Rennes).

#### References

- (1) Perumal, S.; Roychowdhury, S.; Biswas, K. High Performance Thermoelectric Materials and Devices Based on GeTe. *J. Mater. Chem. C* **2016**, 4 (32), 7520–7536.



- (2) Yang, S. H.; Zhu, T. J.; Sun, T.; He, J.; Zhang, S. N.; Zhao, X. B. Nanostructures in High-Performance  $(\text{GeTe})_x(\text{AgSbTe}_2)_{100-x}$  Thermoelectric Materials. *Nanotechnology* **2008**, *19* (24), 245707.
- (3) Schröder, T.; Schwarzmüller, S.; Stiewe, C.; de Boor, J.; Hölzel, M.; Oeckler, O. The Solid Solution Series  $(\text{GeTe})_x(\text{LiSbTe}_2)_2$  ( $1 \leq x \leq 11$ ) and the Thermoelectric Properties of  $(\text{GeTe})_{11}(\text{LiSbTe}_2)_2$ . *Inorg. Chem.* **2013**, *52* (19), 11288–11294.
- (4) Schröder, T.; Rosenthal, T.; Giesbrecht, N.; Maier, S.; Scheidt, E.-W.; Scherer, W.; Snyder, G. J.; Schnick, W.; Oeckler, O. TAGS-Related Indium Compounds and Their Thermoelectric Properties – the Solid Solution Series  $(\text{GeTe})_x\text{AgIn}_y\text{Sb}_{1-y}\text{Te}_2$  ( $x = 1-12$ ;  $y = 0.5$  and  $1$ ). *J. Mater. Chem. A* **2014**, *2* (18), 6384–6395.
- (5) Samanta, M.; Roychowdhury, S.; Ghatak, J.; Perumal, S.; Biswas, K. Ultrahigh Average Thermoelectric Figure of Merit, Low Lattice Thermal Conductivity and Enhanced Microhardness in Nanostructured  $(\text{GeTe})_x(\text{AgSbSe}_2)_{100-x}$ . *Chem. Eur. J.* **2017**, *23*, 7438–7443.
- (6) Fahrnbauer, F.; Souchay, D.; Wagner, G.; Oeckler, O. High Thermoelectric Figure of Merit Values of Germanium Antimony Tellurides with Kinetically Stable Cobalt Germanide Precipitates. *J. Am. Chem. Soc.* **2015**, *137* (39), 12633–12638.
- (7) Gelbstein, Y.; Davidow, J. Highly Efficient Functional  $\text{Ge}_x\text{Pb}_{1-x}\text{Te}$  Based Thermoelectric Alloys. *Phys. Chem. Chem. Phys.* **2014**, *16* (37), 20120–20126.
- (8) Perumal, S.; Roychowdhury, S.; Biswas, K. Reduction of Thermal Conductivity through Nanostructuring Enhances the Thermoelectric Figure of Merit in  $\text{Ge}_{1-x}\text{Bi}_x\text{Te}$ . *Inorg. Chem. Front.* **2016**, *3* (1), 125–132.
- (9) Wu, D.; Zhao, L.-D.; Hao, S.; Jiang, Q.; Zheng, F.; Doak, J. W.; Wu, H.; Chi, H.; Gelbstein, Y.; Uher, C.; et al. Origin of the High Performance in GeTe-Based Thermoelectric Materials upon  $\text{Bi}_2\text{Te}_3$  Doping. *J. Am. Chem. Soc.* **2014**, *136* (32), 11412–11419.
- (10) Wu, L.; Li, X.; Wang, S.; Zhang, T.; Yang, J.; Zhang, W.; Chen, L.; Yang, J. Resonant Level-Induced High Thermoelectric Response in Indium-Doped GeTe. *NPG Asia Mater.* **2017**, *9* (1), e343.
- (11) Yang, L.; Li, J. Q.; Chen, R.; Li, Y.; Liu, F. S.; Ao, W. Q. Influence of Se Substitution in GeTe on Phase and Thermoelectric Properties. *J. Electron. Mater.* **2016**, *45* (11), 5533–5539.
- (12) Perumal, S.; Roychowdhury, S.; Negi, D. S.; Datta, R.; Biswas, K. High Thermoelectric Performance and Enhanced Mechanical Stability of P-Type  $\text{Ge}_{1-x}\text{Sb}_x\text{Te}$ . *Chem. Mater.* **2015**, *27* (20), 7171–7178.

- (13) Srinivasan, B.; Gautier, R.; Gucci, F.; Fontaine, B.; Halet, J.-F.; Cheviré, F.; Boussard-Pledel, C.; Reece, M. J.; Bureau, B. Impact of Coinage Metal Insertion on the Thermoelectric Properties of GeTe Solid-State Solutions. *J. Phys. Chem. C* **2018**, *122* (1), 227–235.
- (14) Lee, J. K.; Oh, M. W.; Kim, B. S.; Min, B. K.; Lee, H. W.; Park, S. D. Influence of Mn on Crystal Structure and Thermoelectric Properties of GeTe Compounds. *Electron. Mater. Lett.* **2014**, *10* (4), 813–817.
- (15) Rosenberg, Y.; Gelbstein, Y.; Dariel, M. P. Phase Separation and Thermoelectric Properties of the  $\text{Pb}_{0.25}\text{Sn}_{0.25}\text{Ge}_{0.5}\text{Te}$  Compound. *J. Alloys Comps.* **2012**, *526*, 31–38.
- (16) Li, J.; Zhang, X.; Lin, S.; Chen, Z.; Pei, Y. Realizing the High Thermoelectric Performance of GeTe by Sb-Doping and Se-Alloying. *Chem. Mater.* **2017**, *29* (2), 605–611.
- (17) Samanta, M.; Biswas, K. Low Thermal Conductivity and High Thermoelectric Performance in  $(\text{GeTe})_{1-2x}(\text{GeSe})_x(\text{GeS})_x$ : Competition between Solid Solution and Phase Separation. *J. Am. Chem. Soc.* **2017**, *139* (27), 9382–9391.
- (18) Perumal, S.; Bellare, P.; Shenoy, U. S.; Waghmare, U. V.; Biswas, K. Low Thermal Conductivity and High Thermoelectric Performance in Sb and Bi Codoped GeTe: Complementary Effect of Band Convergence and Nanostructuring. *Chem. Mater.* **2017**, *29* (24), 10426–10435.
- (19) Srinivasan, B.; Boussard-Pledel, C.; Bureau, B. Thermoelectric Performance of Codoped (Bi, In)-GeTe and (Ag, In, Sb)-SnTe Materials Processed by Spark Plasma Sintering. *Mater. Lett.* **2018**, *230*, 191–194.
- (20) Li, J.; Zhang, X.; Chen, Z.; Lin, S.; Li, W.; Shen, J.; Witting, I. T.; Faghaninia, A.; Chen, Y.; Jain, A.; et al. Low-Symmetry Rhombohedral GeTe Thermoelectrics. *Joule* **2018**, *2* (5), 976–987.
- (21) Srinivasan, B.; Gellé, A.; Gucci, F.; Boussard-Pledel, C.; Fontaine, B.; Gautier, R.; Halet, J.-F.; Reece, M.; Bureau, B. Realizing a Stable High Thermoelectric  $ZT \sim 2$  over a Broad Temperature Range in  $\text{Ge}_{1-x-y}\text{Ga}_x\text{Sb}_y\text{Te}$  via Band Engineering and Hybrid Flash-SPS Processing. *Inorg. Chem. Front.* **2018**. In Press.
- (22) Al Rahal Al Orabi, R.; Mecholsky, N. A.; Hwang, J.; Kim, W.; Rhyee, J.-S.; Wee, D.; Fornari, M. Band Degeneracy, Low Thermal Conductivity, and High Thermoelectric Figure of Merit in SnTe–CaTe Alloys. *Chem. Mater.* **2016**, *28* (1), 376–384.
- (23) Kresse, G.; Joubert, D. From Ultrasoft Pseudopotentials to the Projector Augmented-Wave Method. *Phys. Rev. B* **1999**, *59* (3), 1758–1775.
- (24) Kresse, G.; Furthmüller, J. Efficient Iterative Schemes for Ab Initio Total-Energy Calculations Using a Plane-Wave Basis Set. *Phys. Rev. B* **1996**, *54* (16), 11169–11186.

- (25) Perdew, J. P.; Burke, K.; Ernzerhof, M. Generalized Gradient Approximation Made Simple. *Phys. Rev. Lett.* **1996**, *77* (18), 3865–3868.
- (26) Wang, H.; LaLonde, A. D.; Pei, Y.; Snyder, G. J. The Criteria for Beneficial Disorder in Thermoelectric Solid Solutions. *Adv. Funct. Mater.* **2013**, *23* (12), 1586–1596.
- (27) Roychowdhury, S.; Shenoy, U. S.; Waghmare, U. V.; Biswas, K. Tailoring of Electronic Structure and Thermoelectric Properties of a Topological Crystalline Insulator by Chemical Doping. *Angew. Chem. Int. Ed.* **2015**, *54* (50), 15241–15245.
- (28) Zhang, L. J.; Qin, P.; Han, C.; Wang, J. L.; Ge, Z. H.; Sun, Q.; Cheng, Z. X.; Li, Z.; Dou, S. X. Enhanced Thermoelectric Performance through Synergy of Resonance Levels and Valence Band Convergence via Q/In (Q = Mg, Ag, Bi) Co-Doping. *J. Mater. Chem. A* **2018**, *6* (6), 2507–2516.
- (29) Hong, M.; Chen, Z.-G.; Yang, L.; Zou, Y.-C.; Dargusch, M. S.; Wang, H.; Zou, J. Realizing ZT of 2.3 in  $\text{Ge}_{1-x-y}\text{Sb}_x\text{In}_y\text{Te}$  via Reducing the Phase-Transition Temperature and Introducing Resonant Energy Doping. *Adv. Mater.* **2018**, *30* (11), 1705942.
- (30) Pei, Y.; Shi, X.; LaLonde, A.; Wang, H.; Chen, L.; Snyder, G. J. Convergence of Electronic Bands for High Performance Bulk Thermoelectrics. *Nature* **2011**, *473* (7345), 66–69.





# **Chapter 8**

**Thermoelectric Performance of Codoped (Bi, In)-GeTe and (Ag, In, Sb)-  
SnTe Materials**



## 8.1 Introduction

As mentioned before, amongst the state-of-the-art thermoelectric materials, the extensively studied PbTe based materials are limited by their toxicity for any practical applications, despite their high thermoelectric performance (high  $zT$ ).<sup>1,2</sup> Recently, GeTe and SnTe based materials have emerged as a clear alternative choice, as they have proven to exhibit higher performance ( $zT > 1$ ), if optimally doped with suitable elements.<sup>3-9</sup>

After some unsuccessful attempts with single doping with elements like Ag, Cu, Al, Ba to GeTe (Chapters 6 and 7), Gd, Mg doping to GeTe (not shown in this thesis, but we found them to be detrimental to the thermoelectric performance of GeTe), and also Al, Gd, Ba doping to SnTe (also not shown in this thesis, as they we found them all to be detrimental to the thermoelectric performance of SnTe), the strategy of codoping (doping two or more elements) was adopted, results of which are presented in the current (Chapter 8) and in the next chapter (Chapter 9).

6 mol% Bi doping in GeTe was shown to exhibit  $zT \sim 1.3$  at 723 K,<sup>10</sup> thanks to the collective phonon scattering from nanostructured precipitates and defects, which reduced their lattice thermal conductivity. 2 mol% In doping in GeTe was also shown to exhibit  $zT \sim 1.3$  at 650 K,<sup>11</sup> thanks to the resonant levels induced by In, which enhanced the thermopower. With an objective to take advantage of these effects, if blended together, we tried codoping of Bi and In in GeTe.

Similarly, it has been shown that 15 mol% Sb doping in SnTe has improved the  $zT$  to  $\sim 1$  at 800 K,<sup>6</sup> thanks to the phonon scattering via layered intergrowth nanostructures; and the optimal presence of resonant dopant In in SnTe has helped to achieve a peak  $zT \sim 1.1$  at 873 K;<sup>7</sup> and Ag doping in SnTe has brought in valence band convergence.<sup>12</sup> The improvements achieved with these individual dopants in SnTe, and our foresight to bring in the combined benefits of synergistic band effects and nanostructuring, has inspired us to study the thermoelectric performance of SnTe codoped with Sb, In and Ag.

Hence, in this chapter, a systematic study of the thermoelectric properties of two different codoped material systems: (i) Bi and In codoped GeTe; and (ii) Sb, In and Ag codoped SnTe alloys, processed by Spark Plasma Sintering are presented.



## 8.2 Materials & Methods

### 8.2.1 Reagents

Ge (Umicore, 5N), Bi (Strem Chemicals, 5N), In (Cerac, 5N), Sn (Strem Chemicals, 5N), Sb (Alfa Aesar, 5N), Ag (Strem Chemicals, 4N) and Te (JGI, 5N) were used for synthesis without involving any further purification processes.

### 8.2.2 Synthesis

The samples of  $\text{Ge}_{1-x-y}\text{Bi}_x\text{In}_y\text{Te}$  ( $x = 0.05, 0.07; y = 0.02$ ) and  $\text{Sn}_{1-x-y-z}\text{Sb}_x\text{In}_y\text{Ag}_z\text{Te}$  ( $x = 0.15; y = 0.0025, 0.005; z = 0, 0.0025, 0.005$ ) were synthesized by vacuum sealed-tube melt processing, followed by Spark Plasma Sintering (SPS). The ampules with appropriate stoichiometric amounts of starting elements were sealed under a vacuum of  $10^{-6}$  Torr, then placed in a rocking furnace and slowly heated up to 1223 K over a period of 10 hours, then held at that temperature for 10 hours and slowly cooled down to room temperature over 10 hours. The obtained ingots were crushed into powders and consolidated by SPS (FCT Systeme GmbH) at 773 K for 5 mins under an axial pressure of 60 MPa. Highly dense disc-shaped pellets were obtained with theoretical densities of  $\sim 99\%$  for both the systems. The sintered discs were then cut and polished to required shapes and dimensions for various thermoelectric measurements.

## 8.3 Results and Discussion

### 8.3.1 Structural Analysis

Powder XRD patterns of  $\text{Ge}_{1-x-y}\text{Bi}_x\text{In}_y\text{Te}$  ( $x = 0.05, 0.07; y = 0.02$ ) and  $\text{Sn}_{1-x-y-z}\text{Sb}_x\text{In}_y\text{Ag}_z\text{Te}$  ( $x = 0.15; y = 0.0025, 0.005; z = 0, 0.0025, 0.005$ ) samples are shown in Figure 8.1 and 8.2, respectively. The sharp reflections from XRD for GeTe and SnTe based systems indicate the crystalline nature of the phases.

The main reflections in Figure 8.1 could be indexed to rhombohedral ( $R3m$ ) GeTe phase. The rhombohedral phase was further confirmed by the presence of double reflections [(024) and (220)] in the range of  $2\theta$  values between  $41^\circ$  and  $44^\circ$ .<sup>4,10,13</sup> Minor proportion of Ge-rich secondary phase was

also present, which is consistent with our previous findings on GeTe based systems (reported in Chapters 6, 7 and 9).

In Figure 8.2, the main reflections could be indexed to cubic ( $Fm\bar{3}m$ ) SnTe phase, and the secondary phase closely matched with the pattern of the layered intergrowth Sb-rich compound ( $\text{Sn}_m\text{Sb}_{2n}\text{Te}_{3n+m}$ ).<sup>6</sup>

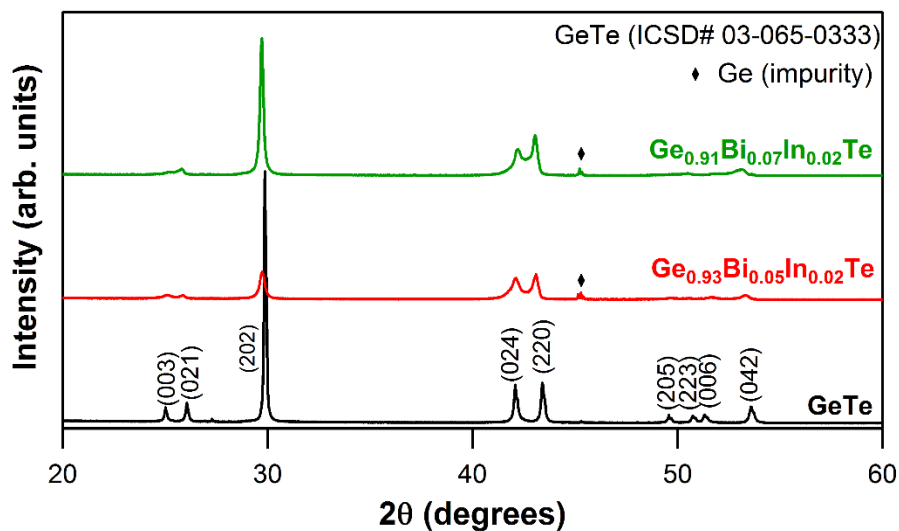


**Figure 8.1** Powder XRD patterns for  $\text{Ge}_{1-x-y}\text{Bi}_x\text{In}_y\text{Te}$  ( $x = 0.05, 0.07$ ;  $y = 0.02$ ) samples.

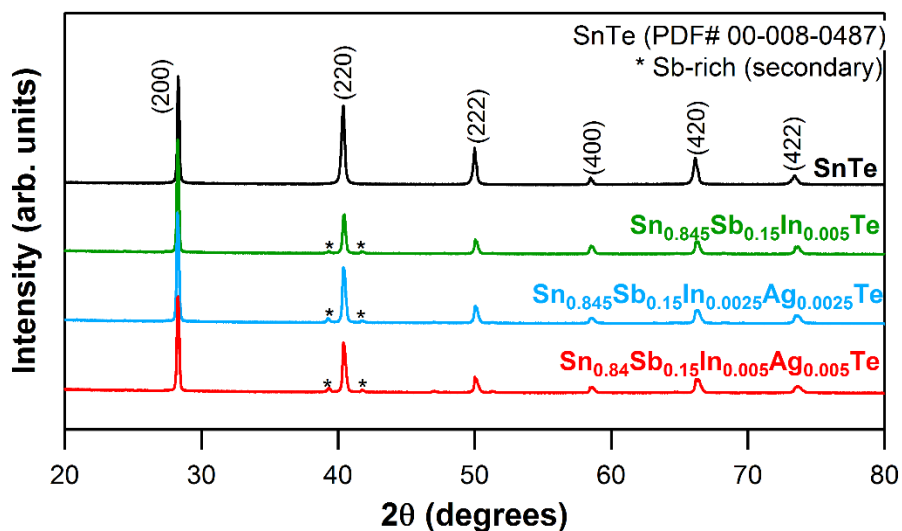


**Figure 8.2** Powder XRD patterns for  $\text{Sn}_{1-x-y-z}\text{Sb}_x\text{In}_y\text{Ag}_z\text{Te}$  ( $x = 0.15$ ;  $y = 0.0025, 0.005$ ;  $z = 0, 0.0025, 0.005$ ) samples.

### 8.3.2 Thermoelectric Properties

The results from Hall measurements tabulating carrier concentration ( $n$ ) and mobility ( $\mu$ ) are presented in Table 8.1. As the Hall voltage was positive in all the samples, holes were the major charge carriers ( $p$ -type) in both GeTe and SnTe codoped systems.

**Table 8.1** Hall measurement results (at 300 K) of carrier concentration,  $n$  and mobility,  $\mu$  for GeTe and SnTe based samples.

Sample	Carrier Concentration, $n$ ( $\text{cm}^{-3}$ )	Mobility, $\mu$ ( $\text{cm}^2\text{V}^{-1}\text{s}^{-1}$ )
GeTe	$1.02 \times 10^{21}$	48.28
$\text{Ge}_{0.93}\text{Bi}_{0.05}\text{In}_{0.02}\text{Te}$	$3.78 \times 10^{20}$	20.17
$\text{Ge}_{0.91}\text{Bi}_{0.07}\text{In}_{0.02}\text{Te}$	$2.21 \times 10^{20}$	16.57
SnTe	$3.52 \times 10^{20}$	480.5
$\text{Sn}_{0.845}\text{Sb}_{0.15}\text{In}_{0.005}\text{Te}$	$4.61 \times 10^{20}$	33.72
$\text{Sn}_{0.845}\text{Sb}_{0.15}\text{In}_{0.0025}\text{Ag}_{0.0025}\text{Te}$	$5.14 \times 10^{20}$	28.65
$\text{Sn}_{0.84}\text{Sb}_{0.15}\text{In}_{0.005}\text{Ag}_{0.005}\text{Te}$	$5.52 \times 10^{20}$	26.98

#### 8.3.2.1 Transport Properties for (Bi, In)-GeTe Codoped System

The electrical and thermal transport properties for  $\text{Ge}_{1-x-y}\text{Bi}_x\text{In}_y\text{Te}$  ( $x = 0.05, 0.07$ ;  $y = 0.02$ ) samples are presented in Figure 8.3. Codoping of Bi and In to GeTe drastically decreased the electrical conductivity (Figure 8.3.a), due to the reduction in carrier density, as evident from the Hall measurement results (Table 8.1). The reduction in hole concentration during codoping in GeTe, which can be attributed to the aliovalent donor dopant natures of  $\text{Bi}^{3+}$  and  $\text{In}^{3+}$  at the  $\text{Ge}^{2+}$  sub-lattices of GeTe, helped to significantly improve the Seebeck coefficient (Figure 8.3.b). This improvement in thermopower is anticipated, as In doping in GeTe is known to create resonant state near the Fermi-level ( $E_F$ ).<sup>11</sup> The power factor,  $\text{PF} = \sigma^2 S$  is presented in Figure 8.3.c. The total thermal conductivity ( $\kappa$ ) was remarkably reduced by codoping of Bi and In to GeTe (Figure 8.3.d). This huge decrease in  $\kappa$  arises from the cumulative decrease of both electronic ( $\kappa_e$ ) and lattice ( $\kappa_{\text{latt}}$ ) contributions, as shown in the Figures 8.3.e and 8.3.f. Decreased carrier density is the key cause for suppression of  $\kappa_e$ , while nanostructuring can be the reason for suppression of lattice contribution, as both Bi doping in

GeTe<sup>10,14</sup> and SPS processing are known to create nano-scale defect layers and precipitates, which are effective phonon scatterers. Bi and In codoping in GeTe has helped to concurrently improve the thermopower and suppress the thermal transport.

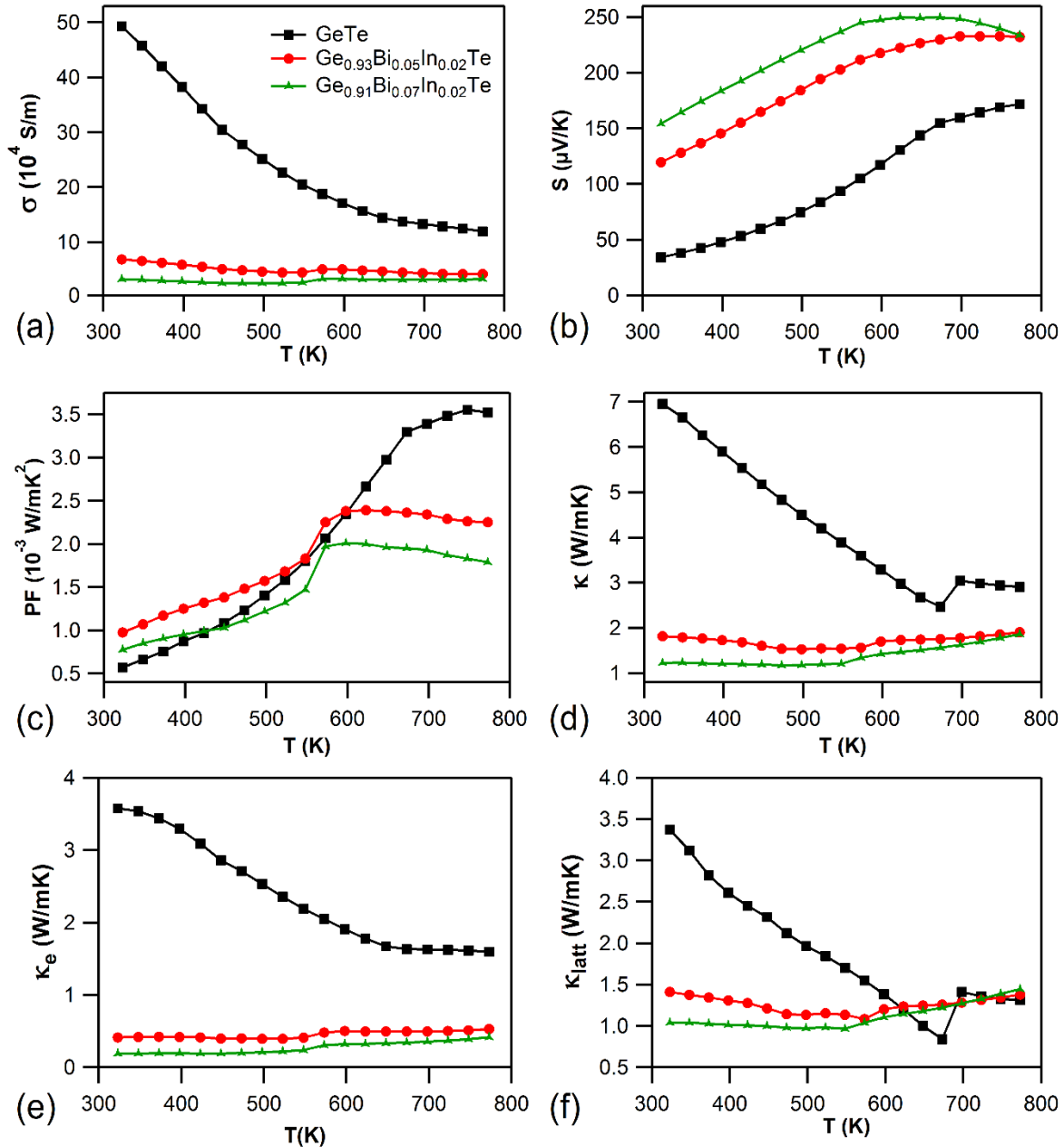


**Figure 8.3.** Temperature dependent transport properties for codoped GeTe based system.

## 8.3.2.2 Transport Properties for (Ag, In, Sb)-SnTe Codoped System

The electrical and thermal transport properties for  $\text{Sn}_{1-x-y-z}\text{Sb}_x\text{In}_y\text{Ag}_z\text{Te}$  ( $x = 0.15$ ;  $y = 0.0025$ ,  $0.005$ ;  $z = 0, 0.0025, 0.005$ ) samples are presented in Figure 8.4.

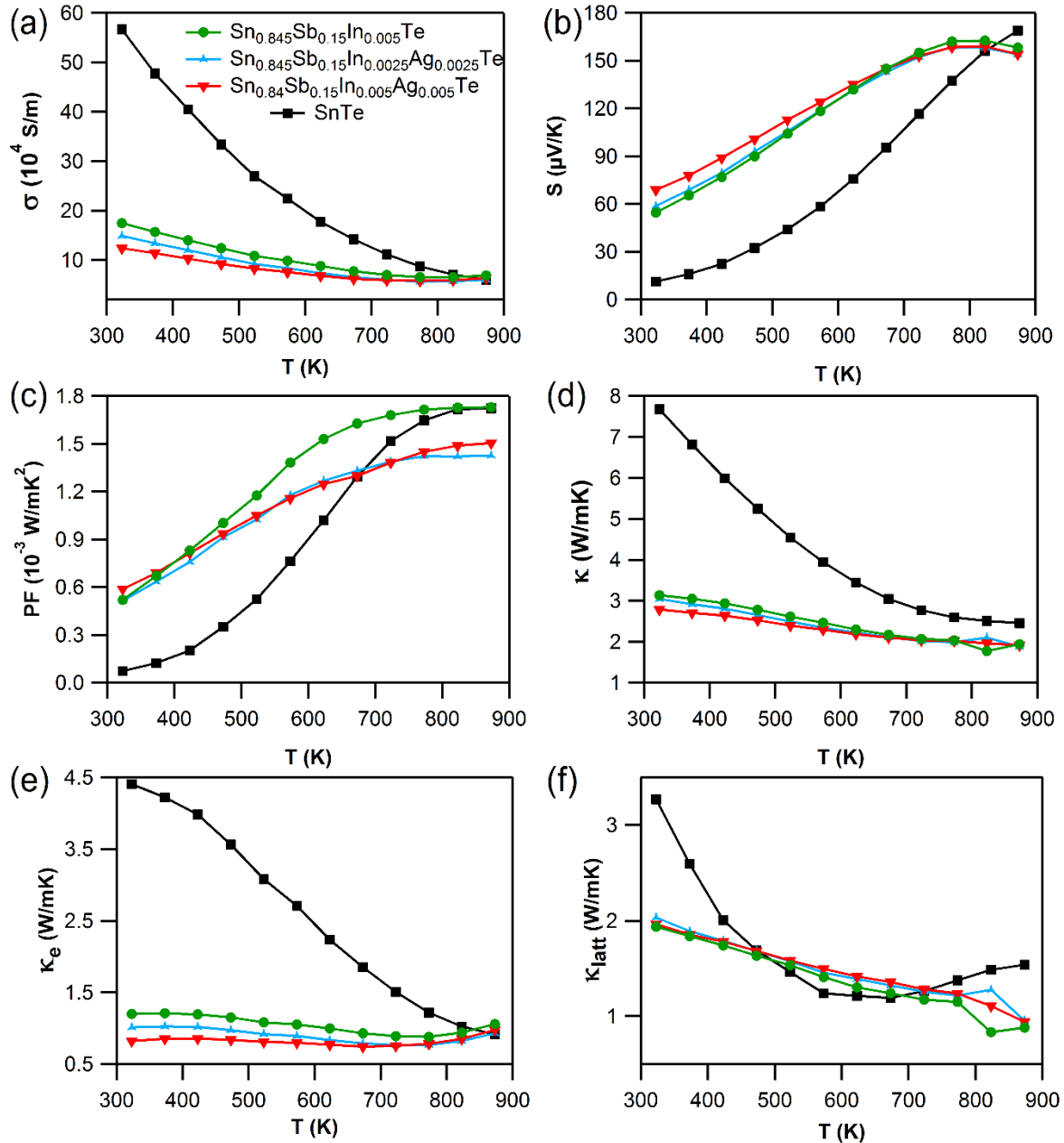


**Figure 8.4** Temperature dependent transport properties for codoped SnTe based system.

Codoping of Sb, In and Ag to SnTe has decreased  $\sigma$  (Figure 8.4.a) by suppressing the charge carrier mobility (due to impurity scattering caused by In doping<sup>7,12</sup>), and expectedly increased the Seebeck coefficient (Figure 8.4.b) due to resonant states created by In.<sup>7</sup> Just like codoped GeTe,  $\kappa$  was notably reduced in codoped SnTe (Figure 8.4.d) due to the cumulative decrease of both electronic and lattice contributions (Figure 8.4.e and 8.4.f). The aggregate effect of nanostructuring, which is expected to arise from Sb doping to SnTe<sup>6</sup> and SPS processing, has strikingly decreased the thermal transport in codoped SnTe. Ag was codoped with an objective to bring in valence band convergence in SnTe,<sup>12</sup> and as well as to compensate for the loss in  $\sigma$  caused by codoping of Sb and In in SnTe. But unfortunately, it was not the case, as addition of Ag to Sb and In codoped SnTe did not have any beneficial impact on its transport properties. The resonance state, supposedly created by In in SnTe<sup>7</sup> has helped the In and Sb codoped sample ( $\text{Sn}_{0.845}\text{Sb}_{0.15}\text{In}_{0.005}\text{Te}$ ) to exhibit a better thermopower from room temperature to 800 K and thereby an improved power factor over a wide spectrum of temperature (Figure 8.4.c).

### 8.3.2.3 Figure of Merit for GeTe and SnTe Codoped Systems

Codoping of In and Bi to GeTe has helped to maintain a better  $zT$  (Figure 8.5.a) compared to pristine GeTe over a broad temperature domain, due to the simultaneous effects of improved thermopower and reduced thermal transport. Pristine GeTe exhibits peak  $zT$  only after 673 K, whereas Bi and In codoped samples exhibit peak  $zT$  at temperatures as low as 550 K. The sample  $\text{Ge}_{0.93}\text{Bi}_{0.05}\text{In}_{0.02}\text{Te}$  maintains a consistently high  $zT$  of 0.8 – 0.9 over a wide range of temperature (550 - 773 K). From a practical point of view, it is not the peak  $zT$ , but it is the average  $zT$  ( $zT_{\text{ave}}$ ) value that determines the overall efficiency of a thermoelectric module. From 550 – 773 K, the maximum  $zT_{\text{ave}} \sim 0.85$  is obtained for  $\text{Ge}_{0.93}\text{Bi}_{0.05}\text{In}_{0.02}\text{Te}$  sample, which is much higher than pristine GeTe ( $zT_{\text{ave}} \sim 0.6$ ) and is better than most of the Sb-free GeTe based materials.<sup>4</sup> The other key reason for such improved properties can be due to the fact that the codoping of Bi and In relaxes the rhombohedral structure of GeTe and pushes the system towards the cubic structure, as the atomic radii of Bi (1.43 Å) and In (1.56 Å) are larger comparing Ge (1.25 Å), evident from merging of the rhombohedral double reflections in range of  $2\theta$  values between  $41^\circ$  and  $44^\circ$  (Figure 8.1). In other words, Bi and In codoping promotes the structural transition ( $R3m \rightarrow Fm-3m$ ) faster in GeTe. This is proved by the DSC data (Annexure 8, Figure A8.3), where the structural transition temperature conspicuously reduced from  $\sim 700$  K for pristine GeTe<sup>3,4</sup> to  $\sim 580$  K for  $\text{Ge}_{0.93}\text{Bi}_{0.05}\text{In}_{0.02}\text{Te}$ .

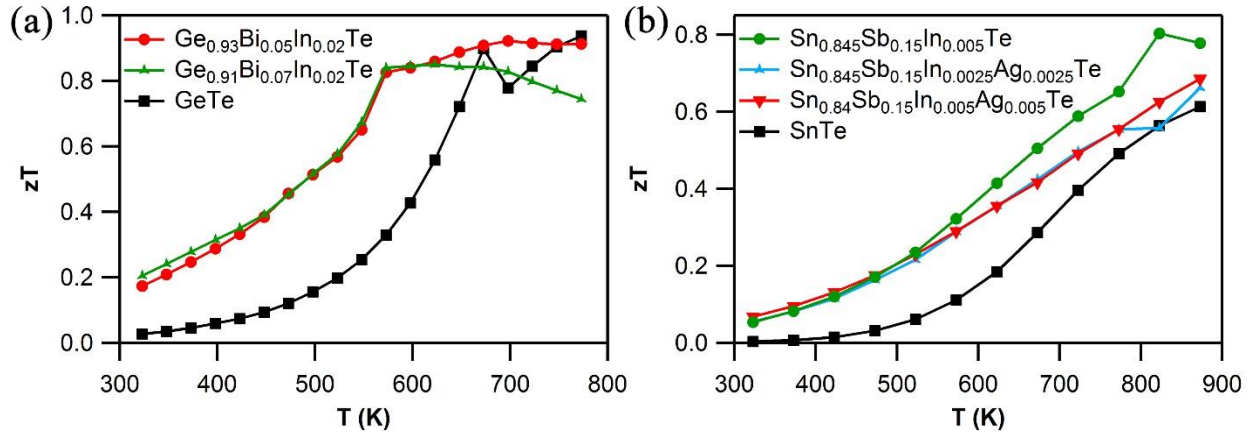


**Figure 8.5** Thermoelectric figure of merit,  $zT$  for (a) codoped GeTe, and (b) codoped SnTe systems.

In the SnTe codoped system,  $\text{Sn}_{0.845}\text{Sb}_{0.15}\text{In}_{0.005}\text{Te}$  exhibits a peak  $zT \sim 0.8$  at 823 K, which is higher than undoped SnTe ( $zT \sim 0.55$  at 823 K), as shown in Figure 8.5.b. Moreover, the cumulative effect of improved power factor over a broad spectrum of temperature and reduced thermal conductivity helps the Sb and In codoped SnTe to exhibit a higher  $zT_{\text{ave}}$  compared to pristine SnTe.

Though the thermoelectric properties for the codoped compositions when compared to their base materials are good, the doping elements which have distinctive roles and cause different band effects can at times heavily distort the density of states (DOS), if the codoping level is not balanced or optimized. Such heavy distortion of DOS can adversely affect  $\sigma$  (as in Figures 8.3.a and 8.4.a). This explains the reason for the codoped compositions (double or triple doping) that is presented in this work for exhibiting a relatively lower  $zT$  when compared to their single doped counterparts.

## 8.4 Conclusion

Codoping of Bi and In to GeTe, expected to foster resonant state near Fermi level (induced by In) and nanostructured precipitation (by Bi and SPS process), has helped to (i) suppress the carrier density, (ii) enhance the thermopower, (iii) reduce the thermal transport, and (iv) favored the rhombohedral to cubic structural transition, thus ultimately making them as potential candidates for mid-temperature device fabrications, as they maintain a constant high average  $zT_{\text{ave}} \sim 0.85$  over a wide spectrum of temperature (550 – 773 K). Similarly, codoping of Sb and In to SnTe, expected to bring in In-induced resonance state and nanostructuring (by Sb and SPS process), has helped to improve the  $zT$  to  $\sim 0.8$  at 823 K by the concurrent effect of enhanced power factor and suppressed thermal conductivity.

➤ **Adaptation**

The results presented in this chapter have been published in Materials Letters (Elsevier). Hence, this chapter is an adaptation from that publication – **B. Srinivasan *et al.*, Mater. Lett. 2018, 230, 191–194.**

➤ **Author Contributions**

B.S conceived the project, designed and performed experiments, analyzed the results and wrote the journal manuscript.

## References

- (1) Zhao, L.-D.; Dravid, V. P.; Kanatzidis, M. G. The Panoramic Approach to High Performance Thermoelectrics. *Energy Environ. Sci.* **2013**, 7 (1), 251–268.
- (2) Srinivasan, B.; Gucci, F.; Boussard-Pledel, C.; Chevire, F.; Reece, M. J.; Tricot, S.; Calvez, L.; Bureau, B. Enhancement in Thermoelectric Performance of N-Type Pb-Deficit Pb-Sb-Te Alloys. *J. Alloys Compd.* **2017**, 729, 198–202.
- (3) Perumal, S.; Roychowdhury, S.; Biswas, K. High Performance Thermoelectric Materials and Devices Based on GeTe. *J. Mater. Chem. C* **2016**, 4 (32), 7520–7536.
- (4) Srinivasan, B.; Gautier, R.; Gucci, F.; Fontaine, B.; Halet, J.-F.; Chevire, F.; Boussard-Pledel, C.; Reece, M. J.; Bureau, B. Impact of Coinage Metal Insertion on the Thermoelectric Properties of GeTe Solid-State Solutions. *J. Phys. Chem. C* **2018**, 122 (1), 227–235.
- (5) Fahrnbauer, F.; Souchay, D.; Wagner, G.; Oeckler, O. High Thermoelectric Figure of Merit Values of Germanium Antimony Tellurides with Kinetically Stable Cobalt Germanide Precipitates. *J. Am. Chem. Soc.* **2015**, 137 (39), 12633–12638.
- (6) Banik, A.; Vishal, B.; Perumal, S.; Datta, R.; Biswas, K. The Origin of Low Thermal Conductivity in  $\text{Sn}_{1-x}\text{Sb}_x\text{Te}$ : Phonon Scattering via Layered Intergrowth Nanostructures. *Energy Environ. Sci.* **2016**, 9 (6), 2011–2019.
- (7) Zhang, Q.; Liao, B.; Lan, Y.; Lukas, K.; Liu, W.; Esfarjani, K.; Opeil, C.; Broido, D.; Chen, G.; Ren, Z. High Thermoelectric Performance by Resonant Dopant Indium in Nanostructured SnTe. *Proc. Natl. Acad. Sci.* **2013**, 110 (33), 13261–13266.



- (8) Al Rahal Al Orabi, R.; Mecholsky, N. A.; Hwang, J.; Kim, W.; Rhyee, J.-S.; Wee, D.; Fornari, M. Band Degeneracy, Low Thermal Conductivity, and High Thermoelectric Figure of Merit in SnTe–CaTe Alloys. *Chem. Mater.* **2016**, *28* (1), 376–384.
- (9) Al Rahal Al Orabi, R.; Hwang, J.; Lin, C.-C.; Gautier, R.; Fontaine, B.; Kim, W.; Rhyee, J.-S.; Wee, D.; Fornari, M. Ultralow Lattice Thermal Conductivity and Enhanced Thermoelectric Performance in SnTe:Ga Materials. *Chem. Mater.* **2017**, *29* (2), 612–620.
- (10) Perumal, S.; Roychowdhury, S.; Biswas, K. Reduction of Thermal Conductivity through Nanostructuring Enhances the Thermoelectric Figure of Merit in  $\text{Ge}_{1-x}\text{Bi}_x\text{Te}$ . *Inorg. Chem. Front.* **2016**, *3* (1), 125–132.
- (11) Wu, L.; Li, X.; Wang, S.; Zhang, T.; Yang, J.; Zhang, W.; Chen, L.; Yang, J. Resonant Level-Induced High Thermoelectric Response in Indium-Doped GeTe. *NPG Asia Mater.* **2017**, *9* (1), e343.
- (12) Banik, A.; Shenoy, U. S.; Saha, S.; Waghmare, U. V.; Biswas, K. High Power Factor and Enhanced Thermoelectric Performance of SnTe-AgInTe<sub>2</sub>: Synergistic Effect of Resonance Level and Valence Band Convergence. *J. Am. Chem. Soc.* **2016**, *138* (39), 13068–13075.
- (13) Perumal, S.; Roychowdhury, S.; Negi, D. S.; Datta, R.; Biswas, K. High Thermoelectric Performance and Enhanced Mechanical Stability of P-Type  $\text{Ge}_{1-x}\text{Sb}_x\text{Te}$ . *Chem. Mater.* **2015**, *27* (20), 7171–7178.
- (14) Srinivasan, B.; Boussard-Pledel, C.; Dorcet, V.; Samanta, M.; Biswas, K.; Lefèvre, R.; Gascoin, F.; Cheviré, F.; Tricot, S.; Reece, M.; et al. Thermoelectric Properties of Highly-Crystallized Ge-Te-Se Glasses Doped with Cu/Bi. *Materials* **2017**, *10* (4), 328.





# **Chapter 9**

**Realizing a Stable High  $zT \sim 2$  over a Broad Temperature Range in  
 $\text{Ge}_{1-x-y}\text{Ga}_x\text{Sb}_y\text{Te}$  via Band Engineering and Hybrid Flash-SPS Processing**



## 9.1 Introduction

As explained in detail in Chapter 1, the main paradigm to achieve high  $zT$  in materials is to enhance their power factor ( $S^2\sigma$ ) and/or reduce their thermal transport properties ( $\kappa_{\text{total}}$ ). Most of the TE research activities are aimed at reducing  $\kappa_{\text{latt}}$  to enhance  $zT$  by phonon scattering due to nanostructuring,<sup>1-3</sup> intrinsic bond anharmonicity,<sup>4-6</sup> rattling impurities,<sup>7</sup> *etc.* However,  $S$  and  $\sigma$  are highly intertwined and present a greater challenge in enhancing the power factor, paramount for better energy conversion efficiency. Advances in recent times have shown that the concept of ‘band structure engineering’, which includes convergence of electronic band valleys,<sup>8,9</sup> quantum confinement of electron charge carriers,<sup>10</sup> electron filtering,<sup>11</sup> inducing resonant levels by impurities near the Fermi level,<sup>12</sup> nestification,<sup>13</sup> dimensionality reduction,<sup>14</sup> deformation potential coefficient,<sup>15</sup> and effective mass,<sup>16</sup> are effective in decoupling  $S$  and  $\sigma$  to a certain extent. Even the idea of utilizing magnetism was explored for this purpose.<sup>17-20</sup>

Though the concept of band engineering is extensively applied to various  $p$ - and  $n$ -type materials like SnTe,<sup>21-25</sup> PbTe,<sup>26-28</sup> half-Heuser<sup>29</sup> and  $\text{Mg}_2\text{Si}$ ,<sup>30</sup> it is applied relatively less on GeTe-based materials. Some of the strategies for GeTe based materials to enhance the power factor and/or to suppress  $\kappa_{\text{latt}}$  have been adopted on compositions such as GeTe-AgSbTe<sub>2</sub> (TAGS),<sup>31</sup> GeTe-LiSbTe<sub>2</sub>,<sup>32</sup> GeTe-AgInTe<sub>2</sub>,<sup>33</sup> GeTe-AgSbSe<sub>2</sub>,<sup>34</sup>  $(\text{GeTe})_n\text{Sb}_2\text{Te}_3$ ,<sup>35</sup>  $\text{Ge}_{1-x}\text{Pb}_x\text{Te}$ ,<sup>36</sup>  $\text{Ge}_{1-x}\text{Bi}_x\text{Te}$ ,<sup>37</sup>  $(\text{Bi}_2\text{Te}_3)_n\text{Ge}_{1-x}\text{Pb}_x\text{Te}$ ,<sup>38</sup>  $\text{Ge}_{1-x}\text{In}_x\text{Te}$ ,<sup>39</sup>  $\text{GeTe}_{1-x}\text{Se}_x$ ,<sup>40</sup>  $\text{Ge}_{1-x}\text{Sb}_x\text{Te}$ ,<sup>41,42</sup>  $\text{Ge}_{1-x}\text{Ag}_x\text{Te}$ ,<sup>43</sup>  $\text{Ge}_{1-x}\text{Mn}_x\text{Te}$ ,<sup>44,45</sup>  $\text{Ge}_{1-x-y}\text{Sn}_x\text{Pb}_y\text{Te}$ ,<sup>46</sup>  $\text{Ge}_{1-x}\text{Sb}_x\text{Te}_{1-y}\text{Se}_y$ ,<sup>47</sup> GeTe-GeSe-GeS,<sup>48</sup>  $\text{Ge}_{1-x-y}\text{Bi}_x\text{Sb}_y\text{Te}$ ,<sup>49</sup>  $\text{Ge}_{1-x-y}\text{Bi}_x\text{In}_y\text{Te}$ <sup>25</sup> and more recently  $\text{Ge}_{0.9-y}\text{Pb}_{0.1}\text{Bi}_y\text{Te}$ .<sup>50</sup> The crystal structure of GeTe-based compounds undergoes a second-order ferroelectric structural transition from rhombohedral symmetry (low temperature phase) to cubic symmetry (high temperature phase) at around 700 K.<sup>51</sup> Motivated by the results of Wu *et al.* on  $\text{Ge}_{1-x}\text{In}_x\text{Te}$ ,<sup>39</sup> showing that the introduction of resonant levels in the vicinity of the Fermi level due to indium doping leads to a reasonably high  $zT$  in GeTe ( $zT \sim 1.3$  at 630 K), we here have tried to explore the effect of another group-13 element, namely Ga on the TE performance of GeTe. From the latest work on  $\text{Ge}_{1-x-y}\text{Bi}_x\text{Sb}_y\text{Te}$ ,<sup>49</sup> it was also established that 8-10 mol% Sb doping in GeTe helped to improve the band degeneracy by pushing the system towards the cubic structure (c-GeTe). Hence aiming at bringing in synergistic band effects, we investigated the effect of codoping of Ga and Sb on the structural, electronic and thermoelectric properties of GeTe. As group-13 elements and Sb have distinctive roles, we expect codoping of Ga and Sb in GeTe to result in a synergistic band effect, *i.e.*,

cumulative effect of resonant states induced by Ga and band degeneracy caused by Sb, which ultimately should increase the thermopower of the material.

In summary, compounds with the nominal compositions of  $\text{Ge}_{1-x}\text{Ga}_x\text{Te}$  ( $x = 0.00 - 0.10$ ) were synthesized by vacuum-sealed tube melt processing, followed by consolidation by Spark Plasma Sintering (SPS). The optimum content of resonant states was achieved when 2 mol% Ga was substituted for Ge in GeTe. Indeed, this substitution marginally improved the thermoelectric performance ( $zT \sim 1.1$  at 720 K) when compared to pristine GeTe ( $zT \sim 0.95$  at 720 K). Further, when 8-10 mol% Sb was codoped to  $\text{Ge}_{0.98}\text{Ga}_{0.02}\text{Te}$ , we successfully realized the co-adjuvant synergistic band effects in GeTe. Thus, the  $\text{Ge}_{0.88}\text{Ga}_{0.02}\text{Sb}_{0.10}\text{Te}$  composition with a high thermopower and ultra-low  $\kappa_{\text{total}}$  manifested a maximum  $zT \sim 1.75$  at 725 K, which was 80% higher than that of pristine GeTe. With the state-of-the art 'hybrid flash-SPS' processing,<sup>52,53</sup> this  $zT$  value was further improved to  $\sim 2$  at 725 K (more than 100% improvement when compared to undoped GeTe). Interestingly, this high value of  $zT$  is notably maintained over a broad temperature range (600 – 775 K). The results obtained for  $\text{Ge}_{1-x}\text{Ga}_x\text{Te}$  ( $x = 0.00 - 0.10$ ) are first discussed, followed by  $\text{Ge}_{1-x-y}\text{Ga}_x\text{Sb}_y\text{Te}$  ( $x = 0.02; y = 0.08 - 0.10$ ). Note that all results are presented together in the same figures and tables for a better comparison. Owing to their meager properties, the results of  $\text{Ge}_{0.90}\text{Ga}_{0.10}\text{Te}$  are given in Annexure 9.

## 9.2 Materials & Methods

### 9.2.1 Reagents

Ge (Umicore, 99.999%), Sb (Alfa Aesar, 99.999%), Ga (Alfa Aesar, 99.999%) and Te (JGI, 99.999%) were used for synthesis without any further purification.

### 9.2.2 Synthesis

Samples of  $\text{Ge}_{1-x}\text{Ga}_x\text{Te}$  ( $x = 0.00 - 0.07$ ) and  $\text{Ge}_{1-x-y}\text{Ga}_x\text{Sb}_y\text{Te}$  ( $x = 0.02; y = 0.08, 0.10$ ) were synthesized using the vacuum-sealed tube melt processing, followed by sintering. Appropriate stoichiometric amounts of the starting elements of Ge, Ag and Te were introduced into a silica tube that had previously been cleaned with hydrofluoric (HF) acid, rinsed with distilled water and dried under vacuum. The ampules were sealed under a vacuum of  $10^{-6}$  Torr, then placed in a rocking furnace and slowly heated up to 950 °C over a period of 12 hours, then held at that temperature for 12 hours and slowly cooled down to room temperature.

The obtained ingots were crushed and milled. The powders were then consolidated by SPS (FCT Systeme GmbH) at 723 K (heating rate  $\sim 80$  °C/min) for 5 mins (holding time) under an axial pressure of 85 MPa. The sample with better TE properties was also consolidated by Hybrid Flash-SPS processing, where the powders were sintered at 893 K and a heating rate of  $\sim 10,000$  °C/min (heated from 293 – 893 K in 3 seconds) under an axial pressure of 55 MPa. More information regarding these processing techniques, experimental set-ups, current flow paths and die designs were provided in Chapter 4. Highly dense disk-shaped pellets were obtained with theoretical densities of 100% for SPS and  $\sim 98\%$  for Hybrid Flash-SPS. The obtained ingots and sintered discs were cut and polished to the required shapes and dimensions for various thermoelectric measurements.

### 9.2.3 Computational Procedures

Density Functional Theory (DFT) calculations were performed to understand the effect of doping on the electronic states. We used the projector-augmented-wave (PAW) approach<sup>54</sup> implemented in the Vienna ab initio simulation package (VASP).<sup>55</sup> Calculations were performed using generalized gradient approximation (GGA) for the exchange-correlation term parametrized by J. P. Perdew *et al.*<sup>56</sup> Spin orbit coupling was also included in the computation.

As we were interested in high temperature behavior of doped GeTe, calculations were performed on the cubic structural models. Impurities were substituted to Ge atom in a  $4 \times 4 \times 4$  supercell. Considering the previous study by Hoang *et al.*<sup>57</sup> on the impurity clustering in GeTe, we adopted a cluster of one Ga atom surrounded by 6 Sb atoms (second neighbors) for the Ga-Sb codoped GeTe composition ( $\text{Sb}_6\text{GaGe}_{57}\text{Te}_{64}$ ). In order to understand the relative effect of both atoms, the calculations were also performed for  $\text{GaGe}_{63}\text{Te}_{64}$  and  $\text{Sb}_6\text{Ge}_{58}\text{Te}_{64}$  models. In all the three cases, the positions were fully relaxed. For the irreducible cell, the Brillouin-zone integration was performed using a  $25 \times 25 \times 25$  Monkhorst–Pack  $k$ -mesh. For the super cell, we used a  $3 \times 3 \times 3$   $k$ -mesh for the atomic relaxation and a  $7 \times 7 \times 7$   $k$ -mesh for the DOS calculations.

The carrier effective mass ( $m^*$ ) was derived for each sample using a single parabolic band model<sup>58,59</sup> and the measured room temperature Seebeck coefficient ( $S$ ) and carrier concentration ( $n$ ). Details on the computation of  $m^*$  were elaborately discussed with pertinent equations in Chapter 4.



### 9.3 Results & Discussion

#### 9.3.1 Structural Analysis

Sharp reflections from powder XRD indicated the good crystalline nature of all of the synthesized ingots (Figure 9.1). All of the main reflections could be indexed to a rhombohedral GeTe phase (PDF#47-1079,  $R3m$  space group). The rhombohedral phase was further confirmed by the presence of double reflections [(024) and (220)] in the range of  $2\theta$  values between  $41^\circ$  to  $44^\circ$  in  $\text{Ge}_{1-x}\text{Ga}_x\text{Te}$ . Minor reflections of Ge impurities (*i.e.*, Ge-rich secondary phase) could be detected in some samples, which could be due to intrinsic Ge vacancies, as GeTe always prefers to have a Te-rich composition, as in agreement with the previous experiments.<sup>43,49,60</sup>

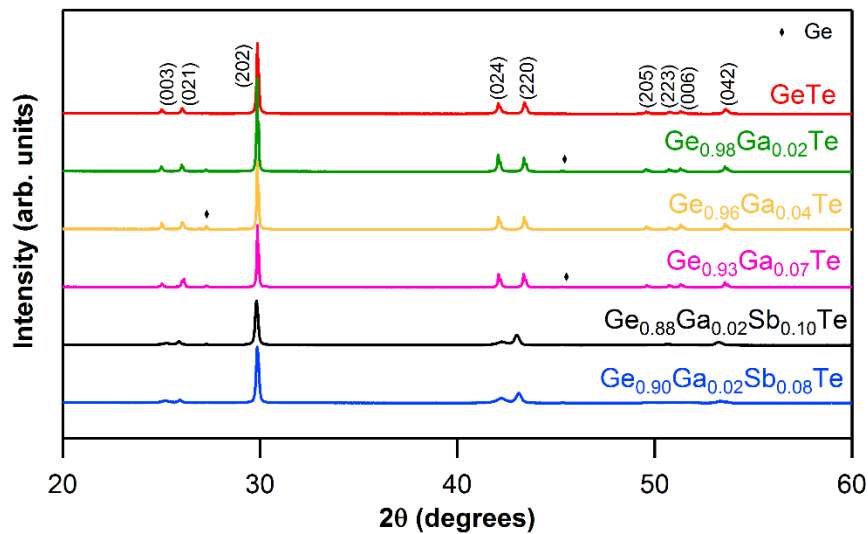


**Figure 9.1.** Powder XRD patterns for  $\text{Ge}_{1-x}\text{Ga}_x\text{Te}$  ( $x = 0$  to  $0.07$ ) and  $\text{Ge}_{1-x-y}\text{Ga}_x\text{Sb}_y\text{Te}$  ( $x = 0.02$ ;  $y = 0.08$ ,  $0.10$ ) samples.

The XRD results of  $\text{Ge}_{1-x-y}\text{Ga}_x\text{Sb}_y\text{Te}$  samples are discussed in the following section, along with their transport properties.

#### 9.3.2 Thermoelectric Properties of $\text{Ge}_{1-x}\text{Ga}_x\text{Te}$ and $\text{Ge}_{1-x-y}\text{Ga}_x\text{Sb}_y\text{Te}$ Systems

Holes were the major charge carriers ( $p$ -type), as the Hall voltage was positive in these samples. The results from Hall measurements are presented in Table 9.1. The carrier concentration

value at room temperature decreased with increasing Ga content. In pristine GeTe, the Ge vacancy has a very low formation energy and is the most easily formed intrinsic defects.<sup>60,61</sup> The addition of Ga to GeTe can suppress these Ge vacancies, thereby leading to a reduction in the density of charge carriers. In most cases, the carrier mobility,  $\mu$ , will increase with the decreasing charge carrier density. However, the mobility values in  $\text{Ge}_{1-x}\text{Ga}_x\text{Te}$  had a contrasting effect, where they consistently reduced with increasing Ga content. This reduction in mobility with Ga content can be due to the increased density of ionized impurities and/or alloy scattering. Such mobility reductions are commonly observed in materials with group-13 dopants.<sup>12,39</sup>

**Table 1.** Hall measurement results (at  $\sim 300$  K) of carrier concentration, mobility, and computed effective mass for  $\text{Ge}_{1-x}\text{Ga}_x\text{Te}$  ( $x = 0.00 - 0.07$ ) and  $\text{Ge}_{1-x-y}\text{Ga}_x\text{Sb}_y\text{Te}$  ( $x = 0.02; y = 0.08, 0.10$ ) samples.

Sample	Carrier Concentration, $n$ ( $\text{cm}^{-3}$ )	Mobility, $\mu$ ( $\text{cm}^2\text{V}^{-1}\text{s}^{-1}$ )	Effective mass, $m^*$ ( $m_e$ )
GeTe	$9.08 \times 10^{20}$	57.01	1.30
$\text{Ge}_{0.98}\text{Ga}_{0.02}\text{Te}$	$8.73 \times 10^{20}$	51.76	1.72
$\text{Ge}_{0.96}\text{Ga}_{0.04}\text{Te}$	$7.85 \times 10^{20}$	43.72	1.64
$\text{Ge}_{0.93}\text{Ga}_{0.07}\text{Te}$	$6.35 \times 10^{20}$	32.04	1.65
$\text{Ge}_{0.88}\text{Ga}_{0.02}\text{Sb}_{0.10}\text{Te}$	$1.83 \times 10^{20}$	29.65	1.97
$\text{Ge}_{0.90}\text{Ga}_{0.02}\text{Sb}_{0.08}\text{Te}$	$3.96 \times 10^{20}$	29.82	2.38
$\text{Ge}_{0.90}\text{Ga}_{0.02}\text{Sb}_{0.08}\text{Te}$ by hybrid flash-SPS	$2.13 \times 10^{20}$	35.81	2.03

As mentioned in the introductory part, the results obtained for  $\text{Ge}_{1-x}\text{Ga}_x\text{Te}$  ( $x = 0.00 - 0.10$ ) are first discussed, followed by  $\text{Ge}_{1-x-y}\text{Ga}_x\text{Sb}_y\text{Te}$  ( $x = 0.02; y = 0.08 - 0.10$ ).

The electrical conductivity of all of the samples decreased with temperature (Figure 9.2.a), which is the archetypal behavior of degenerate semi-conductors. The Ga-doping systematically increased the electrical resistance, a reflection of the cumulative effect of deflation in both the charge carrier density and carrier mobility with Ga content. The Seebeck coefficient,  $S$ , was positive for all the composition over the entire temperature range (Figure 9.2.b). This indicated  $p$ -type charge carriers, consistent with the Hall measurement results. With the increasing Ga content, there was a notable improvement in  $S$ -values both at room temperature and at higher temperature for  $\text{Ge}_{1-x}\text{Ga}_x\text{Te}$

samples. This modest improvement in  $S$ -values can be attributed to the suppression of the carrier concentration by Ga doping.

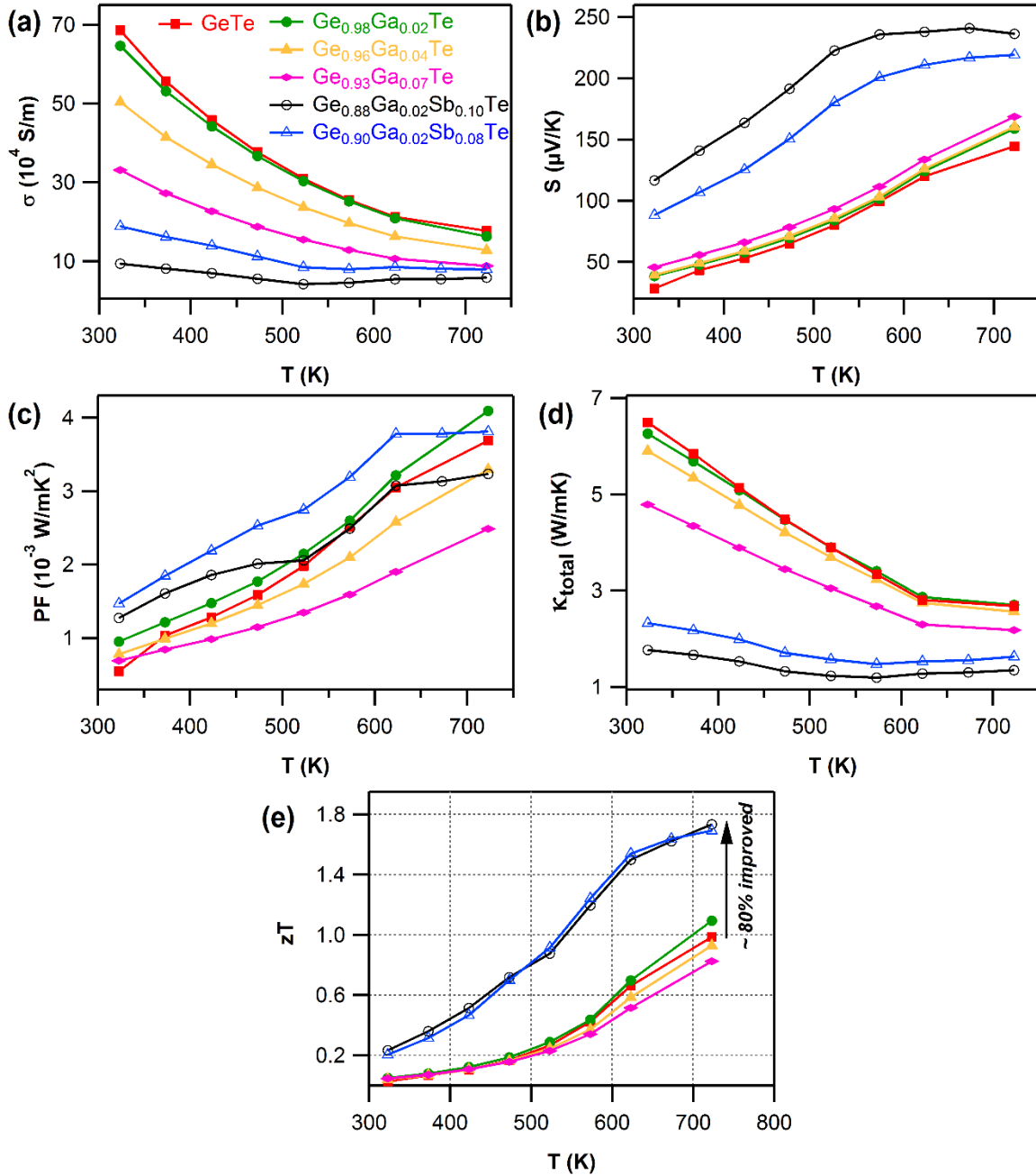


**Figure 9.2** Temperature-dependent (a) electrical conductivity ( $\sigma$ ), (b) Seebeck coefficient ( $S$ ), and (c) power factor ( $PF = S^2\sigma$ ), (d) total thermal conductivity ( $\kappa_{\text{total}}$ ), (e) figure of merit ( $zT$ ) for  $\text{Ge}_{1-x}\text{Ga}_x\text{Te}$  ( $x = 0.00 - 0.07$ ) and  $\text{Ge}_{1-x-y}\text{Ga}_x\text{Sb}_y\text{Te}$  ( $y = 0.02$ ;  $z = 0.08, 0.10$ ) samples.

The temperature dependence of the power factors ( $S^2\sigma$ ) are shown in Figure 9.2.c for  $\text{Ge}_{1-x}\text{Ga}_x\text{Te}$  samples. Compared to pristine GeTe, there was a marginal but significant improvement in the power factor for the 2 mol% Ga doped sample, which exhibited a maximum power factor of  $\sim 4.1 \times 10^{-3} \text{ W/mK}^2$  at 720 K. The advantage of an improved power factor in GeTe by 2 mol% Ga doping was maintained across the measured temperatures. The power factors of other  $\text{Ge}_{1-x}\text{Ga}_x\text{Te}$  samples for  $x > 0.02$  were lower than the undoped sample. Hence in  $\text{Ge}_{1-x}\text{Ga}_x\text{Te}$  system, the optimized value of  $x = 0.02$  provided the needed proper trade-off between the electrical transport properties.

The total thermal conductivity,  $\kappa_{\text{total}}$  (Figure 9.2.d), monotonically decreased with Ga content in  $\text{Ge}_{1-x}\text{Ga}_x\text{Te}$  samples. The contributions from electronic ( $\kappa_e$ ) and lattice ( $\kappa_{\text{latt}}$ ) parts are presented in Annexure 9 (Figure A9.4). The temperature dependent Lorenz number,  $L$ , obtained by fitting their respective Seebeck coefficients for the samples of  $\text{Ge}_{1-x}\text{Ga}_x\text{Te}$  were in the range of  $2.3 \times 10^{-8}$  to  $1.8 \times 10^{-8} \text{ W}\Omega\text{K}^{-2}$  and lower than the metallic limit of  $2.45 \times 10^{-8} \text{ W}\Omega\text{K}^{-2}$  (Annexure 9, Figure A9.3). In the case of  $\text{Ge}_{1-x}\text{Ga}_x\text{Te}$ , the majority of the thermal contribution came from  $\kappa_e$ , which conspicuously decreased with Ga content.  $\kappa_{\text{latt}}$  of the Ga-doped samples was larger than that of the pristine GeTe, and this can arise when the estimation of  $L$  value cannot properly account for the electronic contribution to the thermal conductivity, as similarly observed for previously reported PbTe and SnTe based materials.<sup>62,63</sup>

The maximum thermoelectric figure of merit,  $zT$ , (Figure 9.2.e) achieved within the  $\text{Ge}_{1-x}\text{Ga}_x\text{Te}$  ( $x = 0.00$  to  $0.10$ ) series was  $\sim 1.1$  at 720 K for  $\text{Ge}_{0.98}\text{Ga}_{0.02}\text{Te}$ , which was marginally higher than that of pristine GeTe ( $zT \sim 0.95$  at 720 K). The  $zT$  values systematically decreased for the value of  $x > 0.02$  in the  $\text{Ge}_{1-x}\text{Ga}_x\text{Te}$  system. The heavily Ga-doped sample ( $x = 0.10$ ) exhibited the lowest  $zT$  (Annexure 9, Figure A9.5), due to its high electrical resistivity arising from severe deflation of carrier concentration and mobility. Based on this evidence, it was concluded that 2 mol% Ga doping was optimum to achieve a better trade-off between  $S$ ,  $\sigma$  and  $\kappa_{\text{total}}$  in the  $\text{Ge}_{1-x}\text{Ga}_x\text{Te}$  ( $x = 0.00$  to  $0.10$ ) series. The first-principles (DFT type) calculations reported later in this chapter suggest that resonant states are induced.

It has been reported that 8-10 mol% Sb doping in GeTe significantly helped to achieve band degeneracy.<sup>49</sup> To further improve the thermoelectric performance of  $\text{Ge}_{0.98}\text{Ga}_{0.02}\text{Te}$ , Sb was codoped to it to form the  $\text{Ge}_{1-x-y}\text{Ga}_x\text{Sb}_y\text{Te}$  ( $x = 0.02$ ;  $y = 0.08, 0.10$ ) series, with an objective to bring in synergistic band effects that would help to improve the TE performance.

As observed from the XRD patterns (Figure 9.1), the double reflections [(024) and (220)] in the range of  $2\theta$  values between  $41^\circ$  to  $44^\circ$ , characteristics of the rhombohedral phase, got closer and

almost merged when Sb was codoped into  $\text{Ge}_{1-x}\text{Ga}_x\text{Te}$ . As the atomic radii of Ga (1.36 Å) and Sb (1.33 Å) are larger compared to that of Ge (1.25 Å), the codoping of Ga-Sb has relaxed the rhombohedral structure of GeTe and has pushed the system towards the cubic structure. In other words, Ga-Sb codoping has promoted a faster structural transition ( $R3m \rightarrow Fm-3m$ ) in GeTe. This was proven by the DSC data (Annexure 9, Figure A9.1), where the structural transition temperature was conspicuously reduced from  $\sim 635$  K for  $\text{Ge}_{0.98}\text{Ga}_{0.02}\text{Te}$  to  $\sim 585$  K for  $\text{Ge}_{0.88}\text{Ga}_{0.02}\text{Sb}_{0.10}\text{Te}$ . Considering that the transition temperature for pristine GeTe is  $\sim 700$  K, the codoping of Ga and Sb has tremendously reduced the phase transition temperature and has increased the cubic nature of the sample. From the band structure features of rhombohedral (r) and cubic (c) GeTe, it was shown that the later has a larger total band degeneracy.<sup>64</sup> The effect of the transition is seen in the transport data (explained in the following paragraph).

Because of the combined actions of Ga and Sb at the Ge site in GeTe, an effective suppression of the intrinsic Ge vacancies could take place, which was reflected in the major reduction of the carrier concentration in the codoped samples (Table 9.1). Obviously, this contributed to the decline in  $\sigma$  for Ga-Sb codoped samples (Figure 9.2.a). But this was well compensated by the large increase in the Seebeck coefficient (Figure 9.2.b). The Ga-Sb codoped sample of composition  $\text{Ge}_{0.88}\text{Ga}_{0.02}\text{Sb}_{0.10}\text{Te}$  exhibited a high thermopower of  $\sim 120$   $\mu\text{V}/\text{K}$  at room temperature and a maximum of  $\sim 240$   $\mu\text{V}/\text{K}$  at higher temperatures, an improvement by 70% when compared to pristine GeTe. It is also key to note that the  $S$ -values of the codoped samples increased steeply till 550 K and almost became constant after that. Such a trend once again was a clear indication of the second order structural transition ( $R3m \rightarrow Fm-3m$ ).

**Conundrum:** Is this structural transition really so significant? Pristine GeTe is a highly degenerated  $p$ -type semiconductor with room-temperature carrier concentration ( $n$ ) as high as  $\sim 10^{21}$   $\text{cm}^{-3}$  due to the considerable Ge deficiency,<sup>51</sup> resulting in a large  $\kappa_e$  and a small  $S^2\sigma$ . Consequently, the primary requirement of pursuing high thermoelectric performance in GeTe is to reduce  $n$ . Similar to other rock-salt group IV chalcogenides, c-GeTe has two valence bands with a small energy offset, which however transfer into multi sub-valence bands separated by a large  $\Delta E$  in the r-GeTe material.<sup>65</sup> Therefore, the total band degeneracy of c-GeTe is larger than that of r-GeTe, leading to a higher quality factor in c-GeTe, which is considered to be beneficial to secure high thermoelectric performance.<sup>66,67</sup> So far, the thermoelectric research on GeTe has been mainly focused on the enhancement of its performance in the high temperature cubic phase. Accordingly, reducing this structural transition temperature is considered a key approach to enhance thermoelectric

performance of GeTe by extending the transport behavior of c-GeTe into the low-temperature regime. But very recently (May 2018), Pei and co-workers achieved an unprecedented  $zT \sim 2.4$  at 600 K in rhombohedral-phase GeTe (codoped with Pb and Bi)<sup>50</sup> by exploiting slight symmetry breaking in the structure, which simultaneously improved the electronic properties and reduced the lattice thermal conductivity. They showed a slight reduction of crystal structure symmetry of GeTe alloys from cubic to rhombohedral, which enabled a rearrangement in electronic bands (convergence of split low symmetry bands, as shown in Figure A9.10 in Annexure 9) for more transporting channels of charge carriers and many imperfections for more blocking centers of heat-energy carriers (phonons).<sup>50,68</sup> This is a trend changer, as it moves away from common belief that high symmetry materials are usually good for thermoelectrics and has opened new possibilities for exploring low symmetry materials for thermoelectrics. But certainly, our results seem to be analogous with that recent report by Pei.<sup>50</sup> However, as the results presented in this chapter were obtained and interpreted based on the existing science of GeTe in early 2018 (*i.e.*, before the new idea on low symmetry was proposed by Pei in May, 2018), the emphasis here is more on the high temperature cubic domain. Additional remark has been made on this conundrum in the concluding chapter of this thesis [Page 180, point (e)].

The increased electrical resistivity, due to the lowering of carrier density and carrier mobility has immensely reduced the electronic contribution to thermal transport in the Ga-Sb codoped samples (Annexure 9, Figure A9.4). This has led to an ultra-low  $\kappa_{\text{total}} (< 1.3 \text{ W/mK at } T > 500 \text{ K})$  in the  $\text{Ge}_{1-x-y}\text{Ga}_x\text{Sb}_y\text{Te}$  samples (Figure 9.2.d). At room temperature,  $\text{Ge}_{0.88}\text{Ga}_{0.02}\text{Sb}_{0.10}\text{Te}$  sample exhibited a  $\kappa_{\text{total}} \sim 1.75 \text{ W/mK}$ , which accounted for a reduction by 270% when compared to pristine GeTe ( $\kappa_{\text{total}} \sim 6.5 \text{ W/mK}$  at room temperature).

The combined beneficial effects of improved thermopower and reduced thermal transport, achieved by Ga-Sb codoping of GeTe, have strikingly enhanced the thermoelectric figure of merit (Figure 9.2.e). The Ga-Sb codoped GeTe samples (both  $\text{Ge}_{0.88}\text{Ga}_{0.02}\text{Sb}_{0.10}\text{Te}$  and  $\text{Ge}_{0.90}\text{Ga}_{0.02}\text{Sb}_{0.08}\text{Te}$  compositions) manifested a high  $zT \sim 1.75$  at 730 K, an improvement by 80% compared to undoped GeTe, and it is notably one of the highest reported among the GeTe-based materials.

### 9.3.3 Investigation of Electronic Band Structures and Density of States

To have a more cogent understanding on the effects of doping in GeTe, DFT calculations were performed. As we are interested in the high temperature domain for thermoelectric applications, these DFT calculations were carried out on  $4 \times 4 \times 4$  supercells derived from the cubic structural

arrangement of GeTe. The electronic densities of states (DOS) computed for the cubic models of GeTe and  $\text{Ge}_{0.98}\text{Ga}_{0.02}\text{Te}$  are presented and compared in Figure 9.3.a. As expected, the presence of some amount of Ga in GeTe shifted the Fermi level towards the valence band. The DOS was clearly modified near the top of the valence band with respect to that of GeTe, distinctly indicated by the presence of a sharp hump near the Fermi level ( $E_F$ ). This firmly establishes that Ga doping induces resonant states or deep defect states near  $E_F$  in the electronic band structure of GeTe. According to Mott's relationship,<sup>69</sup> the modified DOS obtained by resonant levels may contribute to an improvement in the Seebeck coefficient. This explains the marginal raise in thermopower for  $\text{Ge}_{1-x}\text{Ga}_x\text{Te}$  at high temperatures (cubic phase). However, the power factor and  $zT$  were improved only for the  $\text{Ge}_{0.98}\text{Ga}_{0.02}\text{Te}$  composition, while they were reduced for higher dopant content of Ga in  $\text{Ge}_{1-x}\text{Ga}_x\text{Te}$  ( $x > 0.02$ ). This happens because the distortion of DOS (resonant states) hinders electrical conductivity (owing to reduced mobility). At higher dopant levels of Ga ( $> 2$  mol%), the DOS of the samples are modified heavily, which was reflected in their poor TE performance due their decreased  $\sigma$  and  $\mu$  values. Hence, the 2 mol% Ga doping in GeTe produced the optimum distortion of the DOS to notably increase the thermopower without compromising much the electrical conductivity. It seems that the Ga-induced resonance level becomes more prominent only at the high temperature cubic phase, as there was not much significant change in the room temperature value of Seebeck coefficient when 2 mol% Ga was doped to GeTe.

To simulate 8-10 mol% Sb doping in GeTe, six Sb atoms were substituted for Ge in GeTe leading to the  $\text{Sb}_6\text{Ge}_{58}\text{Te}_{64}$  ( $\text{Sb}_{0.09}\text{Ge}_{0.91}\text{Te}$ ) composition. Among the different possible Sb distributions, that with Sb aggregation (*i.e.*, Sb atoms close to each other) was considered to be the most thermodynamically stable.<sup>36</sup> Computed DOS for this Sb doped ( $\text{Sb}_6\text{Ge}_{58}\text{Te}_{64} = \text{Sb}_{0.09}\text{Ge}_{0.91}\text{Te}$ ) composition and for the Ga-Sb codoped ( $\text{GaSb}_6\text{Ge}_{57}\text{Te}_{64} = \text{Ga}_{0.02}\text{Sb}_{0.09}\text{Ge}_{0.89}\text{Te}$ ) GeTe (cubic) compositions are presented in Figures 9.3.b and 9.3.c, respectively. Substituting in a 1/10 ratio of divalent Ge with Sb (Sb single doping) or Ga-Sb (codoping of Ga and Sb), suppresses the hole concentration and, assuming a rigid band model, shifts the Fermi level ( $E_F$ ) upwards, *i.e.*, towards the conduction band (Figures 9.3.b and 9.3.c). We would like to mention that these statements must be considered with caution, as the theoretical calculations were performed based on a stoichiometric GeTe, where there is no Ge vacancy. But as found experimentally, GeTe always prefers to be in Te-rich composition and hence there exists some Ge vacancies. The *p*-type charge carriers still dominate the transport in Ga-Sb codoped GeTe, as observed from them the Hall measurement results (Table 9.1). The significant reduction in the carrier density indicates that the DOS at the Fermi-level will decrease and the  $E_F$  should be close to the gap for the Ga-Sb codoped GeTe. According to the

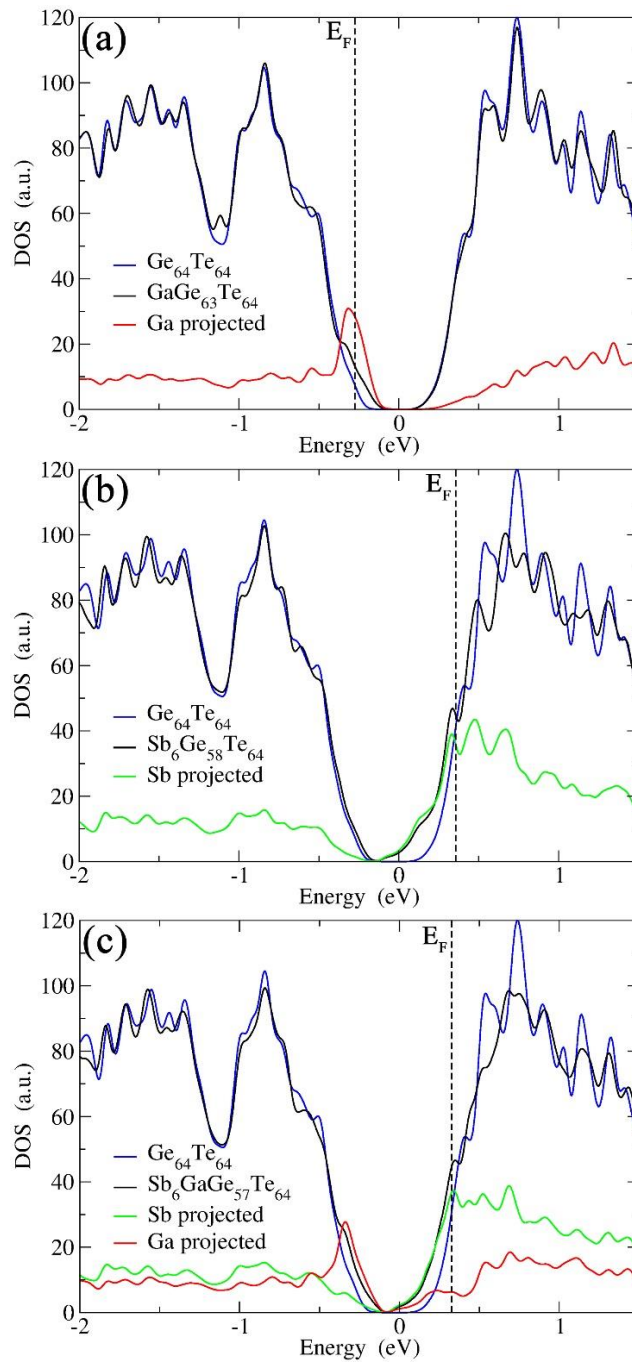


**Figure 9.3** Calculated DOS for (a)  $\text{GaGe}_{63}\text{Te}_{64}$  ( $\text{Ge}_{0.98}\text{Ga}_{0.02}\text{Te}$ ), (b)  $\text{Sb}_6\text{Ge}_{58}\text{Te}_{64}$  ( $\text{Sb}_{0.09}\text{Ge}_{0.91}\text{Te}$ ) (c)  $\text{GaSb}_6\text{Ge}_{57}\text{Te}_{64}$  ( $\text{Ga}_{0.02}\text{Sb}_{0.09}\text{Ge}_{0.89}\text{Te}$ ) models (derived from the high temperature cubic  $\text{GeTe}$  phase). The DOS of each model is compared with that of the pristine cubic phase  $\text{Ge}_{64}\text{Te}_{64}$  ( $\text{GeTe}$ ). The Fermi level ( $E_F$ ) of pristine  $\text{GeTe}$  is set arbitrarily at 0 eV. Green and red curves represent Sb and Ga projections. The dashed line represents the shifted Fermi level for the doped compositions. Additional Gaussian smearing of 25 meV was applied and the Ga projected DOS was magnified for a better readability of the curves.



Boltzmann transport equation, such a scenario will obviously lead to an improved Seebeck coefficient, consistent with our experimental findings. Ga-Sb codoping adds donor states just below the conduction band of GeTe. Interestingly, we still found some Ga-induced resonant states in the top of the valence band when Sb was codoped to the Ge-Ga-Te system, but unlike the single doped  $\text{Ge}_{1-x}\text{Ga}_x\text{Te}$ , the resonant state was not near  $E_F$  in the Ga-Sb codoped system (Figure 9.3.c).

The electronic band structures of the undoped, doped and codoped compositions were also computed and analyzed, hoping to provide useful insight on how the valence band structure is modified upon doping. They are plotted in Figure 9.4 along some high symmetry lines of the cubic Brillouin zone (BZ). From the electronic band structure of GeTe (Figures 9.4.b and 9.4.c), the direct band gap was calculated to be 225 meV at  $\Gamma$  point, which is in agreement with the literature.<sup>49,64</sup> GeTe exhibits a second maximum of the valence band in the  $\Gamma \rightarrow \text{K}$  ( $\Sigma$ ) direction. The energy difference between light and heavy hole valence bands ( $\Delta E_{L\Sigma}$ ) for undoped cubic  $\text{Ge}_{64}\text{Te}_{64}$  was found to be 64 meV, consistent with a recent report.<sup>64</sup> This  $\Delta E_{L\Sigma}$  value for c-GeTe is much lower when compared to that of the low temperature r-GeTe ( $\Delta E_{L\Sigma} = 150$  meV).<sup>64</sup> This is advantageous and is in agreement with the fact that the temperature increases the band convergence in GeTe.<sup>38</sup> As mentioned before, the ferroelectric structural transition was more favored with the codoping of Ga-Sb, since the transition temperature was reduced. This structural strain relaxation from rhombohedral low symmetry ( $R3m$ ) to cubic high symmetry ( $Fm-3m$ ) will increase the electronic band valley degeneracy, a key factor for enhancing the Seebeck coefficient. Thus, codoping of Ga-Sb to GeTe promotes band valley convergence. It must be noted that, in our case, the structural strain relaxation from rhombohedral to cubic played a role in stabilizing the Seebeck coefficient (rather than raising the Seebeck coefficient).

When 2 mol% Ga was added to GeTe, *i.e.*, for  $(\text{Ge}_{0.98}\text{Ga}_{0.02}\text{Te})$ , the new impurity band arising from Ga states reduced the gap at  $\Gamma$  point to 66 meV (Figure 9.4.d). The impurity states were located at the top of the valence band and extended somewhat within the gap. For 8-10 mol% Sb doping in GeTe, *i.e.*,  $\text{Sb}_6\text{Ge}_{58}\text{Te}_{64}$  ( $\text{Sb}_{0.09}\text{Ge}_{0.91}\text{Te}$ ), the Sb states were located at the bottom of the conduction band (Figure 9.4.e). The gap at  $\Gamma$  point decreased to 71 meV, while  $\Delta E_{L\Sigma}$  remained unchanged when compared to that of undoped GeTe, in agreement with the predictions made by Hong *et al.*<sup>64</sup> With 2 mol% Ga and 8 mol% Sb codoping in GeTe, *i.e.*,  $\text{GaSb}_6\text{Ge}_{57}\text{Te}_{64}$  ( $\text{Ga}_{0.02}\text{Sb}_{0.09}\text{Ge}_{0.89}\text{Te}$ ), the gap at  $\Gamma$  point opened up ( $\sim 165$  meV). The presence of Sb and Ga modified the electronic band structure by activating the hole pockets at the bottom of the conduction band. The effective mass,  $m^*$ , associated with these hole pockets became larger (Table 9.1). These  $m^*$  values were calculated from Seebeck

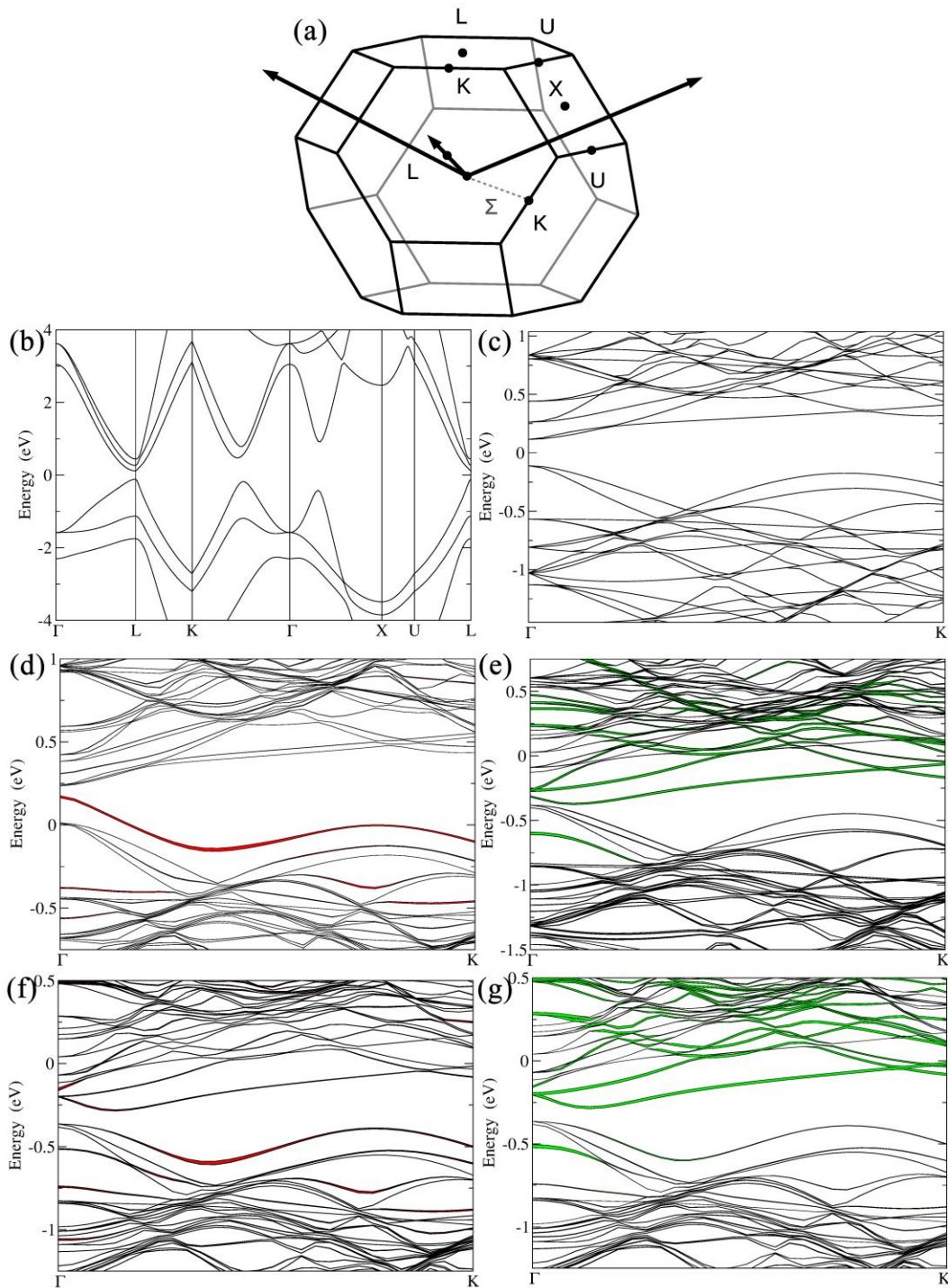


**Figure 9.4** (a) Brillouin zone of  $c\text{-GeTe}$ . The band structures for (b)  $c\text{-GeTe}$  with primitive unit cell; (c)  $c\text{-Ge}_{64}\text{Te}_{64}$  using a  $4 \times 4 \times 4$  supercell showing band folding in the  $\Gamma \rightarrow K$  ( $\Sigma$ ) direction. (d)  $\text{GaGe}_{63}\text{Te}_{64}$  ( $\text{Ge}_{0.98}\text{Ga}_{0.02}\text{Te}$ ) (e)  $\text{Sb}_6\text{Ge}_{58}\text{Te}_{64}$  ( $\text{Sb}_{0.09}\text{Ge}_{0.91}\text{Te}$ ); (f)  $\text{GaSb}_6\text{Ge}_{57}\text{Te}_{64}$  ( $\text{Ga}_{0.02}\text{Sb}_{0.09}\text{Ge}_{0.89}\text{Te}$ ) highlighting Ga projections and (g)  $\text{GaSb}_6\text{Ge}_{57}\text{Te}_{64}$  ( $\text{Ga}_{0.02}\text{Sb}_{0.09}\text{Ge}_{0.89}\text{Te}$ ) highlighting Sb projections. Line thickness is proportional to the projection of the wave function on the Ga (in red) and Sb (in green) orbitals.

coefficient and carrier density and based on a single parabolic band, where acoustic phonon scatterings only were considered. Indeed, the  $m^*$  value for pristine GeTe was calculated to be  $1.30 m_e$  ( $m_e$  = free electron mass) and it markedly increased to  $2.38 m_e$  for the Sb-Ga codoped sample  $\text{Ga}_{0.02}\text{Sb}_{0.08}\text{Ge}_{0.90}\text{Te}$ . This points towards an enhanced valence band degeneracy, which could explain the improved thermopower with Ga-Sb codoping. More importantly, Ga-Sb codoping in GeTe promoted valence band convergence by strikingly reducing the energy separation between the light hole and heavy hole valence bands,  $\Delta E_{L\&H}$ , to 26 meV (60% reduction in  $\Delta E_{L\&H}$  when compared to pristine GeTe). In this Ga-Sb codoped GeTe, the predominant contribution for the top of the valence band comes from Ga (Figure 9.4.f and Figure 9.4.h), indicating that it is not just Sb, but also Ga (of course together with Sb) that played a crucial role in promoting the valence band convergence in  $\text{Ga}_{0.02}\text{Sb}_{0.08}\text{Ge}_{0.90}\text{Te}$ . Thus, our calculations indicate a significant interaction between the substituted Ga and Sb atoms, and though the codoping of Ga-Sb to GeTe did not position the resonance state at a favorable location near  $E_F$ , it enhanced the valence band convergence besides pushing the system towards cubic (band degeneracy). All of this has helped to achieve a high Seebeck coefficient in Ga-Sb codoped GeTe. The synergy achieved between these different band effects via codoping is the prime factor behind the impressive thermoelectric performance of  $\text{Ge}_{1-x-y}\text{Ga}_x\text{Sb}_y\text{Te}$ .

As a matter of fact, as resonant states distort the DOS and reduce the band gap, only a low level of Ga doping (not more than 2 mol%) is beneficial, whereas band convergence is a tuning of the periodical band structure, and hence a relatively high Sb doping (8-10 mol%) and low Ga doping were required to influence the  $k$ -space band dispersion. Refer Annexure 9 (Figure A9.6), where we have showed that an equal proportion doping of Ga and Sb was not beneficial.

### 9.3.4 Comparison of SPS vs Hybrid Flash-SPS for Processing of $\text{Ge}_{1-x-y}\text{Ga}_x\text{Sb}_y\text{Te}$

To remind again about SPS and hybrid flash-SPS processing techniques, the following paragraph (from Chapter 4) is restated here.

More recently, a novel sintering process called 'Flash-SPS', a derivative of the flash and SPS sintering techniques has generated a lot of interest as it has been shown to improve the thermoelectric performance of Mg-Si based materials.<sup>70</sup> During normal SPS (which involves direct Joule heating of electrically conductive dies, usually graphite), the heating rate typically used is  $\sim 100$  °C/min, whereas the flash technique employs thermal runaway to achieve ultra-fast sintering with heating rate as high as  $\sim 10,000$  °C/min, producing dense materials in a matter of few seconds.<sup>71-73</sup> An additional advantage of the flash-SPS method is that no preheating is required when conducting

samples are used. Though flash sintering has been used predominantly to process high temperature ceramics like  $\text{SiC}$ ,<sup>73,74</sup>  $\text{ZrO}_2$ ,<sup>71</sup>  $\text{ZrB}_2$ ,<sup>75</sup> it has not been tried on many thermoelectric materials. Just recently, we have shown how to improve the TE properties of PbTe-based materials by the so called ‘Hybrid Flash-SPS’ processing (Chapter 4).<sup>53</sup> Motivated by those results, we have extended that process to Ga and Sb codoped GeTe. Indeed,  $\text{Ge}_{0.90}\text{Ga}_{0.02}\text{Sb}_{0.08}\text{Te}$  was consolidated by ‘Hybrid’ Flash-SPS processing, where the powders were sintered at 893 K with a heating rate of  $\sim 10,000$  °C/min (heated from 293 – 893 K in 3 seconds) under an axial pressure of 55 MPa. Typically, during a Flash-SPS process, the green compact sample was sandwiched between two graphite punches without a die and inserted in between the pistons of the SPS furnace.<sup>70</sup> But the ‘Hybrid’ Flash-SPS processing route is a variant of the originally developed Flash-SPS method, involving the use of a thin, low thermal inertia metal die to contain the TE powder during sintering.<sup>52</sup> The schematics of the experimental set-up and the current flow paths were shown in Chapter 4. Highly dense disk-shaped pellets were obtained with theoretical densities of  $\sim 98\%$  for Hybrid Flash-SPS.

It was established that higher the ratio of the carrier mobility to lattice thermal conductivity, the greater  $zT$ .<sup>76</sup> Normally, there is a trade-off when alloying a material. The lattice thermal conductivity is decreased due to scattering from impurities, but that also reduces the carrier mobility, meaning limited change in  $zT$ . An improvement in  $zT$  for an alloy system occurs only when  $\kappa_{\text{latt}}$  is reduced by a significant factor with little or no degradation of  $\mu$ . It was found that hybrid flash-SPS processing enhanced the thermopower (by suppressing the charge carrier density), but did not affect the carrier mobility (see Table 9.1). For the sintered codoped samples, the hybrid flash-SPS sample in particular exhibited a mean low  $\kappa_{\text{latt}} \sim 0.6$  W/mK in the temperature range from 550 K to 773 K (Figure 9.5.f). This reduction in  $\kappa_{\text{latt}}$  during flash processing is consistent with our recent report,<sup>53</sup> where we have shown that the ultra-fast sintering rate achieved during hybrid flash-SPS processing has helped to reduce the grain growth and enhance the boundary scattering of heat carrying phonons at the intergrain region. Due to its lowered charge carrier density, the hybrid flash-SPS sample exhibited a lower  $\sigma$  when compared to the SPS sample (Figure 9.5.a), but this was well compensated for by the improvement in the Seebeck coefficient (Figure 9.5.b) and a significant reduction in  $\kappa_e$  (Figure 9.5.e). This has helped the hybrid flash-SPS sample to exhibit ultra-low  $\kappa_{\text{total}} \sim 1$  W/mK at around 600 K (Figure 9.5.d).

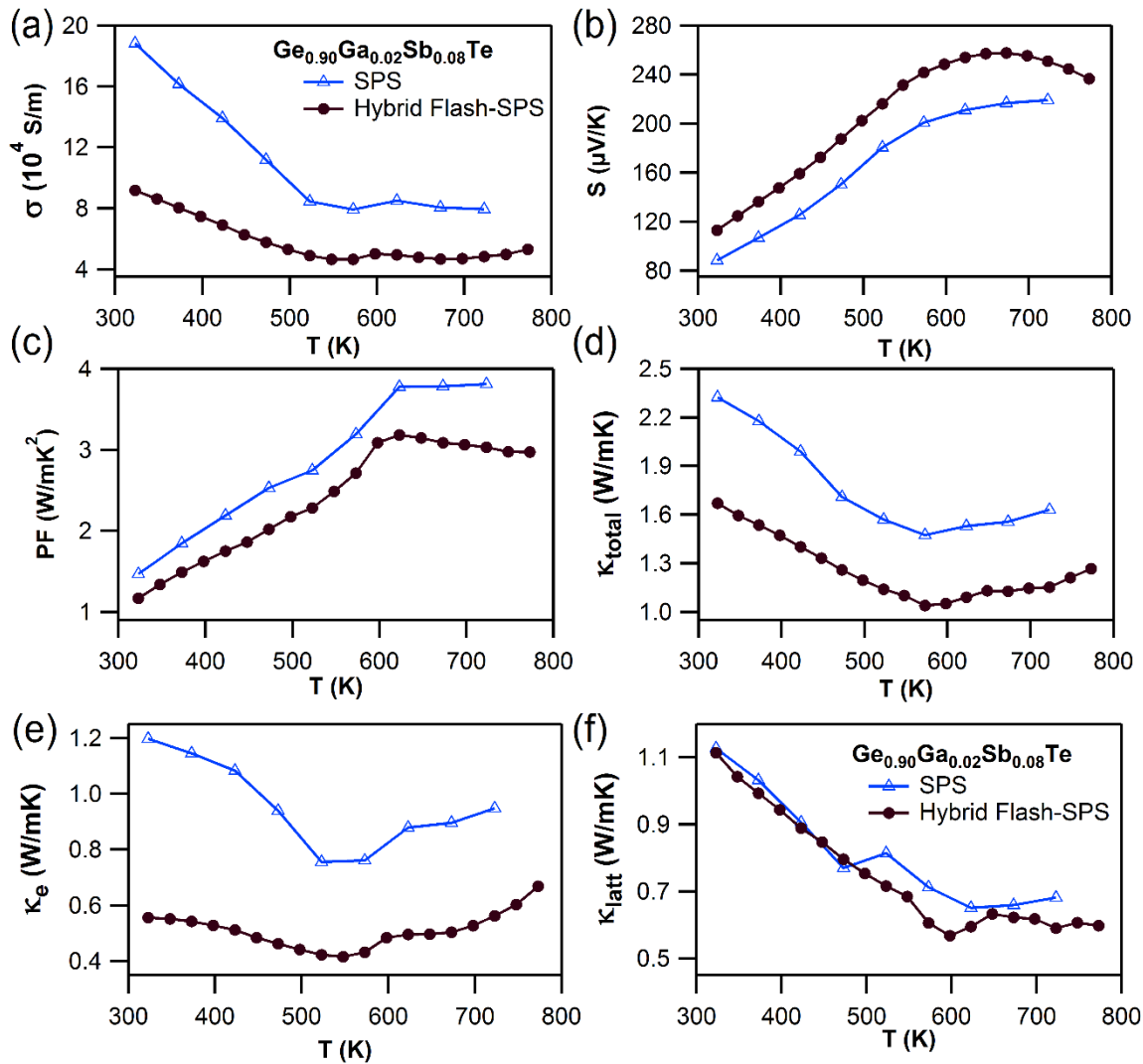


**Figure 9.5** Temperature-dependent electrical and thermal transport properties for  $\text{Ge}_{0.90}\text{Ga}_{0.02}\text{Sb}_{0.08}\text{Te}$  sample prepared by SPS and Hybrid Flash-SPS.

The enhanced thermopower coupled with the reduced electronic and lattice contributions to the thermal conductivity with no degradation in carrier mobility has helped the hybrid flash-SPS sample to reach a peak  $zT \sim 1.95$  at 723 K (Figure 9.6). The hybrid flash-SPS sample crossed  $zT > 1.75$  at a temperature as low as 600 K (whereas the SPS sample exhibited its peak  $zT \sim 1.75$  only at 723 K), thus making it more suitable for mid-temperature practical applications. More importantly, the hybrid flash SPS sample maintained (almost stabilized) the high  $zT$  over a wide temperature range (from 600 K – 773 K). From a practical point of view, it is not the maximum  $zT$  ( $zT_{\text{max}}$ ), but it is the average  $zT$  ( $zT_{\text{ave}}$ ) value that determines the overall efficiency of a TE module. In this temperature

range from 600 – 773 K, the  $zT$  was almost constant ( $zT_{\text{ave}} \sim 1.85$  in the temperature range from 600 – 773 K), thus making it one of the best reported materials among the Pb-free GeTe family. The results obtained were consistent and reproducible during the heating and cooling cycles. With the hybrid flash-SPS sintering process, we have demonstrated that it is possible to optimize the charge carrier density, and at the same time benefit from the decreased thermal conductivity without significantly affecting the carrier mobility (i.e., higher  $\mu/\kappa_{\text{total}}$  ratio). Moving forward, the hybrid flash-SPS technique can potentially be used as a strategic processing route to decouple electrical and thermal transport properties to produce high  $zT$  materials.

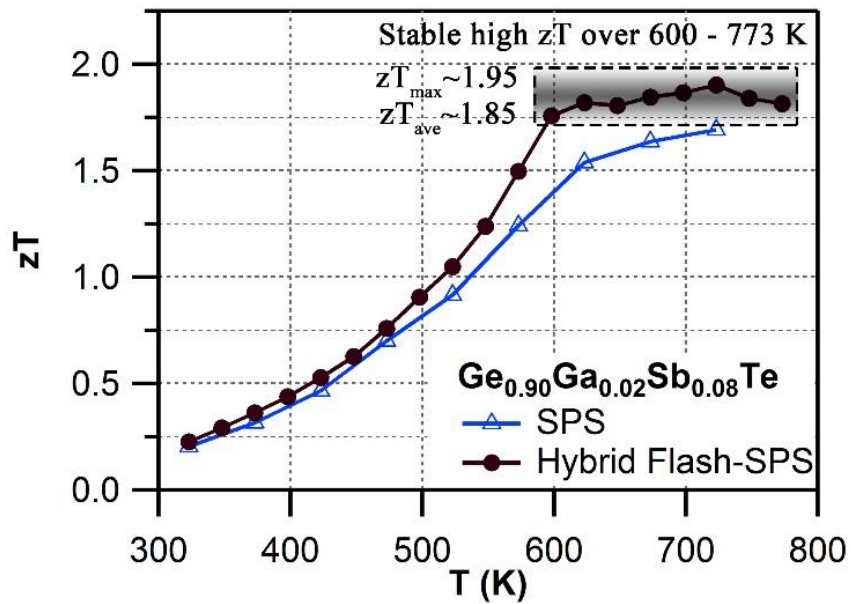


**Figure 9.6** Temperature dependent  $zT$  for SPS Vs Hybrid Flash-SPS processed  $\text{Ge}_{0.90}\text{Ga}_{0.02}\text{Sb}_{0.08}\text{Te}$  sample.

#### 9.4 Conclusion

In summary, on the basis of our experimental and theoretical studies, we conclude that optimized codoping of Ga-Sb in c-GeTe induces multiple effects: (i) suppression of  $p$ -type charge carriers; (ii) fostering of resonant states (induced by Ga) inside the valence band; (iii) activation of several bands with larger effective mass in the transport; (iv) reduction of the structural transition temperature and enhancement of band degeneracy; (v) convergence of light and heavy hole valence bands. These cooperative (synergistic) effects, combined with the benefits of hybrid flash-SPS processing, i.e., improvement of thermopower and reduction of thermal transport without any

degradation in carrier mobility, helped to achieve remarkably high and stabilized  $zT$  values (close to 2 for  $\text{Ge}_{0.90}\text{Ga}_{0.02}\text{Sb}_{0.08}\text{Te}$ , *i.e.* an improvement by 110% compared to undoped c-GeTe), making these Ga-Sb co-doped GeTe materials ideal candidates for mid-temperature power generation or energy harvesting devices.

➤ **Adaptation**

The results presented in this chapter have been published in *Inorganic Chemistry Frontiers* (RSC). Hence, this chapter is an adaptation from that publication – **B. Srinivasan *et al.*, *Inorg. Chem. Front.* 2018, In press. DOI: [10.1039/C8QI00703A](https://doi.org/10.1039/C8QI00703A)**

➤ **Author Contributions**

B.S conceived the project, designed and performed experiments, and wrote the journal manuscript. B.S also wrote the explanations pertaining to the theoretical (DFT) results. The DFT computations were performed by Dr. Alain Gellé (IPR Rennes). The hybrid flash-SPS experiments were carried out by B.S during his secondment activity at Nanoforce, London. Francesco Gucci supported B.S during those flash experiments.

## References

- (1) Sootsman, J. R.; Kong, H.; Uher, C.; D'Angelo, J. J.; Wu, C.-I.; Hogan, T. P.; Caillat, T.; Kanatzidis, M. G. Large Enhancements in the Thermoelectric Power Factor of Bulk PbTe at High Temperature by Synergistic Nanostructuring. *Angew. Chem. Int. Ed.* **2008**, *47* (45), 8618–8622.
- (2) Su, X.; Wei, P.; Li, H.; Liu, W.; Yan, Y.; Li, P.; Su, C.; Xie, C.; Zhao, W.; Zhai, P.; et al. Multi-Scale Microstructural Thermoelectric Materials: Transport Behavior, Non-Equilibrium Preparation, and Applications. *Adv. Mater.* **2017**, *29* (20), 1602013.
- (3) Zheng, Y.; Zhang, Q.; Su, X.; Xie, H.; Shu, S.; Chen, T.; Tan, G.; Yan, Y.; Tang, X.; Uher, C.; et al. Mechanically Robust BiSbTe Alloys with Superior Thermoelectric Performance: A Case Study of Stable Hierarchical Nanostructured Thermoelectric Materials. *Adv. Energy Mater.* **2015**, *5* (5), 1401391.

- (4) Morelli, D. T.; Jovovic, V.; Heremans, J. P. Intrinsically Minimal Thermal Conductivity in Cubic I-IV-VI<sub>2</sub> Semiconductors. *Phys. Rev. Lett.* **2008**, *101* (3), 035901.
- (5) Jana, M. K.; Biswas, K. Crystalline Solids with Intrinsically Low Lattice Thermal Conductivity for Thermoelectric Energy Conversion. *ACS Energy Lett.* **2018**, *3* (6), 1315–1324.
- (6) Samanta, M.; Pal, K.; Pal, P.; Waghmare, U. V.; Biswas, K. Localized Vibrations of Bi Bilayer Leading to Ultralow Lattice Thermal Conductivity and High Thermoelectric Performance in Weak Topological Insulator N-Type BiSe. *J. Am. Chem. Soc.* **2018**, *140* (17), 5866–5872.
- (7) Sales, B. C.; Mandrus, D.; Williams, R. K. Filled Skutterudite Antimonides: A New Class of Thermoelectric Materials. *Science* **1996**, *272* (5266), 1325–1328.
- (8) Banik, A.; Shenoy, U. S.; Anand, S.; Waghmare, U. V.; Biswas, K. Mg Alloying in SnTe Facilitates Valence Band Convergence and Optimizes Thermoelectric Properties. *Chem. Mater.* **2015**, *27* (2), 581–587.
- (9) Pei, Y.; Shi, X.; LaLonde, A.; Wang, H.; Chen, L.; Snyder, G. J. Convergence of Electronic Bands for High Performance Bulk Thermoelectrics. *Nature* **2011**, *473* (7345), 66–69.
- (10) Hicks, L. D.; Dresselhaus, M. S. Effect of Quantum-Well Structures on the Thermoelectric Figure of Merit. *Phys. Rev. B* **1993**, *47* (19), 12727–12731.
- (11) Zide, J. M. O.; Vashaee, D.; Bian, Z. X.; Zeng, G.; Bowers, J. E.; Shakouri, A.; Gossard, A. C. Demonstration of Electron Filtering to Increase the Seebeck Coefficient in InGaAs/InGaAlAs Superlattices. *Phys. Rev. B* **2006**, *74* (20), 205335.
- (12) Zhang, Q.; Liao, B.; Lan, Y.; Lukas, K.; Liu, W.; Esfarjani, K.; Opeil, C.; Broido, D.; Chen, G.; Ren, Z. High Thermoelectric Performance by Resonant Dopant Indium in Nanostructured SnTe. *Proc. Natl. Acad. Sci.* **2013**, *110* (33), 13261–13266.
- (13) Lin, S.; Li, W.; Chen, Z.; Shen, J.; Ge, B.; Pei, Y. Tellurium as a High-Performance Elemental Thermoelectric. *Nat. Commun.* **2016**, *7*, 10287.
- (14) Dresselhaus, M. S.; Chen, G.; Tang, M. Y.; Yang, R. G.; Lee, H.; Wang, D. Z.; Ren, Z. F.; Fleurial, J.-P.; Gogna, P. New Directions for Low-Dimensional Thermoelectric Materials. *Adv. Mater.* **2007**, *19* (8), 1043–1053.
- (15) Wang, H.; Pei, Y.; LaLonde, A. D.; Snyder, G. J. Weak Electron–Phonon Coupling Contributing to High Thermoelectric Performance in n-Type PbSe. *Proc. Natl. Acad. Sci.* **2012**, *109* (25), 9705–9709.
- (16) Pei, Y.; LaLonde, A. D.; Wang, H.; Snyder, G. J. Low Effective Mass Leading to High Thermoelectric Performance. *Energy Environ. Sci.* **2012**, *5* (7), 7963–7969.



- (17) Mori, T. Novel Principles and Nanostructuring Methods for Enhanced Thermoelectrics. *Small* **2017**, *13* (45), 1702013.
- (18) Takaki, H.; Kobayashi, K.; Shimono, M.; Kobayashi, N.; Hirose, K.; Tsujii, N.; Mori, T. Thermoelectric Properties of a Magnetic Semiconductor  $\text{CuFeS}_2$ . *Mater. Today Phys.* **2017**, *3*, 85–92.
- (19) Vandaele, K.; Watzman, S. J.; Flebus, B.; Prakash, A.; Zheng, Y.; Boona, S. R.; Heremans, J. P. Thermal Spin Transport and Energy Conversion. *Mater. Today Phys.* **2017**, *1*, 39–49.
- (20) Ahmed, F.; Tsujii, N.; Mori, T. Thermoelectric Properties of  $\text{CuGa}_{1-x}\text{Mn}_x\text{Te}_2$ : Power Factor Enhancement by Incorporation of Magnetic Ions. *J. Mater. Chem. A* **2017**, *5* (16), 7545–7554.
- (21) Al Rahal Al Orabi, R.; Mecholsky, N. A.; Hwang, J.; Kim, W.; Rhyee, J.-S.; Wee, D.; Fornari, M. Band Degeneracy, Low Thermal Conductivity, and High Thermoelectric Figure of Merit in  $\text{SnTe-CaTe}$  Alloys. *Chem. Mater.* **2016**, *28* (1), 376–384.
- (22) Banik, A.; Shenoy, U. S.; Saha, S.; Waghmare, U. V.; Biswas, K. High Power Factor and Enhanced Thermoelectric Performance of  $\text{SnTe-AgInTe}_2$ : Synergistic Effect of Resonance Level and Valence Band Convergence. *J. Am. Chem. Soc.* **2016**, *138* (39), 13068–13075.
- (23) Wang, L.; Tan, X.; Liu, G.; Xu, J.; Shao, H.; Yu, B.; Jiang, H.; Yue, S.; Jiang, J. Manipulating Band Convergence and Resonant State in Thermoelectric Material  $\text{SnTe}$  by Mn–In Codoping. *ACS Energy Lett.* **2017**, *2* (5), 1203–1207.
- (24) Banik, A.; Roychowdhury, S.; Biswas, K. The Journey of Tin Chalcogenides towards High-Performance Thermoelectrics and Topological Materials. *Chem. Commun.* **2018**, *54* (50), 6573–6590.
- (25) Srinivasan, B.; Boussard-Pledel, C.; Bureau, B. Thermoelectric Performance of Codoped (Bi, In)- $\text{GeTe}$  and (Ag, In, Sb)- $\text{SnTe}$  Materials Processed by Spark Plasma Sintering. *Mater. Lett.* **2018**, *230*, 191–194.
- (26) Bilc, D.; Mahanti, S. D.; Quarez, E.; Hsu, K.-F.; Pcionek, R.; Kanatzidis, M. G. Resonant States in the Electronic Structure of the High Performance Thermoelectrics  $\text{AgPb}_m\text{SbTe}_{2+m}$ : The Role of Ag-Sb Microstructures. *Phys. Rev. Lett.* **2004**, *93* (14), 146403.
- (27) Zhang, Q.; Cao, F.; Liu, W.; Lukas, K.; Yu, B.; Chen, S.; Opeil, C.; Broido, D.; Chen, G.; Ren, Z. Heavy Doping and Band Engineering by Potassium to Improve the Thermoelectric Figure of Merit in P-Type  $\text{PbTe}$ ,  $\text{PbSe}$ , and  $\text{PbTe}_{1-y}\text{Se}_y$ . *J. Am. Chem. Soc.* **2012**, *134* (24), 10031–10038.
- (28) Srinivasan, B.; Gucci, F.; Boussard-Pledel, C.; Cheviré, F.; Reece, M. J.; Tricot, S.; Calvez, L.; Bureau, B. Enhancement in Thermoelectric Performance of N-Type Pb-Deficit  $\text{Pb-Sb-Te}$  Alloys. *J. Alloys Compd.* **2017**, *729*, 198–202.

- (29) Fu, C.; Bai, S.; Liu, Y.; Tang, Y.; Chen, L.; Zhao, X.; Zhu, T. Realizing High Figure of Merit in Heavy-Band p-Type Half-Heusler Thermoelectric Materials. *Nat. Commun.* **2015**, *6*, 8144.
- (30) Liu, W.; Tan, X.; Yin, K.; Liu, H.; Tang, X.; Shi, J.; Zhang, Q.; Uher, C. Convergence of Conduction Bands as a Means of Enhancing Thermoelectric Performance of  $\text{Mg}_2\text{Si}_{1-x}\text{Sn}_x$  Solid Solutions. *Phys. Rev. Lett.* **2012**, *108* (16), 166601.
- (31) Yang, S. H.; Zhu, T. J.; Sun, T.; He, J.; Zhang, S. N.; Zhao, X. B. Nanostructures in High-Performance  $(\text{GeTe})_x(\text{AgSbTe}_2)_{100-x}$  Thermoelectric Materials. *Nanotechnology* **2008**, *19* (24), 245707.
- (32) Schröder, T.; Schwarzmüller, S.; Stiewe, C.; de Boor, J.; Hölzel, M.; Oeckler, O. The Solid Solution Series  $(\text{GeTe})_x(\text{LiSbTe}_2)_2$  ( $1 \leq x \leq 11$ ) and the Thermoelectric Properties of  $(\text{GeTe})_{11}(\text{LiSbTe}_2)_2$ . *Inorg. Chem.* **2013**, *52* (19), 11288–11294.
- (33) Schröder, T.; Rosenthal, T.; Giesbrecht, N.; Maier, S.; Scheidt, E.-W.; Scherer, W.; Snyder, G. J.; Schnick, W.; Oeckler, O. TAGS-Related Indium Compounds and Their Thermoelectric Properties – the Solid Solution Series  $(\text{GeTe})_x\text{AgIn}_y\text{Sb}_{1-y}\text{Te}_2$  ( $x = 1-12$ ;  $y = 0.5$  and  $1$ ). *J. Mater. Chem. A* **2014**, *2* (18), 6384–6395.
- (34) Samanta, M.; Roychowdhury, S.; Ghatak, J.; Perumal, S.; Biswas, K. Ultrahigh Average Thermoelectric Figure of Merit, Low Lattice Thermal Conductivity and Enhanced Microhardness in Nanostructured  $(\text{GeTe})_x(\text{AgSbSe}_2)_{100-x}$ . *Chem. Eur. J.* **2017**, *23*, 7438–7443.
- (35) Fahrnbauer, F.; Souchay, D.; Wagner, G.; Oeckler, O. High Thermoelectric Figure of Merit Values of Germanium Antimony Tellurides with Kinetically Stable Cobalt Germanide Precipitates. *J. Am. Chem. Soc.* **2015**, *137* (39), 12633–12638.
- (36) Gelbstein, Y.; Davidow, J. Highly Efficient Functional  $\text{Ge}_x\text{Pb}_{1-x}\text{Te}$  Based Thermoelectric Alloys. *Phys. Chem. Chem. Phys.* **2014**, *16* (37), 20120–20126.
- (37) Perumal, S.; Roychowdhury, S.; Biswas, K. Reduction of Thermal Conductivity through Nanostructuring Enhances the Thermoelectric Figure of Merit in  $\text{Ge}_{1-x}\text{Bi}_x\text{Te}$ . *Inorg. Chem. Front.* **2016**, *3* (1), 125–132.
- (38) Wu, D.; Zhao, L.-D.; Hao, S.; Jiang, Q.; Zheng, F.; Doak, J. W.; Wu, H.; Chi, H.; Gelbstein, Y.; Uher, C.; et al. Origin of the High Performance in GeTe-Based Thermoelectric Materials upon  $\text{Bi}_2\text{Te}_3$  Doping. *J. Am. Chem. Soc.* **2014**, *136* (32), 11412–11419.
- (39) Wu, L.; Li, X.; Wang, S.; Zhang, T.; Yang, J.; Zhang, W.; Chen, L.; Yang, J. Resonant Level-Induced High Thermoelectric Response in Indium-Doped GeTe. *NPG Asia Mater.* **2017**, *9* (1), e343.
- (40) Yang, L.; Li, J. Q.; Chen, R.; Li, Y.; Liu, F. S.; Ao, W. Q. Influence of Se Substitution in GeTe on Phase and Thermoelectric Properties. *J. Electron. Mater.* **2016**, *45* (11), 5533–5539.

- (41) Perumal, S.; Roychowdhury, S.; Negi, D. S.; Datta, R.; Biswas, K. High Thermoelectric Performance and Enhanced Mechanical Stability of P-Type  $\text{Ge}_{1-x}\text{Sb}_x\text{Te}$ . *Chem. Mater.* **2015**, *27* (20), 7171–7178.
- (42) Nshimiyimana, E.; Su, X.; Xie, H.; Liu, W.; Deng, R.; Luo, T.; Yan, Y.; Tang, X. Realization of Non-Equilibrium Process for High Thermoelectric Performance Sb-Doped GeTe. *Sci. Bull.* **2018**, *63* (11), 717–725.
- (43) Srinivasan, B.; Gautier, R.; Gucci, F.; Fontaine, B.; Halet, J.-F.; Chevirié, F.; Boussard-Pledel, C.; Reece, M. J.; Bureau, B. Impact of Coinage Metal Insertion on the Thermoelectric Properties of GeTe Solid-State Solutions. *J. Phys. Chem. C* **2018**, *122* (1), 227–235.
- (44) Zheng, Z.; Su, X.; Deng, R.; Stoumpos, C.; Xie, H.; Liu, W.; Yan, Y.; Hao, S.; Uher, C.; Wolverton, C.; et al. Rhombohedral to Cubic Conversion of GeTe via MnTe Alloying Leads to Ultralow Thermal Conductivity, Electronic Band Convergence, and High Thermoelectric Performance. *J. Am. Chem. Soc.* **2018**, *140* (7), 2673–2686.
- (45) Lee, J. K.; Oh, M. W.; Kim, B. S.; Min, B. K.; Lee, H. W.; Park, S. D. Influence of Mn on Crystal Structure and Thermoelectric Properties of GeTe Compounds. *Electron. Mater. Lett.* **2014**, *10* (4), 813–817.
- (46) Rosenberg, Y.; Gelbstein, Y.; Dariel, M. P. Phase Separation and Thermoelectric Properties of the  $\text{Pb}_{0.25}\text{Sn}_{0.25}\text{Ge}_{0.5}\text{Te}$  Compound. *J. Alloys Compd.* **2012**, *526*, 31–38.
- (47) Li, J.; Zhang, X.; Lin, S.; Chen, Z.; Pei, Y. Realizing the High Thermoelectric Performance of GeTe by Sb-Doping and Se-Alloying. *Chem. Mater.* **2017**, *29* (2), 605–611.
- (48) Samanta, M.; Biswas, K. Low Thermal Conductivity and High Thermoelectric Performance in  $(\text{GeTe})_{1-2x}(\text{GeSe})_x(\text{GeS})_x$ : Competition between Solid Solution and Phase Separation. *J. Am. Chem. Soc.* **2017**, *139* (27), 9382–9391.
- (49) Perumal, S.; Bellare, P.; Shenoy, U. S.; Waghmare, U. V.; Biswas, K. Low Thermal Conductivity and High Thermoelectric Performance in Sb and Bi Codoped GeTe: Complementary Effect of Band Convergence and Nanostructuring. *Chem. Mater.* **2017**, *29* (24), 10426–10435.
- (50) Li, J.; Zhang, X.; Chen, Z.; Lin, S.; Li, W.; Shen, J.; Witting, I. T.; Faghaninia, A.; Chen, Y.; Jain, A.; et al. Low-Symmetry Rhombohedral GeTe Thermoelectrics. *Joule* **2018**, *2* (5), 976–987.
- (51) Perumal, S.; Roychowdhury, S.; Biswas, K. High Performance Thermoelectric Materials and Devices Based on GeTe. *J. Mater. Chem. C* **2016**, *4* (32), 7520–7536.
- (52) Gucci, F.; Saunders, T. G.; Reece, M. J. In-Situ Synthesis of n-Type Unfilled Skutterudite with Reduced Thermal Conductivity by Hybrid Flash-Spark Plasma Sintering. *Scr. Mater.* **2018**, *157*, 58–61.

- (53) Srinivasan, B.; Fontaine, B.; Gucci, F.; Dorcet, V.; Saunders, T. G.; Yu, M.; Cheviré, F.; Boussard-Pledel, C.; Halet, J.-F.; Gautier, R.; et al. Effect of the Processing Route on the Thermoelectric Performance of Nanostructured  $\text{CuPb}_{18}\text{SbTe}_{20}$ . *Inorg. Chem.* **2018**, *57* (20), 12976–12986.
- (54) Kresse, G.; Joubert, D. From Ultrasoft Pseudopotentials to the Projector Augmented-Wave Method. *Phys. Rev. B* **1999**, *59* (3), 1758–1775.
- (55) Kresse, G.; Furthmüller, J. Efficient Iterative Schemes for Ab Initio Total-Energy Calculations Using a Plane-Wave Basis Set. *Phys. Rev. B* **1996**, *54* (16), 11169–11186.
- (56) Perdew, J. P.; Burke, K.; Ernzerhof, M. Generalized Gradient Approximation Made Simple. *Phys. Rev. Lett.* **1996**, *77* (18), 3865–3868.
- (57) Hoang, K.; Mahanti, S. D.; Kanatzidis, M. G. Impurity Clustering and Impurity-Induced Bands in PbTe-, SnTe-, and GeTe-Based Bulk Thermoelectrics. *Phys. Rev. B* **2010**, *81* (11), 115106.
- (58) May, A. F.; Toberer, E. S.; Saramat, A.; Snyder, G. J. Characterization and Analysis of Thermoelectric Transport in N-Type  $\text{Ba}_8\text{Ga}_{16-x}\text{Ge}_{30+x}$ . *Phys. Rev. B* **2009**, *80* (12), 125205.
- (59) Toberer, E. S.; Zevalkink, A.; Crisosto, N.; Snyder, G. J. The Zintl Compound  $\text{Ca}_5\text{Al}_2\text{Sb}_6$  for Low-Cost Thermoelectric Power Generation. *Adv. Funct. Mater.* **2010**, *20* (24), 4375–4380.
- (60) Levin, E. M.; Besser, M. F.; Hanus, R. Electronic and Thermal Transport in GeTe: A Versatile Base for Thermoelectric Materials. *J. Appl. Phys.* **2013**, *114* (8), 083713.
- (61) Levin, E. M. Effects of Ge Substitution in GeTe by Ag or Sb on the Seebeck Coefficient and Carrier Concentration Derived from  $^{125}\text{Te}$  NMR. *Phys. Rev. B* **2016**, *93* (4), 045209.
- (62) Androulakis, J.; Todorov, I.; Chung, D.-Y.; Ballikaya, S.; Wang, G.; Uher, C.; Kanatzidis, M. Thermoelectric Enhancement in PbTe with K or Na Codoping from Tuning the Interaction of the Light- and Heavy-Hole Valence Bands. *Phys. Rev. B* **2010**, *82* (11), 115209.
- (63) Roychowdhury, S.; Sandhya Shenoy, U.; V. Waghmare, U.; Biswas, K. An Enhanced Seebeck Coefficient and High Thermoelectric Performance in P-Type In and Mg Co-Doped  $\text{Sn}_{1-x}\text{Pb}_x\text{Te}$  via the Co-Adjuvant Effect of the Resonance Level and Heavy Hole Valence Band. *J. Mater. Chem. C* **2017**, *5* (23), 5737–5748.
- (64) Hong, M.; Chen, Z.-G.; Yang, L.; Zou, Y.-C.; Dargusch, M. S.; Wang, H.; Zou, J. Realizing ZT of 2.3 in  $\text{Ge}_{1-x-y}\text{Sb}_x\text{In}_y\text{Te}$  via Reducing the Phase-Transition Temperature and Introducing Resonant Energy Doping. *Adv. Mater.* **2018**, *30* (11), 1705942.
- (65) Li, J.; Chen, Z.; Zhang, X.; Sun, Y.; Yang, J.; Pei, Y. Electronic Origin of the High Thermoelectric Performance of GeTe among the P-Type Group IV Monotellurides. *NPG Asia Mater.* **2017**, *9* (3), e353.

- (66) Hong, M.; Chen, Z.-G.; Pei, Y.; Yang, L.; Zou, J. Limit of  $zT$  Enhancement in Rocksalt Structured Chalcogenides by Band Convergence. *Phys. Rev. B* **2016**, *94* (16), 161201.
- (67) Pei, Y.; Wang, H.; Snyder, G. J. Band Engineering of Thermoelectric Materials. *Adv. Mater.* **2012**, *24* (46), 6125–6135.
- (68) Roychowdhury, S.; Biswas, K. Slight Symmetry Reduction in Thermoelectrics. *Chem* **2018**, *4* (5), 939–942.
- (69) Fritzsche, H. Electronic Processes in Non-Crystalline Materials. N. F. Mott and E. A. Davis. Oxford University Press, New York, 1971. Xiv, 438 Pp., Illus. 24. International Series of Monographs on Physics. *Science* **1972**, *176* (4039), 1117–1117.
- (70) Du, B.; Gucci, F.; Porwal, H.; Grasso, S.; Mahajan, A.; Reece, M. J. Flash Spark Plasma Sintering of Magnesium Silicide Stannide with Improved Thermoelectric Properties. *J. Mater. Chem. C* **2017**, *5* (6), 1514–1521.
- (71) Cologna Marco; Rashkova Boriana; Raj Rishi. Flash Sintering of Nanograin Zirconia in  $<5$  s at  $850^\circ\text{C}$ . *J. Am. Ceram. Soc.* **2010**, *93* (11), 3556–3559.
- (72) Yu, M.; Grasso, S.; Mckinnon, R.; Saunders, T.; Reece, M. J. Review of Flash Sintering: Materials, Mechanisms and Modelling. *Adv. Appl. Ceram.* **2017**, *116* (1), 24–60.
- (73) Olevsky, E. A.; Roling, S. M.; Maximenko, A. L. Flash (Ultra-Rapid) Spark-Plasma Sintering of Silicon Carbide. *Sci. Rep.* **2016**, *6*, 33408.
- (74) Grasso, S.; Kim, E.-Y.; Saunders, T.; Yu, M.; Tudball, A.; Choi, S.-H.; Reece, M. Ultra-Rapid Crystal Growth of Textured SiC Using Flash Spark Plasma Sintering Route. *Cryst. Growth Des.* **2016**, *16* (4), 2317–2321.
- (75) Grasso Salvatore; Saunders Theo; Porwal Harshit; Cedillos-Barraza Omar; Jayaseelan Daniel Doni; Lee William E.; Reece Mike John; Fahrenholtz W. Flash Spark Plasma Sintering (FSPS) of Pure  $\text{ZrB}_2$ . *J. Am. Ceram. Soc.* **2014**, *97* (8), 2405–2408.
- (76) Wang, J. L.; Wang, H.; Snyder, G. J.; Zhang, X.; Ni, Z. H.; Chen, Y. F. Characteristics of Lattice Thermal Conductivity and Carrier Mobility of Undoped  $\text{PbSe-PbS}$  Solid Solutions. *J. Phys. Appl. Phys.* **2013**, *46* (40), 405301.





## **Conclusion & Outlook**





## 1. Conclusion

The generation, storage, and transport of sustainable supply of energy (from renewable sources) are among the greatest challenges, if not the most formidable challenge at all, for years to come. In this context, thermoelectric materials and devices are playing an important role, as they can harvest waste heat, and transform them into useful electric power, via the Seebeck effect. Although there have been exciting new developments in this field like the emergence of novel concepts of band engineering, nanostructuring and discoveries of various novel materials, many open questions remain unanswered. This PhD thesis, developed within the framework of European project CoACH-ETN (2015 – 2018) and aimed at addressing some of those concerns, has extensively covered a wide range of chalcogenide based materials (ranging from amorphous glasses to crystalline ceramics) in engineering their thermoelectric properties.

Firstly, the idea of conducting chalcogenide based glasses as potential thermoelectric materials was looked at, which was a continuation of the previous work by earlier PhD (Shuo Cui from Glasses and Ceramic Laboratory in Rennes). By doping Cu to As-Te glasses, they were able to increase their electrical conductivity by about 5 orders of magnitude, without involving any crystallization and retaining their characteristic high Seebeck coefficient and low thermal conductivity. By understanding the local structure of those Cu-As-Te glasses with the help of Synchrotron studies and multiple scattering based ab-initio calculations (Chapter 2), we were able to decipher the reason for such a raise in electrical conductivity in those Cu doped glasses. Small electron charge transfer from Te 5p non-bonding states to Cu 4s empty states (leading to an unexpected positive valence for Te and negative valence for Cu) was found to be the possible reason.

Next, in the pursuit of phonon-glass electron-crystal approach, the idea of crystallized glasses was explored.  $\text{Ge}_{20}\text{Te}_{77}\text{Se}_3$  glasses were intentionally crystallized by (excessively) doping with Cu and Bi (Chapter 3). These effectively-crystallized materials of composition  $(\text{Ge}_{20}\text{Te}_{77}\text{Se}_3)_{100-x}\text{M}_x$  (M = Cu or Bi;  $x = 5, 10, 15$ ), exhibited increased electrical conductivity due to excess hole concentration. These materials were also found to manifest ultra-low thermal conductivity, especially the heavily Bi-doped samples, which possessed  $\kappa_{\text{latt}} \sim 0.7 \text{ Wm}^{-1} \text{ K}^{-1}$  at 525 K. Owing to their high metallic behavior, Cu-doped samples did not manifest as low thermal conductivity as Bi-doped samples. The high electrical conductivity and exceptionally low thermal conductivity of the Bi-doped materials did not significantly enhance the thermoelectric figure of merit,  $zT$ , as those crystallized glasses could not retain the characteristic high Seebeck coefficient values of semiconducting telluride glasses.

After attempts with glasses and glass-ceramics, the focus shifted to polycrystalline materials. To start with, well-known PbTe based materials were further explored. The quaternary  $\text{AgPb}_{18}\text{SbTe}_{20}$  compound (abbreviated as LAST) is a prominent thermoelectric material with good performance. Endotaxially embedded nanoscale Ag-rich precipitates contribute significantly to decreased  $\kappa_{\text{latt}}$  in LAST alloys. In this work (Chapter 4), Ag in LAST alloys was completely replaced by the more economically available Cu. Herein, we conscientiously investigated the different routes of synthesizing  $\text{CuPb}_{18}\text{SbTe}_{20}$  after vacuum-sealed tube melt processing, including: (i) slow cooling of the melt; (ii) quenching and annealing; (iii) consolidation by spark plasma sintering (SPS); and also the recently developed (iv) Hybrid Flash-SPS. Irrespective of the method of synthesis, the electrical and thermal ( $\kappa_{\text{tot}}$ ) conductivities of  $\text{CuPb}_{18}\text{SbTe}_{20}$  samples were akin to that of LAST alloys. Both the hybrid flash-SPSed and the slow cooled  $\text{CuPb}_{18}\text{SbTe}_{20}$  samples with nanoscale dislocations and Cu-rich nanoprecipitates exhibited an ultra-low  $\kappa_{\text{latt}} \sim 0.58 \text{ W/mK}$  at 723 K, comparable with that its Ag counterpart, regardless of differences in their size of the precipitates, type of precipitate-matrix interfaces and other nanoscopic architectures. The sample processed by flash sintering manifested higher  $zT \sim 0.9$  at 723 K, due to better optimization and trade-off between the transport properties by decreasing the carrier concentration and  $\kappa_{\text{latt}}$  without degrading the carrier mobility. In spite of their comparable  $\sigma$  and  $\kappa_{\text{tot}}$ , the  $zT$  of the Cu samples were low compared to the Ag samples due to their contrasting thermopower values. First-principles calculations attribute this variation in Seebeck to the dwindling of the energy gap (from 0.1 eV to 0.02 eV) between the valence and conduction bands in  $\text{MPb}_{18}\text{SbTe}_{20}$  (M = Cu or Ag), when Cu replaces Ag.

Next, the idea of vacancy tuning or composition engineering was briefly glanced. A systematic study of thermoelectric transport properties of *n*-type Pb-deficit  $\text{Pb}_{0.98-x}\text{Sb}_x\text{Te}$  ( $x = 0.02 - 0.12$ ) alloys was performed (Chapter 5). A maximum  $zT \sim 0.81$  was achieved at 623 K for 4 mol% Sb containing Pb-deficit composition, by the cumulative integration of enhanced power factor and significant reduction in thermal conductivity. The scattering of phonons at Pb vacancies, contributed to the reduction of  $\kappa_{\text{latt}}$ , and thereby strikingly boosted the  $zT$  (by  $\sim 170\%$ ) of the Pb-deficit samples when compared with the pristine (stoichiometric)  $\text{Pb}_{1-x}\text{Sb}_x\text{Te}$ .

After PbTe, the center of attention switched to GeTe based materials, which are more eco-friendlier than toxic PbTe. To begin with, a comprehensive study on the thermoelectric effect of Ag substitution in GeTe solid solutions, a congenital base for high efficient TAGS-m  $[(\text{GeTe})_m(\text{AgSbTe}_2)_{100-m}]$  thermoelectric materials, was performed (Chapter 6). Aliovalent Ag substitution in GeTe increased the hole concentration and decreased the  $zT$  due to the reduction of the Seebeck coefficient, which was ascribed mainly to the lowering of the Fermi level together with

the loss of band degeneracy. Band structure and effective mass calculations of these doped materials also pointed to a soaring contribution from several hole pockets in the valence band. First-principles calculations carried out with two other group-11 transition metals (Cu, Au) reveal that silver substitution has the lowest impact on the thermopower of r-GeTe.

After no real success with group-11 elements, we moved on to group-13 elements. In and Ga were found to enhance the thermoelectric performance in GeTe. However, Al doping (isoelectronic to In and Ga) was rather found to be detrimental to the thermoelectric performance of GeTe, as it reduced the thermopower by increasing the energy separation between the two valence bands (loss of band convergence). Additionally, divalent Ba doping was also found to be detrimental to the TE properties of GeTe (Chapter 7).

The findings from Chapter 6 and 7 highlighted the limits in doping just a coinage metal or at times just a group-13 element or other elements like Ba / Gd / Mg (Gd and Mg doping are not shown in this thesis) to GeTe and recapitulated the need for pair substitution (like TAGS alloys) to enhance the thermoelectric properties of GeTe-based solid-state solutions. Hence, the idea of codoping or double/multiple substitution, where two or more different dopants would play distinctive and complementary roles, was pursued. We started with two different codoped systems (Chapter 8): (i) In-Bi codoped GeTe, and (ii) In-Sb codoped SnTe. Though it did not substantially improve the peak  $zT$  of the respective systems, the obtained results were quite promising as the average  $zT$  ( $zT_{ave}$ ) was significantly improved for both the codoped systems. In particular, the  $\text{Ge}_{0.93}\text{Bi}_{0.05}\text{In}_{0.02}\text{Te}$  sample maintained/stabilized the peak  $zT \sim 0.85$  over a wide spectrum of temperature from 550 – 773 K.

Because of its promise, we persisted with the idea of codoping, which finally yielded rich dividends. A remarkably high and stable thermoelectric  $zT$  of close to 2 was achieved by manipulating the electronic bands in Ga-Sb codoped GeTe, which has been processed by hybrid flash-spark plasma sintering (Chapter 9). According to the experimental results and first-principles calculations, the vast enhancement achieved in the thermopower due to codoping of Ga (2 mol%) and Sb (8 mol%) in GeTe was attributed to a concoction of reasons: (i) suppression of hole concentration; (ii) improved band convergence by decreasing the energy separation between the two valence band maxima to 0.026 eV; (iii) Ga predominantly contributing to the top of the valence band in Ga-Sb codoped GeTe, despite Ga-induced resonance state not located at a favorable position near the Fermi level; (iv) active participation of several bands increasing the hole carrier effective mass; (v) facilitating band degeneracy by reducing the  $R3m \rightarrow Fm-3m$  structural transition temperature from 700 K to 580 K. The synergy between these complementary and beneficial effects, in addition to the reduced thermal conductivity, enabled the flash sintered  $\text{Ge}_{0.90}\text{Ga}_{0.02}\text{Sb}_{0.08}\text{Te}$  composition to not only exhibit a peak of

$zT \sim 1.95$  at 723 K, but also to maintain/stabilize its high performance over a broad range of temperature (600 – 775K), thus making it a serious candidate for mid-temperature range energy harvesting devices.

To summarize, this thesis has covered a wide range of materials for thermoelectrics, starting from novel glasses, glass-ceramics to polycrystalline materials; different synthesis and processing techniques, right from traditional melt processing to advanced flash-spark plasma sintering; distinct approaches like dopant induced glass crystallization, composition engineering, nanostructuring, electronic band structure engineering, *etc.*, to enhance the thermoelectric performance. Many promising results have been obtained and all the findings presented in this thesis will hopefully help in advancing the state of knowledge on thermoelectric materials and devices.

### **2. Future Outlook & Perspectives** (based on the thesis results)

Although a lot of insightful research have been done on thermoelectric materials, there is still a plenty of scope to explore more on the outcome of the results obtained so far. Based on this thesis, some possible areas where the work can be continued in future are as follows,

- (a) To validate further the results that were obtained on Cu-As-Te glasses, it would be interesting to look for positive correlations between the increase in electrical conductivity and the increase in Cu-Te bonds by the study of Cu-Te pair distribution function.
- (b) There seems to be some promise with the idea of crystallizing the glasses. In order to tune the transport properties, additional time and efforts can be devoted in obtaining a particular phase, *i.e.*, single phase, from the crystallization process (maybe partial crystallization).
- (c) During the hybrid-flash SPS process, there is a substantial change (beneficial effects) occurring with charge carrier density and carrier mobility. But the physical mechanisms and the causes for such changes are still not clear. More understanding of this aspect will help in a better control and optimization of electrical transport properties. As the thermal transport was significantly suppressed during flash-SPS processing (thanks to grain size reduction and multi-scale hierarchical architectures), optimizing the electrical transport will certainly help in designing high performance thermoelectric materials.

- (d) Tuning cation vacancies have proved to be quite effective in enhancing thermoelectric properties. Other than  $\text{Th}_3\text{P}_4$  structure compounds, PbTe and SnTe based alloys, the idea have not been tried on several classes of materials, which can be further looked into.
- (e) The results obtained for our Ga-Sb codoped GeTe and the recent suggestion on slight symmetry breaking (by Pei and coworkers) are closely related and the activities in that direction can be actively persisted with. This can pave the way in expanding low symmetry materials (which are known for their lattice thermal conductivity) for efficient thermoelectrics. So far, only the high symmetry cubic (which are known for their high band degeneracy) have been intensely explored. If the symmetry breaking of band degeneracy is small, both high and low symmetry effects (*i.e.*, both band degeneracy and low  $\kappa_{\text{latt}}$ ) may be realized simultaneously.
- (f) Trial experiment on 2 mol% LiI doped GeTe has shown some promise with an improvement in  $zT$  (Annexure 9, Figure A9.11). Might be interesting to see the evolution of  $zT$  with the varying LiI content. It seems likely to reach  $zT > 1.5$  at higher LiI content.

### 3. General Opinion (from a personal point of view)

On a whole, the PhD journey for the past 3 years has been quite amazing. Of course, lots of blocks and obstacles, ups and downs.....a roller-coaster ride, as like in any aspect of life. It has certainly given me the confidence to tackle the challenges with poise.

A word must be added on the CoACH-ETN program. I'm extremely grateful to be part of this Marie-Curie ITN action. It has provided a lot of training opportunities in diversified areas, ranging from scientific trainings to nurturing the soft skills. The secondment activities, periodic workshops / status meetings with the consortium members, opportunity to travel to different European cities, lovely friendships and acquaintances, and many more.....it's a complete package that one would hope for!

The involvement of Nanoforce Technology Ltd., (London) in my thesis work is really a blessing. In particular, my secondment and training activity there was quite enriching. Moreover, I was lucky enough to forge a new network of collaboration with different teams and institutes in Rennes (IPR and ISCR). Without those kind collaborations, my thesis wouldn't have seen the light. I'm hopeful that the network forged during the tenure of my PhD will continue to work together in driving the thermoelectric research in Rennes.



## **Annexures**





## Annexure 1

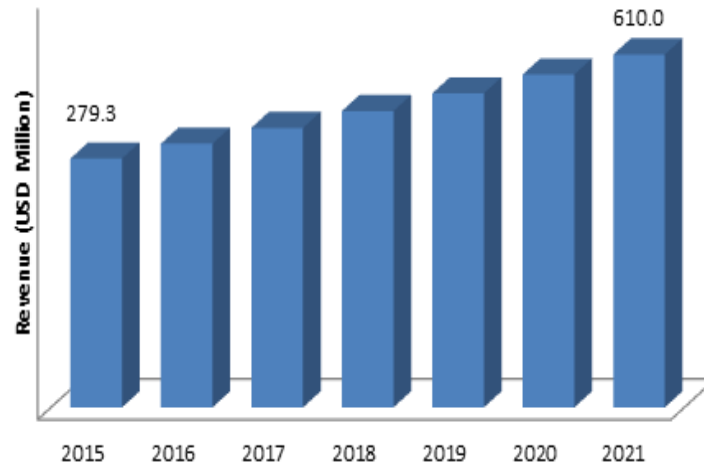


Figure A1.1 Global Thermoelectric Generator Market Revenue 2015-2021.<sup>1</sup>

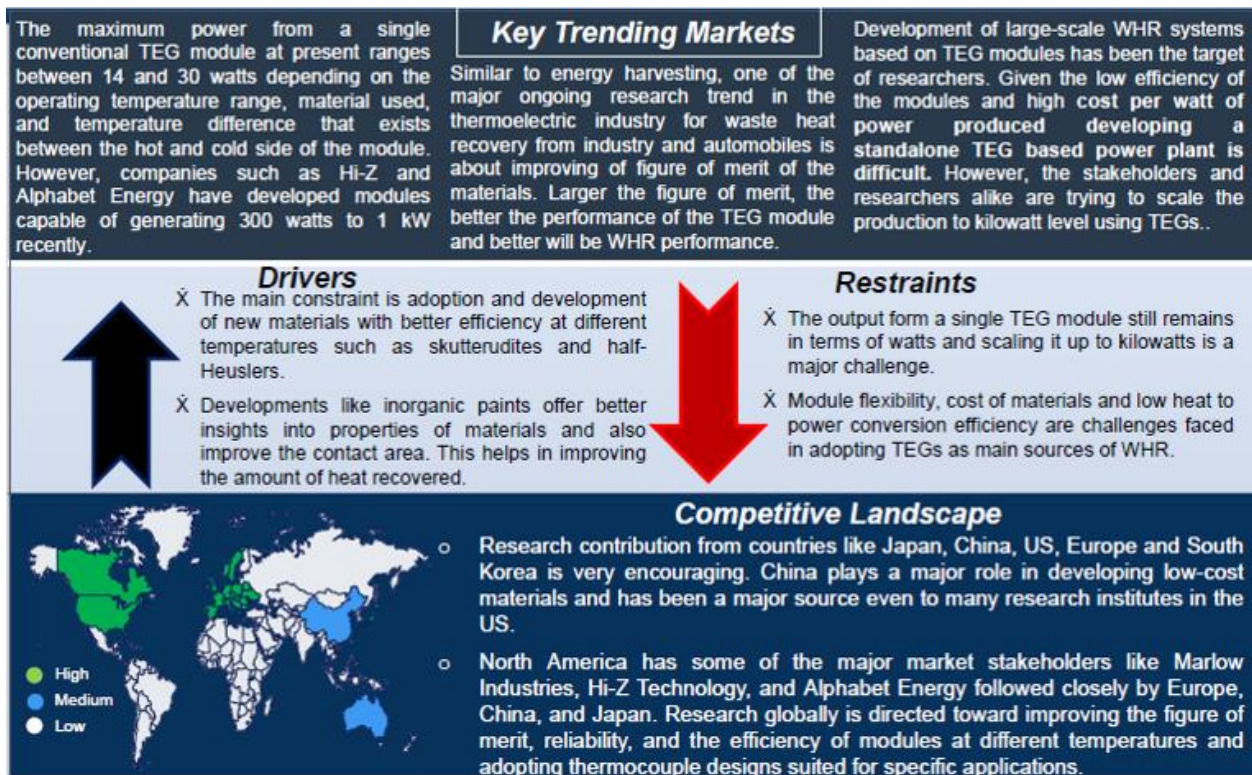


Figure A1.2 Strategic perspective in TEG module diffusion <sup>2</sup>

<sup>1</sup> **Zion Market Research:** “Thermoelectric Generator Market by Source (Waste Heat Recovery, Energy Harvesting, Direct Power Generation, And Co-Generation), and Application for (Automotive, Aerospace & Defense, Industrial and Others Applications) - Global Industry Perspective, Comprehensive Analysis and Forecast, 2015 – 2021”

<sup>2</sup> **Frost & Sullivan:** “Thermoelectric Generators for Energy Harvesting and Waste Heat Recovery - Energy and Power Systems TOE”.

## Annexure 2

## A2.1 Glass / Glass-Ceramic Synthesis

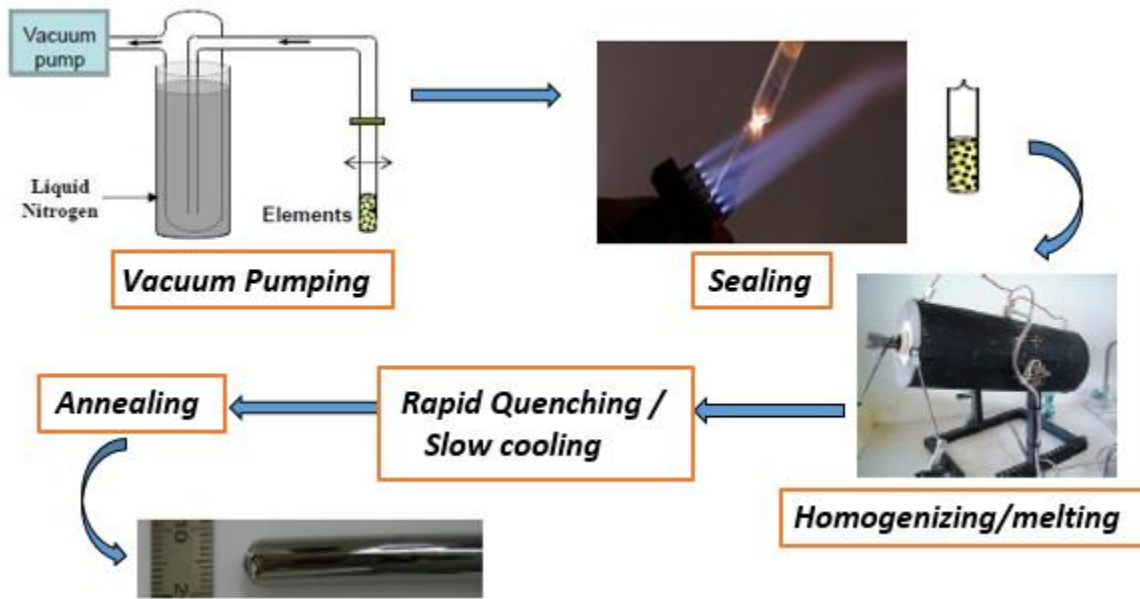
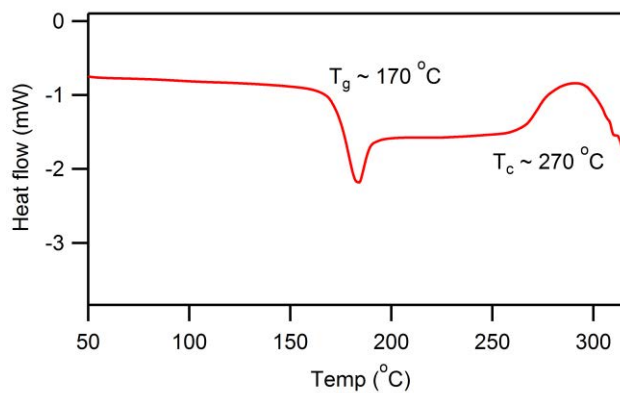


**Figure A2.1** Schematics of glass / glass-ceramic synthesis (by vacuum-sealed tube melting process).

Usually, the process of rapid quenching (in water) and subsequent annealing was employed during glass synthesis, while slow-cooling of the melt was employed for the synthesis of ceramic or crystalline materials.

## A2.2 Thermal Stability of Cu-As-Te Glasses



Properties	Temp.
Glass transition ( $T_g$ )	$\sim 170$ °C
Crystallization ( $T_c$ )	$\sim 270$ °C
Glass stability ( $\Delta T = T_g - T_c$ )	$\sim 100$ °C

**Figure A2.2** DSC curve for  $(Te_{85}Se_{15})_{45}As_{30}Cu_{25}$  glass.

## Annexure 3

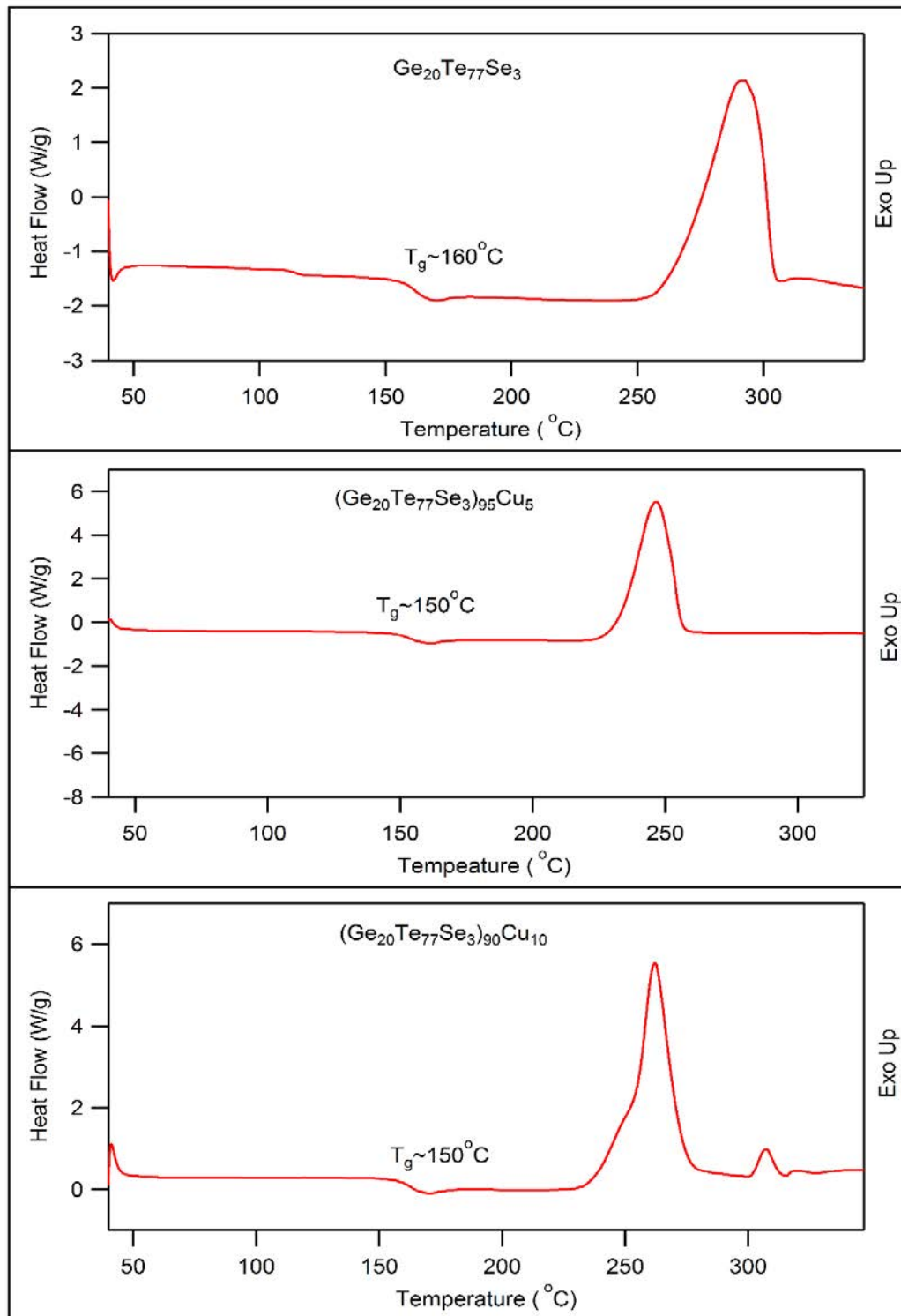


**Figure A3.1** DSC curves for GTS, GTS-Cu05 and GTS-Cu10 samples. Comparing crystallization ( $T_c$ ) and glass transition temperatures ( $T_g$ ), it corresponds to  $\Delta T \sim 100^{\circ}\text{C}$   $\rightarrow$  quite stable glasses.

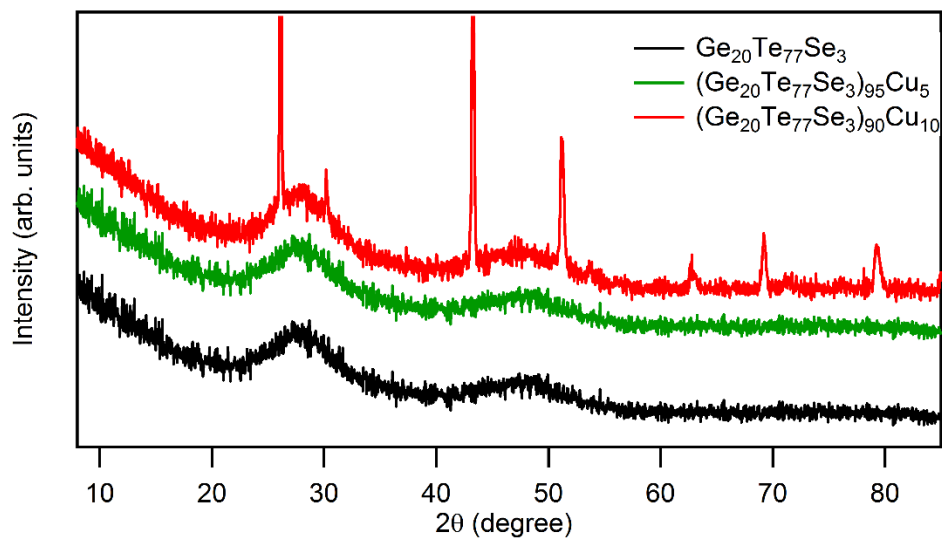


**Figure A3.2** PXRD patterns showing completely amorphous features for GTS and GTS-Cu05, and with a few crystalline peaks for mostly amorphous GTS-Cu10.

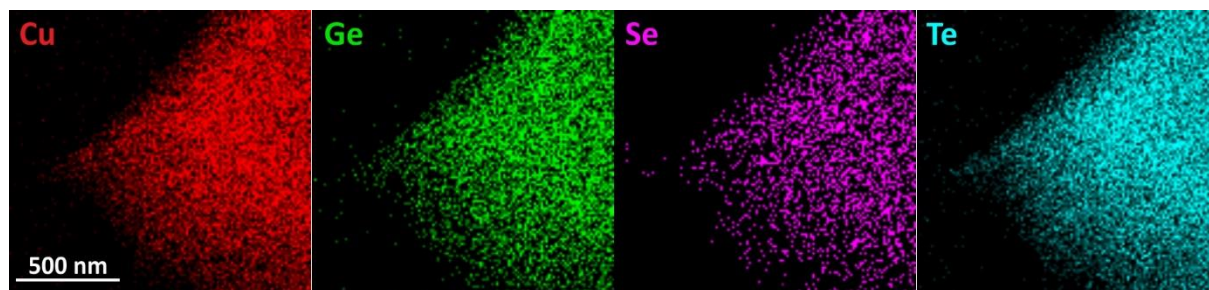


**Figure A3.3** STEM micrographs of GTS-Cu15 showing chemical mapping images, demonstrating homogeneous distribution of elements in the post-synthesized ingots.

**Table A3.1** Details of the Rietveld refinement and quantitative analysis results for GTS-Cu15

Phase	Cu <sub>2</sub> GeTe <sub>3</sub>	Te	GeTe
<b>Lattice</b>			
a (Å)	5.9188(9)	4.4626(7)	4.1714(9)
b (Å)	5.9188(9)	4.4626(7)	4.1714(9)
c (Å)	5.9188(9)	5.9194(10)	10.621(3)
Space group	Cubic $F\bar{4}3m$	Trigonal $P3_121$	Rhombohedral $R3m$
<b>Refinement</b>			
Nb. Background points	19		
Nb. Refined parameters	48		
Nb. Wyckoff positions	2	1	1
Nb. atoms	3	1	2
R <sub>Bragg</sub>	3.39	2.99	3.54
R <sub>f</sub> -factor	2.23	1.77	2.48
R <sub>p</sub>	13.0		
R <sub>wp</sub>	12.2		
R <sub>exp</sub>	8.74		
Chi2	1.94		
<b>Quantitative analysis</b>			
Weight content (%)	55.6 (0.8)	29.7 (0.5)	14.7 (0.6)

It is worth to mention that, both in Cu and Bi doped samples, high resolution EDX predicted the presence of very few Se (< 1.5 at%), indicating that it could have crystallized into the main phase. Considering its negligible proportion and closely similar diffraction peak positions with Te, it was not taken into account for Rietveld refinement.

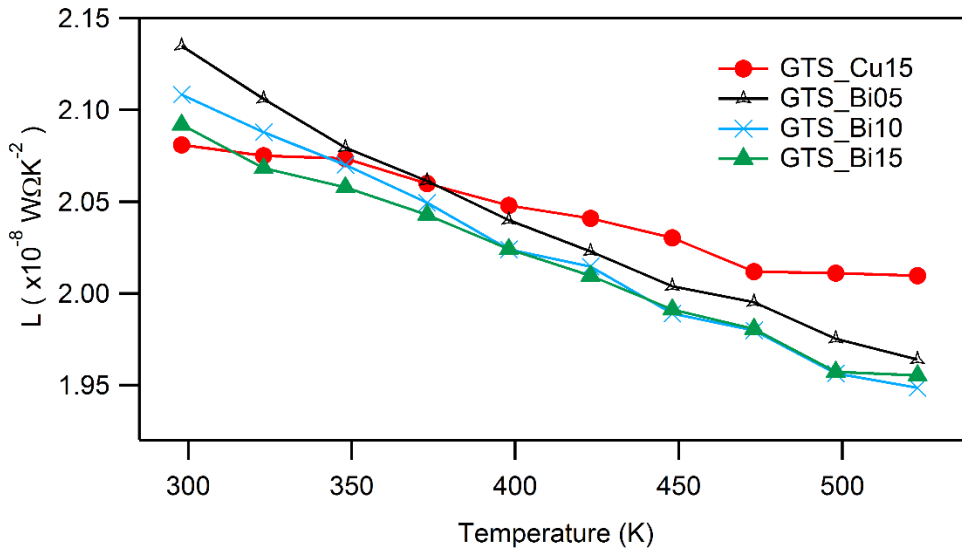


**Figure A3.4** Temperature dependent Lorenz number,  $L$  computed by the condensed version of Single Parabolic Band model with acoustic phonon scattering (SPB-APS).

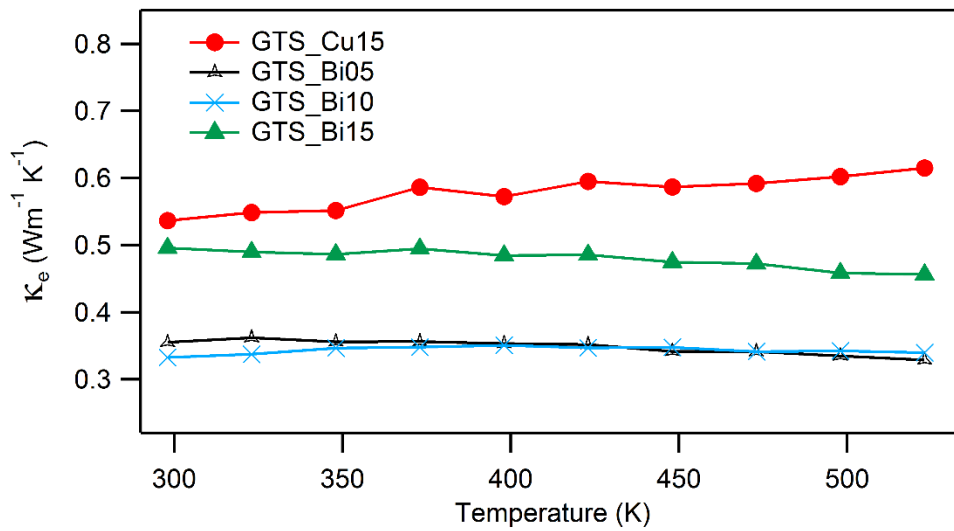


**Figure A3.5** Temperature dependent electronic thermal conductivity,  $\kappa_e$  calculated from Wiedmann-Franz law.

## Annexure 4

The room temperature electrical and thermal transport properties of constituent phases (for slow cooled  $\text{CuPb}_{18}\text{SbTe}_{20}$  sample) are presented in Table A4.1

**Table A4.1** Transport properties of constituent phases (at  $\sim 300$  K)

Phase	$\sigma$ (S/m)	S ( $\mu\text{V/K}$ )	$\kappa$ (W/mK)	Ref.
PbTe	$\sim 1.5 \times 10^4$	-300	$\sim 2.7$	[1-3]
$\text{Sb}_2\text{Te}_3$	$\sim 2.3 \times 10^4$	+150	$\sim 1$	[4,5]
$\text{Cu}_2\text{Te}$	$\sim 6 \times 10^5$	+30	$\sim 4$	[6]

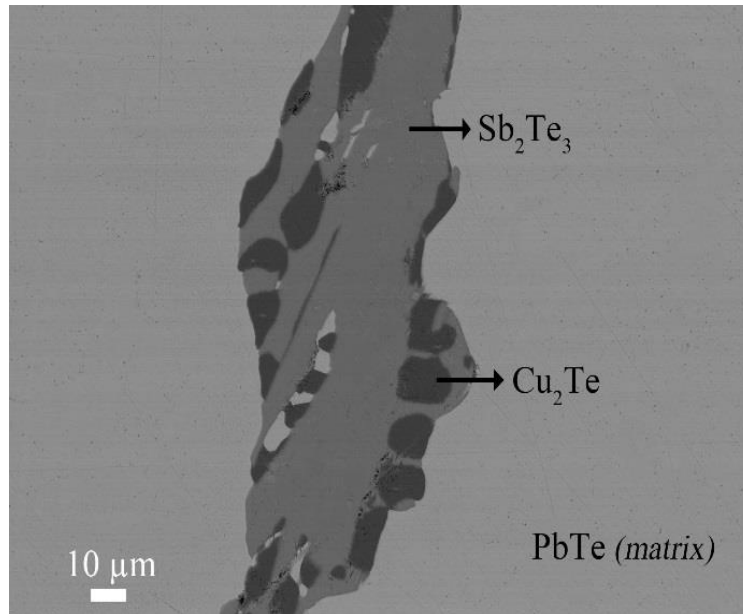


**Figure A4.2** SEM micrograph of slow cooled  $\text{CuPb}_{18}\text{SbTe}_{20}$  sample (SS) confirming the presence of secondary phases ( $\text{Sb}_2\text{Te}_3$  and  $\text{Cu}_2\text{Te}$ ) in the PbTe matrix (main phase).



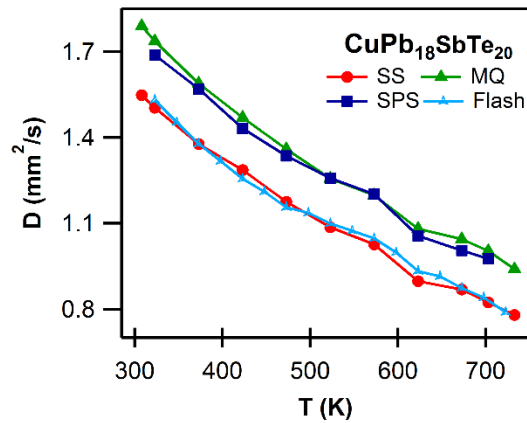


**Figure A4.3** Temperature-dependent thermal diffusivity ( $D$ ) for  $\text{CuPb}_{18}\text{SbTe}_{20}$  samples.

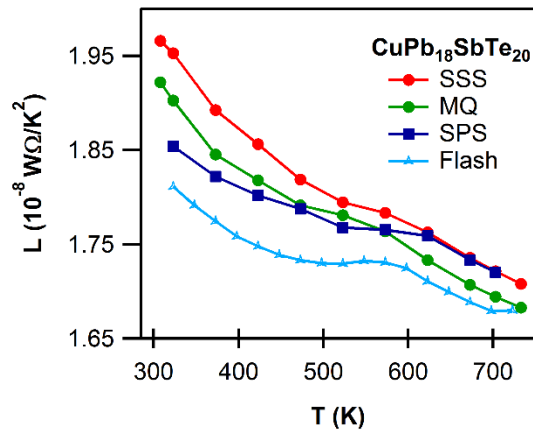


**Figure A4.4** Temperature dependence of the Lorenz number ( $L$ ) for  $\text{CuPb}_{18}\text{SbTe}_{20}$  samples, calculated by fitting the respective Seebeck coefficient values.

### Additional References

- [1] L.D. Borisova *et al.*, Phys. Status Solidi A. 61 (1980) K25–K28.
- [2] J.R. Sootsman *et al.*, Angew. Chem. Int. Ed. 48 (2009) 8616–8639.
- [3] Y. Pei *et al.*, Adv. Energy Mater. 4 (2014) 1400486.
- [4] G.-H. Dong *et al.*, J. Mater. Chem. 20 (2010) 1976–1981.
- [5] B. Srinivasan *et al.*, J. Alloys Compd. 729 (2017) 198–202.
- [6] S. Ballikaya *et al.*, J. Mater. Chem. A. 1 (2013) 12478–12484.

## Annexure 5

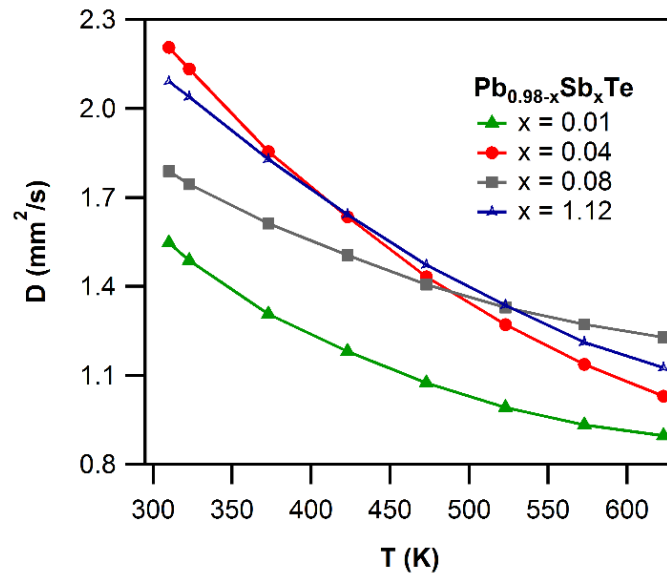


Figure A5.1 Thermal diffusivity,  $D$ , for Pb deficit  $\text{Pb}_{0.98-x}\text{Sb}_x\text{Te}$  ( $x = 0.01 - 1.12$ ) samples.

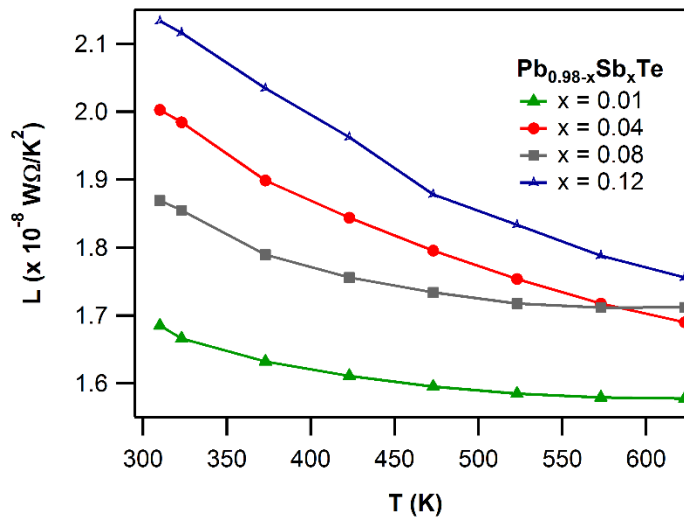
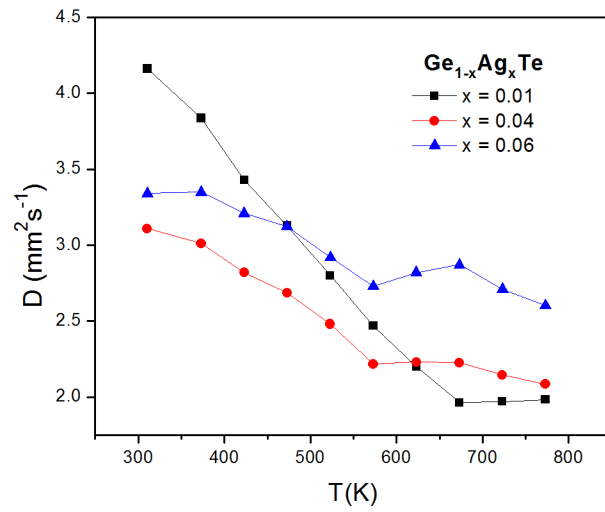
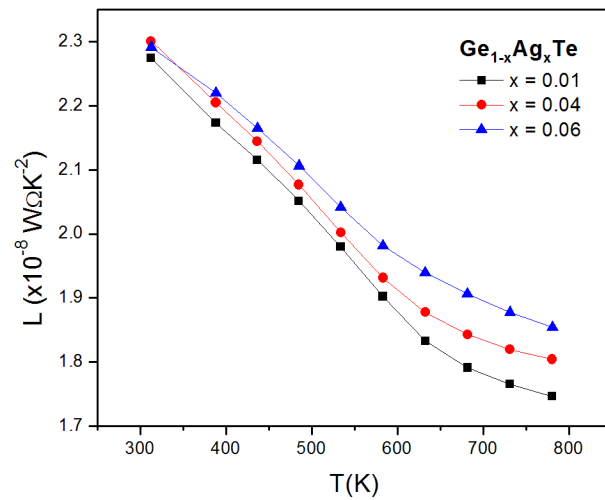


Figure A5.2 Lorenz number,  $L$ , for Pb deficit  $\text{Pb}_{0.98-x}\text{Sb}_x\text{Te}$  ( $x = 0.01 - 1.12$ ) samples.

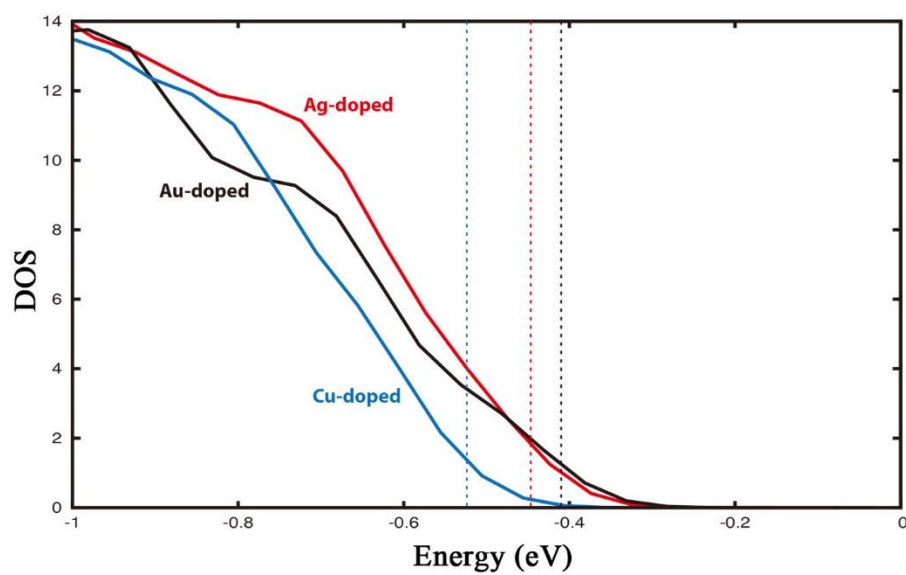
## Annexure 6



**Figure A6.1** Temperature-dependent thermal diffusivity ( $D$ ) for  $\text{Ge}_{1-x}\text{Ag}_x\text{Te}$  ( $x = 0.01 - 0.06$ ) samples.



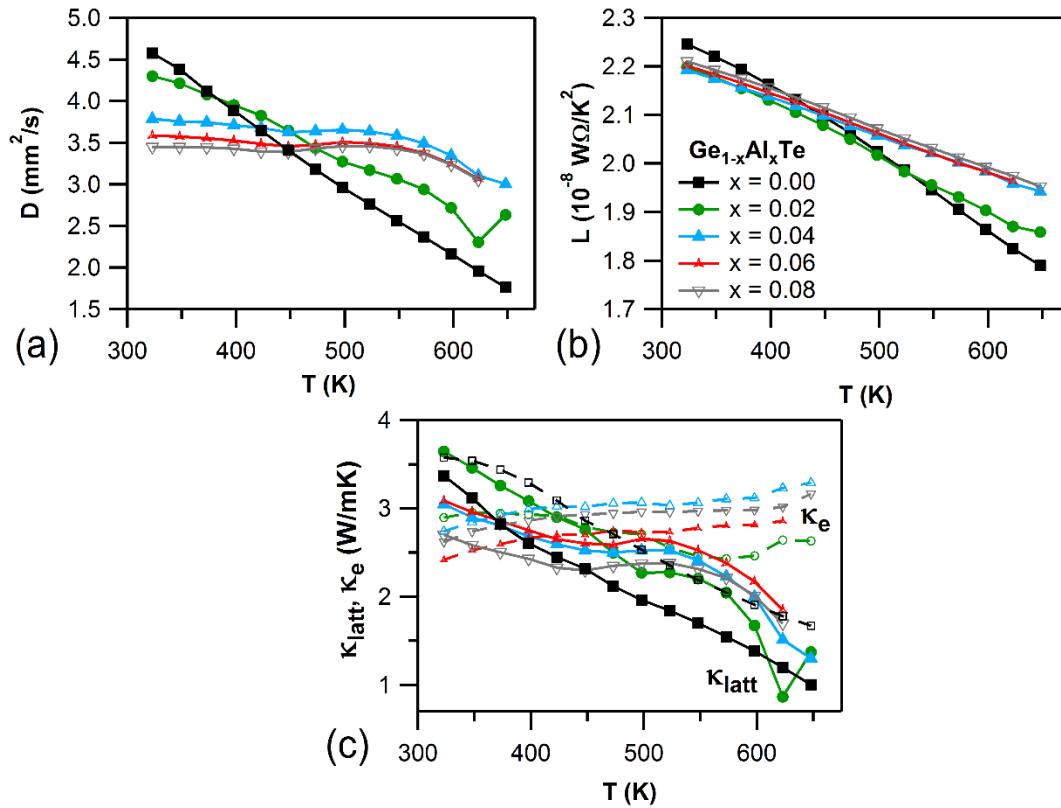
**Figure A6.2** Temperature dependence of the Lorenz number ( $L$ ) for  $\text{Ge}_{1-x}\text{Ag}_x\text{Te}$  ( $x = 0.01 - 0.06$ ) samples, calculated by fitting the respective Seebeck coefficient values.



**Figure A6.3** Density of states (DOS) with Fermi levels,  $E_F$  (dashed lines) for  $M_{0.042}Ge_{0.958}Te$  ( $M = Cu, Ag$  and  $Au$ ) model.

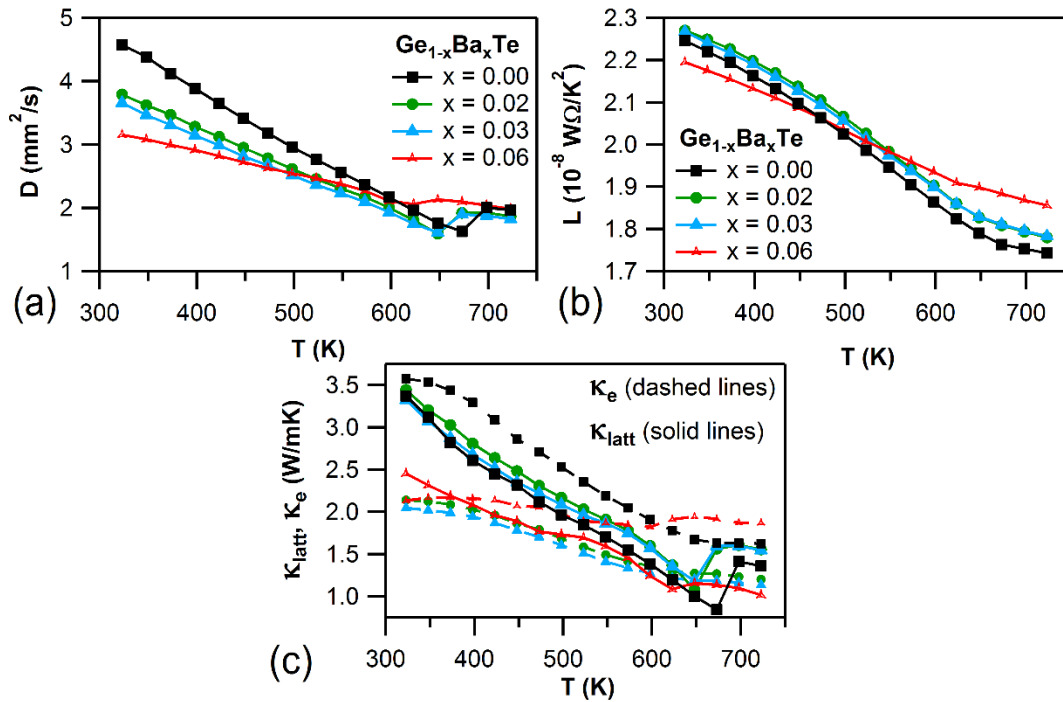
## Annexure 7

## A7.1 Al-doped GeTe System

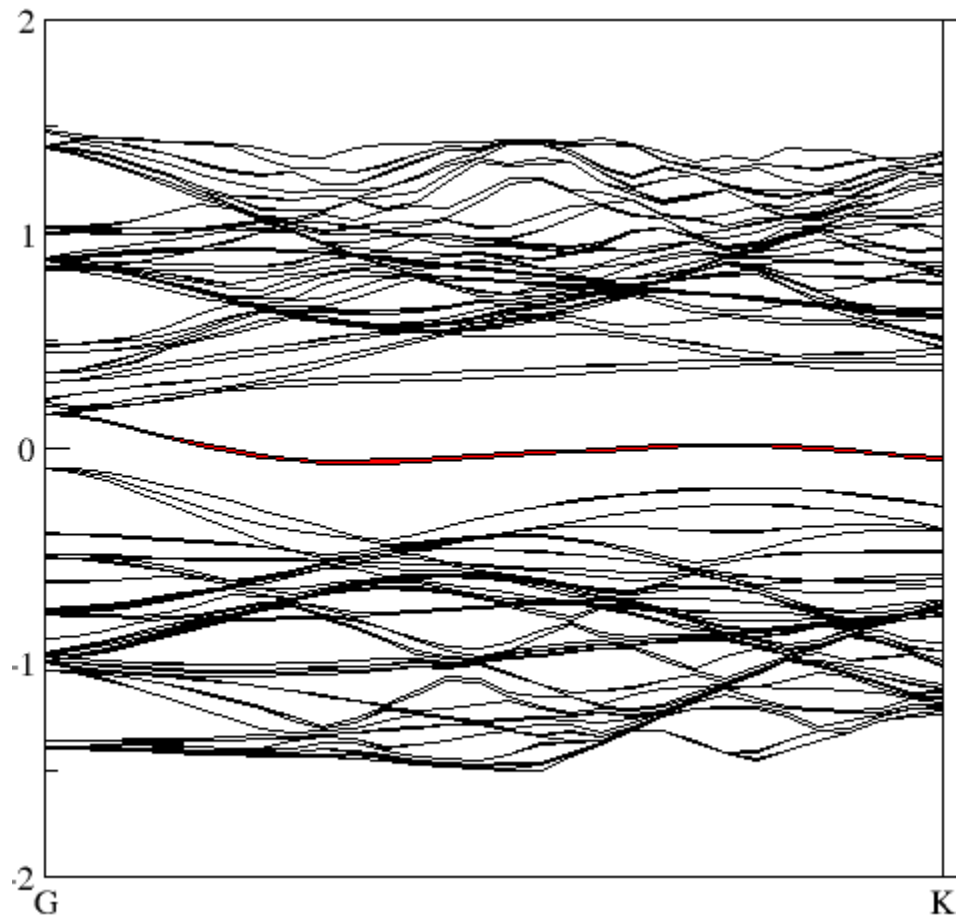


**Figure A7.1** Temperature dependence of (a) thermal diffusivity,  $D$ , (b) Lorenz number,  $L$ , (c) electronic and lattice thermal conductivities (solid lines represent  $\kappa_{\text{latt}}$ , while dashed lines represent  $\kappa_e$ ) for  $\text{Ge}_{1-x}\text{Al}_x\text{Te}$  ( $x = 0.00 - 0.08$ ) samples.

## A7.2 Ba-doped GeTe System



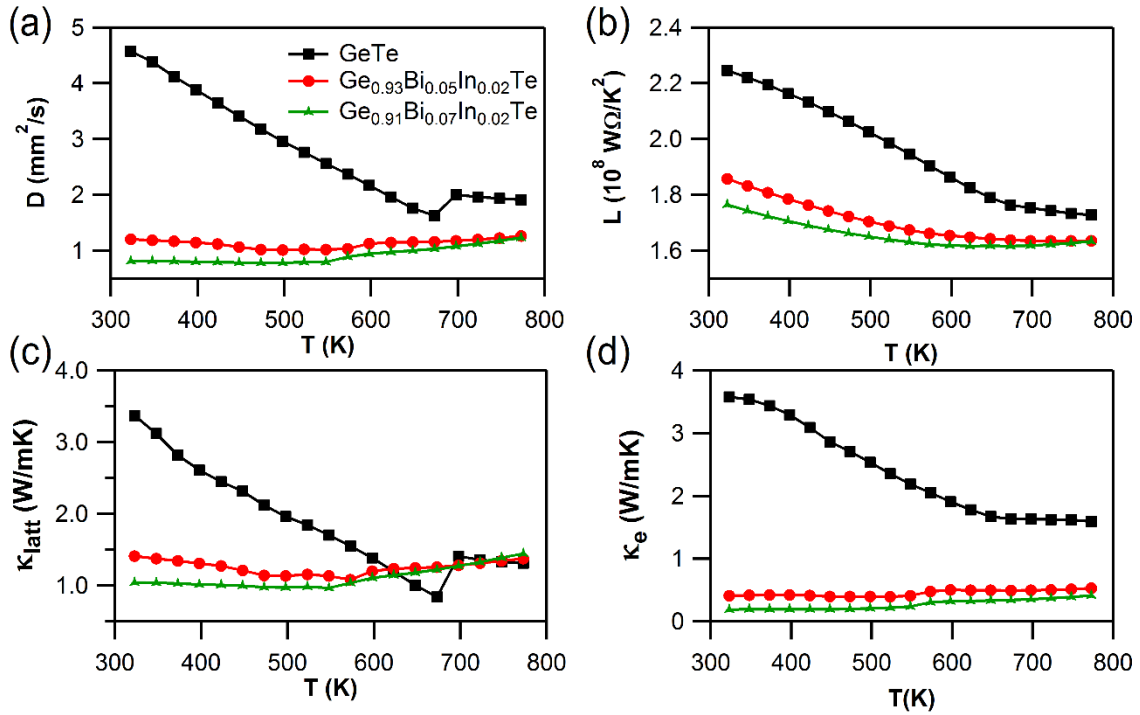
**Figure A7.2** Temperature dependence of (a) thermal diffusivity,  $D$ , (b) Lorenz number,  $L$ , (c) electronic and lattice thermal conductivities (solid lines represent  $\kappa_{\text{latt}}$ , while dashed lines represent  $\kappa_{\text{e}}$ ) for  $\text{Ge}_{1-x}\text{Ba}_x\text{Te}$  ( $x = 0.00 - 0.06$ ) samples.

**A7.3 Band Structure of In-doped GeTe**

**Figure A7.3** Band structure for  $\text{InGe}_{63}\text{Te}_{64}$  ( $\approx \text{Ge}_{0.98}\text{In}_{0.02}\text{Te}$ ) highlighting In projections (in red). The energy difference between the highest and second valence band is estimated to be  $\sim 95$  meV.

## Annexure 8

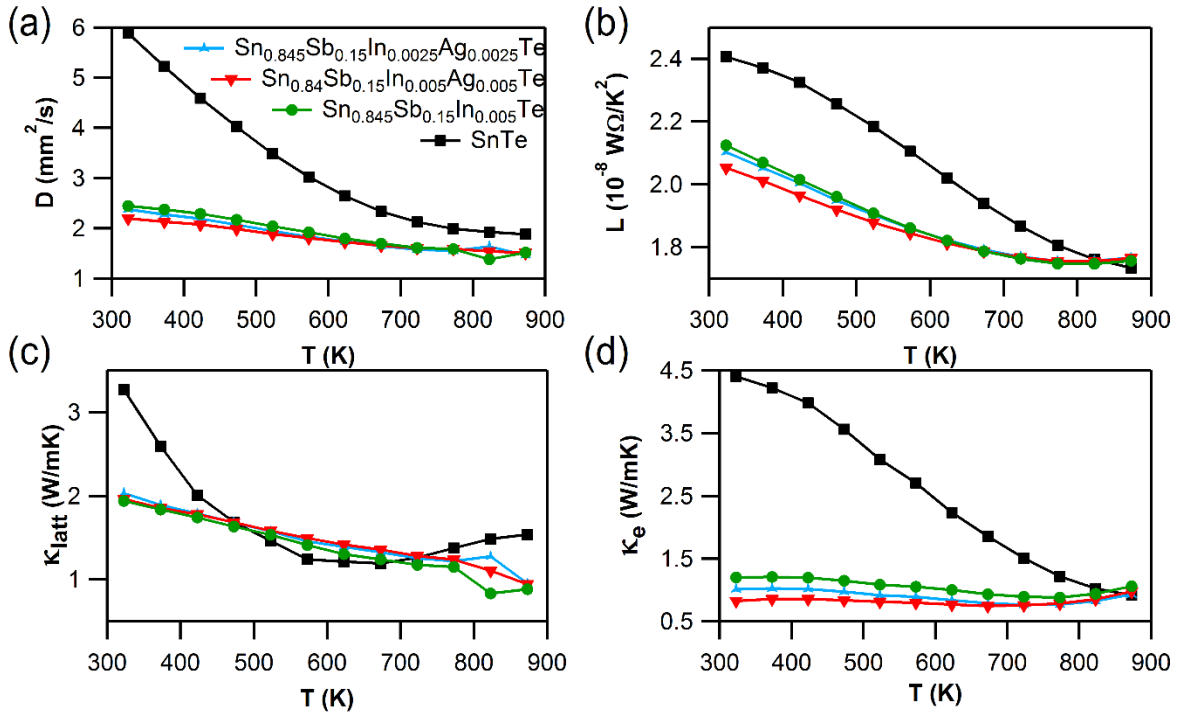
## A8.1 Thermal Transport in Bi and In codoped GeTe



**Figure A8.1** Temperature dependent, (a) thermal diffusivity,  $D$ , (b) Lorenz number ( $L$ ) calculated by fitting the respective Seebeck coefficient, (c) lattice thermal conductivity,  $\kappa_{\text{latt}}$  and (d) electronic thermal conductivity,  $\kappa_e$  for Bi and In codoped GeTe.

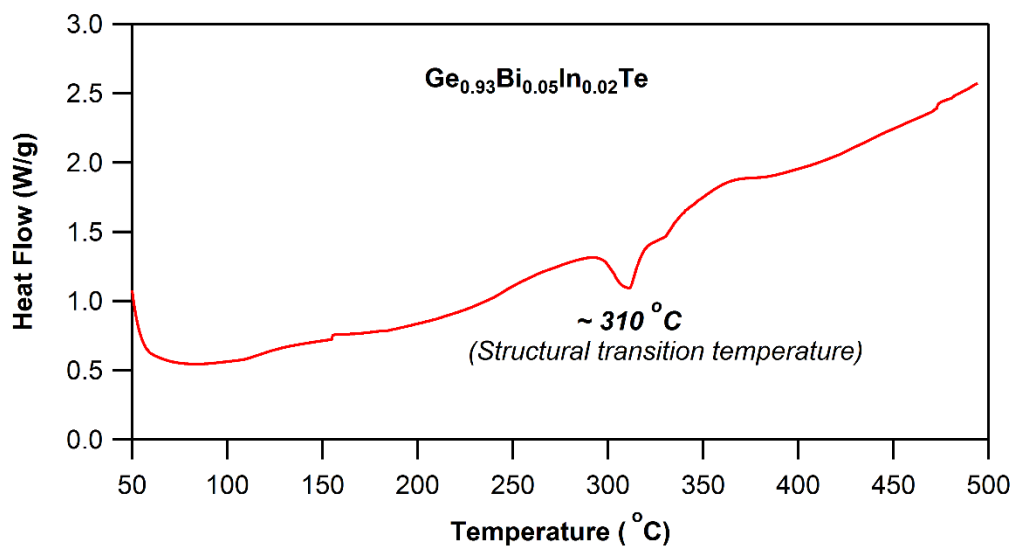


## A8.2 Thermal Transport in Sb, In and Ag codoped GeTe



**Figure A8.2** Temperature dependent, (a) thermal diffusivity,  $D$ , (b) Lorenz number ( $L$ ) calculated by fitting the respective Seebeck coefficient, (c) lattice thermal conductivity,  $\kappa_{\text{latt}}$ , and (d) electronic thermal conductivity,  $\kappa_e$  for Sb, In and Ag codoped SnTe.

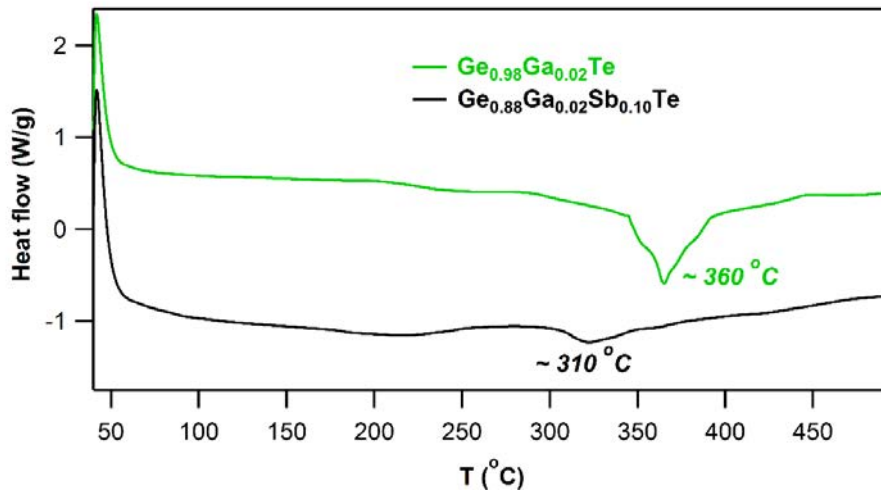
### A8.3 Phase Transition in Bi and In codoped GeTe



**Figure A8.3** DSC profile for  $\text{Ge}_{0.93}\text{Bi}_{0.05}\text{In}_{0.02}\text{Te}$  sample. The rhombohedral to cubic phase transition is observed at  $\sim 310^{\circ}\text{C}$ . It's more than  $100^{\circ}\text{C}$  lower than pristine GeTe, which clearly indicates that codoping of Bi and In to GeTe pushes the system towards cubic by favoring the  $R3m \rightarrow Fm-3m$  structural transition.

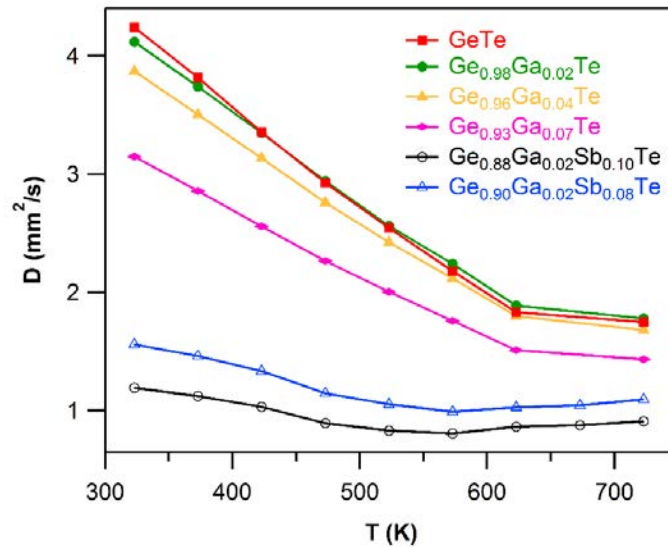
## Annexure 9

## A9.1 Phase Transition in Ga-doped and Ga-Sb codoped GeTe

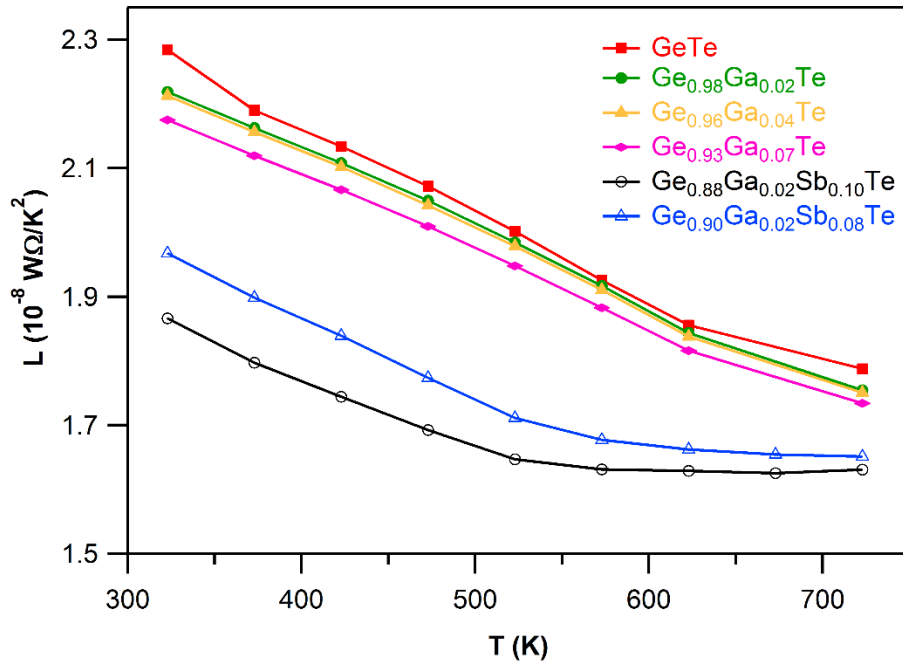


**Figure A9.1** DSC curves for  $\text{Ge}_{1-x}\text{Ga}_x\text{Te}$  ( $x = 0.02$ ) and  $\text{Ge}_{1-x-y}\text{Ga}_x\text{Sb}_y\text{Te}$  ( $x = 0.02$ ;  $y = 0.10$ ) samples. For pristine GeTe, the transition temperature was around 700 K, which reduces to 630 K for Ga-doped GeTe and further to 580 K for Ga-Sb codoped GeTe.

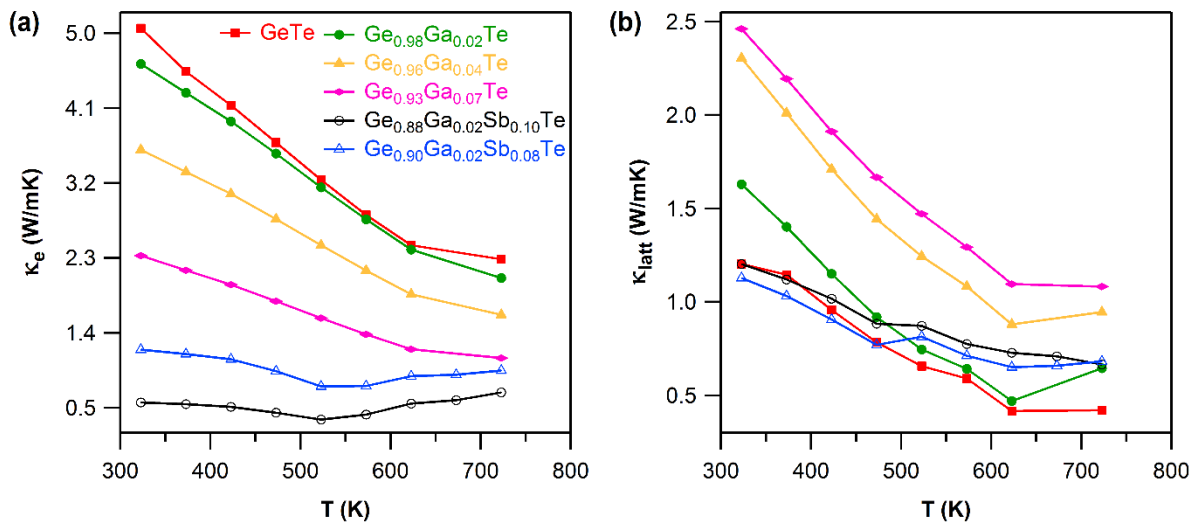
## A9.2 Thermal Transport in Ga-doped and Ga-Sb codoped GeTe



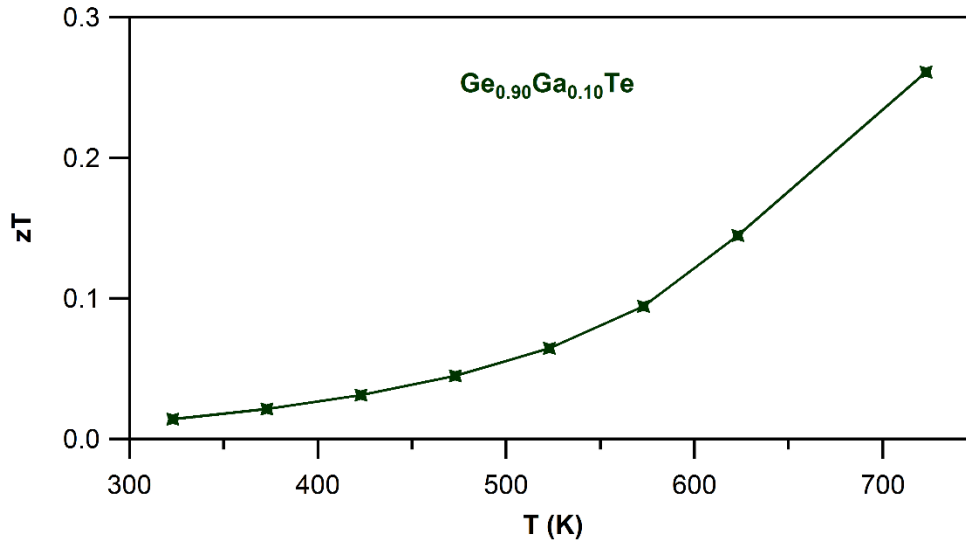
**Figure A9.2** Temperature-dependent thermal diffusivity,  $D$ , for  $\text{Ge}_{1-x}\text{Ga}_x\text{Te}$  ( $x = 0.00 - 0.07$ ) and  $\text{Ge}_{1-x-y}\text{Ga}_x\text{Sb}_y\text{Te}$  ( $x = 0.02$ ;  $y = 0.08, 0.10$ ) samples.



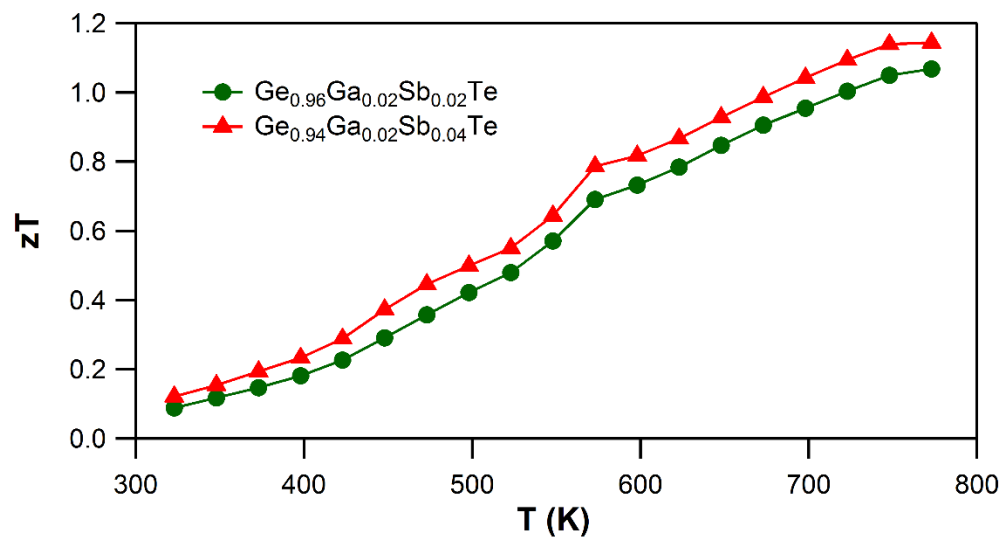
**Figure A9.3** Temperature dependence of the Lorenz number ( $L$ ) for  $Ge_{1-x}Ga_xTe$  ( $x = 0.00 - 0.07$ ) and  $Ge_{1-x-y}Ga_xSb_yTe$  ( $x = 0.02$ ;  $y = 0.08, 0.10$ ) samples, calculated by fitting the respective Seebeck coefficient values.



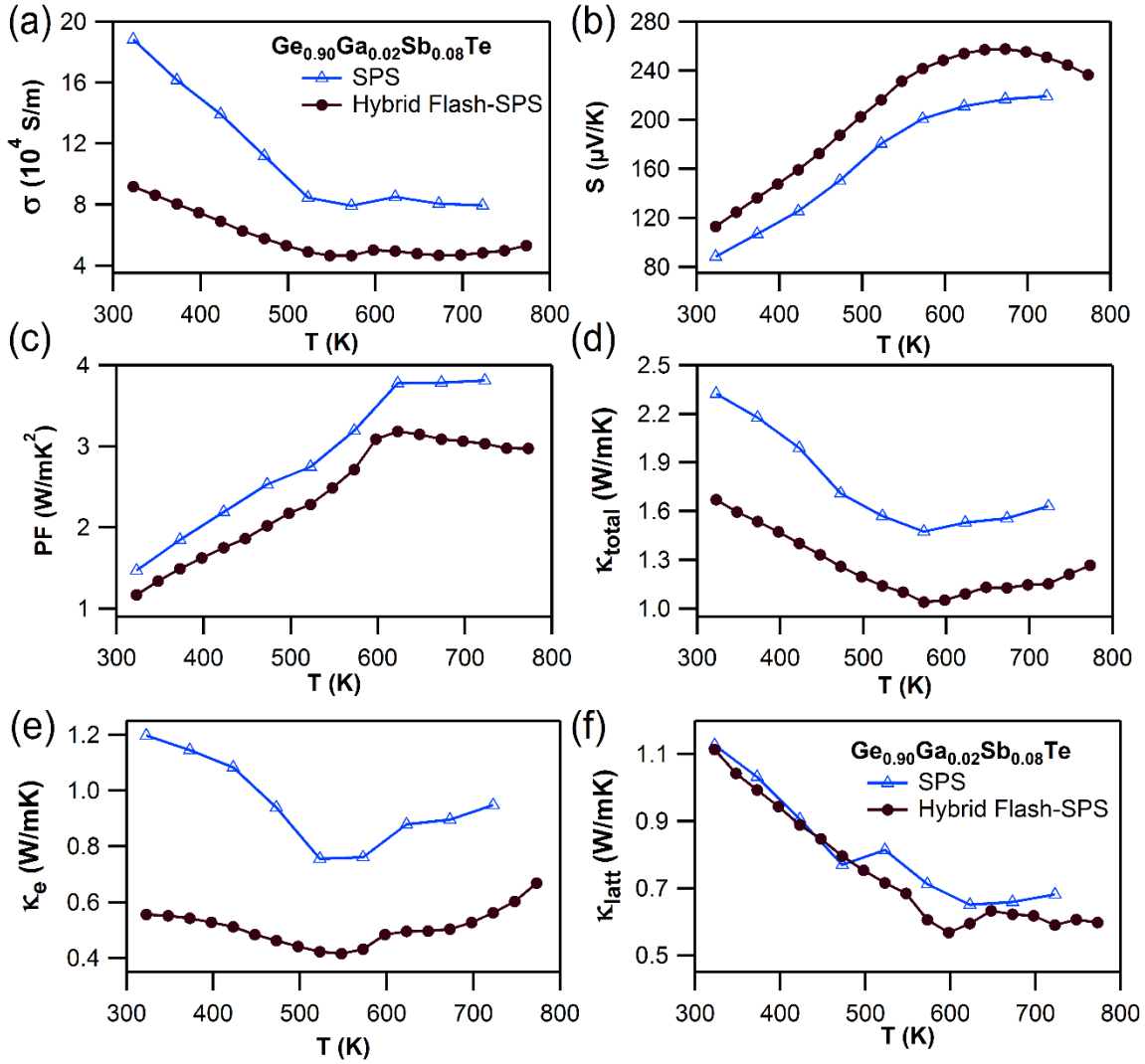
**Figure A9.4** Temperature-dependent (a) electronic ( $\kappa_e$ ) thermal conductivity and (b) lattice ( $\kappa_{latt}$ ) thermal conductivity, for  $Ge_{1-x}Ga_xTe$  ( $x = 0.00 - 0.07$ ) and  $Ge_{1-x-y}Ga_xSb_yTe$  ( $x = 0.02$ ;  $y = 0.08, 0.10$ ) samples.

**A9.3 Thermoelectric Performance of Heavily Ga-doped GeTe**

**Figure A9.5** Temperature-dependent figure of merit,  $zT$  for  $\text{Ge}_{1-x}\text{Ga}_x\text{Te}$  ( $x = 0.10$ ) sample.

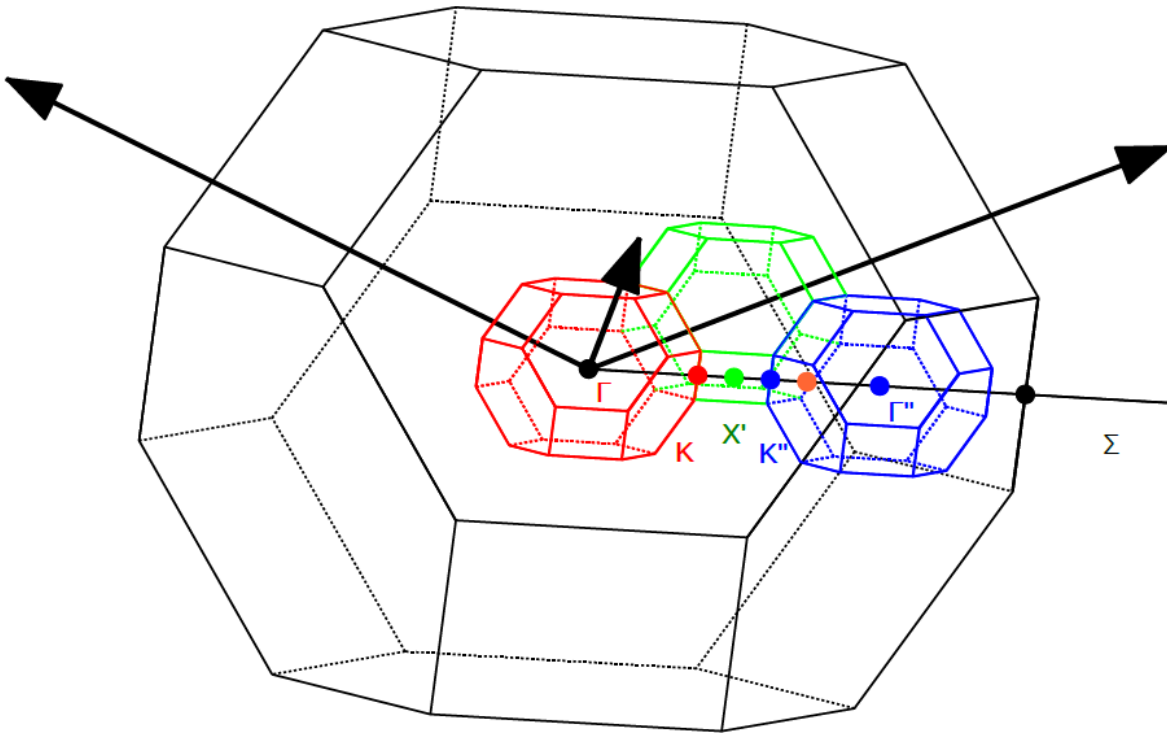
**A9.4 Thermoelectric Performance of Ga-Sb codoped GeTe (when Sb content is as low as Ga)**

**Figure A9.6** Temperature-dependent  $zT$  for  $\text{Ge}_{0.96}\text{Ga}_{0.02}\text{Sb}_{0.02}\text{Te}$  and  $\text{Ge}_{0.94}\text{Ga}_{0.02}\text{Sb}_{0.04}\text{Te}$  samples.

A9.5 Transport Properties for  $\text{Ge}_{0.90}\text{Ga}_{0.02}\text{Sb}_{0.08}\text{Te}$  – Hybrid Flash-SPS Vs SPS

**Figure A9.7** Temperature-dependent electrical and thermal transport properties for  $\text{Ge}_{0.90}\text{Ga}_{0.02}\text{Sb}_{0.08}\text{Te}$  sample prepared by SPS and Hybrid Flash-SPS.

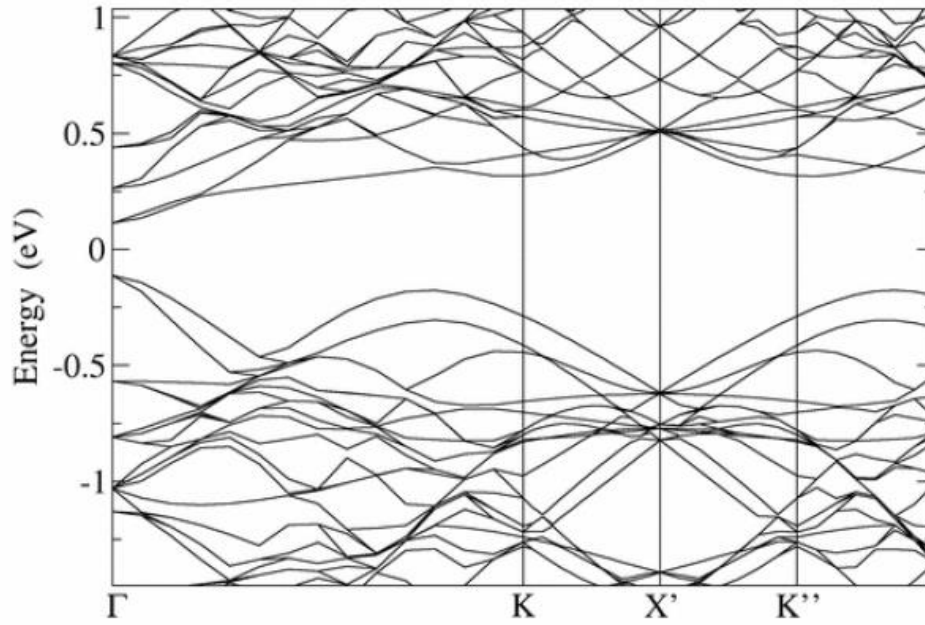
### A9.6 Band Folding in GeTe Super-cell



**Figure A9.8** Brillouin zone of the irreducible cell (black) and several Brillouin zones of the  $4 \times 4 \times 4$  c-GeTe super-cell (red, green, blue). The orange point indicates the approximate position of the second valence band maximum.

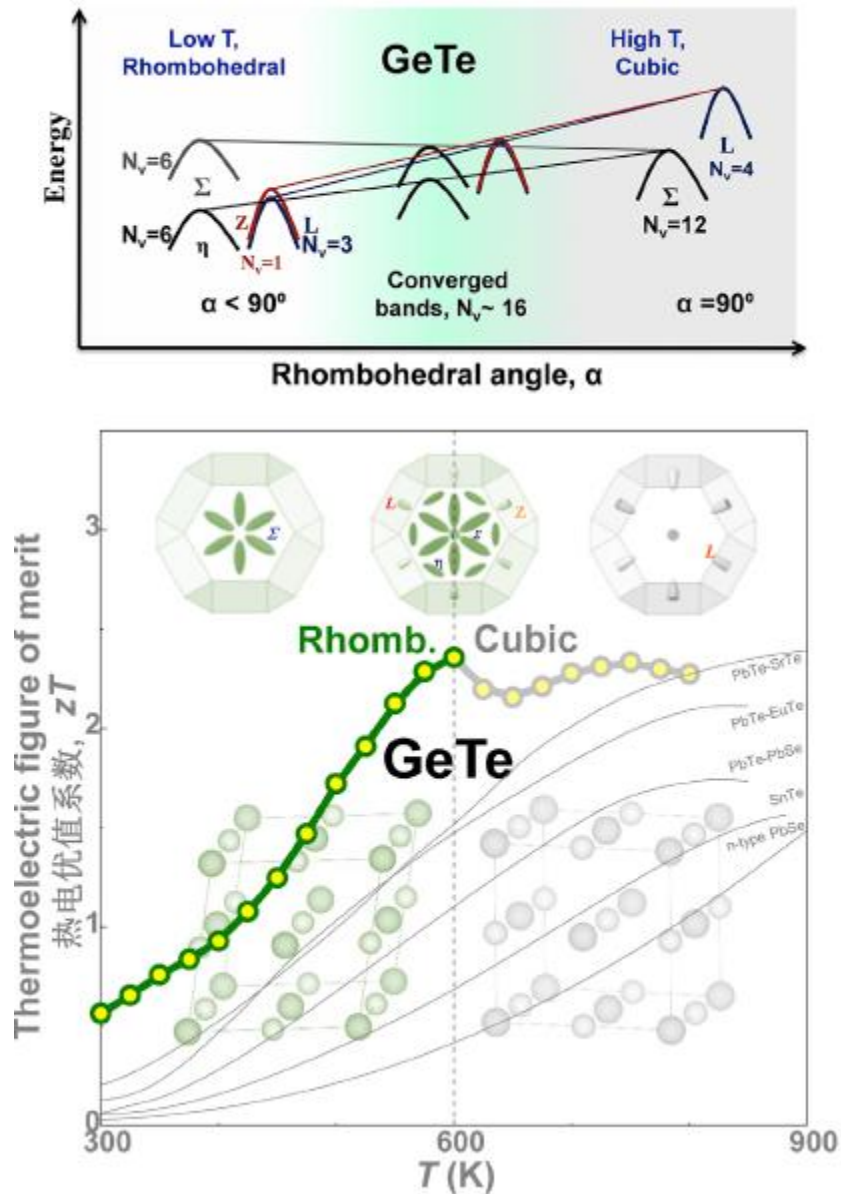
For the  $4 \times 4 \times 4$  c-GeTe super-cell, the reciprocal vectors (and the Brillouin zone) are four times smaller. To understand where the  $\Sigma$  direction is folded, one can draw the adjacent Brillouin zones. The  $\Sigma$  direction corresponds to a path  $\Gamma K X' K'' \Gamma''$  (where prime and double prime indicate nearest and next nearest Brillouin zone special points). What can be confusing is that the K point for the first zone (red) corresponds to the U' point of the adjacent zone (green).

To study the band structure of a super-cell in the  $\Sigma$  direction, one needs to represent the path  $\Gamma K X'$  (or equivalently the two paths  $\Gamma K$  and  $UX$ ). However, for the  $4 \times 4 \times 4$  super-cell, the maximum is located on the  $\Gamma K$  path, which is the one that is actually considered in our computations. But the case of  $3 \times 3 \times 3$  super-cell is quite different, where the maximum is located on the  $UX$  path.



**Figure A9.9** Band structure of the  $4 \times 4 \times 4$  c-GeTe super-cell along the  $\Sigma$  direction. The L maximum is folded on the  $\Gamma$  point. The second maximum is located just after the  $K''$  point and is thus folded just before the K point.



A9.7 Low Symmetry Rhombohedral GeTe:  $zT$  Enhancement by Slight Reduction in Symmetry

**Figure A9.10** Very recently, Pei and coworkers showed that by increasing the rhombohedral angle (a measure of the degree of directional lattice distortion along  $[111]$ ), particularly through codoping with Pb and Bi, they were able to achieve a favorable band structure (green shaded region in top figure) for improved electronic performance. Combining the advantage of good electronic performance with a lower inherent lattice thermal conductivity, Pei et al., realized a  $zT \sim 2.4$  at 600 K in rhombohedral domain of Pb-Bi codoped GeTe (Figure 1B). This  $zT$  achieved in Pb-Bi codoped r-GeTe is much higher than any of its cubic analogs. *Image courtesy:* © Joule – Cell Press (Pei et al., Joule 2, 976–987, May 2018).

## A9.8 Unsuccessful Trials

### A9.8.1 Based on crystalline GeTe and SnTe (that are not presented in this thesis)

Some of the unsuccessful results that were obtained during my PhD are not presented in this thesis. Such unsuccessful doping experiments includes the following,

- (i) Mg-doped GeTe
- (ii) Gd-doped GeTe
- (iii) Al-doped SnTe
- (iv) Ba-doped SnTe
- (v) Gd-doped SnTe.

### A9.8.2 Based on glasses (that are not presented in this thesis)

Some unsuccessful experiments to improve the thermoelectric properties in the glasses includes the following,

- (i)  $\text{Sn}_{20-x}\text{Ga}_x\text{Se}_{80}$  ( $x = 0 - 5$ )
- (ii)  $(\text{As}_{33}\text{Al}_{20}\text{Te}_{47})_{97-x}\text{Se}_3\text{Cu}_x$  ( $x = 0 - 10$ )
- (iii)  $\text{Ge}_{20}\text{Se}_{80-x}\text{Bi}_x$  ( $x = 0 - 10$ )

## A9.9 Promising Trials based on GeTe (that are not presented in this thesis)

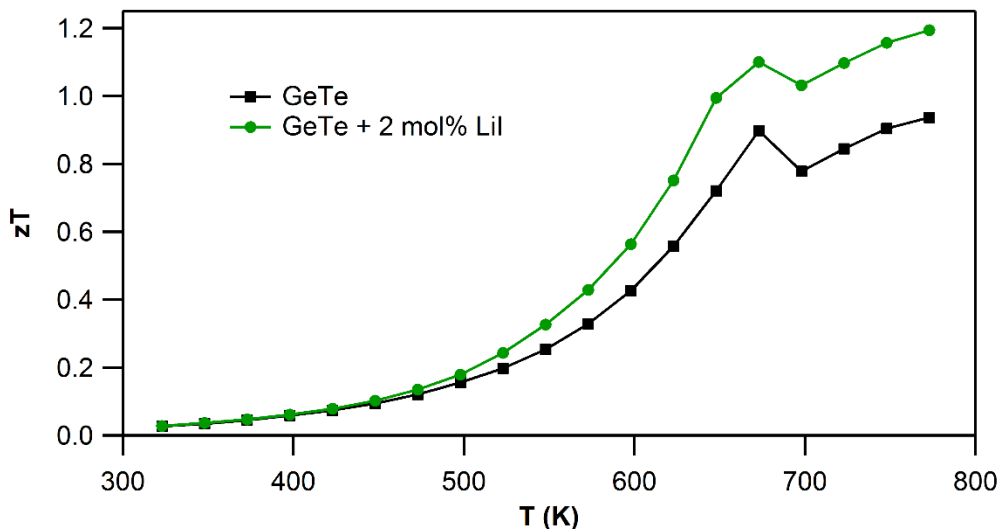


**Figure A9.11** Temperature-dependent figure of merit,  $zT$  for 2 mol% Lil doped GeTe (this was a trial experiment that I did in June 2018) → results look promising, should be explored further (by varying the content of Lil) in future.



## **Short CV – Bhuvanesh Srinivasan**



# Bhuvanesh Srinivasan

Equipe V&C, ISCR UMR 6226, Bat 10B, Office 254/2  
Campus Beaulieu, Université de Rennes 1  
263 Avenue du General Leclerc  
35042 Rennes, France

Phone (O) : +33223233688 ; Mobile : +33751382797  
[bhuvanesh.srinivasan@univ-rennes1.fr](mailto:bhuvanesh.srinivasan@univ-rennes1.fr) /  
[s.bhuvanesh5@gmail.com](mailto:s.bhuvanesh5@gmail.com)  
Skype : bhuvanesh.srinivasan1

---

<b>Education</b>	Oct 2015 – Dec 2018	PhD in Materials Science Carried out in the framework of <b>European Commission's Horizon 2020</b> research & innovation program under the Marie Skłodowska-Curie ITN actions – <a href="#">CoACH-ETN</a> University of Rennes 1 (ISCR CNRS UMR 6226), France. Advisors: <a href="#">Prof. Bruno Bureau</a> , <a href="#">Dr. Catherine Boussard</a> (Rennes) Industrial Advisor: <a href="#">Prof. Mike Reece</a> , Nanoforce, QMUL (London)
	Mar 2015 – Aug 2015	Master Thesis (Supervisor - <a href="#">Prof. Paul Bowen</a> ) Dept. of Materials Engineering, EPFL Lausanne, Switzerland. Grade: 1.0 (German system; Equiv. to 6.0 in Swiss system)
	Oct 2014 – Feb 2015	Erasmus Mundus Master (M2) in Materials Science (MaMaSELF) Ludwig Maximilian & Technical Univ. Munich, Germany. Overall Grade: 1.61 (German system)
	May 2014 – Jul 2014	Master 1 Internship (Supervisor - <a href="#">Prof. Jeroen von Bokhoven</a> ) Inst. for Chemical & Bioengineering, ETH Zurich, Switzerland. GPA: 9/10
	Sep 2013 – Apr 2014	Erasmus Mundus Master (M1) in Materials Science (MaMaSELF) University of Rennes 1, France. CGPA: 14.54/20
	Aug 2009 – Jul 2013	Bachelor of Engineering in Materials Science & Metallurgy College of Engineering Guindy, Anna Univ., Chennai, India. CGPA: 8.58/10; First Class with Distinction

---

## Publications

- [1] [B. Srinivasan](#), S. Cui, C. Prestipino, A. Gellé, C. Boussard-Pledel, S. Ababou-Girard, A. Trapananti, B. Bureau, S. Di Matteo, *Possible Mechanism for Hole Conductivity in Cu-As-Te Thermoelectric Glasses: A XANES and EXAFS Study*, *J. Phys. Chem. C* 121 (2017) 14045–14050. [DOI: 10.1021/acs.jpcc.7b04555](https://doi.org/10.1021/acs.jpcc.7b04555).
- [2] [B. Srinivasan](#), C. Boussard-Pledel, V. Dorcet, M. Samanta, K. Biswas, R. Lefèvre, F. Gascoin, F. Cheviré, S. Tricot, M. Reece, B. Bureau, *Thermoelectric Properties of Highly-Crystallized Ge-Te-Se Glasses Doped with Cu/Bi*, *Materials* 10 (2017) 328. [DOI: 10.3390/ma10040328](https://doi.org/10.3390/ma10040328).
- [3] A. Kumar, B.J. Walder, A. Kunhi Mohamed, A. Hofstetter, [B. Srinivasan](#), A.J. Rossini, K. Scrivener, L. Emsley, P. Bowen, *The Atomic-Level Structure of Cementitious Calcium Silicate Hydrate*, *J. Phys. Chem. C* 121 (2017) 17188–17196). [DOI: 10.1021/acs.jpcc.7b02439](https://doi.org/10.1021/acs.jpcc.7b02439).
- [4] [B. Srinivasan](#), F. Gucci, C. Boussard-Pledel, F. Cheviré, M.J. Reece, S. Tricot, L. Calvez, B. Bureau, *Enhancement in thermoelectric performance of n-type Pb-deficit Pb-Sb-Te alloys*, *J. Alloys Compd.* 729 (2017) 198–202. [DOI: 10.1016/j.jallcom.2017.09.135](https://doi.org/10.1016/j.jallcom.2017.09.135).
- [5] [B. Srinivasan](#), R. Gautier, F. Gucci, B. Fontaine, J.-F. Halet, F. Cheviré, C. Boussard-Pledel, M.J. Reece, B. Bureau, *Impact of Coinage Metal Insertion on the Thermoelectric Properties of GeTe Solid-State Solutions*, *J. Phys. Chem. C* 122 (2018) 227–235. [DOI: 10.1021/acs.jpcc.7b10839](https://doi.org/10.1021/acs.jpcc.7b10839).
- [6] M.R. Andalibi, A. Kumar, [B. Srinivasan](#), P. Bowen, K. Scrivener, C. Ludwig, A. Testino, *On the mesoscale mechanism of synthetic calcium-silicate-hydrate precipitation: a*

population balance modeling approach, *J. Mater. Chem. A* 6 (2018) 363–373. DOI:10.1039/C7TA08784E.

[7] B. Srinivasan, C. Boussard-Pledel, B. Bureau, *Thermoelectric performance of codoped (Bi, In)-GeTe and (Ag, In, Sb)-SnTe materials processed by Spark Plasma Sintering*, *Mater. Lett.* 230 (2018) 191–194. DOI:10.1016/j.matlet.2018.07.132.

[8] B. Srinivasan, B. Fontaine, F. Gucci, V. Dorcet, T.G. Saunders, M. Yu, F. Cheviré, C. Boussard-Pledel, J.-F. Halet, R. Gautier, M.J. Reece, B. Bureau, *Effect of the Processing Route on the Thermoelectric Performance of Nanostructured CuPb<sub>18</sub>SbTe<sub>20</sub>*, *Inorg. Chem.* 57 (2018) 12976–12986. DOI:10.1021/acs.inorgchem.8b02248.

[9] B. Srinivasan, A. Gellé, J.-F. Halet, C. Boussard-Pledel, B. Bureau, *Detrimental Effects of doping Al and Ba on the Thermoelectric Performance of GeTe*, *Materials* 11 (2018) 2237. DOI:10.3390/ma11112237.

[10] B. Srinivasan, A. Gellé, F. Gucci, C. Boussard-Pledel, B. Fontaine, R. Gautier, J.-F. Halet, M.J. Reece, B. Bureau, *Realizing a Stable High Thermoelectric  $zT \sim 2$  over a Broad Temperature Range in Ge<sub>1-x-y</sub>Ga<sub>x</sub>Sb<sub>y</sub>Te via Band Engineering and Hybrid Flash-SPS Processing*, *Inorg. Chem. Front.* (2018) In press. DOI:10.1039/C8QI00703A.

[11] T. Zhang, Z. Wang, B. Srinivasan, Z. Wang, J. Zhang, K. Li, C. Boussard-Pledel, J. Troles, B. Bureau, L. Wei, *Ultra-Flexible Glassy Semiconductor Fibers for Thermal Sensing and Positioning*, *ACS Appl. Mater. Interfaces* (2018) In press. DOI:10.1021/acsami.8b20307.

[12] A. Kumar, B. Srinivasan, A.K. Mohamed, D. Lambert, G. Massonnet, K. Scrivener, P. Bowen, *Controlled synthesis and characterization of homogeneous Calcium Silicate Hydrates phase with high Calcium to Silicate ratio*, Submitted to *Cem. Concr. Res.*

---

## Conferences

[1] Annual Seminar of the French Ceramic Society (GFC), 21<sup>th</sup>-23<sup>th</sup> March, 2017, Rennes, France. [Oral]

[2] 15<sup>th</sup> International Conference on Advanced Materials (IUMRS-ICAM), 27<sup>th</sup> August – 1<sup>st</sup> September 2017, Kyoto University, Kyoto, Japan. [Oral]

[3] 37<sup>th</sup> International Conference on Thermoelectrics (ICT), 1<sup>st</sup>-5<sup>th</sup> July, 2018, Caen, France. [Oral]

[4] 15<sup>th</sup> International Conference on the Physics of Non-Crystalline Solids (PNCS-ESG), 9<sup>th</sup>-13<sup>th</sup> July 2018, Saint-Malo, France. [Poster Contribution / Presented by Dr. Catherine Boussard-Pledel].

---

## Academic Activities during PhD

- Tutor: Mentored and supervised the undergraduate students (2 L3, 1 M1 and 1 M2) in their thesis work and internships.
- Editorial Assignments: Has peer reviewed for Journal of Materials Chemistry A (RSC), Journal of Materials Science (Springer), and Journal of Alloys & Compounds (Elsevier). Publons ID: [publons.com/a/1453302/](https://publons.com/a/1453302/)

---

## Additional Info

Date of Birth	04-November-1991 (Pollachi, India)
Nationality	Indian
Native Language (Mother tongue)	Tamil
Hobbies & Interests	Cricket, Politics, History, Travelogues
ORCID & Researcher ID	<a href="https://orcid.org/0000-0002-4472-2780">0000-0002-4472-2780</a> & <a href="https://orcid.org/E-4045-2017">E-4045-2017</a>
LinkedIn Profile	<a href="https://www.linkedin.com/in/bhuvanesh-srinivasan-578a66164">bhuvanesh-srinivasan-578a66164</a>





**Titre :** Développement de verres, vitro-céramiques et céramiques de chalcogénures pour des applications en thermoélectricité

**Mots clés :** Thermoélectricité, Chalcogénures, Nano-structuration, Dopage, Ingénierie de bandes, GeTe

**Résumé :** L'intérêt porté au développement de matériaux thermoélectriques est grandissant car ils permettent de créer des sources d'énergie renouvelable, dites « vertes », ce qui s'inscrit pleinement dans la stratégie de lutte contre le réchauffement climatique. A ce jour le rendement de tels systèmes reste faible, le coût de développement élevé, et les plages de températures d'utilisation sont limitées. Dans ces travaux de thèse différentes pistes sont explorées pour développer des matériaux innovants à base de chalcogènes, principalement le tellure.

Les principaux résultats portent sur les points suivants. (i) Une étude par spectroscopies couplée à des calculs théoriques a permis de mieux comprendre les phénomènes de conduction dans les verres du système Cu-As-Te. (ii) La recristallisation complète de verres de formulation  $Ge_{20}Te_{77}Se_3$  dopés a été réalisée pour pousser à son terme la logique dite du Phonon Glass Electron Crystal (PGEC).(iii) Différents modes de

synthèses ont été mis en œuvre pour suivre les propriétés thermoélectriques de matériaux de formulation  $CuPb_{18}SbTe_{20}$  (frittage, SPS, flash-SPS, hybrid flash-SPS). (iv) Accroissement de 170% des performances d'alliage du système Pb-Sb-Te en générant des vacances de sites (composés non-stœchiométriques). (v) Le suivi des conséquences du dopage de GeTe par un seul élément a montré la nécessité d'un co-dopage pour simultanément accroître la conductivité électronique et le Seebeck. (vi) Le co-dopage In-Bi de GeTe a permis de créer des niveaux résonants (In) et d'accroître la diffusion thermique (Bi). (vii) Enfin, le résultat le plus remarquable porte sur le co-dopage Ga-Sb de GeTe qui permet d'effectuer de l'ingénierie de structure de bandes. Couplé à une synthèse par hybrid flash SPS ces matériaux prometteurs permettent d'obtenir un  $zT \sim 2$  sur une large gamme de température (600–773 K).

**Title :** Novel Chalcogenide based Glasses, Ceramics and Polycrystalline Materials for Thermoelectric Application

**Keywords :** Thermoelectrics, Chalcogenides, Material Processing, Nanostructuring, Band Engineering, GeTe

**Abstract :** With the performance of direct conversion between thermal and electrical energy, thermoelectric materials, which are crucial in the renewable energy conversion roadmap, provide an alternative for power generation and refrigeration to solve the global energy crisis. But the low efficiency of the current materials, their usual costs, availability, and limited working temperatures, drastically constrain their application. Hence, the search for new and more efficient thermoelectric materials is one of the most dynamic objectives of this thesis.

The key milestones achieved from this thesis work includes: (i) elucidating the mechanism for hole conductivity in Cu-As-Te glasses by X-ray absorption spectroscopy and quantum simulations; (ii) formulating a novel approach to achieve phonon-glass electron-crystal mechanism by crystallizing the  $Ge_{20}Te_{77}Se_3$  glasses by excess doping with metals or semi-metals (glass-ceramics); (iii) demonstrating the effect of processing route

on the thermoelectric performance of  $CuPb_{18}SbTe_{20}$  and highlighting the advantage of hybrid flash-spark plasma sintering technique, *i.e.*, better optimization of electrical and thermal transport properties and achieving multi-scale hierarchical architectures; (iv) improving the thermoelectric performance of Pb-Sb-Te alloys (enhancement by ~170%) by tuning their cation vacancies (Pb deficiencies); (v) understating the impact of doping just a group-11 coinage metal, or group-13 element on GeTe solid-state solution and recapitulating the need for pair substitution; (vi) substantially enhancing the average  $zT$  of In-Bi codoped GeTe; (vii) achieving a remarkably high and stable  $zT$  of close to 2 over a wide temperature range (600 – 773 K) by manipulating the electronic bands in Ga-Sb codoped GeTe, which has been processed by hybrid flash-SPS, thus making it a serious candidate for energy harvesting systems.